Bell, Christopher James (2014) *Mechanical loss of fused silica fibres for use in gravitational wave detectors*. PhD thesis.

http://theses.gla.ac.uk/5274/

Mechanical Loss of Fused Silica Fibres for use in Gravitational Wave Detectors

Christopher James Bell MSci

School of Physics and Astronomy

College of Science and Engineering

University of Glasgow

Presented as a thesis for the degree of

Doctor of Philosophy

2014

c.bell.physics.gla@gmail.com

Contents

List of Figures

List of Tables

Acknowledgements

The work presented in this thesis was made possible by the many people who gave their time, patience and wisdom to help me out. I am honoured to have had the opportunity to work and be fully involved with the research undertaken at the Institute of Gravitational Research (IGR) in the University of Glasgow. The Institute's work in the field of gravitational wave astronomy has been of huge interest both to learn about and to be involved with.

Firstly, I would like to thank my supervisor, Dr Giles Hammond. I am grateful to him for the help and guidance he has offered me over the years and also for his willingness to take me on as his student. It has been great to work with someone like Giles who is hard working and has an ability to understand difficult concepts and create solutions to the experimental challenges which have arisen throughout the course of my PhD. His ability to understand difficult concepts and to explain them in a simplified fashion was of great benefit to me. I would also like to thank Professor Sheila Rowan, my second supervisor for giving me the opportunity to carry out the research presented in this thesis and for her continued support and guidance without which none of this research would have been possible. Both supervisors have also been very supportive in encouraging me to travel and present my work at conferences. I have been fortunate to have had have two supervisors who are widely known and respected, both in and outside their field of research. Even more impressively both supervisors, although extremely busy, have always been easily contactable and free to speak to me when I needed their assistance. Thank you again to both supervisors. Professor James Hough should also be mentioned as he has been involved with discussions and provided very helpful decisions about my work. I would also like to thank STFC for helping to secure the funding to carry out my PhD studies. Without this I would not have been able to participate in such incredible and challenging research.

A big thank you to everyone I have worked with over the years. I would like to thank Dr Rahul Kumar, Dr Alan Cumming and Dr Liam Cunnigham for their advice and patience in teaching me how to build and analyse models and suspensions in ANSYS. Dr Stuart Reid, Dr Iain Martin, Dr Angus Bell and Dr Marielle Veggel gave freely their help, support and advice during my time at the IGR. Stuart deserves a special mention as the work described in chapters 3 and 6 had prototype experiments built by Stuart before he moved to the Thin Film Research Centre at the University of West of Scotland. Without his input the work presented in these chapters would be more in the form of an experimental design chapter than one containing valuable experimental results. A special thank you to Dr Kirill Tokmakov who has always shown an interest in my research and, when most needed, has offered me practical help with suspension set-ups. He is also a good friend and I have enjoyed his company over the years. Thank you to Dr Jamie Scott for his IT support and endless supply of floppy disks needed to record data from old spectrum analysers. Great help and support was also given from the research group technicians, Colin Craig, Stevie Craig, Steven O'Shea and Alastair Grant. Russell Jones and Michael Perreur-Lloyd have been a huge help during the construction stages of the experiments. They provided excellent support in producing Solidworks drawing and other engineering solutions. I would also like to thank Dr Matt Pitkin for his help with writing data analysis codes and also for his useful discussions on analysing data. The secretarial staff also helped me out when dealing with finances and travel so thank you to Jenny Anderson, Jean Greig, Karen Hegyi and Ethel Folan.

My office mates both past and present made the ”sky pitt” a fun place to be: Dr Matt Abernathy, Dr Riccardo Bassiri, Dr Nicola Beverage, Dr Paul Campsie, Kieran Craig, Rebecca Douglas, Dr Keith Evans, Martin Hart, Dr Karen Haughian, Jan Hennig, Sean Leavey, Valentina Mangano, Richard Middlemiss, Dr Peter Murray and Raymond Robie. I do, however, feel sorry for whoever has to take my desk when I leave as Richard, Kieran and Rayray are probably already thinking up pranks to play on them.

There are many people within the group that I did not share an office with but to whom I am grateful to have spent time with: Sheena Barclay, Bryan Barr, Neil Gordon, Professor Martin Hendry, Alasdair Houston, Dr Stefan Hild, Yiming Hu, Dr Christian Killow, Josh Logue, John Macarthur, Dr Chris Messenger, Dr Gail Penny and Dr Borja Sorazu to name but a few. They have all been there to talk to and to take my mind off things when they went wrong in the lab.

On a personal note I would like to thank my mum Joyce, dad William and brother Adam for their unconditional love and support through out my eight and a half years as a student. I would also like to thank my friends, both from home and from university for being great craic. A special thank you goes to my girlfriend Catriona who has given me love and support throughout my entire PhD and has had to put up with me continuously leaving her and running into the lab to push buttons.

Preface

This thesis is an account of work carried out at the Institute for Gravitational Research (IGR). In the University of Glasgow between October 2010 and March 2014. The research presented contributes to the design of ultra-low mechanical loss suspensions for use in gravitational wave detectors and other kinds of interferometry. This thesis focusses on measuring the parameters of mechanical loss in fused silica suspensions that will limit the sensitivity of advanced gravitational wave detectors and other kinds of interferometers where fused silica suspensions are used. These investigations were carried out under the supervision of Dr Giles Hammond and Professor Sheila Rowan.

Chapter 1 gives an introduction to gravitational wave astronomy and provides an insight into which astrophysical objects are able to emit gravitational radiation. The chapter goes on to describe current and future detection techniques that are used and planned in order to make the first direct detection of gravitational waves, noting some results and limits which have been achieved to date. The chapter also introduces the different noise sources that will limit the sensitivity of gravitational wave detectors. The information detailed in this chapter has all been derived from previously published literature.

Chapter 2 introduces the theory of thermal noise and derives the relationship between the mechanical loss and thermal noise in fused silica suspensions via the fluctuation dissipation theorem. Discussion covers how this limits the sensitivity of a gravitational wave detector. The chapter includes the theory of loss mechanisms present in fused silica. Again the information contained in this chapter has all been derived from previously published literature.

Chapter 3 contains details and results of an experiment, where the expansion coefficient of fused silica fibres was measured under varying amounts of stress. Results demonstrate that the effective thermal expansion co-efficient of a fused silica fibre can be nulled by placing the fibre under a particular level of stress. This nulling of the effective thermal expansion coefficient should lower the thermoelastic noise contribution in silica suspensions, essential for allowing second generation gravitational wave detectors to reach their target thermal noise sensitivity of below $10^{-19}\,\mathrm{m}/\sqrt{\mathrm{Hz}}$ at 10 Hz. The experimental work in this chapter was conceived by Professor James Faller with a prototype demonstrated by Dr Stuart Reid. The set-up was then revised and modified by the author and Dr Giles Hammond to achieve the results presented in this thesis. Throughout this experiment Colin Craig helped with the machining of the invar set-up and Dr Kirill Tokmakov with suspending the silica fibres placed under large amounts of stress. Experimental measurements and analysis were carried out by the author.

Chapter 4 describes an experiment in which a fused silica fibre was held under tension and the harmonic violin mode losses over a range of frequencies were measured. The fibre was then cut and cantilever modes of the fibre measured. The contributions from excess losses were calculated and shown not to limit the experiment. A theoretical dilution factor was determined along with the modal strain distribution of the violin and cantilever modes from finite element analysis (FEA). The FEA was aided by Dr Rahul Kumar and Dr Alan Cumming. The data measured was then compiled with a loss model to give information about the loss contributions of fused silica such as thermoelastic loss, surface loss and weld loss. Designing of the silica pendulum system used in this experiment was helped by Russell Jones and the machining of the silica mass holders for CO2 welding was done by Steven Craig. Construction of the silica pendulum system was undertaken by Dr Giles Hammond and the author, who carried out the experimental measurements. Analysis of the data presented in this chapter was aided by Dr Matthew Pitkin who contributed a Markov Chain Monte Carlo regression fitting code.

Chapter 5 repeats the above experiment; where the author used a modified fused silica fibre to measure violin mode losses. The modified silica fibre allowed loss measurements to be made at a much lower frequency than in the previous violin mode set-up. In an attempt to study the nonlinear thermoelastic loss in more detail. The stress on the silica was also varied to observe the nulling of the effective thermal expansion coefficient directly through measurements of the mechanical loss. This experiment used many of the components described in chapter 4 and so the same people are acknowledged for their contribution. Construction of the silica pendulums used was carried out by Dr Giles Hammond, Dr Kirill Tokmakov and the author.

Chapter 6 focusses on measuring the mechanical loss of 20-30μm diameter fused silica fibres, for use in the Hannover AEI 10 m prototype interferometer. This chapter illustrates the problems faced when trying to measure the mechanical losses of thin fibres. The mechanical loss data was then compiled with a loss and finite element model to give information about the loss contributions of fused silica such as thermoelastic, surface and weld loss in thin silica fibres. This experiment was constructed initially by Dr Stuart Reid with some of the welding being performed by Dr Kirill Tokmakov. All of the experimental measurements and analysis were the work of the author.

Chapter 7 details the conclusions that can be drawn from the various experiments in previous chapters.

The results will be be applicable across many areas of research where low mechanical thermal noise is required. More generally the results can be used as a basis for research that requires mechanical systems at room temperatures for example systems needed to produce stable optical cavities. A further important discovery emerging from this thesis is the ability to cancel and reverse the effective thermal expansion coefficient of fused silica by placing the silica under stress. This process allows stressed silica to be used in systems were low thermal expansion coefficient materials are needed. Thus fused silica can be used as an alternative to composite materials such as invar.

Summary

In 1916 Albert Einstein, wrote his General Theory of Relativity [1]. In this theory he predicted that fluctuations in the gravitational field would propagate at the speed of light. These fluctuations in gravity can be thought of as ripples in the curvature of space-time known as gravitational waves. These gravitational waves were first viewed indirectly, when Hulse and Taylor [2] measured the inspiral rate of a binary star system. Since then research towards direct detection of gravitational radiation from astrophysical sources has been ongoing for many years but to date no direct detection of these gravitational waves has been achieved. More recently in 2014 an experimental detection of the B-mode polarisation present in Cosmic Microwave Background Radiation (CMBR) was made using the BICEP2 detector [3] stationed at the south pole. The amount of polarisation that was measured is concluded to have been produced from gravitational waves produced shortly after the Big Bang during a period of rapid inflation [4]. This indirect observation of gravitational radiation has once again help fuel the search for a direct detection.

Gravitational waves are quadrupole in nature, and produce a tidal strain in space, they also interact very weakly with matter. This makes them difficult to detect but makes them less likely to be attenuated when traveling through matter unlike electromagnetic radiation. The strain amplitude h predicted for gravitational waves that may be detected on Earth are of the order of $h \sim 10^{-22}$ to 10^{-23} (in the frequency range from 10 Hz to a few kHz) for the most violent astrophysical events [5]. To directly detect these small strain amplitudes an international collaboration of long baseline interferometers are being used; such as the two LIGO detectors in America [6], the GEO600 detector in Germany [7] and the Virgo detector in Italy [8].

Two of the detectors are currently being upgraded from LIGO to Advanced LIGO [9–14] and Virgo to Advanced Virgo [15–17], while GEO600 remains in "astrowatch" mode. These detectors all use fused silica suspensions to hang the end test mass mirrors as part of their design. This thesis focusses on measuring directly the mechanical loss in fused silica suspensions. Mechanical loss is important for gravitational wave detectors as it tells us exactly how the suspension thermal noise is limiting the sensitivity of the gravitational wave detector via the fluctuation dissipation theorem. It is hoped that the results presented in this thesis can be used to give accurate information about the suspension thermal noise estimates for gravitational wave detectors and other systems such as the AEI 10 m prototype in Hannover [18, 19] where fused silica suspensions are also used.

Chapter 1

The Origin of Gravitational Waves

1.1 The Historical Perspective of General Relativity

Newton's laws of Gravity were first published in his famous book the "Philosophiae Naturalis Principia Mathematica" on the 5th of July 1687 [20]. The laws were so powerful that they remained unchanged for 200 years with little question that they could possibly be flawed. In 1864 James Clerk Maxwell released his paper "A Dynamical Theory of the Electromagnetic Field" [21]. In this paper he proposed that the motion of charges produced electric and magnetic fields which propagated through space as waves, perpendicular to each other and traveling in the same direction at the constant speed of light. His proposal, propagation of a field traveling at a constant speed of light, disagreed with the Newtonian way of thinking where "action at a distance" was widely accepted. Newton's laws always assumed that if there was change in a field at the source then the effect would be felt everywhere instantly rather than taking time to propagate. Newton's laws of gravity could also not explain the orbital path taken by Mercury as each year the perihelion of Mercury's orbit was found to change at a rate of 42"(arc seconds) per century. This was the first evidence that there were shortcomings within Newton's laws.

It was Albert Einstein who started to question the Newtonian way of thinking when in 1905 he revealed to the world his theory of special relativity [22]. Until then both space and time had been thought of as constant with everyone experiencing the same passage of time around them no matter their frame of reference. Einstein's way of thinking was that instead of time being the constant, which everyone must adhere to, we should instead think that the speed of light is constant in all frames. In 1887 Albert Michelson and Edward Morley showed with their famous Michelson-Morley experiment [23] that the speed of light from the Sun was observed as being constant no matter whether the Earth was moving towards or away from the Sun. This way of thinking was revolutionary. The new concept proposed that when we observe something moving in a frame relative to us, its length will contract and its time will pass more slowly. Only the speed at which light propagates will remain constant for both frames of reference. In turn this refuted the Newtonian idea of absolute space and absolute time; now everything was relative and Maxwell's laws had the same mathematical form in all reference frames. This new idea proposed that nothing can travel faster than the speed of light and that mass can be converted into energy. The paper declaring this concept was sent to *Annalen der Physik* where it was passed as acceptable and published. The theory was named special relativity as it could only be used in special cases where gravity was not important, a point which no doubt troubled Einstein and would do so for a further ten years.

During 1909-1911, Einstein's attention had strayed to the world of atoms, but in mid 1911 he returned to the idea that gravity somehow warped space-time. Hermann Minkowski who was Einstein's mathematics professor at Eidgenössiche Technische Hochschule (ETH) had built on Einstein's notion that space and time were relative to give a four dimensional "space-time". Einstein had the idea that gravity was a manifestation of space-time curvature. It was his friend Marcel Grossmann, by then a professor of Mathematics, who led Einstein to read about Bernhard Riemann, Gregorio Ricci and Tullio Levi-Civita's work on what is today called "tensor analysis". Using tensor analysis Einstein could now let mass or energy warp space-time to describe how gravity works as represented in figure 1.1.

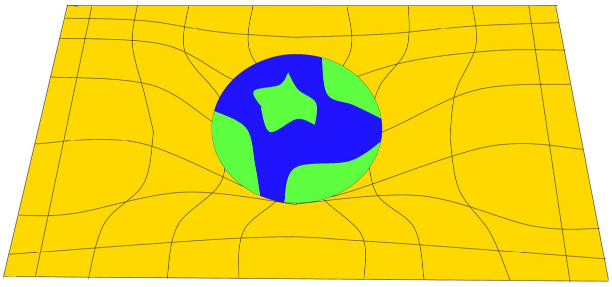

Figure 1.1: *A 2D generalisation of the warping effect of gravity on space-time around a planet or large mass*

In 1916, Einstein's theory of General Relativity was published [1]. The theory showed that the gravitational field propagates at the speed of light. This concept conflicted with Newtonian gravity in which the gravitational field propagates instantly over an infinite distance. In Einstein's theory any object moving through space-time simply follows a geodesic, the shortest path in the curved space-time which describes the gravitational interaction. In this sense matter 'tells' space-time how to warp (figure 1.1) and space-time tells matter how to move. This was described mathematically first by David Hilbert in what is known today as "Einstein's Field Equation"

$$R_{\mu\nu} - \frac{1}{2} g_{\mu\nu} R + g_{\mu\nu} \lambda = \frac{8\pi G}{c^4} T_{\mu\nu}. \tag{1.1}$$

Here $R_{\mu\nu}$ is the Ricci curvature tensor describing the local curvature in space-time, μ and ν are positive integer value numbers used to represent the different components of the tensors, R the scalar curvature, $g_{\mu\nu}$ the metric tensor, λ is the cosmological constant, G is Newton's gravitational constant, c the speed of light and $T_{\mu\nu}$, is the stress-energy tensor. The implications of this equation were significant as they predicted the bending of starlight around large masses, an effect known as gravitational lensing. This prediction was later confirmed by observations made by Sir Arthur Eddington during the solar eclipse on the 29th of May 1919 [24]. The orbital path taken by Mercury could also now be correctly described to include the observed perihelion shift, something that Newton's laws of gravity failed to do (figure 1.2).

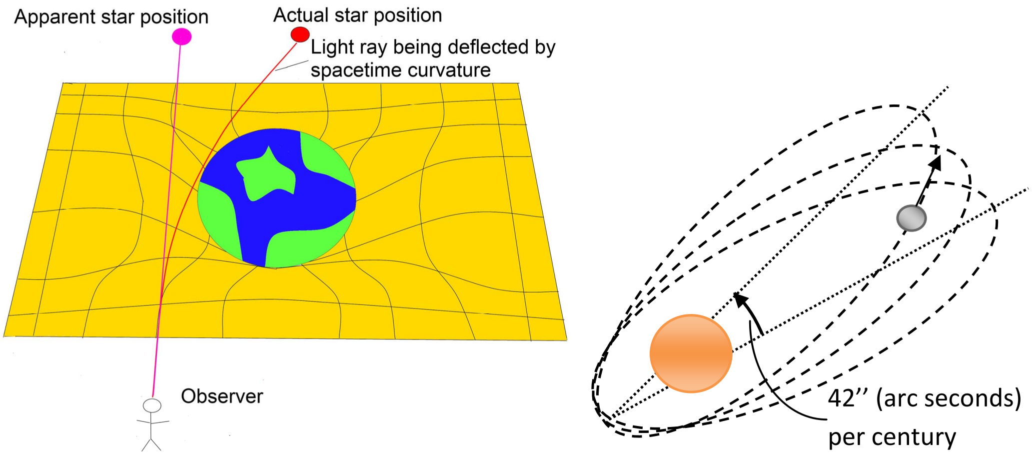

Figure 1.2: *Left: How light from distant stars is deflected by the curvature of spacetime. Right: The perihelion shift of Mercury being 42" (arc seconds) per century*

In 1974, Russell Hulse and Joseph Taylor discovered a pulsar rotating around a neutron star and measured the radio wave emissions. The pulsar is now known as PSR1913+16 [2]. A pulsar is a neutron star which is rotating and has an extremely strong magnetic field whose axis is not aligned with rotational axis. As a result electrons in the star are accelerated, producing a beam of energetic particles and electromagnetic waves forced out of their magnetic poles. If this beam intersects with the Earth the star appears to be pulsing like clockwork. Repeated measurements of the radio wave emissions over many years showed that as the the pair of objects rotated around their center of mass the period of rotation was not constant but in fact speeding up. This showed that the system was losing energy resulting in an inspiral of the binary system. The energy loss from the system was thought to come from gravitational wave emission, a direct prediction from Einstein's theory. When the predicted inspiral rate was compared with the observed value they were found to match within 1% accuracy [2, 25, 26]. These measurements, shown in figure 1.3, provided indirect evidence of gravitational radiation and in 1993 Hulse and Taylor were awarded the Nobel Prize for Physics. Their findings fueled a major international search for direct detection of gravitational waves, discussed later in section 1.4.

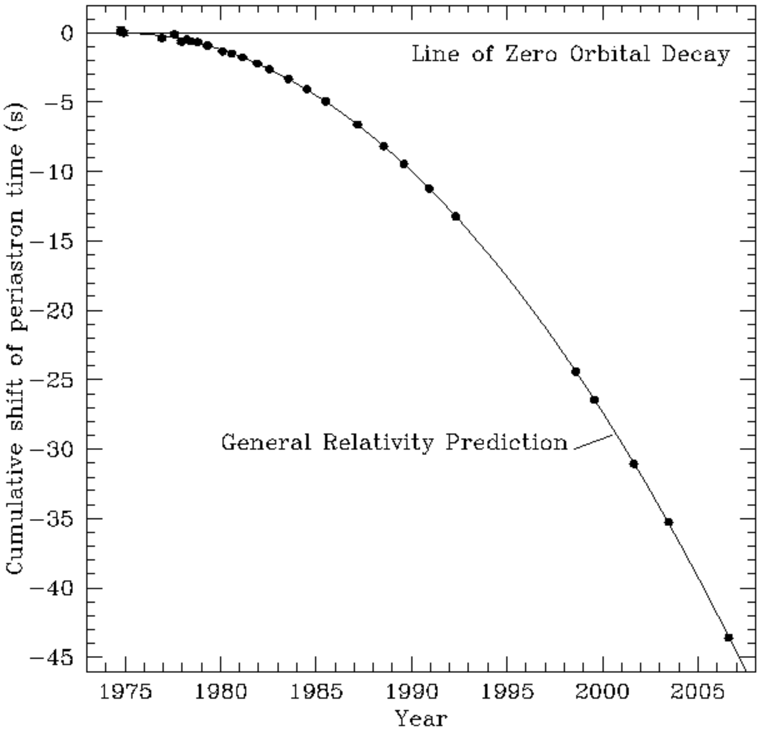

Figure 1.3: *The orbital decay of PSR1913+16. The line fit shows the expected orbital period due to emission of energy via gravitational waves predicted by General Relativity and the points show the measured data. Credit: Weisberg, Nice and Taylor [27]*

1.2 Gravitational Waves

1.2.1 Description of Gravitational Waves

In special relativity the space-time interval is:

$$ds^2 = -c^2t^2 + dx^2 + dy^2 + dz^2 \tag{1.2}$$

where ds can be thought of as consisting of one time component ct and three spacial components x, y, z, hence the term space-time. This can be abbreviated to,

$$ds^2 = \sum_{i=0}^{\mu}\sum_{j=0}^{\nu}\eta_{\mu\nu}dx^{\mu}dx^{\nu} = \eta_{\mu\nu}dx^{\mu}dx^{\nu} \tag{1.3}$$

here μ and ν refer to the specific components of the space-time component of x and η is the 'Minkowski' metric of flat space-time,

$$\eta_{\mu\nu} = \begin{pmatrix} -1 & 0 & 0 & 0 \\ 0 & 1 & 0 & 0 \\ 0 & 0 & 1 & 0 \\ 0 & 0 & 0 & 1 \end{pmatrix}. \tag{1.4}$$

Equation 1.3 makes use of the Einstein summing convention where it is assumed that repeated indices (μ, ν) are summed. With general relativity, space-time is now warped or perturbed to describe gravity. Gravitational waves are idealised as ripples propagating as strain fluctuations traveling at the speed of light throughout space-time so

$$ds^2 = g_{\mu\nu}dx^{\mu}dx^{\nu} \tag{1.5}$$

where

$$g_{\mu\nu} = \eta_{\mu\nu} + h_{\mu\nu} \tag{1.6}$$

here $|h_{\mu\nu}| << 1$ and shows the small perturbations in the curvature of space-time. The complicated mathematical expressions that describe Einstein's gravitational field equation can be simplified if a *transverse traceless gauge* or TT gauge, is chosen for $h_{\mu\nu}$. This allows the freely propagating field equation to be represented as a simple wave equation.

$$\left(\nabla^2 - \frac{1}{c^2}\frac{\partial^2}{\partial t^2}\right) h_{\mu\nu} = 0, \tag{1.7}$$

which results in wave solutions (known as gravitational waves) moving at the speed of light c in the z direction. In the transverse traceless gauge we are left with

$$h_{\mu\nu} = \begin{pmatrix} 0 & 0 & 0 & 0 \\ 0 & a & b & 0 \\ 0 & b & -a & 0 \\ 0 & 0 & 0 & 0 \end{pmatrix} \tag{1.8}$$

where $h_{\mu\nu}$ is a linear combination of two polarised states of the wave at 45° to each other h_+ and $h_\times$.

$$h_+ = \begin{pmatrix} 0 & 0 & 0 & 0 \\ 0 & 1 & 0 & 0 \\ 0 & 0 & -1 & 0 \\ 0 & 0 & 0 & 0 \end{pmatrix} \qquad h_\times = \begin{pmatrix} 0 & 0 & 0 & 0 \\ 0 & 0 & 1 & 0 \\ 0 & 1 & 0 & 0 \\ 0 & 0 & 0 & 0 \end{pmatrix} \tag{1.9}$$

Figure 1.4 shows what is expected to happen when a ring of masses are acted on by a wave emitted by sources that are quadrupolar in nature [6] where the wave is propagating into the page. It shows that a ring of diameter L is stretched by length ΔL in one direction whilst compressed by the same amount in the orthogonal direction. This property arises from the quadrupolar nature of gravity. The h_+ and $h_\times$ modes are orthogonal to each other and this can be seen by focusing on a particular mass and comparing its movements in both cases. If we look at the mass located at the top of the circle notice that for the h_+ case it moves vertically whereas in the $h_\times$ mode it oscillates horizontally. Gravitational radiation must be at least quadrupolar in nature as other types of radiation would break down when tested using general relativity. Monopole radiation would refer to the total mass-energy of a system changing with time

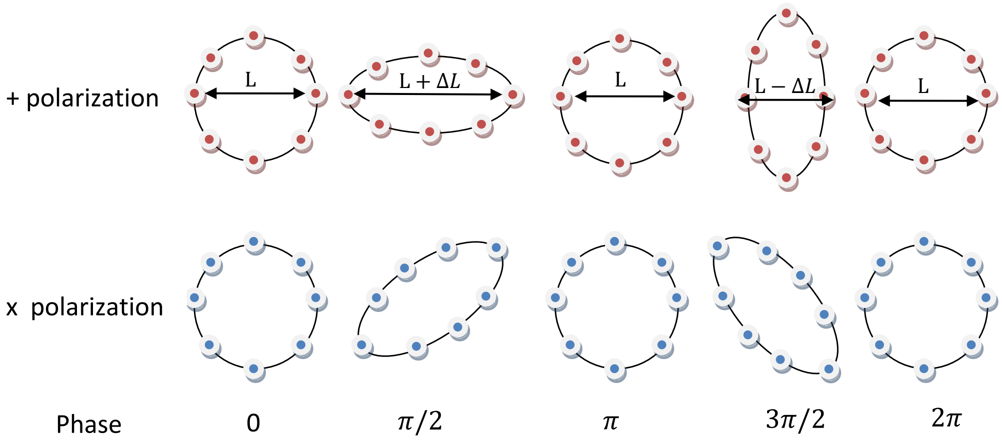

Figure 1.4: *The effect of a gravitational wave with two orthogonal polarisations* h_+ *and* $h_\times$*, incident normal to the page, on a ring of test particles.*

and this violates the conservation of mass. Dipole radiation corresponds to the center of mass of a system changing with respect to time which would violate the conservation of linear angular momentum. Gravitational waves are thus only emitted by non-axisymmetric accelerations of mass. This relates to the moment of inertia of the system varying in time and is allowed, as no conservation laws exist that can prevent this from happening. The quadrupolar effect is utilised in modern day orthogonal gravitational wave detectors described in section 1.4. The idea of accelerating matter producing waves is analogous to the radiation produced by accelerating charges. The amplitude of a gravitational wave is described in terms of the strain it produces in space:

$$h = \frac{2\Delta L}{L}. \tag{1.10}$$

It is important to state just how weak the gravitational effect is. Because space-time is extremely stiff it takes a very large mass to produce a significant curvature in space-time. In order to detect gravitational radiation, detectors must be designed to detect a signal with a strain amplitude of the order 10^{-21}.

1.3 Sources of Gravitational Waves

The amplitude of a gravitational wave strain is given by [28],

$$h_{\mu\nu} = \frac{2G}{rc^4}\frac{d^2Q_{\mu\nu}}{dt^2}, \tag{1.11}$$

where the amplitude of the gravitational wave strain h varies as $1/r$ and r is the distance from the source. This is due to it being the strain amplitude of the waves that is measured rather than the intensity which would vary as $1/r^2$. The strain amplitude increases directly as the second time derivative of the mass distribution

$$Q_{\mu\nu} = \int \rho x_\mu x_\nu \mathrm{d}^3x, \tag{1.12}$$

where ρ is the mass density and x are the position vectors. Consider a binary mass system where two stars with masses $m > 1.4M_\odot$ are in circular orbit around a common centre of mass each with an orbital radius A and angular velocity ω. When viewed from side-on the position vector $x = (Asin\omega t, 0, 0)$ for each star. The wave amplitude is also directly proportional to the frequency of the orbit squared and the waves are emitted at twice the orbital frequency. If this scenario was to occur in the Virgo Cluster located 16.5 Mpc from Earth, and if the gravitational wave signal was produced at 1 kHz it would produce a strain amplitude of the order $\sim 9 \times 10^{-22}$.

Gravity is to date known as the weakest of natures forces. Thus because of this it is impractical to recreate gravitational waves in the lab. There is a thought experiment described by Saulson [29] which considers two, 1000 kg masses, separated by 2 meters, rotating at 1 kHz. Even this setup will only produce strain amplitudes of the order 10^{-38} meters at a distance of one wavelength from the source which is around ~150 km. The large distance is chosen because wave phenomena are only distinguishable from near-field effects, at distances comparable to or larger than one wavelength from the source. To have any chance of detecting gravitational radiation we instead have to look at extremely large mass scales and non-axisymmetric accelerations such as those produced by astronomical events. Discussed here are sources which emit in the frequency bandwidth from ∼10 Hz to a few kHz. For ground based detectors we are limited by the many noise sources in this frequency regime (see section 1.5).

1.3.1 Burst Sources

1.3.1.1 Coalescing Compact Binaries

As shown in section 1.1, gravitational waves were indirectly detected by looking at stars moving in a binary orbit around a common center of mass. In the case studied by Hulse and Taylor [25, 26] a pulsar orbited around a neutron star. Other types of binary system can consist of: two neutron stars (NS/NS) as shown in figure 1.5; two black holes (BH/BH); or a neutron star with a black hole in orbit around a common center of mass (NS/BH). Combinations can exist with multiple stars in orbit. All these combinations show that gravitational radiation will be emitted as the stars lose energy, inspiral and coalesce at their center of mass. In the final seconds before they collide the signal frequency rapidly increases to be greater than 10 Hz allowing the signal to be potentially detected by ground based detectors. This source is known as a 'chirp' with strain amplitude

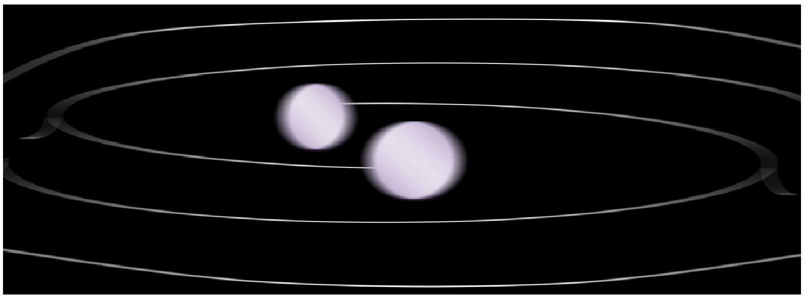

Figure 1.5: *Two neutron stars in a binary orbit emitting gravitational waves.*

$$h \approx 5 \times 10^{-23} \left(\frac{100\,\mathrm{Mpc}}{r}\right) \left(\frac{M_{\mathrm{b}}}{1.2 M_{\odot}}\right)^{\frac{5}{3}} \left(\frac{f}{200\mathrm{Hz}}\right)^{\frac{2}{3}} \tag{1.13}$$

where $M_{\mathrm{b}} = \frac{(m_1 m_2)^{\frac{3}{5}}}{(m_1+m_2)^{\frac{1}{5}}}$ where m_1 and m_2 are the masses of the two stars [5], and f is the orbital frequency of the binary. The orbital frequency has a maximum limit given by,

$$f_{max} = 220 \left(\frac{20 M_{\odot}}{M} \right) \text{ Hz.} \tag{1.14}$$

After this limit has been reached the orbits of the binary system becomes unstable and the binary system will coalesce. Consider a binary neutron star source from the Virgo cluster based at 16.5 Mpc distance, with each star having a mass of 1.4 $M_{\odot}$ and giving off a gravitational wave signal of 50 Hz. The strain amplitude h that would be detected is 1.23×10^{-22}.

Binary coalescence is the most likely source of gravitational waves that will be detected first by ground based gravitational wave detectors. The NS/BH binary population is expected to be lower than that of NS/NS binaries. However as the strain amplitude of gravitational waves produced from NS/BH coalescence will be much larger, they will potentially be more visible to the gravitational wave detectors. It is predicted that by 2019 the Advanced LIGO (aLIGO) detector will be able to view to a distance of 200 Mpc giving a search volume of $2 \times 10^7 \mathrm{Mpc}^3$, resulting in a detection rate of 0.2-200 NS/NS events annually, with the most likely detection rate being estimated at $\sim 40 \mathrm{yr}^{-1}$ [30].

1.3.1.2 Supernovae

Stars are massive gas clouds in which the fusion of hydrogen creates larger heavier elements such as helium. The energy to initiate fusion comes from all of the gas falling inwards towards the center of the star's mass, the decent resulting in a decrease of potential energy and increase in the kinetic energy of the gas particles. The kinetic energy is related to the temperature and pressure of the gas and so the star becomes hot enough to begin the fusion of hydrogen to give helium. This internal pressure pushes against the in-falling matter and so the star can continue to burn in hydrostatic equilibrium for millions to billions of years.

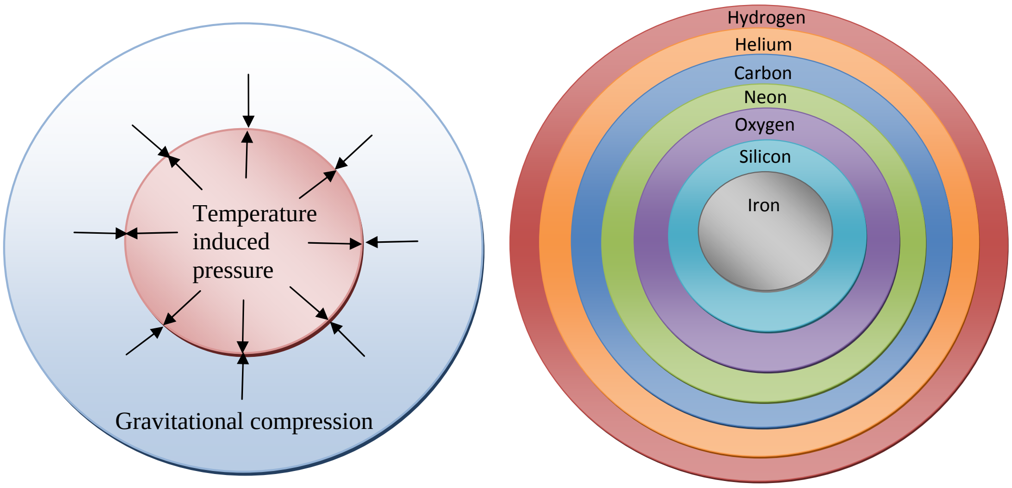

Figure 1.6: *Left: A star in hydrostatic equilibrium. Right: The layers of fusion created elements just before the star collapses.*

If the star is massive enough then temperatures can be so high that helium fuses to produce carbon. This will increase massively the temperature of the star making it swell to produce a star type known as a red giant. The death of a star (when there is no fuel left to burn or high enough temperatures cannot be created to force more fusion) varies greatly from star to star. It could be ferocious and as spectacularly explosive as a supernova producing new elements and particles as well as transmitting a wide range of energetic electromagnetic waves. The results could be viewed for several weeks or months. Alternatively it could be a slow gradual process like the cooling of a dwarf star.

If a star is over five solar masses ($5M_\odot$) a red giant star continues to burn via fusion to create carbon from the fusion of helium. The reaction continues further to create oxygen, neon, sulphur, nitrogen, and eventually iron. Due to iron being atomically stable[1] the iron settles to the core of the star where it is supported by electron degeneracy pressure, and the Pauli exclusion principle maintains the core shape. As the fusion reaction stops the gravitational squeeze takes over collapsing the star in less than a second. When the mass needing support exceeds what is known as the Chandrasekhar limit ($1.4M_\odot$),

---

[1] Iron is the most stable element it requires to much energy to break it up or to fuse it.

the electron degeneracy pressure can no longer support the core and electrons as they are forced to join protons in the nucleus to form neutrons where neutron degeneracy pressure now supports the core. Such a quick collapse, lasting only for around 10 seconds, excites the outer layers of the star and they are thrown away from the star with an illuminating explosion known as a supernova. If the remnant mass of the explosion is 1.4-$3M_\odot$, it will form a neutron star.

The core of a massive star that has more than roughly $3M_\odot$, after the explosion, will form a black hole. Stars that consist of gas less than $1.4M_\odot$ will form white dwarfs, stars that are held up by electron degeneracy pressure. Supernova can be split into two main types, Type I and Type II. Type I sources are expected to be spherically symmetric core-collapses and so are weak sources of gravitational waves whereas type II sources are expected to be more pronounced.

Type I: These supernova have had their outer layer of hydrogen stripped off before collapse and so spectroscopy measurements show a lack of the hydrogen absorption line compared to those of type II. Type I are predominantly produced from the mass transfer between two dense stars, such as two white dwarfs accreting matter from each other. When the two stars combine their combined mass is briefly beyond the Chandrasekhar limit, the sudden change in shape and angular acceleration of the system resulting in the emission of gravitational radiation.

Type II: This supernova starts off as a large star, large enough that it can fuse many elements to produce iron at its core (figure 1.6). The difference between type I and type II supernova is that type II spectral lines show the presence of hydrogen. Rates are calculated to be about 0.1-0.01 /yr/MWEG (Milky Way Equivalent Galaxy) [31].

Hypernova: This is an extreme case where the star being looked at is over $100M_\odot$ being so heavy it forms a black hole at its core. The explosion can be compared in magnitude to 100 supernova and are estimated to occur once every 200 million years/MWEG.

The strain amplitude given off from supernovae is calculated to be [32]:

$$h \approx 5 \times 10^{-22} \left(\frac{E}{10^{-3} M_{\odot} c^2} \right)^{\frac{1}{2}} \left(\frac{15\mathrm{Mpc}}{r} \right) \left(\frac{1\,\mathrm{kHz}}{f} \right) \left(\frac{1\,\mathrm{ms}}{\tau} \right)^{\frac{1}{2}} \tag{1.15}$$

where E is the energy of gravitational radiation expelled by the exploding star at a frequency f over time τ, where the explosion occurs at a distance r. These burst sources only release gravitational waves over a short timescale from milliseconds to minutes. The method for how these explosions occur is largely unknown although many assumptions and predictions have been made [33, 34]. It is hoped that when the gravitational waves from these burst signals are detected the method causing the explosion can be inferred.

1.3.1.3 Gamma-ray Bursts

Gamma-ray bursts are the brightest electromagnetic events know to occur in cosmology. They appear as gamma-ray flashes associated with extremely energetic explosions that have been observed in distant galaxies. The initial gamma-ray burst is typically followed by a longer-lived ‘after glow’. Gamma-ray bursts are known to exist in two forms. The first is short gamma-ray burst with durations lasting $\leq$2 s. The true nature of these objects is currently unknown, although the leading hypothesis is that they originate from NS/NS or NS/BH mergers [35]. The second form known as a long gamma-ray bursts, have durations lasting $\geq$2 s and are produced from core-collapse supernovae.

In 2008 a short gamma ray burst occurred, where the electromagnetically determined sky position from gamma-ray and X-ray satellites was coincident with the galaxy M31 (Andromeda) spiral arms. Short gamma-ray bursts are predicted to be produced when coalescing compact binaries collide. Coincident searches of the gravitational wave data runs did not detect any signal produced from this event [36]. This lead to the conclusion that the gamma-ray burst was either not the result of a NS/NS or NS/BH coalescing binary, or that the source of the gamma-ray emission did not originate in the M31 galaxy but at a greater distance along the same line of sight. While it is disappointing that no gravitational waves were detected it is important to appreciate the powerful conclusions that were made through this use of gravitational wave detectors.

1.3.2 Continuous Sources

1.3.2.1 Pulsars

If the shape of a pulsar is asymmetric then gravitational radiation may be produced from pulsars due to them having a density comparable to that of an atomic nucleus (the equivalent of the Sun's mass, but squashed into a diameter measuring of only a few ten's of kilometers). The non-axisymmetric property of the pulsar may be a consequence of misalignment between the rotational axis and the magnetic field axis. This misalignment could create a bump on the surface of the pulsar. The Crab pulsar is a promising pulsar for this kind of gravitational wave emission due to it's high spin down rate of -3.7×10^{-10} Hz/s. Like most pulsars it is a remnant of a supernova that from Earth could be seen in daylight for weeks and was noted by Chinese astronomers in 1054. This pulsar spins very quickly and so is likely to have surface perturbations and emit gravitational waves. Waves from sources of this kind are expected to have strain amplitudes of the order [37, 38],

$$h \approx 6 \times 10^{-25} \left(\frac{f_{\rm rot}}{500{\rm Hz}}\right)^2 \left(\frac{1{\rm kpc}}{r}\right) \left(\frac{\epsilon}{10^{-6}}\right) \tag{1.16}$$

where ϵ is a measure of stars non-symmetry called the equatorial ellipticity. A calculation [37] shows that for the Crab pulsar if $\epsilon = 7 \times 10^{-4}$, $r \approx$1.8 kpc and $f_{\rm rot}$=30 Hz this would emit a gravitational wave with a frequency of 60 Hz and have a strain amplitude of the order $h \approx 10^{-24}$. It also shows us that if we can ever study the signals from this kind of source it will allow us to deduce information about the crustal deformations. This would be an important step in astronomy modeling where there are many forces and factors playing a huge part such as general relativity, magneto-hydro dynamics, neutrino transport and nuclear physics. Many of these have theories based on speculation and philosophy; by studying gravitational waves hopefully more secrets will be revealed. A study of the fifth science run data from LIGO allowed the value of ϵ for the Crab pulsar to be constrained to a value of less than 1.8×10^{-4} [38].

Low-mass X-ray Binaries

Low-mass X-ray binaries occur when matter from a star is pulled off by the strong gravitational field of another companion star. The accretion process causes the star to gain enough angular momentum to reach the Chandrasekhar-Friedman-Schutz (CFS) instability point [39, 39]. At this point the self gravitating body begins to deform and wobble. This can be due to a wide variety of mechanisms; such as ‘p-mode’ oscillations that arise due to pressure perturbations in the fluid, or ‘g-mode’ oscillations caused by the star’s strong gravitational field trying to reduce perturbations in the density profile. Many more perturbation modes exist and these instability points occur in the 100’s of Hz frequency range [40]. These perturbations mean that the rotation of the star is now non-axisymmetric and so the moment of inertia is changing with respect to time. This results in gravitational waves being produced as the angular momentum of the star increases [41]. The X-ray flux occurs as the matter is being accelerated towards the stars surface. The strain amplitude predicted from this kind of source varies as L_γ which is the time average X-ray flux. It provides an indicator of the rate at which matter is being accreted. The strain amplitude of gravitational waves predicted from this kind of source is [29]:

$$h \approx 3 \times 10^{-27} \left(\frac{330\mathrm{Hz}}{f_{\mathrm{rot}}}\right)^{1/2} \left(\frac{1\mathrm{kpc}}{r}\right) \left(\frac{L_\gamma}{10^{-11}\mathrm{Jm}^{-2}\mathrm{s}^{-1}}\right)^{1/2}. \tag{1.17}$$

The fact that the amplitude of these gravitational waves is of the order $\approx 1 \times 10^{-26}$ makes it an unlikely source to be detected by ground based gravitational wave detectors in the near future.

1.3.3 Stochastic Sources

Stochastic radiation sources are created from many different types of random background signals and are similar to those that created the Cosmic microwave background (CMB) studied using electromagnetic radiation. It will most likely appear as noise on a gravitational wave detector and the hope is that when two or more detectors are correlated these signals can be monitored. Though difficult to detect stochastic sources are probably some of the most interesting to look at, as they can tell us about how the universe was constructed. One possible source of this type is the waves left over from the Big Bang rapid inflation period. With all the matter being forced to accelerate this would no doubt have produced space-time shock waves. Another possible stochastic source is from the cosmic string model of galaxy formation, the amplitude of strain for the source being given by [42]:

$$h \approx 1.8 \times 10^{-25} \left(\frac{H_{\mathrm{o}}}{100 \mathrm{kms}^{-1} \mathrm{Mpc}^{-1}} \right) \left(\frac{\Omega_{\mathrm{gw}}}{10^{-8}} \right)^{\frac{1}{2}} \left(\frac{f}{100 \mathrm{Hz}} \right)^{-\frac{3}{2}} \left(\frac{\mathrm{B}}{2 \mathrm{Hz}} \right)^{\frac{1}{2}} \tag{1.18}$$

where B is the frequency bandwidth, H_{o} is the current Hubble constant and Ω_{gw} is the energy density required for a closed Universe.

From the fifth science run (S5) upper limits were placed on the amplitude of background stochastic sources to be less than 3×10^{-22} rms in a 100 Hz band around 100 Hz [43]. This was used to show that the energy density of the Universe is $< 6.9 \times 10^{-6}$. The result also helped to explore and constrain the parameter space of cosmic string and pre-Big Bang models.

More indirect evidence for the existence of gravitational waves came from the BICEP2 experiment based at the south pole. BICEP2 measured the polarisation of the B-mode power spectrum in the CMB. In 2014 the BICEP2 science group reported measurements of the B-mode power spectrum polarisation in excess of what could have been created purely from gravitational lensing [3]. It is believed that this excess polarisation is a byproduct of gravitational waves generated by inflation. Current inflation modes predict that during the Big Bang rapid inflation period quantisation of the gravitational field coupled to the exponential space-time expansion to produce a stochastic primordial background of gravitational radiation. The CMB was expected to be left polarised from this effect as during the early stages of the universe light was scattered off from free electrons during matter-radiation decoupling. For the BICEP2 results reported it is believed that these primordial gravitational waves induced local quadrupole anisotropies in the CMB radiation field, thus inducing polarisation in the scattered light [4] that observed by the BICEP2 detector.

1.4 Gravitational Wave Detectors

Gravitational waves potentially span decades in frequency from the order of 10^{-9}Hz to a few kHz. As a result a variety of detectors are employed to detect the small strain fluctuations in space-time. In this section I will discuss briefly pulsar timing arrays which are used to detect gravitational waves in the frequency regime from 10^{-9}-10^{-6} Hz and two current designs for ground-based detectors that are used today. These are resonant bar detectors with a frequency bandwidth of 1-10 kHz and laser interferometers with a frequency bandwidth of 10 Hz-2 kHz. A space based detector which is capable of detecting gravitational waves in the frequency range of 0.1 mHz-1 Hz is also being planned and is discussed in section 1.4.4.

1.4.1 Pulsar Timing Arrays (10^{-9}-10^{-6} Hz)

Pulsar timing arrays [44] are used to study gravitational waves with frequencies of the order $\sim 10^{-9}$Hz. Several pulsar timing arrays currently exist: they are the EPTA (European Pulsar Timing Array)[45]; PPTA (Parks Pulsar Timing Array) [46]; NANOGRAV (North American Nanohertz Observatory) [47]; and those from a collaboration called the IPTA (International Pulsar Timing Array) [48].

Pulsars (section 1.3.2.1) emit a beam of radio wave signals. This beam is not inline with the rotational axis of the pulsar, which means that the beam is constantly being rotated by the pulsar. If this beam of radio signals is directed at the Earth it will appear to be flashing similar to a light house. This periodic flashing at Earth is monitored by the pulsar timing arrays, where the actual arrival time of these flashes at the detectors can be compared to the predicted arrival time for these flashes, to give timing residuals. The timing residuals can then be used to show correlations between the timing residuals and gravitational waves.

Atomic clocks are be used to monitor the pulsar signals arriving at the detector and how these timing residuals vary over time. Atomic clocks give best precision over long time frames, meaning that detection of signals using this method is suited to frequency bandwidths of $\approx 10^{-9}$ to $10^{-6}\,\mathrm{Hz}$ and have a strain sensitivity of $\sim 10^{-14}$ at $10^{-8}\,\mathrm{Hz}$ [49].

This method of detection will not be elaborated further, instead we will study ground based interferometry (section 1.4.3) and space based detectors (section 1.4.4). First we describe briefly resonant bar detectors.

1.4.2 Resonant Bar Detectors (1-10 kHz)

At the start of the 1960's Joseph Weber at the University of Maryland in College Park built the first gravitational wave detector now known as the resonant bar detector. The idea behind this design was that when a gravitational wave passed through the detector it would apply a tidal force to the massive metal cylindrical bar (Weber bar). This metal core would then be stretched and compressed by the wave and the movements could be detected using a transducer sensitive to the motion of the bar.

The core itself is made from low mechanical loss material like aluminium or niobium to reduce any effects from thermal noise (see section 1.5).

There were five bar detectors achieving a sensitivity order of $10^{-19}\sqrt{\mathrm{Hz}}$ [16] these being ALLEGRO (operated by the Louisiana State University in Baton

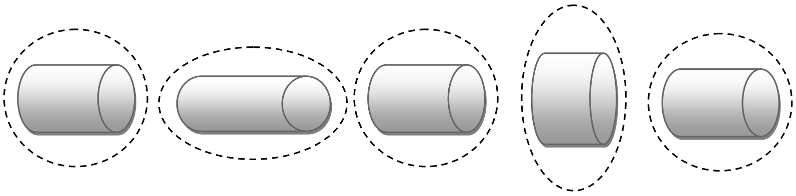

Figure 1.7: *A Weber bar being acted on by a gravitational wave.*

Rouge, Louisiana, USA), AURIGA (operated by the Instituto Nazionale di Fisica Nucleare at Legnaro National Laboratories, Italy), EXPLORER (Operated by the Rome group at CERN), NAUTILUS (also operated by the Instituto Nazionale di Fisica Nucleare at the Laboratori Nazionali di Frascati, Italy) and NIOBE (operated by the university of Western Australia in Perth, Australia). Detectors of this kind are very sensitive to thermal noise. The seismic noise was minimised by hanging the bar from vibrational isolation stages and placing the whole system in a vacuum. Another way to reduce the thermal noise is to use low mechanical loss materials (the reasons for this are discussed in chapter 2) and run the detectors at cryogenic temperatures $\approx 0.1\,\mathrm{K}$ as was achieved by AURIGA (operated by the Instituto Nazionale di Fisica Nucleare at Legnaro National Laboratories, Italy). Only AURIGA and NAUTILUS are still operating today [6].

The latest resonant mass detectors are termed spherical detectors. These use a spherical mass rather than a cylindrical bar. They have the advantage of being sensitive to multiple resonant frequencies as well as being sensitive to both polarisations of gravitational waves. Because a spherical mass has five modes of resonance as opposed to a bar detector which has just one the detectors also provide information about the propagation direction of the gravitational wave. Thus, if a gravitational wave passed through the sphere, the direction of waves could be found by comparing the ratio of the excitation on each mode. This enables the direction of the source to be obtained. Two detectors of this kind operating at the moment are the MiniGRAIL [50] at the

University of Leiden in Holland and the Mario Schanberg detector in Brazil [51, 52], Together these will also increase the chances of detection, allowing coincidences in detectors to be spotted. These detectors operate with a 60 Hz bandwidth and can measure strains of $10^{-21}\sqrt{\mathrm{Hz}}$ at 3,000 Hz.

The bandwidths of the detector are dependant on the resonant nature of the detector itself. If the detector's natural resonance is not close to the frequency of the incoming gravitational wave then no resonance and hence no detection of the gravitational wave signal will occur as the signal will be hidden in noise. One way around this single frequency bandwidth was an idea proposed by Cerdonio and colleagues [53]. Their proposal was to use a dual resonant mass detector, whereby a full cylinder with a resonant frequency was nested inside a larger hollow cylinder. The cylinders would be chosen so that the hollow cylinder had a resonant frequency two to three times less than that of the inner cylinder. If a gravitational wave propagated through this detector the masses would be excited in anti-phase amplifying the signal and making it detectable. These detectors are predicted to reach strain sensitivities of $\sim 10^{-23}\sqrt{\mathrm{Hz}}$ over a bandwidth of 2 kHz. This sensitivity level is unlikely to be reached however as the system requires a more complicated read out system which would reduce the sensitivity levels.

It is worth mentioning that Weber in 1968 reported detections of gravitational waves using his two bar detectors [54] separated by 1000 km. These have since been dismissed following similar experiments being setup in Germany, Russia, Britain and the US, none of which could confirm the claims made by Weber. Not only that, but the detectors built at that time simply were not sensitive enough to the strains predicted theoretically by astrophysical sources. Since then there has also been strain coincidences of around 10^{-18} reported between the detectors at CERN and Rome [55] but these have been dismissed as statistical coincidences [56]. The ALLEGRO detector was running in 1993 when the supernova 1993J occurred although it did not detect any gravitational waves.

1.4.3 Ground Based Laser Interferometric Detectors (10 Hz-2 kHz)

1.4.3.1 Michelson Interferometer

For these detectors we shall consider the simplest design and work up adding in complexity until we reach the current state of detectors around the world. It should be noted that in the current detectors many more optical and noise reduction techniques are used, detailed discussion of which is beyond the scope of chapter.

It is expected that as a gravitational wave passes it will stretch and contract space-time by $h = \frac{2\Delta L}{L}$. It is clear that by taking a larger L we will see a larger length change ΔL for the same size of gravitational strain. The optimum length to study for a gravitational strain of frequency 1 kHz would be [29]:

$$L_{\mathrm{optimum}} = \frac{\lambda_{\mathrm{gw}}}{4} = \frac{c}{4f_{\mathrm{gw}}} = \frac{3\times10^{8}}{4\times10^{3}} = 75\mathrm{km} \tag{1.19}$$

and thus a long-baseline Michelson interferometer design is utilised. The idea that one could look for small shifts in the fringe pattern of a Michelson interferometer was first proposed in 1962 by M.E. Gertsenshtein and V.I. Pustovoit [57]. It is important to note that for longer arm lengths the signal begins to cancel as the round trip time is greater than half a wavelength.

Modern interferometers use a Nd:YAG laser, with a wavelength of 1064 nm. Light is directed onto a beam splitter which splits the light into two separate beams at 90° to each other. The beams are sent to two highly reflective end mirrors. The entire system is kept in a vacuum to reduce noise from particle bombardment with the mirrors and the laser light. The mirrors themselves are polished to a very high accuracy $\sim \lambda_{\mathrm{Nd:YAG}}/100$, in order to reduce the amount of light being scattered. The end mirrors reflect the light back towards the beam splitter where the two beams are recombined and pass to a

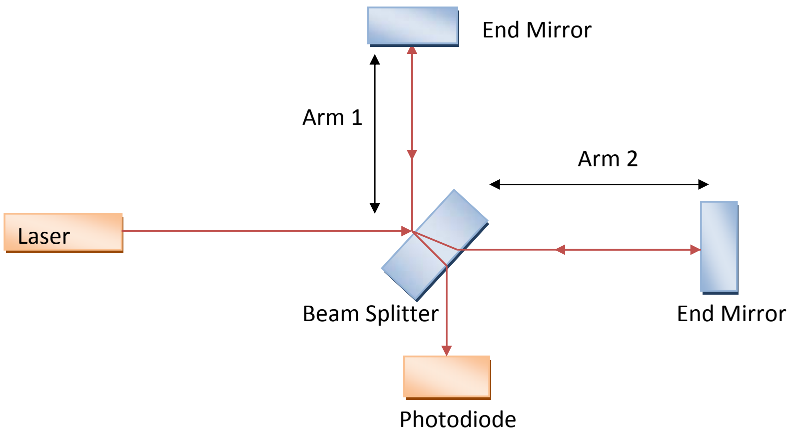

Figure 1.8: *Schematic layout of a Michelson interferometer.*

photodiode which monitors the intensity of the light as it is recombined either constructively or destructively. As a gravitational wave interacts with the interferometer the separations of the beam splitter and test masses will be modulated as space-time compresses and expands. This will change the relative path length traveled by the light in each arm thus changing the intensity of light at the photodiode. In practice control systems are used to lock the detector just off a dark fringe at the output photodiode and maintain the detector operating point.

Conventional detectors operate with an arm length of a few km which is shorter than the optimum length described earlier in equation 1.19. So instead optical techniques are used to create a larger optical path without increasing the size of the detector. Delay line interferometry and Fabry-Perot cavities are two of these techniques which keep the light in the arms of the interferometer for longer and so increase the sensitivity of the detectors.

The Laser Interferometric Gravitational-Wave Observatory (LIGO) is a detector with an arm length of 4 km. LIGO was established as a joint project between scientists at MIT and Caltech to detect and study gravitational waves from astrophysical sources that radiate in the audio-frequency regime [9]. There are two LIGO laboratories; one in Hanford, Washington and the other in Livingston, Louisiana [6]. Both of these detectors are being upgraded to Advanced LIGO, aLIGO, which is discussed in section 1.6.1. More projects have been developed in Europe such as the Virgo (Italy/France) collaboration with a 3 km detector in Cascina, Italy [8] which is currently being upgraded to Advanced Virgo (section 1.6.2) and the GEO600 (UK/German) collaboration in Hanover, Germany with a 600 m arm length detector [7] which incorporates a folded arm technique. The latter detector has already undertaken some of the design enhancements as part of the GEO-HF upgrade programme (section 1.6.3). GEO600 is the only detector currently taking data and is running in “astrowatch” mode while all other ground based gravitational wave interferometers are being upgraded. There was also the TAMA300 project in Japan consisting of a 300 m long detector in Tokyo [58] this detector is now off line. More recently the Japanese have been focussing on the CLIO and KAGRA detectors which are mentioned in section 1.6.4. The international network of these ground based detectors is shown in figure 1.9. The advantage of having detectors spread all over large distances is that source positions can be determined by the difference in signal arrival times. Furthermore, noise sources in one part of the world may produce a false signal on one detector but if the signal is not seen on the other detectors we can conclude that it was a false detection.

1.4.3.2 Delay Line and Folded Arm Interferometer

The use of Delay line interferometers to detect gravitational waves was proposed independently in the 1970’s by Rainer Weiss and Philip Chapman [60, 61]. The idea here is to put a mirror between the end mirrors and the beam splitter which will allow light to bounce between the input mirrors and end mirrors essentially giving the light more time in the cavity (figure 1.10). During this time the light occupies the cavity and the beams do not cross paths. The light then leaves through a hole on the inboard mirror. Delay line in-

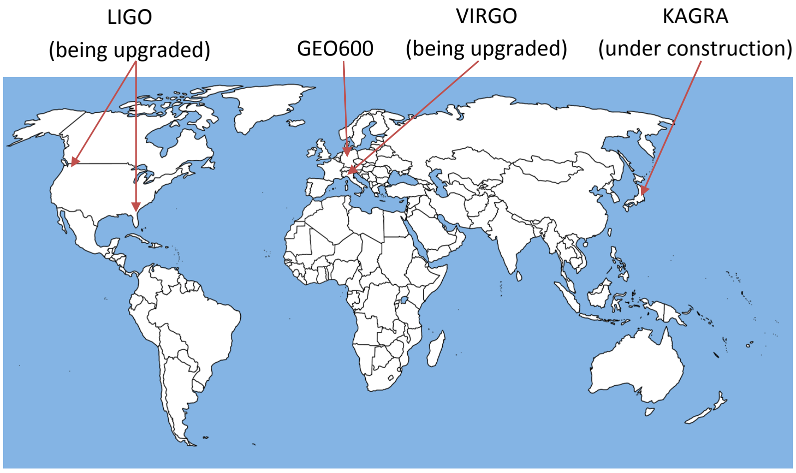

Figure 1.9: *Distribution of the current ground based detector network [59].*

terferometers were tested at the short Caltech interferometer [61], which now has an arm length of 40 m and uses Fabry-Perot cavities (see section 1.4.3.3). In Germany a 3 m prototype was used, this was later developed to form a 30 m instrument which resided at the Max-Plank-Institute for Astrophysics in Garching [61]. The main problem with this design is that light is scattered by the mirrors which feeds back into the output of the interferometer causing interference [62]. Even when mirrors are polished to a high accuracy this is a problem that for the moment is not well understood.

The German-UK collaboration detector GEO600 uses a folded arm interferometer. In this arrangement the laser light is reflected off a secondary mirror which is positioned at an angle in the vertical direction [63] to the end test mass mirror. This arrangement is combined with 12 Watt Nd:YAG laser, signal recycling (discussed in section 1.5.2.3), power recycling (discussed in section 1.5.2.2) and two mode cleaners to improve the beam noise [64]. Both the delay line interferometer and folded arm interferometer are shown in figure 1.10

Figure 1.10 shows a N=3 pass delay line interferometer. GEO600 uses the folded arm interferometer shown on the right of Figure 1.10. The folded arm technique effectively doubles the arm length of GEO600 making the arm length

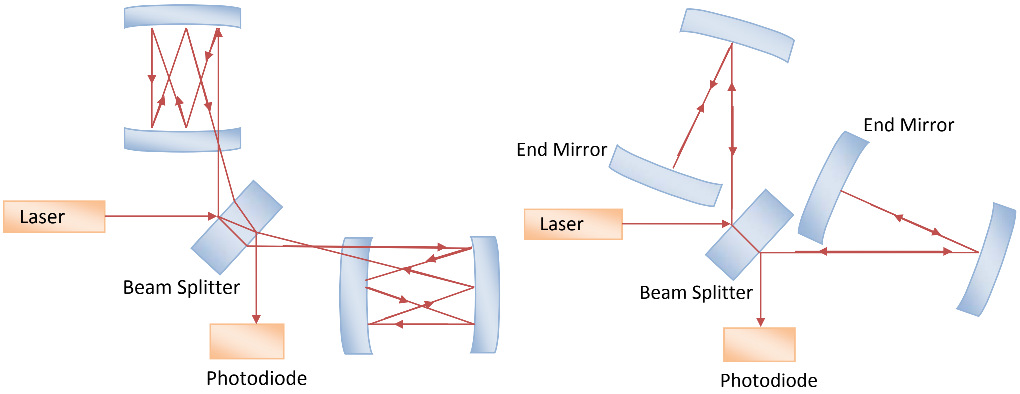

Figure 1.10: *Left: Schematic layout of a delay line interferometer. Right: Schematic layout of a folded arm interferometer.*

1.2 km [65].

1.4.3.3 Fabry-Perot Interferometer

The alternative to delay line interferometers is to use Fabry-Perot cavities (see figure 1.11). These were developed at Glasgow University in the early 1980's [66] using a 10m long detector. Thereafter a 40 m instrument was constructed at Caltech [67]. This method requires constant monitoring of the entire interferometer. The setup looks similar to the delay line except instead of having a fully reflecting inboard mirror it is only partially reflective so that some light still enters in the cavity. When the system is in operation both cavities must be held in resonance. Resonance is when the cavity length in the arm is equal to an integral number of a half wavelengths of the laser light being stored in the cavity. To keep both arms in resonance requires a complex electronic control servo system. One arm is locked in resonance by changing the wavelength of the laser light as the strain produced by the gravitational wave changes cavity arm length. The other arm of the interferometer is kept in resonance by feedback of a filtered and amplified signal from the photodiode. This is used to control an actuator at the end mirror.

Fabry-Perot cavities can increase interferometer sensitivity beyond that of a delay line interferometer. With a finesse of around a few 100 these cavities make the laser light travel for about the optimum length, which is why this design has been used in both the LIGO [68] and Virgo detectors [8]. The trade off between delay line and Fabry-Perot interferometers is that delay line interferometers scatter light off of multiple sections of the mirror surface where as Fabry-Perot cavity has to be continually locked in resonance. Each method should have a finesse of around a few 100 making the light travel for around the optimum length. However, as delay line interferometers trap even the scattered light which causes interference, a finesse of a few 100 is very hard to achieve in practice [62].

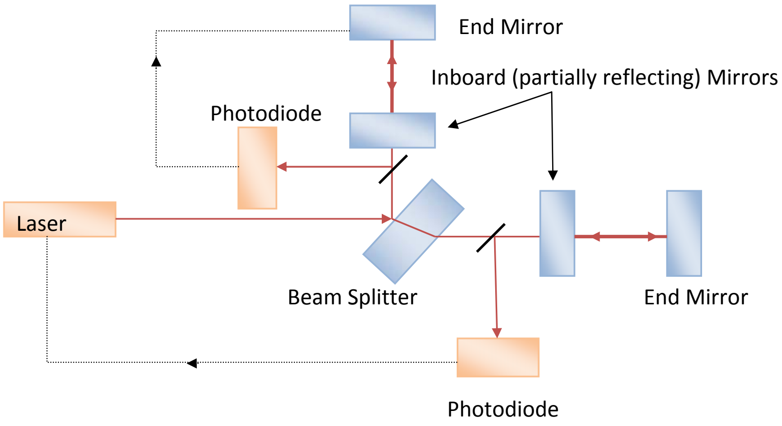

Figure 1.11: *Schematic layout of a Fabry-Perot interferometer.*

1.4.4 Space Based Interferometric Detector: eLISA (0.1 mHz-1 Hz)

As the size of an interferometer is limited on Earth the next stage is to build a detector in space where confinement is not an issue. By building a space based detector many of the noise sources found on Earth also disappear such as seismic and gravity gradient noise section 1.5. This gives the advantage that lower frequency bands can be studied. The Laser Interferometer Space Antenna (LISA) was a combined project between NASA and ESA. LISA was due to be made up of three spacecraft which instead of forming an L shaped arm they are arranged as the vertices of an equilateral triangle spread 5×10^9m apart, with the plane of the triangle tilted 60° out of the ecliptic. It would have flown 20° behind the orbit of the Earth (see figure 1.12). The project was stopped due to the NASA budget cuts. It has now been reformed by ESA as eLISA-NGO [69]. The New Gravitational-wave Observatory (NGO) mission concept was used as a design review for eLISA [70]. Each spacecraft is now separated only by 1×10^9m instead of 5×10^9m and consists of one 'mother' spacecraft looking outwards onto the two adjacent 'daughter' spacecraft. Each 'daughter' craft contains one telescope, one laser and one test mass known as a payload, whilst the 'mother' spacecraft houses two of these payloads. This forms a Michelson-like interferometer. Each spacecraft is constructed as a zero-drag satellite and effectively follows the free floating masses, using capacitive sensors to monitor the positions of the masses relative to the spacecraft [71]. This is known as drag-free as it isolates the optics from non-gravitational forces such as solar wind and radiation pressure. eLISA has a detection frequency range of 1 mHz to 1 Hz. With this detection bandwidth eLISA has a range of missions to carry out. It is hoped it will help to model the expansion of the universe, the dark energy equation of state, monitor black hole and galaxy mergers [1], provide a complete white dwarf mapping of our galaxy and test for primordial gravitational radiation left over from the Big Bang. What is even more incredible about this design is that it can accurately tell the distance, direction and polarisation from which the wave source was emitted [72], This is done by monitoring how the strength of the signal varies as eLISA moves around the Sun (figure 1.12). This is possible as eLISA is sensitive to sources that emit signals on a time scale of months-years.

Before eLISA will be launched at test mission called LISA Pathfinder is planned. This involves sending up one spacecraft capsule to test the design of

---

[1] As galaxies are thought to have a massive black hole at the centre. eLISA is sensitive to monitor massive black hole mergers and hence galaxy mergers

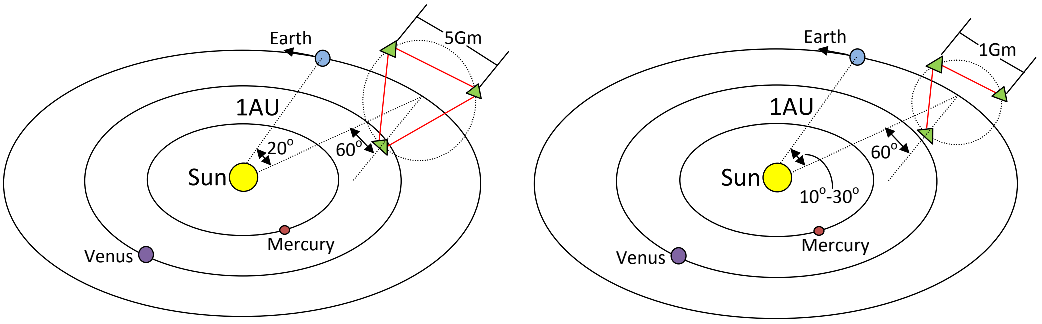

Figure 1.12: *Left: Initial LISA project. Right: eLISA-NGO project.*

eLISA. It will contain one arm of the eLISA interferometer, shortened from 1 million km to 35 cm. The mission aims to test the drag-free altitude control of a spacecraft with two proof test masses, ensure that laser interferometry is possible at low frequencies and finally to check that the components such as capacitive sensors, micro thrusters, lasers and optics are reliable and robust enough to cope with the extreme conditions they face in space and during launch. It is hoped that if the Pathfinder mission goes as planned in 2015 and if successful then eLISA will potentially be launched in 2034 as part of the ESA L3 "Invisible Universe" project [69, 73].

1.4.5 Conclusions

The work presented in this thesis was aimed at developing suspension thermal noise for use in ground based detectors where stable optical cavities are required such as aLIGO, GEO600 and the Virgo detectors. While the research presented here was not intended for use in other detectors discussed in section 1.4, all detectors require low thermal noise to some degree and so the findings presented are also likely to be of use for future developments and upgrades to these detectors.

1.5 Detector Noise Sources

1.5.1 Photon Shot Noise

Photon shot noise essentially comes from Poisson statistics when we look at the number of photons detected at the output of an interferometer. For a standard Michelson interferometer assume that N photons arrive at the output over some time τ (the time light is stored in the arms of length L); then the uncertainty in the number of photons measured will be $\sqrt{N}$. From considering the number of photon measured in a time $\tau \sim 1/2\Delta f$, the amplitude strain sensitivity of the interferometer depends on P_{in} the input power of the laser, λ the wavelength of the laser light and Δf, the frequency bandwidth, in the following way [29, 74, 75],

$$h_{\text{shot}}(f) = \frac{1}{L}\left(\frac{\hbar c \lambda \Delta f}{2\pi P_{\text{in}}\epsilon}\right)^{\frac{1}{2}} \frac{1}{\cos(\phi/2)} \text{ per } \sqrt{\text{Hz}}, \tag{1.20}$$

here $\hbar$ is the reduced Planck's constant, ϵ is the quantum efficiency of the photodiode, c is the speed of light and ϕ is the phase difference between the light in the two arms of the interferometer. Hence to lower shot noise, lasers with a high power that remain stable are used in detectors. Other techniques are employed as well such as power recycling, signal recycling and squeezed light all of which can be used to help lower the shot noise. The stain sensitivity can be optimised by setting $\phi \sim 0$ so that the output intensity is zero, which is why current gravitational wave detectors operate on a dark fringe.

1.5.2 Radiation Pressure Noise

As the power of the laser is increased to reduce shot noise it is seen that the radiation pressure noise increases. Radiation pressure arises from momentum exchange as photons bounce off the test mass mirrors. The power spectral density of the strain noise at a frequency f, for a simple Michelson interferometer with light hitting off a mirror of mass m, can be predicted by [29, 75],

$$h_{\mathrm{rp}}(f) = \frac{1}{mf^2L}\left(\frac{\hbar P_{in}\Delta f}{2\pi^3\lambda c}\right)^{1/2} \quad \text{per } \sqrt{\mathrm{Hz}}, \tag{1.21}$$

where for simplicity the mass of the beam splitter is assumed to be infinite.

By comparing equations 1.20 and 1.21 it can be seen that an increase in light power increases the radiation pressure noise while reducing the shot noise, therefore we must find a balance at which the interferometer will produce a minimum in this combined noise. This minimum is produced when $h_{\mathrm{rp}}(f) = h_{\mathrm{shot}}(f)$. This lowest level of noise is called the Standard Quantum Limit (SQL). The quantum limit comes from Heisenberg's uncertainty when considering the position and momentum of uncorrelated mirrors.

1.5.2.1 Squeezed Light

Squeezed light relies on the quantum description of light and was first demonstrated in 1985 [76]. An intuitive way to picture it is that light will arrive at a point with a certain amplitude and phase in the complex quantum description of light. The light field can have different values within an uncertainty region (Heisenberg's uncertainty relation) and this is commonly shown on a quadrature diagram as shown in figure 1.13. Squeezed light exhibits reduced noise in one quadrature component of the light's amplitude or phase. In doing so there is increased noise in the quadrature component not being squeezed. The uncertainty in the product of these two components remains constant and is given by Heisenberg's uncertainty relation. Light can be squeezed using nonlinear optical crystals. By focussing coherent light onto a highly transparent but birefringent crystal the light polarises the crystal. Thus when more light enters the crystal it undergoes nonlinear interactions with the noise in one of the quadrature components being reduced (usually light is phase squeezed). Light is passed back out of the crystal and the noise component which is being squeezed is below the standard quantum limit, allowing shot noise to be reduced. Recently, a squeezing factor of 10 dB was realised at the Albert Einstein Institute in Hannover. This improves the amplitude spectral density of the quantum noise by a factor of 3 [77–79]. Squeezed light is planned for use in GEO-HF (section 1.6.3) where light is squeezed at frequencies above 1 kHz to make the detector more sensitive at higher frequencies.

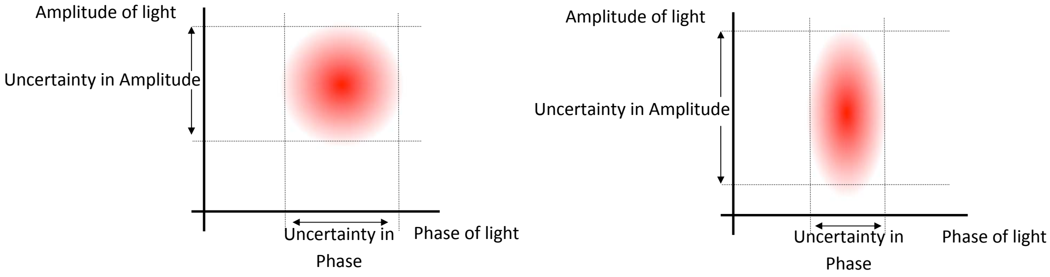

Figure 1.13: *Left: Quadrature picture of coherent unsqueezed light with Heisenberg's uncertainty in phase and amplitude of light. Right: Quadrature picture of squeezed light with lowered uncertainty in phase of light*

1.5.2.2 Power Recycling

Shot noise as shown in section 1.5 is a problem for detector sensitivity. The easiest way to reduce it would be to use a high powered laser. An alternative strategy is to use power recycling. As the interferometer is operating close to a dark fringe at the output, the majority of the light from the interferometer will head back towards the laser. By placing a partially reflected mirror between the laser and the beam splitter another resonant cavity can be formed between this new mirror and the interferometer acting as the second mirror [80, 81]. The gain in laser power through power recycling for aLIGO is ∼40-50 [82].

1.5.2.3 Signal Recycling

Signal recycling is similar to power recycling except that, instead of trapping the original carrier frequency of the laser light it is the signal at the output photodiode of the interferometer which is recycled. The sidebands (phase modulated carrier frequency) produced by a passing gravitational wave are held in a resonance cavity and the power from a side band frequency is allowed to build up within the interferometer [83]. In practice this is done by placing a partially transmitting mirror between the output photodiode and the beam splitter. The shot noise for this side band frequency is now decreased as the laser power of this frequency has been allowed to build up in the cavity. This is known as narrow band operation which enhances the signal size and it will allow for targeted gravitational wave searches to be made (i.e. for continuous wave sources).

1.5.3 Seismic Noise

Seismic noise is a low frequency noise source which limits the sensitivity of ground based interferometers at frequencies lower than 10 Hz. Seismic noise can be either natural or man-made in origin. Natural sources include the motion of the oceans, waves crashing on the beach, earthquakes and trees falling while man-made sources include nearby traffic, trains and machinery. To reduce seismic noise the interferometer mirrors are suspended from a multiple stage pendulum. Each simple pendulum attenuates displacement by approximately a factor of $\omega_{\mathrm{o}}^2/\omega^2$ [29] where ω_{o} is the natural frequency of the pendulum and ω is the frequency of the top clamp of the pendulum being oscillated i.e. ground motion. If multiple pendulums are used with N pendulum stages then the displacement attenuates by a factor $\left(\frac{\omega_{\mathrm{o}}}{\omega}\right)^{2N}$. This only limits the horizontal motion of the test masses and so to combat vertical displacement cantilever springs are used to hang the pendulum system as shown in figure 1.14. It is clear that pendulums with low resonant frequencies are most useful. Currently the seismic isolation factor for the aLIGO quadruple pendulum system is $\sim 1 \times 10^3$ [84].

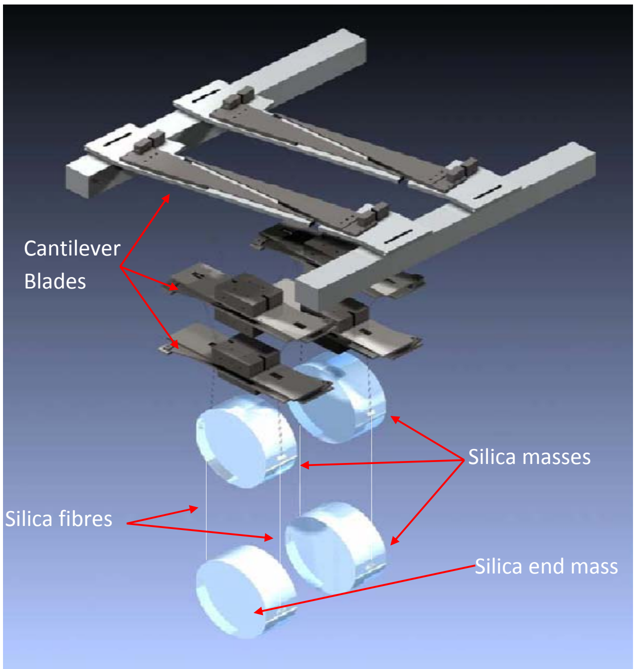

Figure 1.14: *Multiple pendulum used in advanced LIGO to reduce seismic noise. Credit: D. Shoemaker [85]*

1.5.4 Gravitational Gradient Noise

Gravitational gradient noise or Newtonian noise comes from fluctuations in the gravitational field near to a detector caused by the changing mass distribution around the detector [86]. It sets the fundamental limit on the lowest frequency that a detector can monitor at a frequency of less than 10 Hz. Seismic isolation systems cannot reduce this effect as it is the changing gravitational field acting directly on the end mass that makes it oscillate. A possible way to reduce the noise is to monitor the ground accelerations with seismometers and use this information to remove the ground noise from the detector signal [87]. Another way to reduce this noise is to build detectors under ground where gravitational gradients are less likely to play a part KAGRA is already trying this and it is also planned for the future Einstein detector. The space based detectors will also be immune to this seismic noise.

1.5.5 Thermal Noise

Thermal noise in interferometers arises through the thermal energy fluctuations of atoms and molecules in the suspensions, test masses and coatings. One of these contributions to thermal noise is Brownian motion. From the equipartition theorem each degree of freedom has $\frac{1}{2}k_{\mathrm{B}}T$ Joules of energy, where k_{B} is the Boltzmann's constant and T is the temperature of the molecule or atom. Brownian motion of the material is a direct result of the fluctuation dissipation theorem. In this theorem the random displacement of the material is related to the mechanical loss of a system and so by using materials with a lower mechanical loss, or high Q-value, thermal fluctuations can be concentrated into narrow bands around resonant frequencies. This reduces the noise away from the resonant frequencies. Another way to reduce Brownian motion thermal noise is to use cryogenic cooling of the detectors but this requires new technologies and different materials to those that are used in room temperature detectors. Thermal noises will be discussed further in chapter 2.

The thermoelastic noise studied in this thesis, plays an important part in limiting the sensitivity of gravitational wave detectors. It comes from the statistical temperature distribution making its appearance as mechanical movement e.g. as part of the suspension heats up it will expand and as a part cools it will compress. This noise source forms the basis of this thesis and is discussed more in chapters 2, 3, 4 and 5.

1.5.6 Thermo-optic Noise

Thermal refractive noise is another noise in the interferometer arising due to the effect that temperature has on the refractive indices of the beam splitter and mirror coatings [88]. As the refractive index of the material changes with temperature the phase of light being transmitted or reflected is not constant, leading to phase noise in the output of the interferometer, equivalent to changes in the inferred position of the end mirrors of a gravitational wave detector.

Similarly if the coating or substrate materials used expands or contracts with temperature fluctuations (via the thermal expansion coefficients) this could be wrongly interpreted as changes in the position of the end mirrors. The total thermo-optic noise spectral density can be described as [89]

$$S\left(\Delta x\right) \approx S\left(\Delta T\right)\left(\bar{\alpha}_c d - \bar{\beta}\lambda - \bar{\alpha}_s d\frac{C_c}{C_s}\right)^2, \tag{1.22}$$

where Δx is the change in the sensed position of the mirror, ΔT is the temperature change experienced by the mirror coating, $\bar{\alpha}_c$, C_c and $\bar{\alpha}_s$, C_s is the thermal expansion coefficient and the heat capacity per unit volume of the mirror coating and substrate respectively, λ is the wavelength of light being used to sense the position of the mirror, $\bar{\beta}$ is the effective thermorefractive coefficient and d is the thickness of the coating. It is interesting to note that the thermal expansion of the coating would potentially be a dominant noise source. If however, the materials used to manufacture/coat the mirrors and beam splitters is chosen correctly then the effective thermorefractive coefficient of the coating and thermal expansion coefficient of the substrate can cancel out the thermal noise produced from the coating thermal expansion coefficient, this allows

$$\bar{\alpha}_c d = \bar{\beta}\lambda + \bar{\alpha}_s d\frac{C_c}{C_s}, \tag{1.23}$$

thermo-optic noise to be completely nulled.

1.5.7 Other Noise Sources in aLIGO

The noises discussed above are the main fundamental noises in the detection frequency band of 10 Hz to a few kHz. There are also a variety of technical noise sources. The intensity and frequency of the laser light is another factor giving rise to noise. Scattered light recombing with the centered laser light will also produce noise. Frequency noise is dealt with by using a reference cavity via a process called frequency stabilisation. Intensity noise uses modulation to move the noise to a different frequency where it is not the dominant noise source.

The scattered light can be reduced with the use of baffles to absorb the stray beams but this can introduce fluctuations in the laser intensity. Variations in the orientation, shape and position of the laser also introduce noise. These effects are minimised by using a mode cleaning cavity or a single optical fibre [90]. Work is currently being done to see how using different mode types of the laser could increase the detector sensitivity. There will also be noise from surface charges on the test masses [91] especially in the presence of an external electric field. Residual gas pressure noise can have effects such as mechanical gas damping and Rayleigh scattering of light. In order to limit these effects the whole system is operated in a vacuum tank which is pumped to a base pressure of $\approx 10^{-8}$ Torr to provide a contaminant-free environment.

1.6 Future Interferometric Detectors

Interferometric detectors search for gravitational waves with their large frequency bandwidth range and ability to provide sensitivities in the range at which we expect to detect gravitational waves. There is research being done all over the world aimed at improving sensitivities of interferometric detectors and reducing the dominant noise sources. This section discusses the upgrade programs which are already ongoing for current detectors and also discusses a few detectors that are proposed for the distant future and are still at R&D stages of development.

1.6.1 Advanced LIGO

The upgrade to Advanced LIGO is already under way. During this update the inner test masses and the end mirrors, currently consisting of a 10.7 kg silica mass, hung from a single steel wire loop, will be changed to a quasi-monolithic quadruple pendulum system (see figure 1.14). This is hung from a two stage passive and active vibration isolation system with cantilever blades to reduce vertical and horizontal displacement noise. The quasi-monolithic suspensions hang a 40 kg silica mass, and the silica fibre suspensions developed for GEO600 at the University of Glasgow will also be part of this upgrade [10–14]. The damping of low frequency modes can now be done by acting on the highest stage of the pendulum with a magnetic actuator while electrostatic forces act on the lowest stage of the pendulum. The silica masses with the dielectric mirror coatings and the intermediate masses have silica attachments bonded to them using hydroxide catalysis bonding [92, 93]. Hydroxide catalysis bonding is used because it provides a strong and rigid bond which is very thin between two sections of fused silica. The silica fibres can then be welded at both ends to connect the horn on the intermediate mass to the horn on the silica end mass to form the quasi-monolithic suspension. During this upgrade the laser power will be increased from 10 Watts to 180 Watts and signal recycling will be added to the setup [94, 95].

This whole upgrade is hoped to decrease the noise of the LIGO detectors by a factor of 10 meaning that advanced LIGO can study a volume of space 1000 times greater than initial LIGO for astronomical sources [96] (figure 1.15).

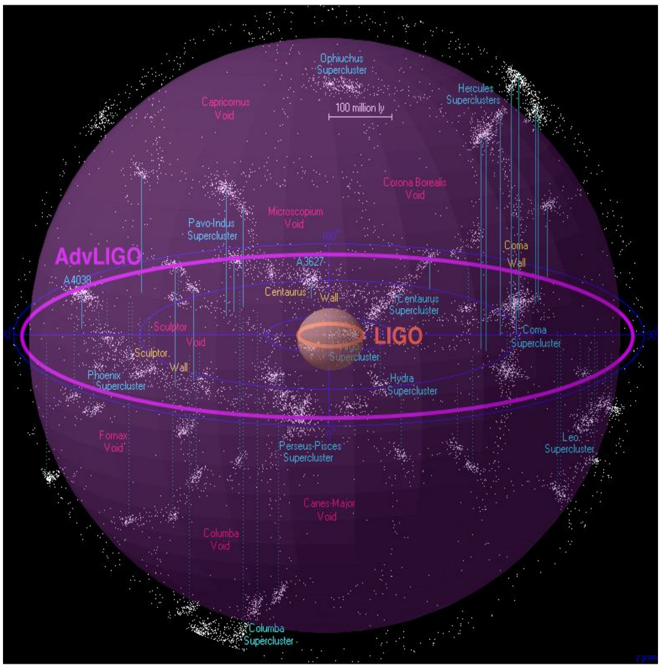

Figure 1.15: *Increased volume of the universe to which advanced LIGO is sensitive. Each dot represents a galaxy. Credit: R. Powell [97]*

Advanced LIGO will have a detection range for binary neutron star inspirals of around 200 Mpc and is expected to detect up to ∼40 neutron star inspiral events per year. It is also expected to detect neutron star-black hole inspirals at a rate of ∼10 per year [98].

1.6.2 Advanced VIRGO

Advanced VIRGO aims to achieve approximately the same detector sensitivity as Advanced LIGO and it will also implement the use of monolithic silica suspensions [15] to improve upon Virgo sensitivities by a factor of 10 [16]. This detector is unique in the design of the seismic isolation system. Vertical oscillations are damped out by the use of a super attenuator which consists of triangular cantilever blade springs mounted on multiple pendulum stages. The chain of seven pendulums hangs from an inverted pendulum system and is connected to an actively stabilised platform which compensates for very low frequency and large amplitude oscillations. At the bottom of this chain hangs the end mirror and a recoil mass is suspended. Fine control of the mirrors is provided by small forces between the mirror and the recoil mass using electrostatic actuators. Advanced Virgo also introduces a signal recycling mirror and increases the laser power of Virgo up to 175 W [17].

1.6.3 GEO-HF

GEO600 has a unique optical layout as discussed previously in section 1.4.3.2. The test masses for GEO600 are suspended as triple pendulums, however as GEO600 is about seven times smaller than advanced LIGO it is hard for it to compete and play a role in future gravitational detections. It is competing however by investigating new optical layouts which are expected to be extremely sensitive at high frequency bands above 1 kHz [99, 100]. This upgrade to GEO600 is called GEO-HF [101] and includes methods of getting below the standard quantum limit. The laser power will also be increased to 35 W to reduce shot noise.

1.6.4 CLIO & KAGRA

CLIO stands for Cryogenic Laser Interferometer Observatory. Its main aim was to test the instrumentation to be used in the KAGRA (formally known as LCGT). CLIO is situated 1000 m underground in the Kamioka mine, Japan. Building the detector below the Earths surface helps to decrease the level of seismic noise the detector is sensitive to. CLIO consisted of a 100 m Michelson interferometer and aimed to see how the mirrors react when cooled cryogenically as this reduces noise in the mirrors. Now the work of CLIO is complete, KAGRA is currently being built adjacent to the CLIO site in the same Kamioka mine. KAGRA has an arm length of 3 km with a low-frequency vibration-isolation system, cryogenic sapphire mirrors cooled to 20 K and a high-power laser system [102]. The aim of KAGRA is to detect chirp waves from binary neutron star coalescence. It hopes to detect two or three of these events each year. Its sensitivity will be similar to Advanced LIGO and Advanced Virgo.

1.6.5 Einstein Telescope

The Einstein Telescope is known as a third generation detector [103] as it aims to put together all previous knowledge of ground based detectors to give the most sensitive detector possible. The plan is to build three separate Michelson interferometers in a triangular formation 100-200 m underground with an arm length of 10 km. Each detector would be linked via tunnels to its neighboring detector (shown in figure 1.16) with each consisting of two interferometers for measuring high and low frequency signals (HF and LF). The initial design has 21 long suspensions, 45 short suspensions, 12 cryogenic mirrors and will implement 10 dB of effective light squeezing. ET HF will be at room temperature with a high power 1064 nm wavelength laser, making use of similar techniques to that of advanced LIGO. The ET LF design plans to operate with a low power 1550 nm wavelength laser at cryogenic temperatures giving what is known as a xylophone configuration. This xylophone configuration allows the detector to monitor both low and high frequency gravitational waves at the same time, thus allowing the future detector to be sensitive to a wider range of sources than aLIGO. The Design Study project [103] was supported by the European Commission under the Framework Programme 7 (FP7, Grant Agreement 211743). This project is open to all the scientists willing to collaborate to the ET venture.

1.6.6 IndIGO

In 2010 the Gravitational Wave International Committee (GWIC) issued a roadmap of their future plans [104]. In this roadmap it was very clear that the gravitational wave community would benefit greatly with source localisation by building a detector based in the southern hemisphere. One idea which is now being utilised is the chance to move one of the LIGO detectors currently

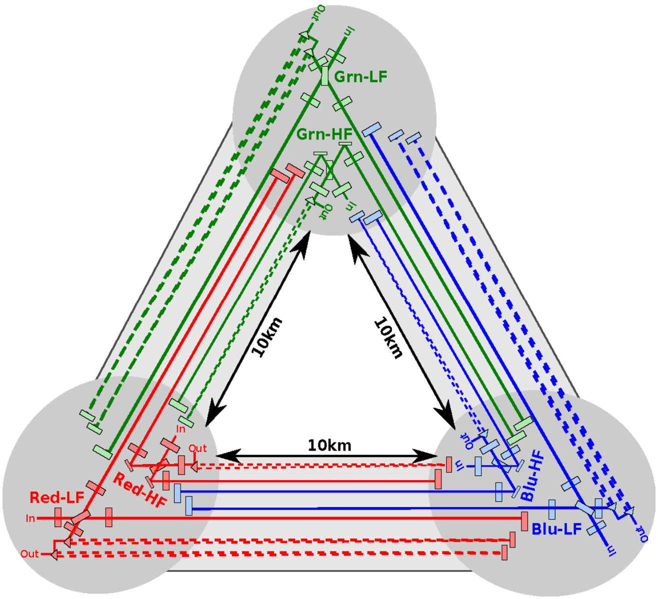

Figure 1.16: *Schematic layout of Einstein telescope. [103]*

based in North America and construct it in India. This would give three LIGO detectors; two aLIGO detectors in America and one LIGO detector in India. Whilst the Indian Interferometric Gravitational Wave Observatory (IndIGO) is not actually in the southern hemisphere, it will be a good compromise and allows 2-3 times as many sources to be localised to within 20 deg^2 when combined with the Hanford LIGO and Livingston LIGO [105].

1.6.7 DECIGO

DECIGO is a Japanese idea aimed at being their next big project after construction of KAGRA. The DECi-hertz Interferometer Gravitational wave Observatory is a gravitational wave antenna to be launched into space operating in the 0.1-10 Hz frequency band, thus bridging the gap between space based detectors and ground based detectors. The design is similar to initial LISA in that it has three drag-free spacecraft in a triangular formation although this time the arm length is only 1,000 km long. The main objective of DECIGO is to observe Big Bang remnants or more precisely gravitational radiation produced

10^{-36} to 10^{-34} seconds after the Big Bang. Electromagnetic waves cannot give us direct information about the first 380,000 years[2] so we must instead look at gravitational waves to understand the beginning of our universe. DECIGO is planned for launch in 2027 [106]. Before this happens two separate DECIGO pathfinders will be launched to test the ideas used in the DECIGO design. The first of these launches is scheduled for 2015 [107, 108] but it is likely to be delayed.

1.6.8 BBO

The Big Bang Observer (BBO) follows on from eLISA with the detectors being placed in a triangular formation. In total there are four individual triangles with BBO arm lengths being only 50,000 km, 100 times smaller than that of eLISA. This detector is sensitive to gravitational waves produced shortly after the Big Bang and binary signals that last for at most a few days. Like ground based detectors, cross correlation of detections from amongst the four detectors is planned. All of the triangles like eLISA follow the Earths trajectory around the Sun. Two of the triangular formation detectors will be on top of each other and rotated by 60 degrees, into a hexagram formation. The other two triangles will be located at distant points along Earth's orbit in order to triangulate the gravitational source when it is detected as shown in figure 1.17. The BBO requires the use of larger telescopes and higher power lasers than that planned for eLISA to improve sensitivity. The power of light received by eLISA due to the large arm length distances is less than 1 Watt. The BBO has shorter arms meaning it will receive ≈10 Watts. This is too large a power for photo detectors to handle so the interferometer is planned to operate on a dark fringe. This

---

[2] According to the current Big Bang Theory the universe was completely opaque to electromagnetic radiation for the first 380,000 years, meaning that any electromagnetic radiation monitored now was created after this time. Gravitational radiation on the other hand could propagate uninterrupted long before this, so by looking at gravitational radiation we can effectively view remnants from a much earlier universe.

means that unlike eLISA the distances between the spacecraft is kept constant, however because of the shorter arms less propellant is needed to manipulate the test masses [109]. Funding has not been allocated for this development. It is unlikely to proceed unless the eLISA mission is successful.

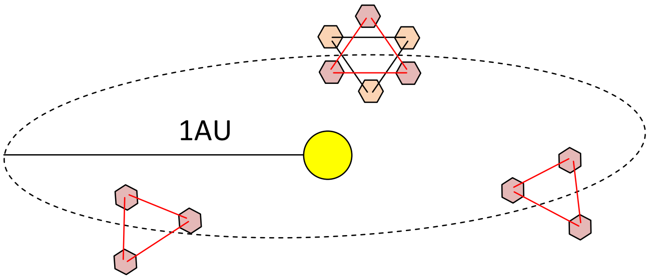

Figure 1.17: *Schematic of Big Bang Observer space craft arrangement.*

1.6.9 Conclusions

The direct detection of gravitational waves is one of the most anticipated events in the field of gravitational physics and astronomy, ever since Joseph Weber attempted to observe them in the 1960's with his resonant bar detector. Since then the science has developed and several long base line interferometers have carried out many science runs. These science runs have proved useful in setting limits on the strength of gravitational waves emitted from astrophysical sources. Disappointingly however, there has been no direct detection of gravitational wave signals but this is in accordance with current theoretical predictions for the strain amplitudes expected from astrophysical sources as discussed in this chapter.

The upgrades which are planned for the current detector network are needed in order to make this first direct detection a reality. In order to achieve this first detection and advance the field of gravitational wave astronomy noise sources in a gravitational wave detector must be reduced. This thesis focusses on suspension thermal noise and the mechanical loss of fused silica fibres used in gravitational wave detectors by measuring the parameters associated with thermoelastic, surface and weld loss mechanisms, which will limit the sensitivity of current ground based detectors via the fluctuation dissipation theorem as described in chapter 2. The work presented will allow for a much more robust and accurate suspension thermal noise estimation to be performed. This will be important not just for the current network of gravitational wave detectors but also for future upgrades which will be considered in the near future.

Chapter 2

Thermal Noise

2.1 Introduction

Thermal noise (discussed briefly in section 1.5.5) is a significant noise source limiting the sensitivity of gravitational wave detectors in the frequency range of 10 Hz to 100 Hz. Thermal noise can act in two separate ways. Firstly, the thermal energy is distributed to the translational, vibrational and rotational degrees of freedom of the atoms and molecules in the suspension or mirror coating. From thermodynamics each degree of freedom has $\frac{1}{2}k_{\mathrm{B}}T$ Joules of energy. When the atoms obtain energy they become more excited and consequently affect the overall motion of the mirrors (Brownian motion). The thermal energies of the mirrors and suspensions combine to give a displacement noise of the mirrors that are sensed by the gravitational wave detector and limit the amplitude of gravitational wave sources we can detect. Secondly, thermal noise can also reveal itself when there is a random temperature fluctuation in the material. These temperature fluctuations can give rise to a displacement of the end test mass mirrors, as the material expands and contracts through the coefficient of thermal expansion or through the Young's modulus varying as a function of temperature when the material is under stress (thermoelastic noise).

This chapter looks at the theoretical description of thermal noise and shows the relation between low thermal noise materials and low mechanical loss (high quality factor, Q) materials through the fluctuation-dissipation theorem.

2.2 Brownian Motion Noise

In 1785 Jan Ingenhousz had observed the irregular motion of coal dust particles on the surface of alcohol [110] but this effect was unexplained. In 1827 botanist Robert Brown watched with a microscope minute particles ejected by pollen grains floating freely on the surface of water moving in a vigorous and irregular manner [111]. Repeating his experiment with particles of inorganic matter, he was able to rule out that the motion was life-related and so the seemingly random motion became known as Brownian motion. In 1905 Einstein showed that the subsequent motion of the particles is a result of stochastic collisions with the water molecules [112]. It was also noted that with each stochastic collision the particles had with the water molecules, the initial kinetic energy of the particle was dissipated. The dissipation could be described by the viscosity of the water [112]. Einstein predicted that the average displacement of a particle undergoing Brownian motion in a fluid at a temperature T after some time t will be $\sqrt{2Dt}$ where the diffusion constant is $D = k_{\mathrm{B}}T/b(\omega)$ and $b(\omega)$ is the linear drag coefficient on the particle. It is this relation between viscosity and displacement which was developed to give the fluctuation-dissipation theorem [113, 114].

2.3 The Fluctuation-Dissipation Theorem

The fluctuation-dissipation theorem gives a general relationship between the excitation of a linear system and the dissipation of that excitement. The theorem also helps to predict the stochastic fluctuations in displacement of the material when it is in thermal equilibrium. In this thesis we measure the mechanical dissipation of fused silica fibres (chapters 4, 5 and 6). When the system is linear and obeys Hooke's law (force proportional to displacement). Any oscillations of the fibre will decay with time and hence energy is being dissipated from the system via internal and external friction.

The single sided power spectral density of the thermal or mechanical driving force $S_F(\omega)$ is related to the dissipative (real) part of the mechanical impedance $Z(\omega)$, such that [115]

$$S_F(\omega) = 4k_{\mathrm{B}}T\Re\left[Z(\omega)\right], \tag{2.1}$$

where k_{B} is the Boltzmann constant and T temperature of the material. This is similar to what was seen by Robert Brown [111] and Einstein [112] whereby some impedance or viscosity present in the system introduces random noise fluctuations in this case displacement noise onto the particles. The mechanical impedance is defined as $Z = F/V = F/i\omega X = 1/Y$ where F is the force, V is velocity, X is displacement and Y is the admittance in Fourier space. The power spectral density of the thermal or mechanical displacement is then given directly as [116]

$$S_X(\omega) = \frac{4k_{\mathrm{B}}T}{\omega^2}\Re\left[Y(\omega)\right]. \tag{2.2}$$

If we know how much energy is dissipated by a material then we can predict the thermal noise in a material.

The example below considers a simple case pendulum being acted upon by a viscous force. The equation of motion for the pendulum is given by,

$$F = m\ddot{x} + \dot{b}(\omega)x + kx, \tag{2.3}$$

where F is the force which is acting on the pendulum, m is the mass of the pendulum, $b(\omega)$ is the viscous damping coefficient, and k is the spring constant of the pendulum. For a harmonic solution to this equation $x = Ae^{i\omega t}$.

This allows the above equation to be rewritten as

$$F = (-m\omega^2 + i\omega b(\omega) + k)x \tag{2.4}$$

and so the mechanical impedance can be expressed as,

$$Z(\omega) = \frac{F}{i\omega X} = b(\omega) + i\left(m\omega - \frac{k}{\omega}\right). \tag{2.5}$$

The real part of $Z(\omega)$ is now $b(\omega)$ and so we have,

$$S_F(\omega) = 4k_{\mathrm{B}}Tb(\omega). \tag{2.6}$$

Looking at the displacement power spectral density it is the admittance which is important and this can be described as,

$$Y(\omega) = \frac{1}{b(\omega) + i\left(m\omega - \frac{k}{\omega}\right)}. \tag{2.7}$$

and so

$$\Re[Y(\omega)] = \frac{b(\omega)}{b(\omega)^2 + (m\omega - \frac{k}{\omega})^2}. \tag{2.8}$$

Substituting this into equation 2.2, the power spectral density can be written as,

$$S_X(\omega) = \frac{4k_{\mathrm{B}}Tb(\omega)}{\omega^2\left(b(\omega)^2 + \left(m\omega - \frac{k}{\omega}\right)^2\right)}. \tag{2.9}$$

As $\omega_o^2 = k/m$ and $\phi(\omega) = b(\omega)/m\omega$ the equation can also be written as,

$$S_X(\omega) = \frac{4k_{\mathrm{B}}T\phi(\omega)\omega_o^2}{m\omega\left(\omega^4\phi(\omega)^2 + (\omega_o^2 - \omega^2)^2\right)} \tag{2.10}$$

where $\phi(\omega)$ is the phase lag between stress (σ) and strain (ϵ) in radians, and is also known as the mechanical loss of the pendulum. From equation 2.10 the best way to lower thermal noise in gravitational wave detectors is to use low loss materials such as fused silica at room temperature or sapphire at cryogenic temperatures. These materials have a high quality factor where Q (the quality factor) is related to the mechanical loss by $Q(\omega) = 1/\phi(\omega)$. Figure 2.1 shows the thermal noise of a simple pendulum where the mass hanging is 40 kg point mass and the length of the pendulum suspension is 0.6 m. This gives a resonance peak at ∼650 mHz. It is clear to see that for a higher Q material the on-resonance thermal noise is higher and contained to a narrower resonance frequency bandwidth than a lower Q material. Note that the area under the graph has remained constant and so the width of the Lorentzian peak is proportional to $\phi(\omega_o)$. This will allow gravitational wave detectors to be much more sensitive away from the resonance peak if high Q (low loss) materials are used.

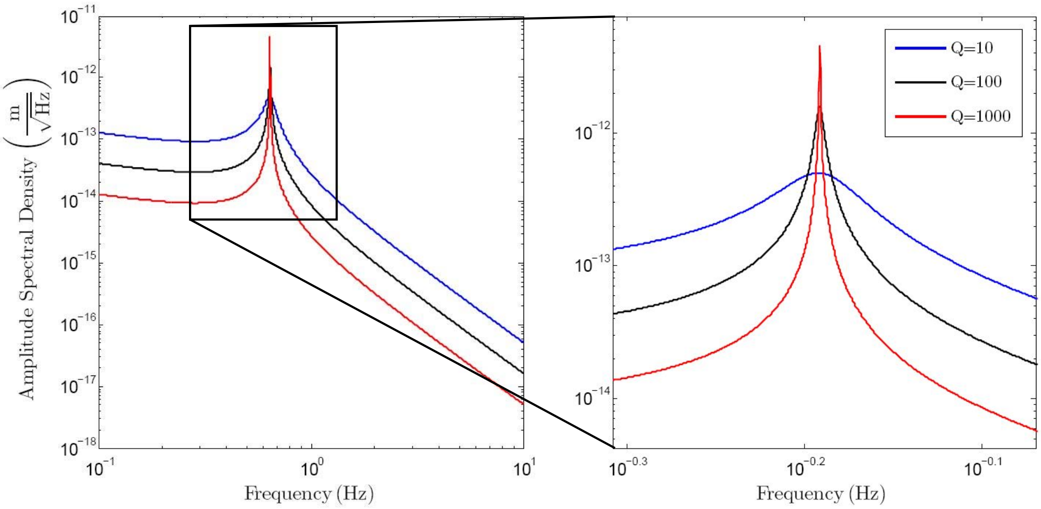

Figure 2.1: *A plot showing the thermal noise amplitude spectral density estimate for a pendulum system with different values of mechanical loss. The sensitivity plot was calculated from equation 2.10 for a pendulum 0.6 m in length supporting a point mass of 40 kg with a resonant pendulum mode at ∼650 mHz, for a range of ϕ values.*

2.4 Sources of Dissipation

In gravitational wave detectors it is important to keep the amount of energy dissipated in materials as low as possible. This will allow gravitational wave detectors to reach a lower sensitivity level and increase the amount of astrophysical sources we can detect. This section looks at the sources of energy dissipation which will limit the sensitivity of a gravitational wave detector.

2.4.1 External Sources of Dissipation

There are a number of external loss mechanisms which contribute to the noise of a suspension system used in a gravitational wave detector. External sources of dissipation include friction at the suspension point. This could include the point at which the wire is used to hang the test mass or in monolithic suspensions the point where the test masses and suspension elements are in contact, otherwise known as frictional (stick-slip) damping. In addition there may also be dissipative recoil damping where energy is transmitted from the test mass pendulum system to the supporting structure used to hold the pendulum. If this supporting structure is for example made from steel and bolts this will dissipate energy at a much higher rate than the silica pendulum where the majority of the strain energy is being stored. Damping from collisions with surrounding gas molecules in the vacuum vessel is another major energy loss although it is dealt with by pumping the vacuum system to as low a level as possible (approximately 10^{-8}mbar making the loss $\leq 1 \times 10^{-10}$). Both recoil damping and gas damping are discussed and explored in chapters 4 and 6. Magnetic hysteresis and eddy current damping are also present and these effects come from the upper stages of the pendulum system where magnetic fields are used to reduce the motion of the upper pendulum stages.

2.4.2 Internal Sources of Dissipation

The external sources of dissipation can be minimised such that the internal loss mechanisms become the dominant noise source. This loss arises when a material behaves anelastically. The two kinds of idealised internal dissipations are described as being either viscous or structural. When a stress (force per unit area) is applied to a suspension it will stretch in the direction of the applied force and exhibit a strain (fractional change in length). If a wire is treated as having internal bonds which act like a Hooke's law spring we expect to apply a stress and observe the wire to stretch. When the stress is no longer applied it would be expected that the wire returns immediately to its unstressed and un-stretched state which is known as an ideal solid. For such a solid we would expect stress (σ) and strain (ϵ) to vary directly and linearly with each other and sketch out a straight line in stress-strain space with $\sigma = k\epsilon$. Here k is the compliance (similar to the concept of a spring constant) of the material which is related to the energy stored in the material due to the induced deformation. However for many materials this is not the case. When a steel or glass wire is stressed it does not reach its final state of strain immediately [117, 118] and there is a finite relaxation time for the strain to fully occur after the stress is applied. Such a material is said to exhibit anelasticity. Furthermore when the length displacement is cycled around a closed loop this traces out a hysteresis loop in stress-strain space as shown in figure 2.2. This indicates that mechanical hysteresis may also be present in the wire and could attribute to energy loss in a system.

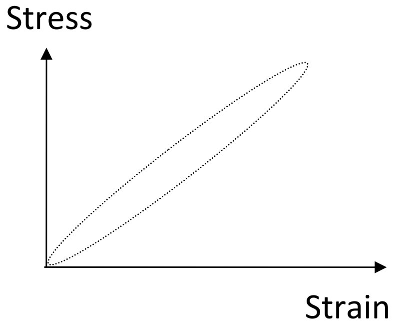

Figure 2.2: *A plot of how an anelastic material behaves under stress to form a hysteresis loop for one complete oscillation of a resonant mode experiencing viscous damping.*

For anelastic materials, the strain lags behind the stress by some phase-lag ϕ also known as the loss angle such that

$$\sigma = \sigma_o e^{i\omega t} \tag{2.11}$$

$$\epsilon = \epsilon_o e^{i(\omega t+\phi)} \tag{2.12}$$

For an ideal elastic material $\phi(\omega) = 0$; here ω introduces an angular frequency dependance to the phase-lag. The anelasticity of a material can be caused by many factors such as the flow of heat through a material as it expands and compresses. This is known as thermoelastic damping [119] and this particular relaxation mechanism will cause the dissipation to have a peak at a certain frequency called the Debye peak. There may be more than one of these peaks, with each peak associated with a separate anelastic relaxation process. This could include molecules moving in different degrees of freedom, pinning sites trapping molecules, dislocations of bonds and other processes of migration across the material. These Debye peaks can be separated by many decades of frequency.

The loss of a material is usually measured via the quality factor, Q. The Q for a resonant angular frequency ω_o is defined as

$$Q\left(\omega_o\right) = 2\pi \frac{E_{\text{stored}}}{E_{\text{lost}}(\omega_o)} \tag{2.13}$$

where $E_{\text{stored}} = \frac{1}{2}kA^2$ for an oscillation with amplitude A, and where $E_{\text{lost}}(\omega_o)$ is the energy lost per oscillation. In equation 2.12 it was shown that anelastic loss results in a phase difference between stress and strain. Alternatively we can rewrite Newton's elastic equation $F = -\hat{k}x$ in terms of equation 2.12 as

$$F = -\hat{k}x = -ke^{i\phi(\omega)}.Ae^{i\omega t} = -Ak[\cos(\omega t + \phi(\omega)) + i\sin(wt + \phi(\omega))] \tag{2.14}$$

Integrating the real part over the displacement x caused by the oscillation will give us the work done by the material.

$$\mathrm{W} = \int_0^A F\,dx = \int_0^A -Ak\cos(\omega t + \phi(\omega))\,dx \tag{2.15}$$

Substituting $x = A\cos(\omega t)$ and hence $dx = -A\omega\sin(\omega t)dt$ we can integrate the work done for one complete oscillation which will occur over some time period T to get,

$$\mathrm{W} = \int_0^T -Ak\cos(\omega t + \phi(\omega))A\omega\sin(\omega t)\,dt = -\frac{1}{2}k\omega A^2 T\sin(\phi(\omega)). \tag{2.16}$$

Thus equation 2.13 can be re-written for resonant frequencies ω_o as

$$Q\left(\omega_o\right) = \frac{2\pi\frac{1}{2}kA^2}{\frac{1}{2}k\omega_o A^2 T\sin(\phi(\omega_o))} = \frac{1}{\sin(\phi(\omega_o))} \approx \frac{1}{\phi(\omega_o)} \tag{2.17}$$

for low values of loss where $\phi(\omega_o) << 1$.

2.4.3 The Dissipation Dilution Factor

The pendulum systems used to support the test mass mirrors both minimise seismic noise and thermal noise. An additional benefit is the reduction in the

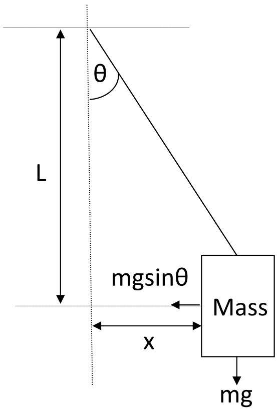

Figure 2.3: *Schematic showing the gravitational restoring force*

loss angle due to the fact that gravity is a conservative field and provides an extra restoring force for horizontal motion of a pendulum. Figure 2.3 shows a simple pendulum suspended on a fibre in order to demonstrate dissipation dilution. It can be seen from the figure that the gravitation pull acting on the mass provides a restoring force in this case $F_{\text{gravity}} = mg\sin(\theta)$ and an effective spring constant of:

$$k_{\text{gravity}} = \frac{mg}{L} \tag{2.18}$$

This spring constant is conservative and will not produce any loss. Therefore we can write the energy lost per cycle as some fraction, ϕ_{fraction}, of the energy stored in the fibre. We can do this because only bending strain energy will be dissipated [120]. This gives us the following expression:

$$E_{\text{lost per oscillation}}(\omega_o) = \phi_{\text{fraction}}(\omega_o)\frac{1}{2}k_{\text{fibre}}x^2, \tag{2.19}$$

where k_{fibre} is the spring constant for the fibre described by [116]. The loss of the fibre can be calculated by equation 2.20

$$\phi_{\text{material}}(\omega_o) = \frac{1}{Q} = \frac{E_{\text{lost per oscillation}}(\omega_o)}{2\pi E_{\text{stored}}} = \frac{\phi_{\text{fraction}}(\omega_o)}{2\pi} \tag{2.20}$$

Now calculating the loss of the pendulum system, the total energy stored in the pendulum is

$$E_{\text{stored in pendulum}} = \frac{1}{2}(k_{\text{fibre}} + k_{\text{gravity}})x^2 \tag{2.21}$$

so the loss of the pendulum is

$$\phi_{\text{pendulum}}(\omega_o) = \frac{\phi_{\text{fraction}}(\omega_o)\frac{1}{2}k_{\text{fibre}}x^2}{2\pi\frac{1}{2}(k_{\text{fibre}} + k_{\text{gravity}})x^2} = \frac{\phi_{\text{fraction}}(\omega_o)k_{\text{fibre}}}{2\pi(k_{\text{fibre}} + k_{\text{gravity}})} \tag{2.22}$$

which can be simplified as $k_{\text{gravity}} >> k_{\text{fibre}}$ leaving

$$\phi_{\text{pendulum}}(\omega_o) \approx \phi_{\text{material}}(\omega_o)\frac{k_{\text{fibre}}}{k_{\text{gravity}}} \tag{2.23}$$

The ratio $k_{\text{fibre}}/k_{\text{gravity}}$ is known as the dilution factor as it reduces the loss of the pendulum system.

When the pendulum system is suspended at the center of mass by n fibres then the analytical expression of the elastic spring constant of the fibres is [116]:

$$k_{\text{fibres}} = \frac{n\sqrt{TYI}}{2L^2}, \tag{2.24}$$

where T is the tension in each fibre and $I = \pi r^4/4$ is the second area moment of the fibre being used to suspend the pendulum. The total pendulum loss is then given by [121]

$$\phi_{\text{pendulum}}(\omega_o) \approx \phi_{\text{material}}(\omega_o)\frac{\xi n\sqrt{TYI}}{2mgL} \tag{2.25}$$

here $\xi = 1$ for a simple pendulum and the dilution factor is defined as $1/\mathrm{D} = \phi_{\text{pendulum}}(\omega_o)/\phi_{\text{material}}(\omega_o)$. We can substitute mg for nT to give the dilution factor:

$$\mathrm{D} = \frac{2L\sqrt{T}}{\sqrt{YI}} \tag{2.26}$$

It is also useful to note that the simple-pendulum mode (figures 2.5 and 2.4a) will bend around the top end of the fibre while a multiple fibre pendulum mode will have bending at the top and bottom, shown in figure 2.4b. The resulting loss of energy from a multiple fibre pendulum is twice that of a simple fibre pendulum mode and we can set $\xi = 2$. aLIGO uses a suspension system were four fibres are used to support the silica mirrors. A four fibre suspension pendulum mode has two bending points; one at the top and one at the bottom of each of the fibre, as shown in figure 2.4b. This again results in the loss of energy from a four fibre pendulum mode twice that of a simple pendulum mode; and so we can set $\xi = 2$ for this case.

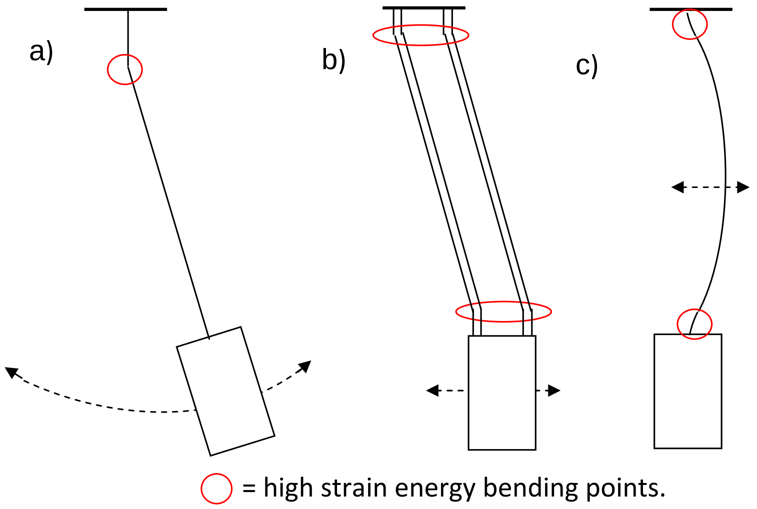

Figure 2.4: *a): Simple pendulum mode showing one bending point in the silica fibre. b): Four fibre pendulum mode showing two bending points in the silica fibre. c): Violin mode showing two bending points in the silica fibre.*

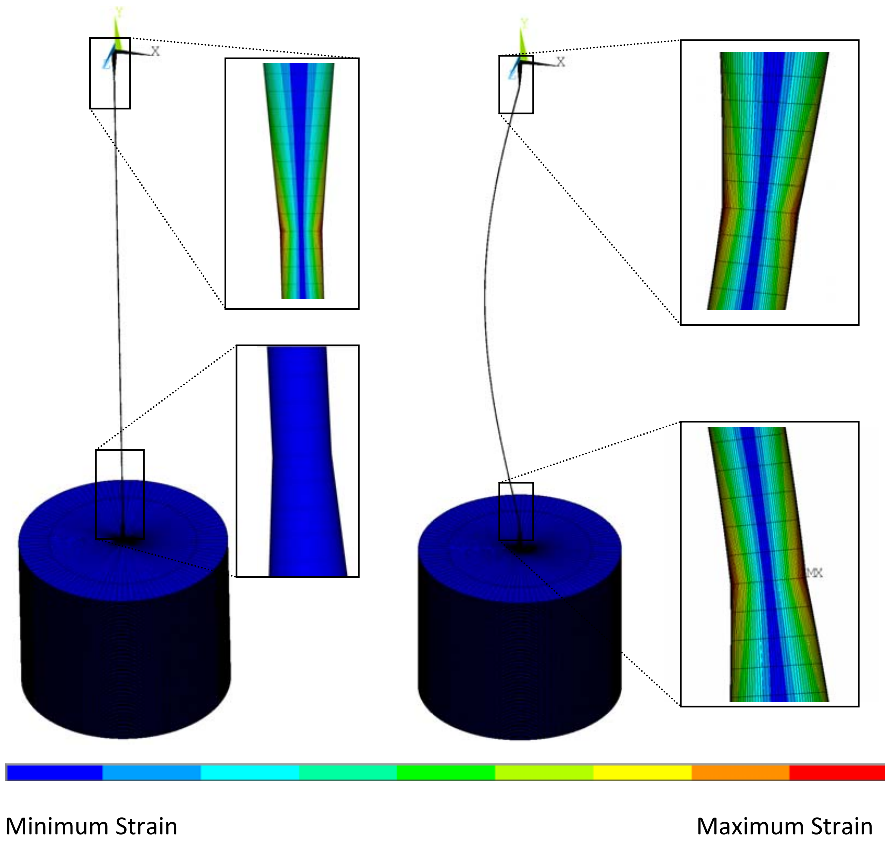

Figure 2.5: *Picture taken from ANSYS showing the strain distribution comparison between a pendulum mode oscillation and violin mode. Left: Simple fibre pendulum mode showing all of the bending strain in the top section of the silica fibre. Right: Violin mode showing the bending strain distributed between the top and bottom sections of the silica fibre.*

Work was carried out by Gonzalez and Saulson [122] where they calculated the analytical dilution values for violin modes. Similar to multiple fibre pendulums the fundamental violin modes have two bending points one at the top and one at the bottom of the fibre as shown by figures 2.4c and 2.5. Higher order harmonic violin modes, m where m=1,2,3.., may have more bending points and this is accounted for using

$$\mathrm{D} = \frac{2}{L}\sqrt{\frac{YI}{T}}\left(1+\frac{(m\pi)^2}{2L}\sqrt{\frac{YI}{T}}\right). \tag{2.27}$$

The dilution is calculated from ANSYS (Finite Element Analysis Software) by first building an accurate pendulum model and running a static analysis. The static analysis models how the system behaves when a gravitational pull is acting on that system. Once the static analysis is complete a modal analysis is carried out and this calculates the eigenmodes of the system along with the kinetic and strain energy distributions of the system for each individual eigenmode. This also means that the total energy of the eigenmode can be calculated from the sum of the kinetic energies in the system. The dilution contribution of each individual element, D_i, in the system can be calculated as

$$\mathrm{D}_i = \frac{E_{\text{kinetic energy}_i}}{\sum_{i=1}^{n} E_{\text{strain energy}_i}}, \tag{2.28}$$

where $E_{\text{kinetic energy}_i}$ is the kinetic energy and $E_{\text{strain energy}_i}$ is the strain energy being stored in each element $1...n$ of the ANSYS model. This can be summed to calculate the total system dilution given by equation 2.25

$$\mathrm{D} = \sum_{i=1}^{n} \mathrm{D}_i = \frac{\sum_{i=1}^{n} E_{\text{kinetic energy}_i}}{\sum_{i=1}^{n} E_{\text{strain energy}_i}}. \tag{2.29}$$

Using ANSYS to model dilution rather than just having analytical approximations has became widely accepted in recent years. As fibre geometries become more complex the strain distribution and hence kinetic energy distribution along the elements of the fibre can change. ANSYS is very good at modeling these energy distributions and gives us a neat way to calculate dilution. This way of modeling dilution was investigated and found to agree with analytical formulas to within 1% [123] for uniform fibres. Results of modeling dilution in this way are presented in chapters 4 and 5. The dilution of the pendulum mode in the aLIGO suspension systems is calculated from FEA to be ∼91 [13, 124, 125] and this compares with the analytical expression (equation 2.25) which returns a value of ∼156. The reason for the mismatch in values is because the energy distribution in the neck region is an important factor in the calculation of dilution. For the analytical expression in (equation 2.25) it was assumed that all the strain energy was constrained in a uniform 880µm diameter section of fibre, which for a real case scenario is not true [123]. As fractions of the fibres bending energy will reside in the thicker stock and neck regions of the fibre. This is an important point as later in chapters 4 and 5 the dilution from real fibre violin modes is calculated and the dilution values returned from ANSYS are found to vary significantly from expected analytical values.

2.4.4 Thermoelastic Noise and Damping

Thermoelastic loss comes from heat flow across flexing fibres and mirrors. It was first studied by Zener [126] and then by Norwick [119]. This dissipation mechanism is best understood by considering a thin fibre that is oscillating. When the fibre is bending, one side of the fibre will be compressed while the other side is stretched. The side that is being compressed will increase in temperature and the stretched side will decrease in temperature. This will cause heat (energy) to flow from the hot side of the fibre to the colder region until thermal equilibrium is reached. This dissipation mechanism is also important in test mass mirrors as discussed by Braginsky et al [127].

In a test mass or an un-deflected fibre, statistical fluctuations in temperature will cause motion through the temperature dependance of the thermal expansion coefficient α,

$$\alpha = \frac{1}{L}\frac{dL}{dT}, \tag{2.30}$$

where L is the original length of the of the fibre and dL/dT is the change in length with respect to the temperature. The characteristic time for heat to transfer across a fibre with a circular cross section is given by [128, 129]

$$\tau = \frac{1}{4.32\pi}\frac{\rho C d^2}{\kappa} \tag{2.31}$$

where d is the diameter of the fibre section, C is the specific heat capacity of material per mass unit, κ is the thermal conductivity and ρ is the density of the material. τ also known as the thermal time constant at which the temperature gradient decays in the fundamental eigenmode of the system. The thermoelastic loss is given by

$$\phi(\omega) = \frac{YT\alpha^2}{\rho C}\frac{\omega\tau}{1+(\omega\tau)^2}. \tag{2.32}$$

Equation 2.32 is true for an unloaded fibre (or mirror) and has a Debye peak in the loss at a specific frequency where $\omega\tau = 1$ as shown by figure 2.6. This figure estimates the thermoelastic loss from a 400 µm fused silica suspension fibre where the temperature dependance of the Young's modulus Y is negligible i.e. the fibre is oscillating freely with no stress or dilution. For a loaded suspension fibre there is a second term in equation 2.32 due to the change of Young's modulus with temperature [130–133], and so an effective α can be described as [134]

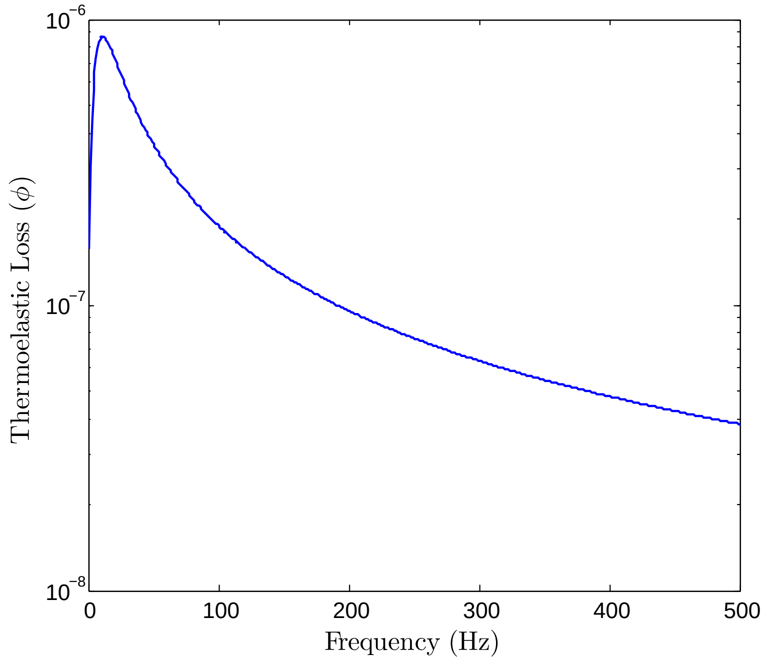

Figure 2.6: *Graph showing the Debye peak for thermoelastic loss in a 400µm diameter fused silica fibre when no stress is applied to it. Calculated using equation 2.32 where* $\alpha = 3.7\times10^{-7}K^{-1}$, $C = 770Jm^{-1}K^{-1}$ *and* $Y = 7.2\times10^{10}Pa$.

$$\alpha_{\text{new}} = \frac{1}{L_{\text{total}}}\frac{dL_{\text{total}}}{dT} = \alpha - \frac{\sigma_o}{Y^2}\frac{dY}{dT} \tag{2.33}$$

This will be discussed in more detail in chapter 3, but for now we can re-write the thermoelastic loss as

$$\phi(\omega) = \frac{YT}{\rho C}\left(\alpha - \sigma_o \frac{\beta}{Y}\right)^2 \left(\frac{\omega\tau}{1+(\omega\tau)^2}\right) \tag{2.34}$$

where

$$\beta = \frac{1}{Y}\frac{dY}{dT} \tag{2.35}$$

and σ_o is the static stress on the fibre. For almost all materials β the thermal elasticity coefficient acquires a negative value, increasing the thermoelastic loss as a larger stress is applied to the material. However very importantly fused silica, which is used in the gravitational wave detector suspensions, has a positive β value allowing thermoelastic loss to be reduced if a static stress is applied and in theory completely removed when

$$\alpha = \frac{\sigma_o Y}{\beta}. \tag{2.36}$$

This technique is essential for reaching the target sensitivity of aLIGO (shown later in figure 2.7) and is the focus of this thesis (see Chapters 3, 4 and 5).

2.4.5 Modeling Suspension Loss

The suspension and mirror loss is made up of several different sources. As the fibre dimension changes along its length the stress, and the strain energy also vary. It is easiest when using theoretical predictions to look at individual elements along the suspension fibre using ANSYS. To obtain the total loss of the suspension each element loss contribution ϕ_i needs to be weighted by the ratio of elastic energy stored in that element E_i over the total elastic energy in the system E_{total}. The total loss of the silica system is then described by:

$$\phi_{\text{total}}(\omega) = \frac{1}{\text{D}}\left(\frac{E_1}{E_{\text{total}}}\phi_1(\omega) + \frac{E_2}{E_{\text{total}}}\phi_2(\omega) + ... + \frac{E_{\text{n}}}{E_{\text{total}}}\phi_{\text{n}}(\omega)\right) \tag{2.37}$$

where $\phi_1 ... \phi_{\text{n}}$ is the loss from each element $1...n$ in the ANSYS model. As previously described, dilution is caused by storing energy from the oscillations in gravity which is a conservative field, rather than storing strain energy in the suspension material which dissipates energy. This dilution is negligible $\sim$1 for cantilever modes, due to the fact that tension from gravity on the oscillating part of the system is close to zero. However, in the case of violin or pendulum modes where a mass is attached to the end of a fibre the dilution plays an important role and has a value $>> 1$.

The total loss of a suspension fibre is made up of a contribution from several terms including thermoelastic, surface, weld and bulk loss. The loss therefore in the i th element of the fibre from equation 2.37 is

$$\phi_i(\omega) = (\phi_{\text{thermoelastic}}(\omega) + \phi_{\text{surface}} + \phi_{\text{bulk}}(\omega))_i \tag{2.38}$$

except in the weld region where only the weld loss is taken into account. This value has been previously measured on thin fibre welding ($\sim$400 µm diameter welds)[135] such that

$$\phi_i = \phi_{\text{weld}} \approx 5.8 \times 10^{-7}. \tag{2.39}$$

The weld loss mechanism is believed to come from excess thermal stresses left behind from the melting and solidifying process [136] when attaching the silica fibre to the silica ears. The weld region of the fibre for flame welds is measured to be $\sim$2 mm long, however for CO_2 welds like those carried out for aLIGO it is closer to 1 mm as this is the typical length of the fibre that gets melted and solidified during welding.

The thermoelastic loss is given by equation 2.34 [126, 134] as described in section 2.4.4. In that section τ describes the characteristic heat flow time across the fibre element, and σ_o is the static stress on that particular element. All other coefficient values are listed in table 2.1.

In thin fibres it is assumed that a surface layer of a certain thickness $h \approx$1 µm exists and has higher loss contribution than the bulk loss [139–141]. This surface loss mechanism is believed to originate from micro-cracks on the surface of the fused silica. It is believed that as energy is transferred to the fused silica

$\alpha\,(\mathrm{K}^{-1})$	$(4.5 \pm 1.5) \times 10^{-7}$	[132, 135, 137]
$C\,(\mathrm{Jm}^{-1}\mathrm{K}^{-1})$	(770 ± 5)	[138]
$Y\,(\mathrm{Pa})$	$(7.2 \pm 0.1) \times 10^{10}$	[130, 131]
$\beta\,(\mathrm{K}^{-1})$	$(1.5 \pm 0.1) \times 10^{-4}$	[130–133]

Table 2.1: *Table of coefficients used to calculate the thermoelastic loss.*

the crack surfaces grind and rub together dissipating energy. Thus we can describe the surface loss as being a function of energy stored in the surface:

$$\phi_{\mathrm{surface}} = \frac{E_{\mathrm{surface}}}{E_{\mathrm{bulk}}}\phi_{\mathrm{s}}, \tag{2.40}$$

where ϕ_{s} is the mechanical loss of the material surface and so the surface loss of an element of a circular fibre with diameter d is given by a coefficient C_1 (determined by the fibre geometry) multiplied by the ratio of surface S to volume V [139].

$$\phi_{\mathrm{surface}} = C_1\frac{S}{V}h\phi_{\mathrm{s}} = C_1\frac{2\pi rL}{\pi r^2 L}h\phi_{\mathrm{s}} \approx \frac{8h\phi_{\mathrm{s}}}{d} \text{ for } C_1 \approx 2. \tag{2.41}$$

The product of $h\phi_{\mathrm{s}}$ is taken as 6.15×10^{-12} m [139] for normal suprasil grade 2A silica. More recent results show that CO_2 laser polishing of silica fibres can reduce this value of $h\phi_{\mathrm{s}}$ to be as low as 3.4×10^{-12} m [142]. CO_2 laser polishing involves heating the surface of the fused silica to a temperature where the surface begins to flow. This allows surface cracks to fuse or ‘heal’ under the influence of surface tension. This process not only seems to reduce the surface loss but also increases the strength of fused silica as any sharp geometric features in the cracks are rounded off leading to a higher breaking strength [142–144].

Bulk loss is defined by [141]:

$$\phi_{\mathrm{bulk}}(\omega) = C_{\mathrm{bulk}} \times (\frac{\omega}{2\pi})^b = C_{\mathrm{bulk}} \times f^b = 7.6 \times 10^{-12} f^{0.77}. \tag{2.42}$$

here the frequency of resonance f plays a dominant role. This loss mechanism is thought like most amorphous materials to stem from bonds in the molecules flipping or moving, in this case the silicon and oxygen molecules are thought to be flipping and dissipating energy.

The loss therefore of the full structure is the sum of all these loss mechanisms added up over each element of the structure.

$$\phi_{\text{total}} = \frac{1}{\mathrm{D}}\left(\sum_{i=1}^{n-w}\frac{E_i}{E_{\text{total}}}\phi_i + \sum_{i=w}^{n}\frac{E_i}{E_{\text{total}}}\phi_{\text{weld}}\right), \tag{2.43}$$

where ϕ_i is the loss contributions from thermoelastic, surface, and bulk loss of the ith element.

The sum of these losses limit the sensitivity of Advanced LIGO as calculated by the fluctuation-dissipation theorem (equation 2.44) and shown as the blue line in figure 2.7.

$$S_X(\omega) = \frac{4k_{\mathrm{B}}T}{m\omega}\left(\frac{\omega_o^2\phi_{\text{total}}(\omega)}{\omega_o^4\phi_{\text{total}}^2(\omega) + \left(\omega_o^2 - \omega^2\right)^2}\right) \tag{2.44}$$

where ω is the angular frequency at which the noise level is being calculated and ω_o is the modal resonant frequency of the system; this could be a vertical, horizontal or violin mode. It is important to note that all of these resonant modes must be considered when calculating the total suspension sensitivity. It can clearly be seen from figure 2.7 that in the frequency regime from 10 Hz to 100 Hz thermal noise from the suspension system is one of the dominant terms which limits the sensitivity of aLIGO.

2.4.6 Conclusions

Thermal noise from suspension systems and mirrors of the current gravitational wave detectors is a dominant noise source that limits the detection sensitivity of detectors. The fluctuation-dissipation theorem is very useful in helping to design gravitational wave detectors as it allows for the thermal noise to be determined from the known mechanical losses of the suspension. The gravitational wave detectors are designed such that they operate with a very low mechanical loss and as such a very low off-resonance thermal noise.

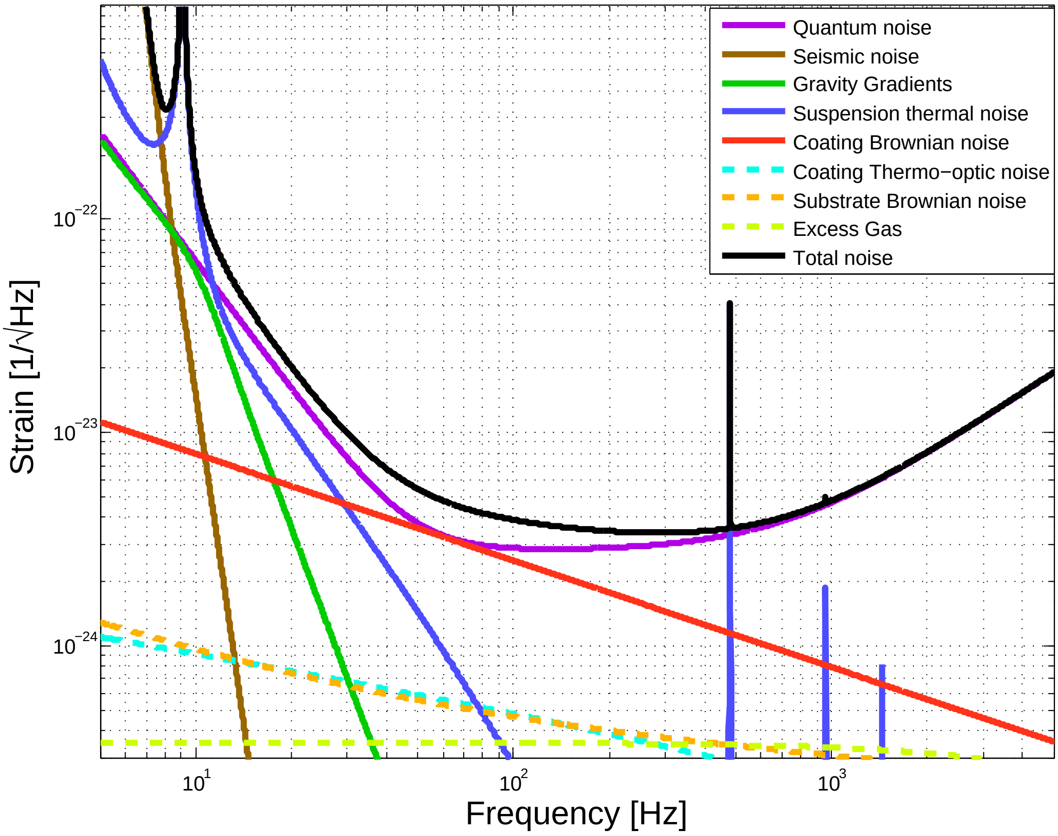

Figure 2.7: *Plot showing the noise source limitations for Advanced LIGO.*

To achieve this low mechanical loss it is important to design a system that lowers the thermoelastic loss arising from the flexing of the suspension fibres. This is possible by choosing the value of stress in the suspension elements such that the overall thermoelastic loss is significantly reduced. Other loss mechanisms such as surface loss, weld loss and bulk loss also contribute to the suspension thermal noise. A study of these suspension loss mechanisms is presented in this thesis with the aim that the findings can be used to provide robust estimates of suspension thermal noise and in the hope that the data presented can be used in future upgrades to increase detector sensitivities.

Chapter 3

Experimental Results for Nulling the Effective Thermal Expansion Coefficient of Fused Silica Fibres Under a Static Stress.

3.1 Introduction

In the following chapter we experimentally demonstrate that the effective thermal expansion coefficient of a fused silica fibre can be nulled by placing the fibre under a particular level of stress. This is useful as not only does it suggest that the thermoelastic loss of fused silica can be nulled. It also shows that by stressing silica we can cancel and even reverse it's effective thermal expansion coefficient allowing stressed silica to be used as an alternative material in systems that require low thermal expansion or low thermal noise components. This chapter details an experiment and measurements made to inform a paper that was accepted for publication by *Classical and Quantum Gravity* [145]. Our technique involves heating the fibre and measuring how the fibre length changes with temperature as the stress on the fibre was systematically varied. The experiment was repeated four times using four identical fused silica fibres. This nulling of the effective thermal expansion coefficient should allow for the complete elimination of thermoelastic noise and is essential for allowing second generation gravitational wave detectors to reach their target thermal noise sensitivity of below $10^{-19}\,\mathrm{m}/\sqrt{\mathrm{Hz}}$ at 10 Hz [11]. Fused silica is the low loss material of choice for gravitational wave detector suspensions as it can be pulled into strong fibres [143] and welded to form a quasi-monolithic suspension [11–14]. Thermoelastic loss would be a dominant noise source except for the fact that fused silica has a Young's modulus which increases with temperature (figure 3.1) [130–133, 146] and this should allow the effective thermal expansion coefficient of fused silica to be nulled by using fibres that are appropriately stressed [134] as discussed in Chapter 2.

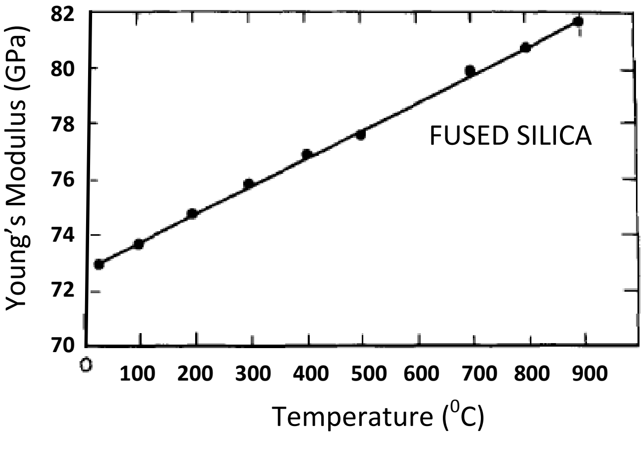

Figure 3.1: *Plot showing the Young's modulus for silica increasing with temperature. Credit: S. Spinner [131]*

The required suspension thermal noise for Advanced LIGO can only be achieved if the effective thermal expansion coefficient can be significantly reduced by applying the correct amount of static stress to the suspension fibre. This nulls the thermoelastic loss of each suspension fibre under tension, which is given by equation 2.34. It is convenient to consider $\left(\alpha - \frac{\sigma_o \beta}{Y_o}\right)$ as the effective thermal expansion coefficient. In Advanced LIGO there are four fibres used to support the 40 kg silica test mass [14]. Most of the bending energy contained in the fused silica suspensions is stored in the 800 μm diameter region of the fibres. This corresponds to a stress in the 800 μm diameter region of 195 MPa which is used to null the thermoelastic loss mechanism.

This chapter describes an experiment which was conceived by Professor Jim Faller and had a prototype demonstrated by Dr Stuart Reid. The setup was then revised and modified by the author and Dr Giles Hammond for the results presented in this chapter, which shows for the first time that the thermal expansion coefficient of a fused silica fibre can be cancelled by the application of a suitable static stress. It is instructive to derive an equation that shows how the extension of silica under static stress varies with temperature. Consider a fibre under some static stress σ_{o}. For a temperature change, ΔT, the strain due to the coefficient of linear thermal expansion, α and the change of the Young's modulus with temperature is

$$\frac{\Delta L}{L} = \alpha \Delta T + \frac{\sigma_{\mathrm{o}}}{Y} = \alpha \Delta T + \frac{\sigma_{\mathrm{o}}}{Y_{\mathrm{o}} + \frac{dY}{dT}\Delta T}. \tag{3.1}$$

The term $\sigma_{\mathrm{o}}/(Y_{\mathrm{o}} + dY/dT)$ allows for a temperature dependent Young's modulus. Rearranging and keeping only first order terms gives

$$\frac{\Delta L}{L} = \alpha \Delta T + \frac{\sigma_{\mathrm{o}}}{Y_{\mathrm{o}}}\left(1 - \frac{1}{Y_{\mathrm{o}}}\frac{dY}{dT}\Delta T\right) = \alpha \Delta T + \frac{\sigma_{\mathrm{o}}}{Y_{\mathrm{o}}}\left(1 - \beta \Delta T\right), \tag{3.2}$$

where the term $\frac{\sigma_{\mathrm{o}}}{Y_{\mathrm{o}}}$ is the static stretch of the fibre. The effective thermal expansion coefficient α_{eff} is thus [134]

$$\alpha_{\mathrm{eff}} = \left(\alpha - \sigma_{\mathrm{o}}\frac{\beta}{Y_{\mathrm{o}}}\right). \tag{3.3}$$

For low values of stress, $\alpha_{\mathrm{eff}} \approx \alpha$ and thus the fibre expands when the temperature increases. However, the magnitude of the Young's modulus for fused silica increases with temperature (figure 3.1) [130–133, 146] making β positive, and thus for high stress values the β term causes contraction of the fibre as the temperature increases.

By choosing a suitable static stress the effective thermal expansion coefficient can thus be nulled to eliminate the thermoelastic loss given by equation 2.34.

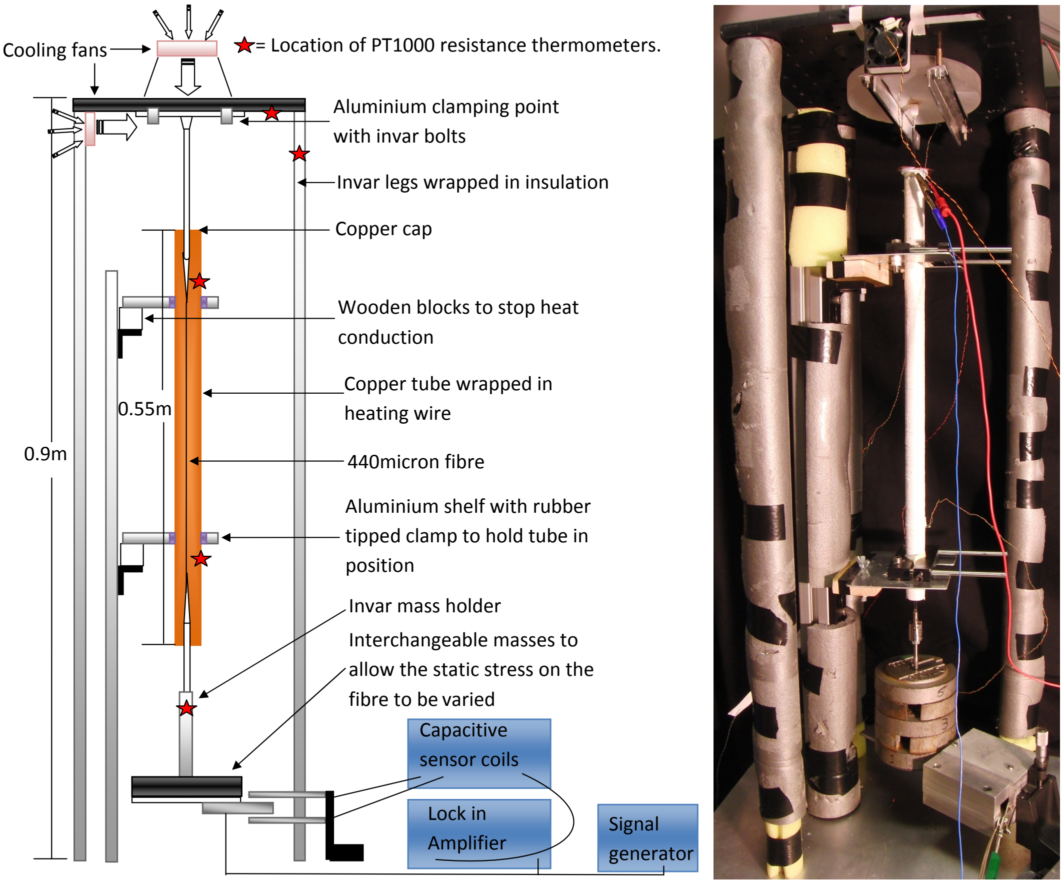

Figure 3.2: *Left: Schematic of the apparatus used to measure the thermal expansion coefficient. Right: Photograph of the experimental setup.*

3.2 Experimental Set-up and Procedure

Measurements of the thermal expansion coefficient of a loaded fibre were performed by placing a 440 µm diameter Suprasil 2A [135, 138] fused silica fibre, which was fabricated using a CO_2 laser based pulling machine [129], inside a copper tube wrapped in heating wire as shown in figure 3.2. A previous set-up used is shown in figure 3.3. This initial set-up is discussed only briefly in this chapter as there was found to be a very large error incorporated into the measurements, caused by the set-up having aluminium legs and an

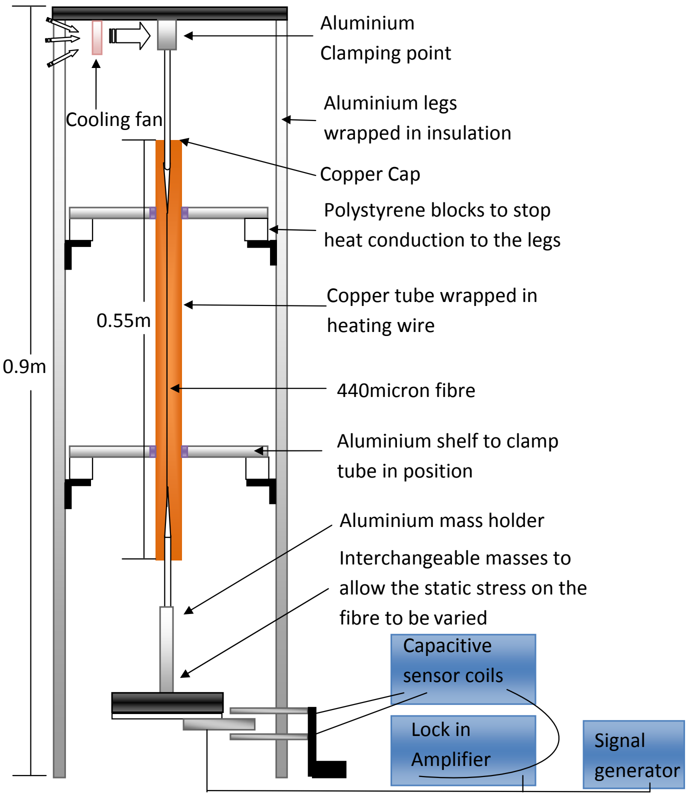

Figure 3.3: *Schematic of the initial apparatus used to measure the thermal expansion coefficient.*

aluminium clamping system which has a large thermal expansion coefficient $\sim 22 \times 10^{-6}\text{K}^{-1}$ [147, 148]. For this reason the updated invar legs (with a thermal expansion coefficient of $\sim 1.5 \times 10^{-6}\text{K}{-1}$ [149]) and silica/invar clamping system which is shown in figure 3.2 was used instead. The set-ups allowed the fibres to be heated and cooled repeatedly from around 290 K to 310 K. A capacitive sensor connected to a lock-in amplifier was used to monitor the fibre extension.

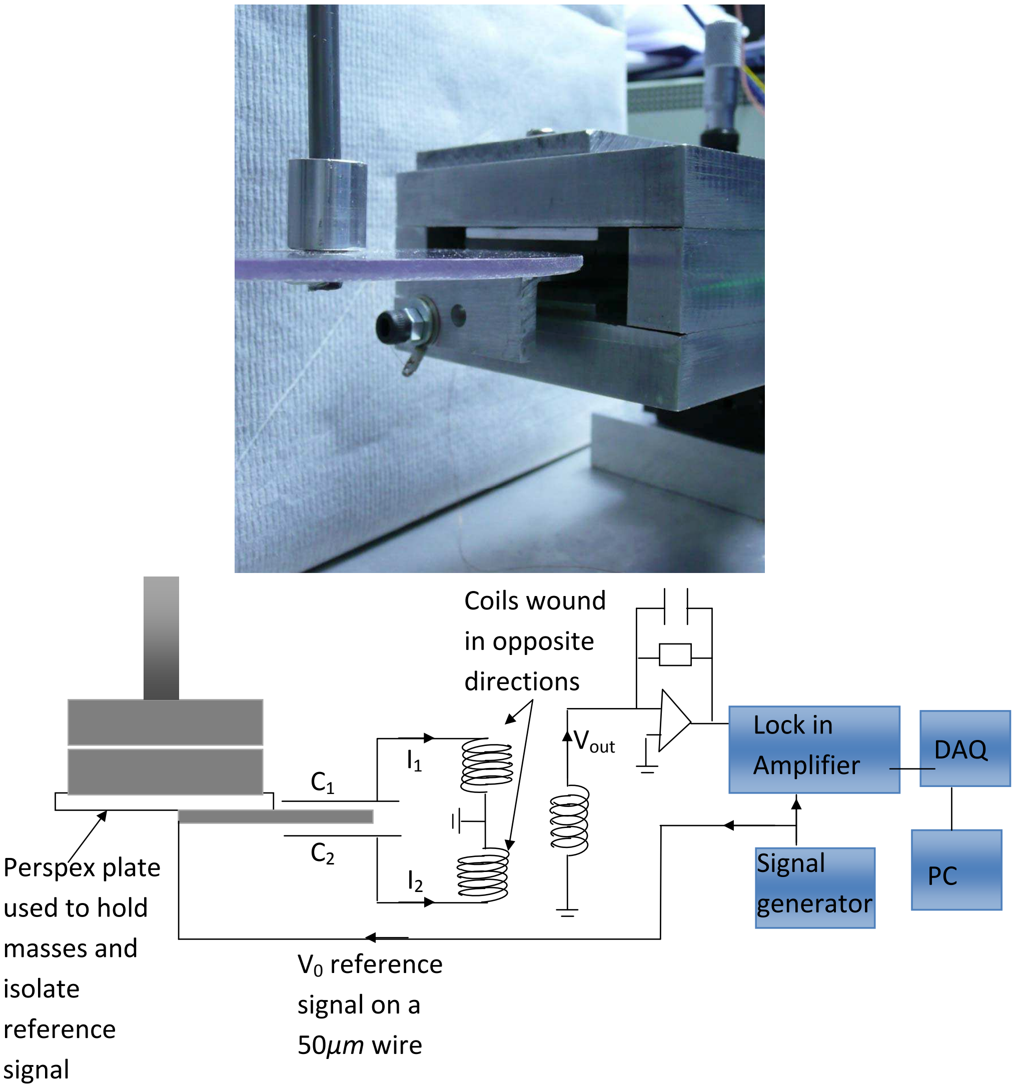

Figure 3.4: *A schematic of the circuit diagram for the capacitive sensor.*

3.2.1 Capacitive Sensor

The circuit diagram for the capacitive sensor is shown in figure 3.4. The lock-in amplifier applies a voltage of 5 Vrms onto the centre plate at 80 kHz. The net current flowing to the sensor plates (through capacitances C_1 and C_2) was compared by coupling through a counter-wound transformer with a common center ground. This was a convenient method to ensure the output voltage was zero when the currents I_1 described by equation 3.4 and I_2 described by equation 3.5 are identical.

$$I_1 = V\left(\frac{1}{C_1 j\omega}\right)^{-1} = VC_1 j\omega, \tag{3.4}$$

$$I_2 = V\left(\frac{1}{C_2 j\omega}\right)^{-1} = VC_2 j\omega, \tag{3.5}$$

where $V = V_o e^{i\omega t}$ describes the voltage on the center capacitive plate. V_0 is the reference signal voltage and ω is the frequency of the reference signal used. C_1 and C_2 is the capacitance between the plate which has the reference signal on it and the sensor plates. The output voltage (V_{out}) can be calculated as

$$V_{\text{out}} = M\frac{dI}{dt} = Mj\omega\left(C_1 j\omega V_0 - C_2 j\omega V_0\right) = -M\omega^2 V_0\left(C_1 - C_2\right), \tag{3.6}$$

where M is the mutual inductance between the coils connected to the sensing plates (primary coils) and the coils at the input to the amplifier (secondary coil), and I is the sum of current flowing into the primary coils. As the fibre expands/contracts vertically the value of C_2 increases/decreases while C_1 decreases/increases, respectively. This in turn changes the value of V_{out}. The output voltage was amplified and demodulated with the lock-in amplifier. A time constant of 10 seconds was selected on the lock-in amplifier to remove torsional motion as well as the pendulum/tilt motion of the fibre. The sensor was designed such that the plate carrying the 5 Vrms reference signal had a large overlap compared to the sensing plates. The large overlap was shown to reduce the voltage fluctuations caused by translation and/or torsional motion of the mass holder, as well as from the roof tilt effects, as both of these coupled to horizontal motion of the center plate during the heating/cooling cycles. The resulting DC voltage, which was proportional to the fibre extension, was then read into a PC through a Labjack U12 Data Acquisition card. The capacitive sensor was calibrated before each data taking run. This was done by mounting the capacitive sensor onto a translation stage with vertical adjustment. The sensor was then moved by an increment of 0.05 mm and once the signal had

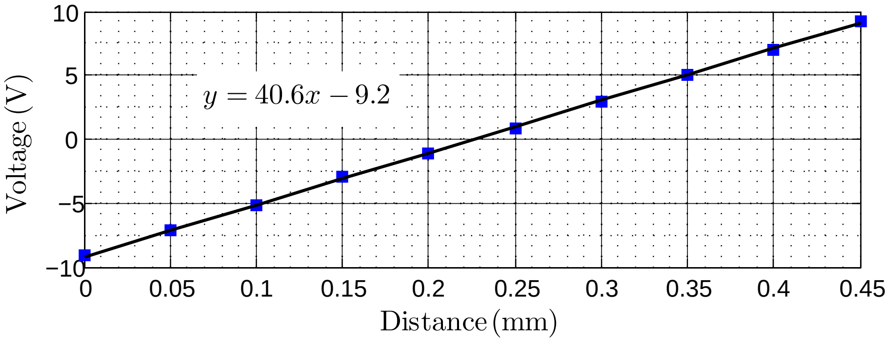

Figure 3.5: *A calibration plot showing the linear output of the capacitive sensor with a sensitivity of 40.6 V/mm.*

reached a fixed value (roughly after 20 seconds) the sensor was then moved another 0.05 mm. The voltage changes from the sensor were monitored for a series of calibration steps and a straight line fit through the data gave a sensitivity of 40.6 V/mm as shown in figure 3.5. The noise from the output of the capacitive sensor when it is connected to the lock-in amplifier is also shown in figure 3.6. In the mid-frequency regime ($10^{-2} - 10^{-3}$ Hz) the capacitive sensor has a sensitivity of $\sim 3 \times 10^{-8}\,\mathrm{m}/\sqrt{\mathrm{Hz}}$. At the signal frequency and lower ($< 10^{-4}$ Hz) the noise of the detector is seen to increase. This is most likely due to the long term drifts of the experimental set-up and local environment, which are removed with a polynomial data fit as described in section 3.2.2.

3.2.2 Thermal Effects

The temperature was measured at various locations in the experiment; at the top/bottom of copper tube on the legs and on the roof as detailed in figure 3.2. PT1000 resistance thermometers attached to a Keithley Instruments 2000 multimeter and integrated scan card were used. The following precautions were taken to minimise systematic heating effects:

- The top stock of the silica fibres were made longer to ensure the roof clamp was sufficiently far away from the heating tube.

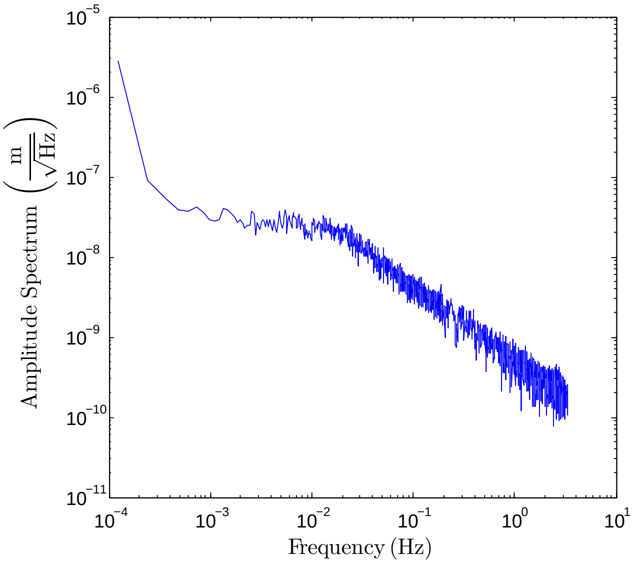

Figure 3.6: *A noise plot from the capacitive sensor output signal.*

- A copper cap was placed on top of the heating tube to reduce the convection current out of the pipe and make the temperature inside the pipe more uniform.

- Two cooling fans were positioned to keep the temperature of the roof at room temperature.

- The silica fibres were welded to a silica mass (shown in figure 3.7) to reduce expansion which would occur if a metal clamping mechanism had been used to grip the fibres.

- The legs and heating tube were decoupled by holding the heating tube on an independent stand.

- The legs and lower mass holder were made from invar and the legs were wrapped in insulation to minimise expansions due to heating.

3.2.2.1 Temperature Monitoring of the Experimental Apparatus

To remove the thermal influence due to the legs and roof, the fibre was removed from the heating tube and clamped to the roof. A series of heating and cooling

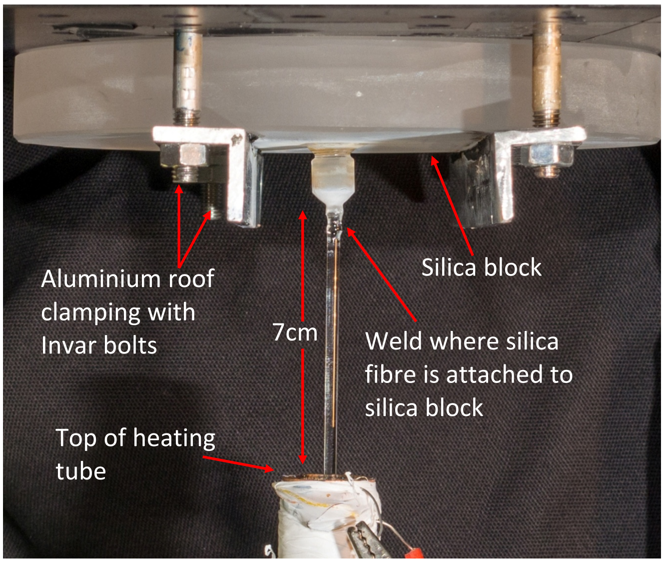

Figure 3.7: *The silica block held in place using two aluminium brackets and held to the roof with invar bolts to which the silica fibres are welded.*

cycles were initiated while the fibre motion was monitored using the capacitive sensor, the temperatures of the roof and legs were monitored using PT1000 thermometers. This arrangement is shown in figure 3.8. During this test no correlation was found between the motion of the fibres and the leg temperature, suggesting that the legs were not expanding or contracting to produce a false fibre expansion or contraction measurement. It is interesting to note that when the legs were made of aluminium the legs expanded and contracted by as much as 1.5×10^{-5}m/°C (shown in figure 3.9). The lower clamp mass holder was also not expanding or contracting enough with temperature to be of concern.

The fibres were then returned to being inside the heating tube. The roof was heated using a heat gun while the temperature of the roof and length change of the system were monitored. This data as shown in figure 3.10 found that the fibre position changed by 1.3×10^{-7}m/°C and allows for a correlation coefficient to be measured (R_{Roof}). The measurement of R_{Roof} allows us to remove the signal changes due to the roof deformations as described in section 3.2.3 which otherwise would wrongly be interpreted as fibre expansions. This again is a

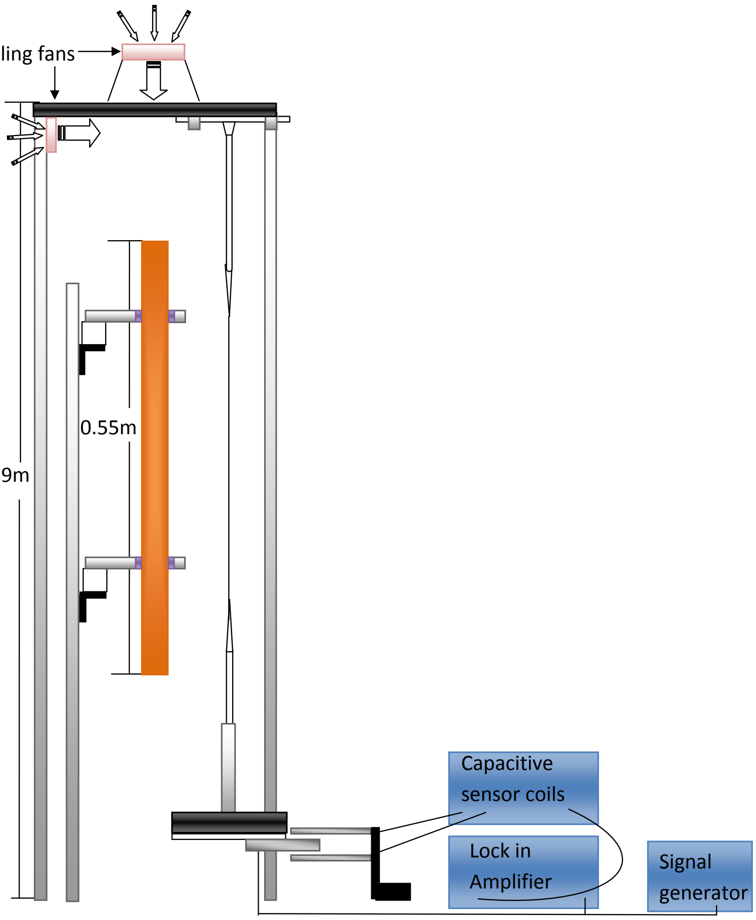

Figure 3.8: *The arrangement of the calibration set-up used to determine that changes of the leg temperature had little effect on the measured result and that roof temperature played a more substantial role.*

vast improvements from the aluminium roof clamping set-up which was used for a previous measurement where the fibre position was found to change by 1×10^{-6}m/°C as a function of roof temperature [147].

3.2.2.2 Poisson Ratio Variations

The Poisson effect is another mechanism which could affect the stress on the fibre and thus the measurement of the effective thermal expansion coefficient. The Poisson effect is used to describe how a material responds to strain. As fused silica is stretched in one direction it will compress in the two orthogonal

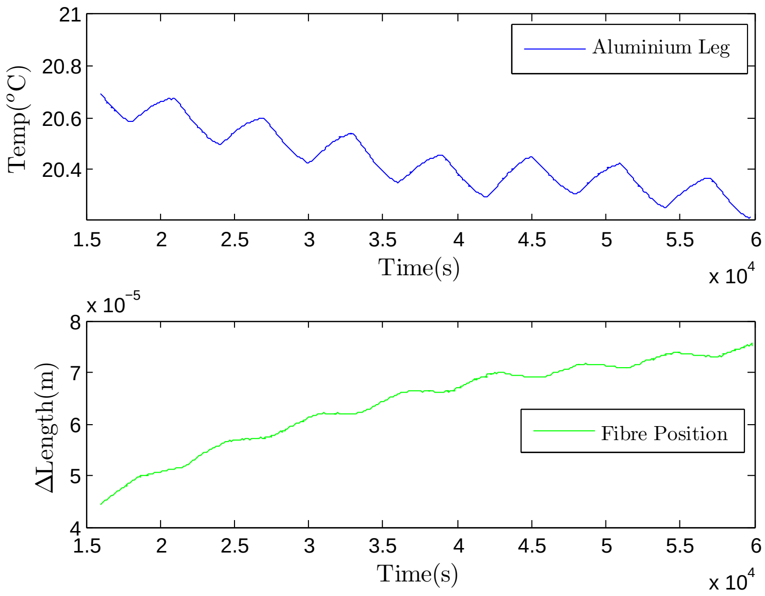

Figure 3.9: *Plot showing how the changing temperature of the aluminium leg set-up varies the apparent change in length of the silica fibre. This correlation did not appear with the upgraded invar leg set-up*

directions. The Poisson ratio, ν, is a measure of this effect and is defined as the fraction of compression divided by the fraction of expansion. Similarly if the material is compressed rather than stretched it will expand in both the perpendicular directions. As the length of the fibre L is extended under stress, the radius of the fibre r will decrease by Δr such that

$$\frac{\Delta r}{r} = -\nu \frac{\Delta L}{L} \tag{3.7}$$

where ΔL is the extension of the silica fibre when it is stressed. This will make the stress on the fibre larger than initially predicted if the initial fibre radius r is used to calculate the stress on the fibre. Two factors were considered; the static change in the stress and the effect of the Poisson ratio varying with temperature. For the static effect, the Poisson ratio for fused silica is 0.17 at 20°C [150]. A Poisson ratio of 0.17 only changes the stress in the fibre by ∼0.04% for a fibre with a radius of 220 µm suspending 1 kg. For the temperature dependent effect, the Poisson ratio has been shown to increase with

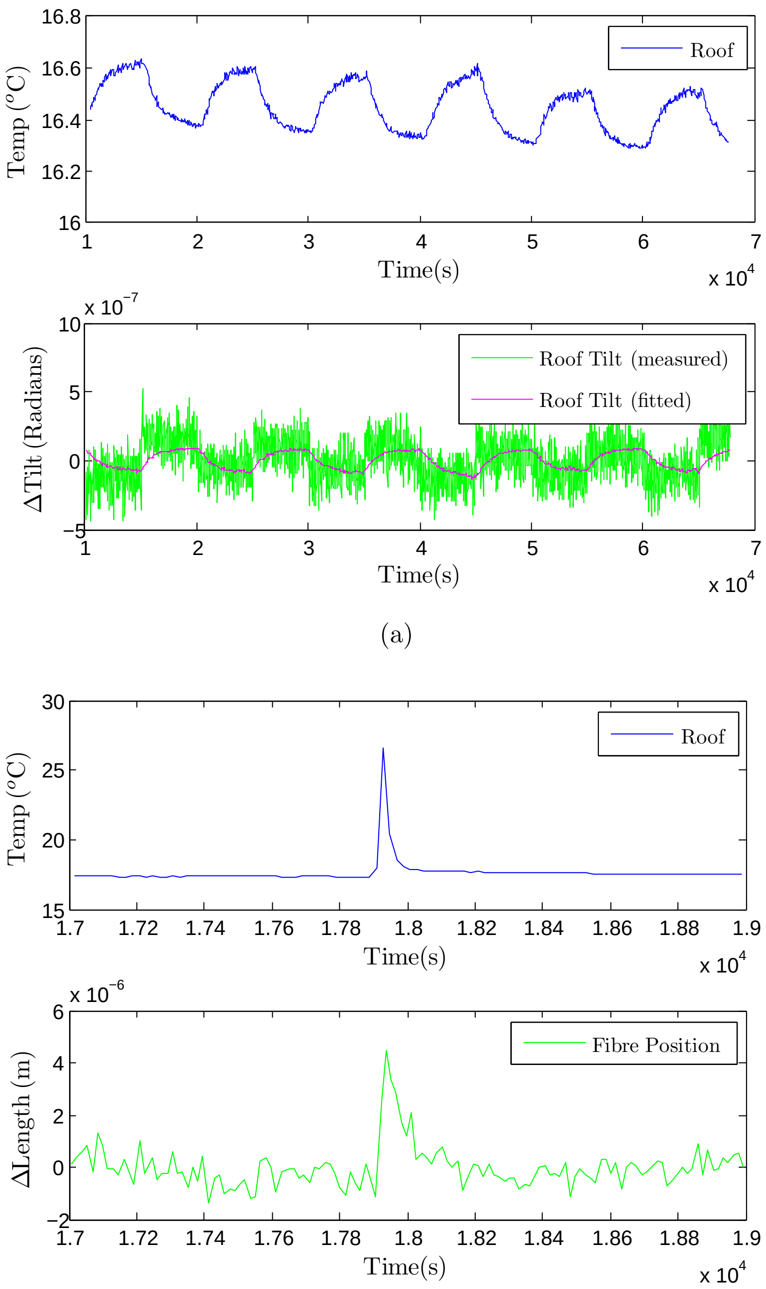

(a)

(b)

Figure 3.10: *Plots showing how the roof temperature was correlated with the fibre movements using a simple correlation model* $\Delta L = R_{Roof}\Delta T_{Roof}$*, as described in section 3.2.2.1. Plot (a) shows how the changing roof temperature varies the roof tilt and (b) shows how the changing roof temperature varies with the apparent change in length of the silica fibre.*

temperature [150] and at 40°C the value is $\sim$0.172 [150] (i.e. 1×10^{-4}/°C). This in turn will increase the stress on the fibre by another 0.005%. To check this was a safe assumption a static analysis was carried out in ANSYS using a 440μm radius fibre which was 0.5m long (created with 1000 elements and 2001 nodes) and suspending 7 kg of mass. By comparing the nodal displacements of a fibre with a low temperature Poisson ratio (0.17) and comparing it to the displacements that would be seen from a high temperature value Poisson ratio (0.172). Figure 3.11 shows that systematic effects due to the Poisson ratio and its change with temperature are insignificant compared with the long term erroneous temperature variations.

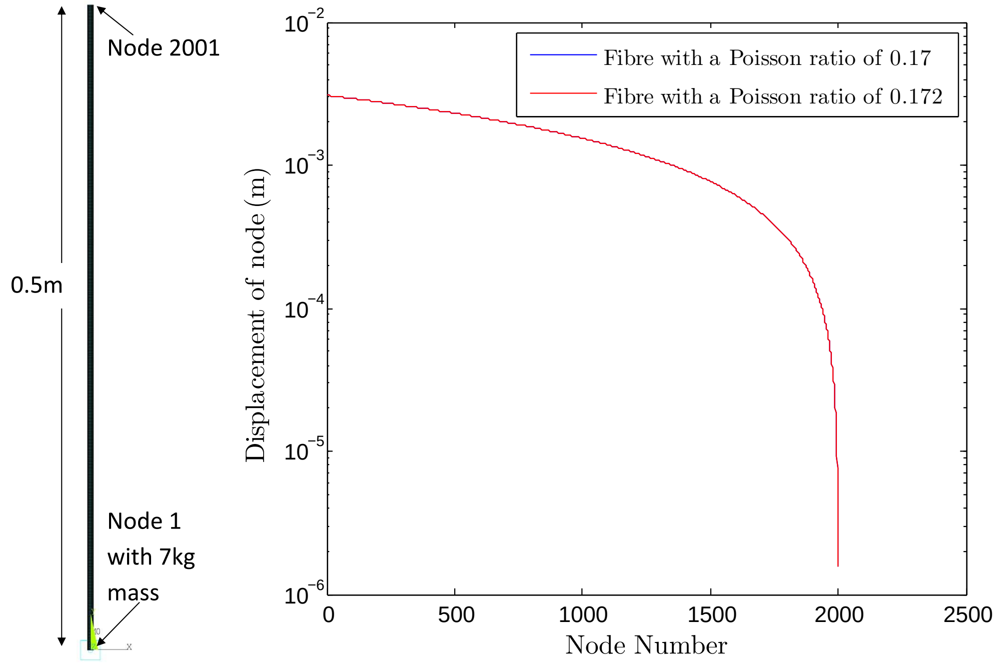

Figure 3.11: *Right: ANSYS model used to determine effects of Poisson ratio the model fibre is 0.5 m long and has a radius of 220 μm supporting a 1 kg mass. Left: Plot showing that the fibres extension has not been affected by the changing Poisson ratio with temperature. The blue line shows the extension of the fibre for a low temperature Poisson ratio of 0.17 and the red line shows the extension for a high temperature Poisson ratio of 0.172.*

3.2.2.3 Long Term Drifts

The full data set for this experiment consists of 5-7 individual measurements of fibre extension as a function of the suspended load. This is combined with systematic tests of the heating tube and fibre temperature profile and results in a measurement campaign of $\simeq$ 4 weeks. It is therefore clear that systematic temperature effects due to environmental factors can be significant. Drifts over the course of a day, or an individual measurement at a given load, in both the temperature and fibre extension data are removed by subtracting a second order polynomial fit so all the data was centered around zero. These drifts are likely due to the tilt of the table on which the apparatus was sitting as the room temperature varies throughout the course of the day.

Longer term variations, due for example to changes in the ambient temperature of the lab over several weeks, are removed by calibrating the capacitive sensor at the start and end of each measurement. However, it is further possible that such temperature variations can affect the measured temperature change profile along the fibre. As this profile can only be measured once, due to the fact that the temperature sensors are glued onto the fibre, it is believed that these are the main sources of error in the experiment at a level of roughly $\pm 0.7°$C.

3.2.3 Measurements

For each individual data point the fibre was heated and cooled consecutively 12 times with a heating and cooling cycle time of 10,000 seconds. The displacement of the fibre was measured with the capacitive sensor every 2 seconds along with the temperature of the roof and legs as shown in figure 3.12a. To calculate the effective thermal expansion coefficient of the fibres a regression fit for equation 3.8, below, was used

$$\Delta L - R_{\mathrm{Roof}} \Delta T_{\mathrm{Roof}} = \alpha_{\mathrm{eff}} L \Delta T_{\mathrm{Top\ Tube}}. \qquad (3.8)$$

where ΔL was the output of the capacitive sensor, $R_{\mathrm{Roof}}\Delta T_{\mathrm{Roof}}$ was the length change due to any roof tilt and $\alpha_{\mathrm{eff}}L\Delta T_{\mathrm{Top\ Tube}}$ was the corrected value.

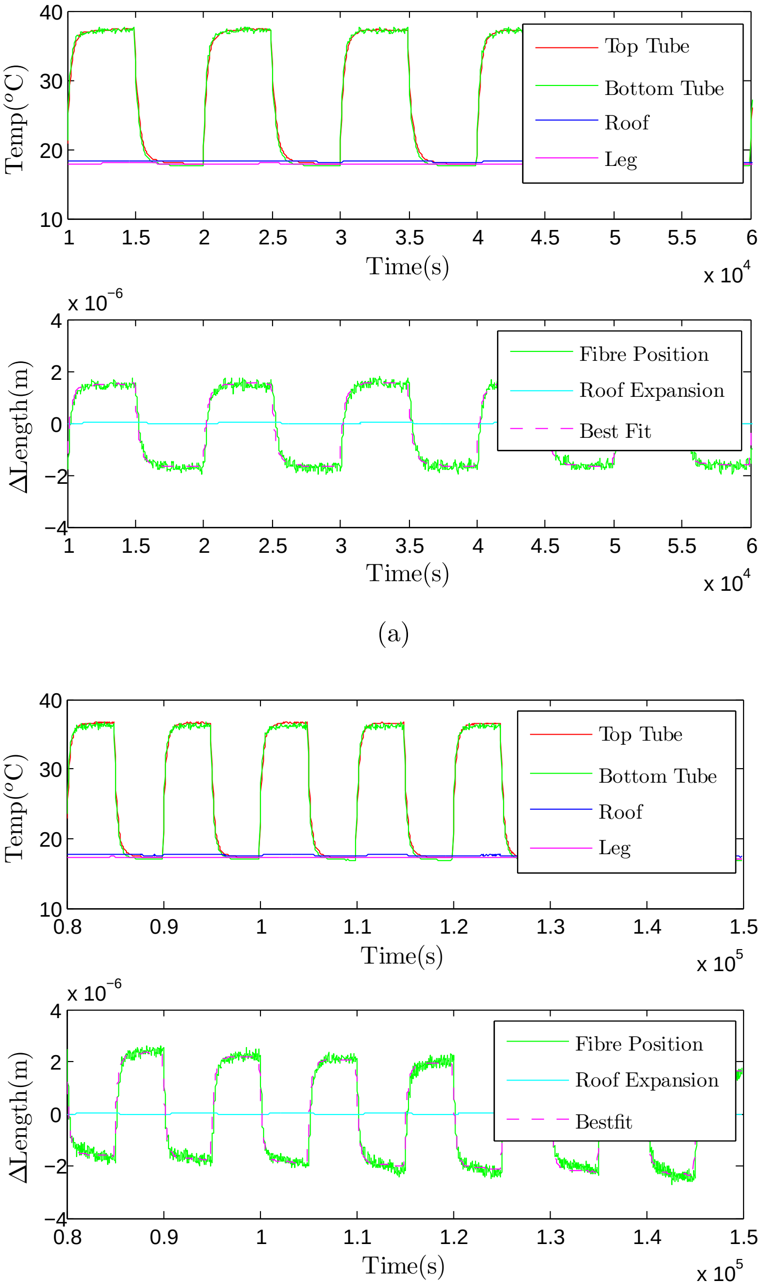

(a)

(b)

Figure 3.12: *Plots showing the comparison of expansions when heating the fused silica fibre under low and high stress values. (a) Data taken when a mass of 0.2 kg was hanging from the fibre. Top Plot (a): The heating tube temperature, roof temperature and the temperature of the support structure legs. Bottom Plot (a): A plot of the fibre position after the long term drifts and calibrated expansions for the roof have been removed. The best fit line shows the fit for the calculated effective thermal expansion coefficient assuming the top tube temperature was the temperature of the fibre. (b) Data taken when a mass of 7.1 kg was hanging from the fibre showing that the fibre reduces in length as it is heated. This gives a negative effective thermal expansion coefficient.*

The mass supported by the fibre was increased up to a maximum of 7.1 kg by adding masses onto the lower clamp. Figures 3.12a and 3.12b shows the data gathered when the experiment was run with masses of 0.2 kg and 7.1 kg respectively. In comparing top and bottom graphs on these figures it is clear that there was a phase change between the heating and extension of the fibre, signifying that the fibre extends for the low mass case and contracts for the high mass case. Figure 3.13 shows the length change observed for all mass cases of Fibre 1. For Fibres 2, 3 and 4 the mass was only increased up to 5.2 kg as this reduced the chance of the fibre breaking under high stress.

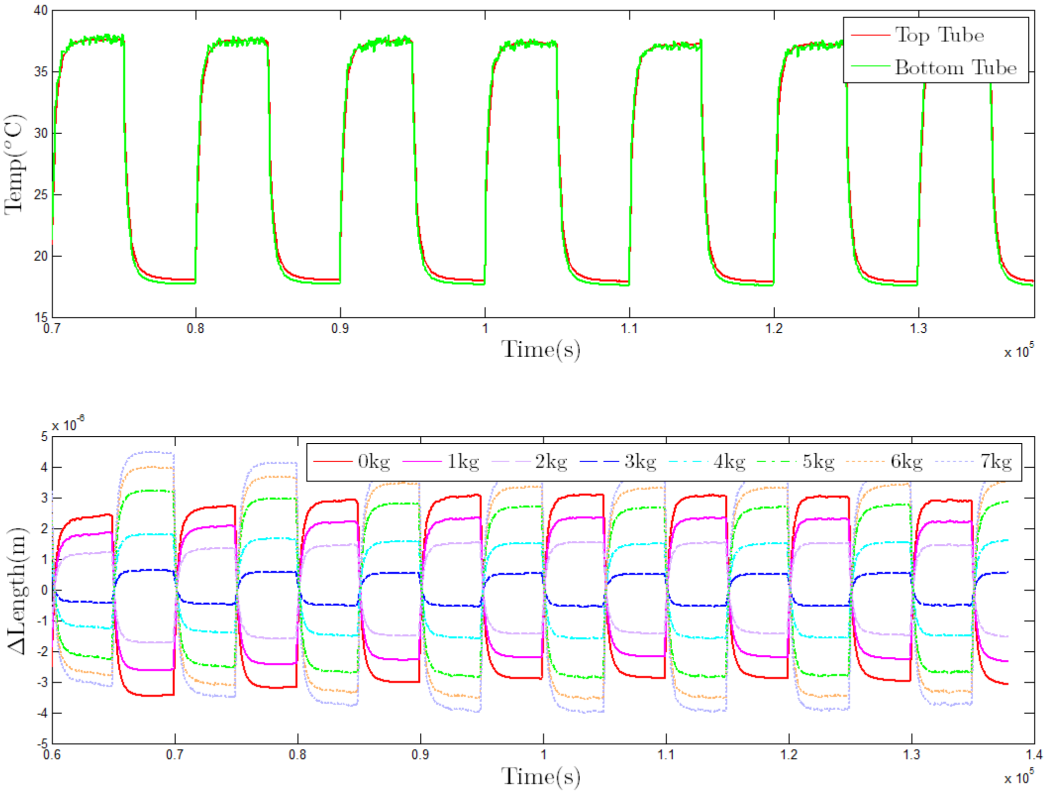

Figure 3.13: *Plot showing the length change of fibre 1 that is observed as the temperature of the fibre is heated and cooled and the stress on the fibre is varied. The expected zero expansion point on this graph is expected to occur at ∼3.5 kg.*

It was not sufficient to assume that the temperature change experienced by the fibres was uniform along their length and that they experienced the same temperature change as the copper tube. After the measurements had been taken, PT1000 resistance thermometers were glued onto the fibres every 2-3 cm to monitor the change in temperature along the fibres. Originally for the aluminium set-up the thermometers were glued on with larger spacing intervals (shown by figure 3.14). This led to an inconclusive result and so these measurements are shown but not discussed in detail. The temperature change profiles for the invar set-up fibres are shown in figure 3.15. The fibre radii was measured using the apparatus described by Cumming et al [151]. The values obtained from these measurements for Fibres 1, 2, 3 and 4 are shown in figure 3.15. There was an error of $\pm 2 \times 10^{-6}$m on the measurement of the fibre radius while the temperature changes plotted have an error of ±0.7°C in the thin section of the fibre L_o shown by figure 3.15 and this is the dominant error when taking measurements. These temperature change profiles were then

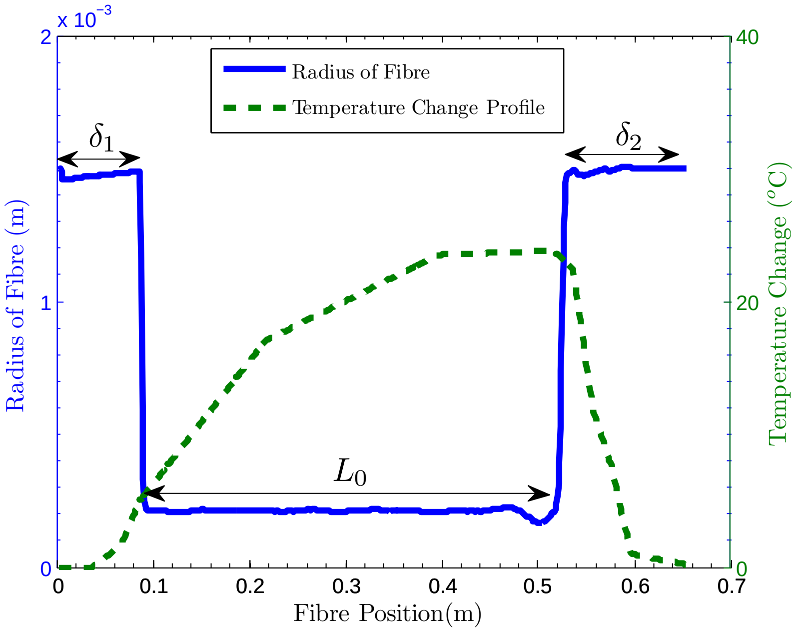

Figure 3.14: *Temperature change profiles plotted on-top of the fibre dimension profiles for the fibre studied using the aluminium set-up, showing that the temperature profile was not uniform along the fibre. It also shows that the profile is not defined well enough, due to the large spacing between consecutive temperature measurements along the fibre. This made the calculation of* α_{eff} *unreliable.*

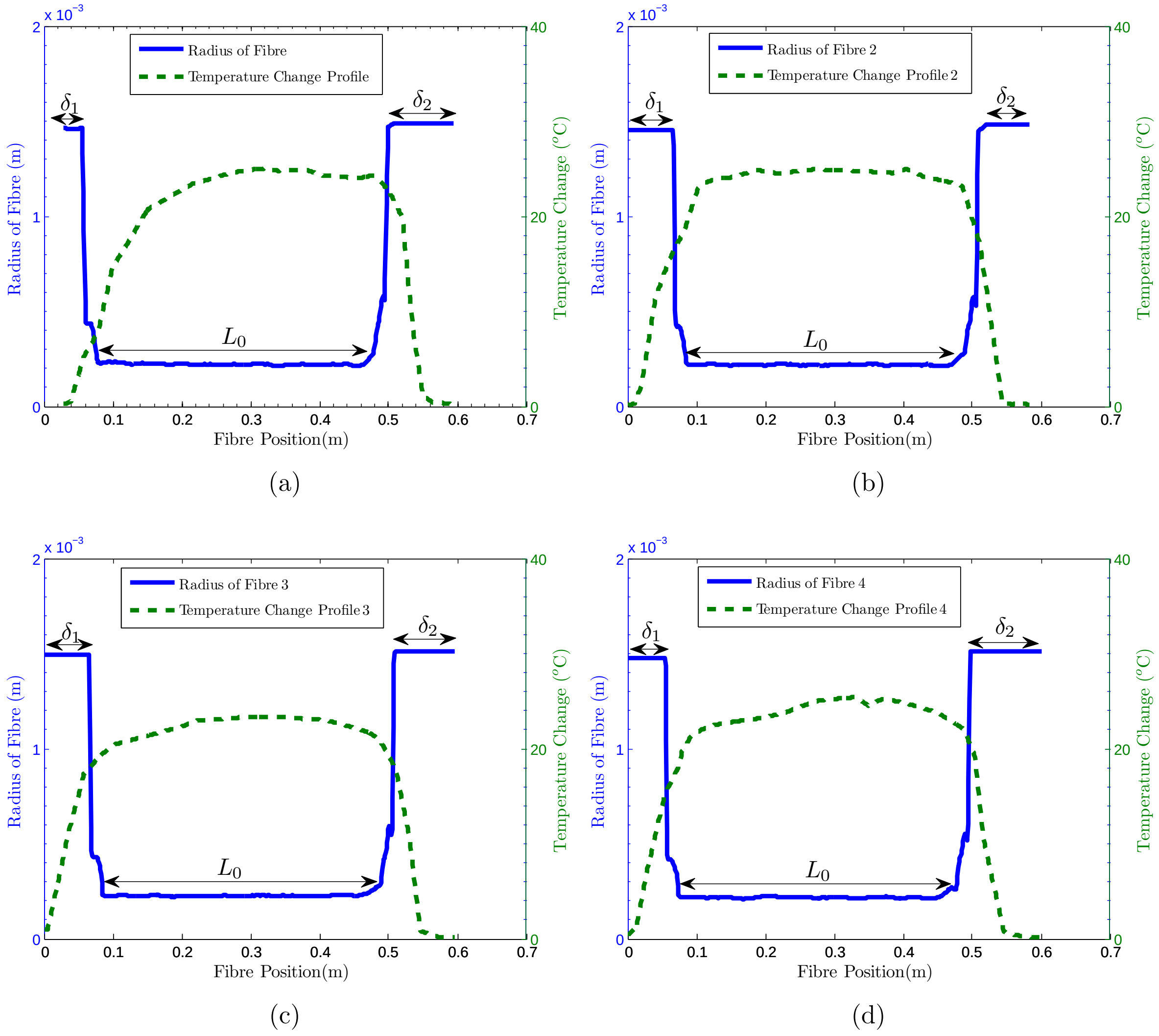

(a)

(b)

(c)

(d)

Figure 3.15: *Temperature change profiles plotted on-top of the fibre dimension profiles for the four fibres studied using the invar set-up, showing that the temperature profiles were not uniform along the fibre. The plots show the temperature change profile for Fibre 1 (a), Fibre 2 (b), Fibre 3 (c) and Fibre 4 (d).*

used to recalculate the effective thermal expansion coefficients as discussed in the following section.

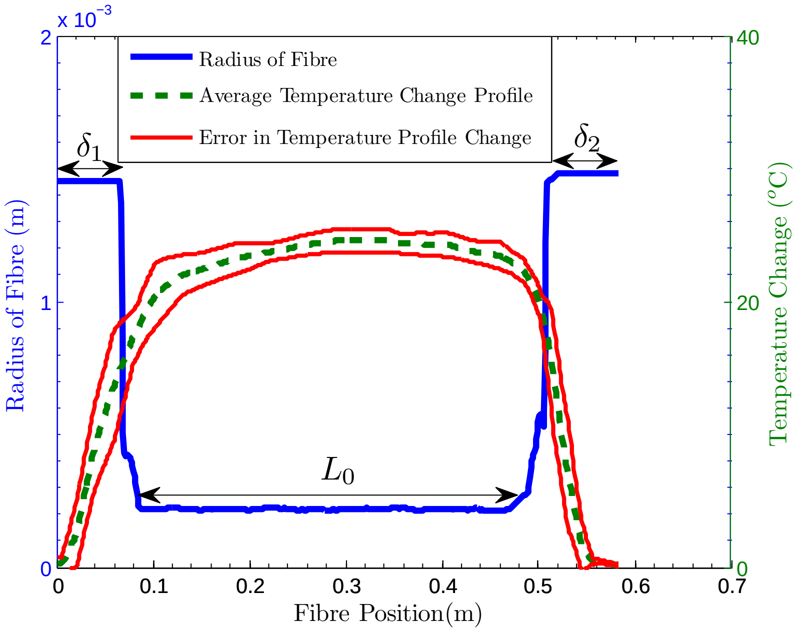

Figure 3.16: *Plot showing the temperature change profile averaged over all four fibres and the error in this averaged value.*

3.3 Results

Figures 3.14 and 3.15 show clearly that the temperature changes experienced by each of the fibres varies along the length of the fibre. An effective expansion coefficient α_{eff} was calculated using this temperature change profile rather than assuming the entire length of the fibre experienced the same magnitude of temperature change. To do this the fibres temperature change profile was interpolated and divided into 1 mm sections.

It is further important to note that to accurately analyse the fibre the effective expansion coefficient also depends on the geometry of the fibre. As there is a low value of stress in the 1.5 mm radius regions, δ_1 and δ_2 (see figure 3.15, in this figure δ_1 is the bottom section of the fibre attached to the sensing plate and δ_2 is at the top of the fibre closest to the roof), the expansion from the β term in these parts of the fibre was negligible. Therefore the expansion of all the 1 mm long sections in these regions of the fibre can be attributed to be purely from the α coefficient. In the thin 400 µm section L_o, the stress σ_o on the silica plays a more dominant role and so the expansion coefficient of all the 1 mm sections in this part can be attributed to $\alpha - \frac{\sigma_\mathrm{o}\beta}{\mathrm{Y_o}}$. This can be described by equation 3.9 where n refers to the position of the element being studied on the fibre, L_n is the length of the element being studied in this case 1 mm, σ_n is the stress in each element and ΔT_n is the temperature change experienced by each element,

$$\alpha_\mathrm{eff} L \Delta T_\mathrm{Top\ Tube} = \alpha \sum_{\mathrm{n}=1}^{\delta_1+L_o+\delta_2} L_\mathrm{n} \Delta T_\mathrm{n} - \frac{\beta}{Y_\mathrm{o}} \sum_{\mathrm{n}=\delta_1}^{\delta_1+L_o} \sigma_\mathrm{n} L_\mathrm{n} \Delta T_\mathrm{n}. \tag{3.9}$$

During this analysis the assumption was made that the value of α was constant with temperature and uniform across the entire fibre despite the different 1 mm sections experiencing different magnitudes of temperature changes. This assumption will not effect the integrity of the results calculated in this chapter as previous results show [137, 152] that when the thermal expansion coefficient of fused silica was measured over a temperature range of 0°C to 40°C. The largest variation in α that was determined is $\sim 0.1 \times 10^{-7}\,\mathrm{K}^{-1}$ and so will contribute to an error of <3% to the value of α calculated in this chapter.

3.3.1 Aluminium Set-up

A plot of the effective thermal expansion coefficient against the average static stress in the 440 µm diameter section of the fibre studied using the aluminium set-up is shown in figure 3.17. The linear best fit line to this data is shown by the blue line. The gradient of this fit was used to calculate a β value of $(1.3 \pm 0.2) \times 10^{-4}$. The y intercept of the graph also determines the values of α to be $(4.5 \pm 0.4) \times 10^{-7}\mathrm{K}^{-1}$, where the error for these fitted values is shown by the red lines. The black line indicates the stress at which α_{eff} becomes zero, the error on this value is shown by the dashed black lines. In this case the effective thermal expansion coefficient is predicted to be nulled at 255±58MPa. The data shown in figure 3.17 does show some scatter about the linear trend. We performed a P-value statistical test to validate the hypothesis that the data

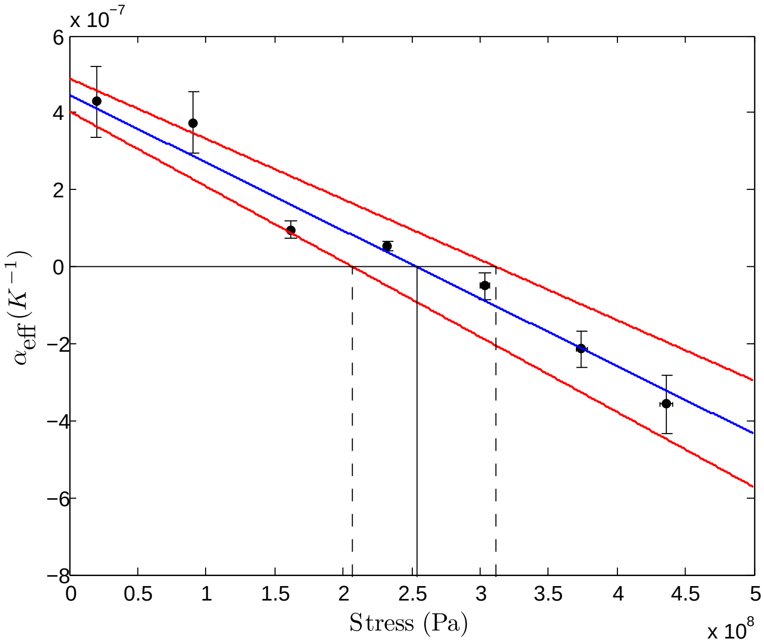

Figure 3.17: *Plot showing the data gathered from the aluminium set-up used.*

does indeed follow a straight line fit. The P-value statistic from the measured data and the theoretical straight line fit is calculated as 0.03. The P-value is useful here as it provides a way to test that the model being fitted to the data does indeed coincide with what was measured. The P-value is given by [153, 154],

$$\text{P-value} = 1 - F(\chi^2|\nu) = 1 - \int_0^{\chi^2} \frac{t^{(\nu-2)/2}e^{-t/2}}{2^{\nu/2}\Gamma(\nu/2)}dt, \tag{3.10}$$

where χ^2 is the chi-squared value of the distribution from the hypothesis, $\Gamma(..)$ is the Gamma function, and ν is the degrees of freedom in each of the plots. This is calculated directly in Matlab using the chi2cdf function such that

$$\text{P-value} = 1 - \text{chi2cdf}(\chi^2, \nu). \tag{3.11}$$

By setting up a significance level of $\leq$0.05 it allows us to compare the straight line fit "the null hypothesis" to our data and examine if the data we measured is significantly different from this trend. For this test, a P-value below 0.05 (95% confidence value) is used to reject the null hypothesis and so we cannot be confident from this result that this data is consistent with a linear trend. The reasons for this are clear, firstly there is too much noise imparted on to our data from the aluminium arrangement used and it is very susceptible to environmental temperature fluctuations that will affect the ability to fit the data accurately as discussed in section 3.2.3. There was also the problem that the temperature change profile from figure 3.14 is not detailed enough to allow the effective thermal expansion coefficient to be calculated accurately, although this effect is not likely to affect the linearity of the fit. In order to make a more accurate measurement of the effective thermal expansion coefficient we must use a system which is not as susceptible to environmental changes in temperature, hence why the invar arrangement shown in figure 3.2 was chosen. These results are discussed next.

3.3.2 Invar Set-up

Plots of the effective thermal expansion coefficient against the average static stress in the 440 μm diameter section of the four fibres are shown in figure 3.18. The linear best fit lines to this data are shown by the blue lines. The gradients of these fits were used to calculate the values of β. The y intercept of the graphs also determines the values of α. The error for these fitted values is shown by the red lines. The black lines indicate the stress at which α_{eff} becomes zero, and the error on this value is shown by the dashed black lines. Results for the four identical fibres studied are shown in table 3.1. The data shown in figure 3.18 does show some scatter about the linear trend, and so the P-value statistic from the measured data and the theoretical straight line fit is also listed in table 3.1. Thus from the P-values listed in table 3.1 we are confident that the scatter in all the data sets is consistent with a linear trend as the P-values are all greater than 0.05.

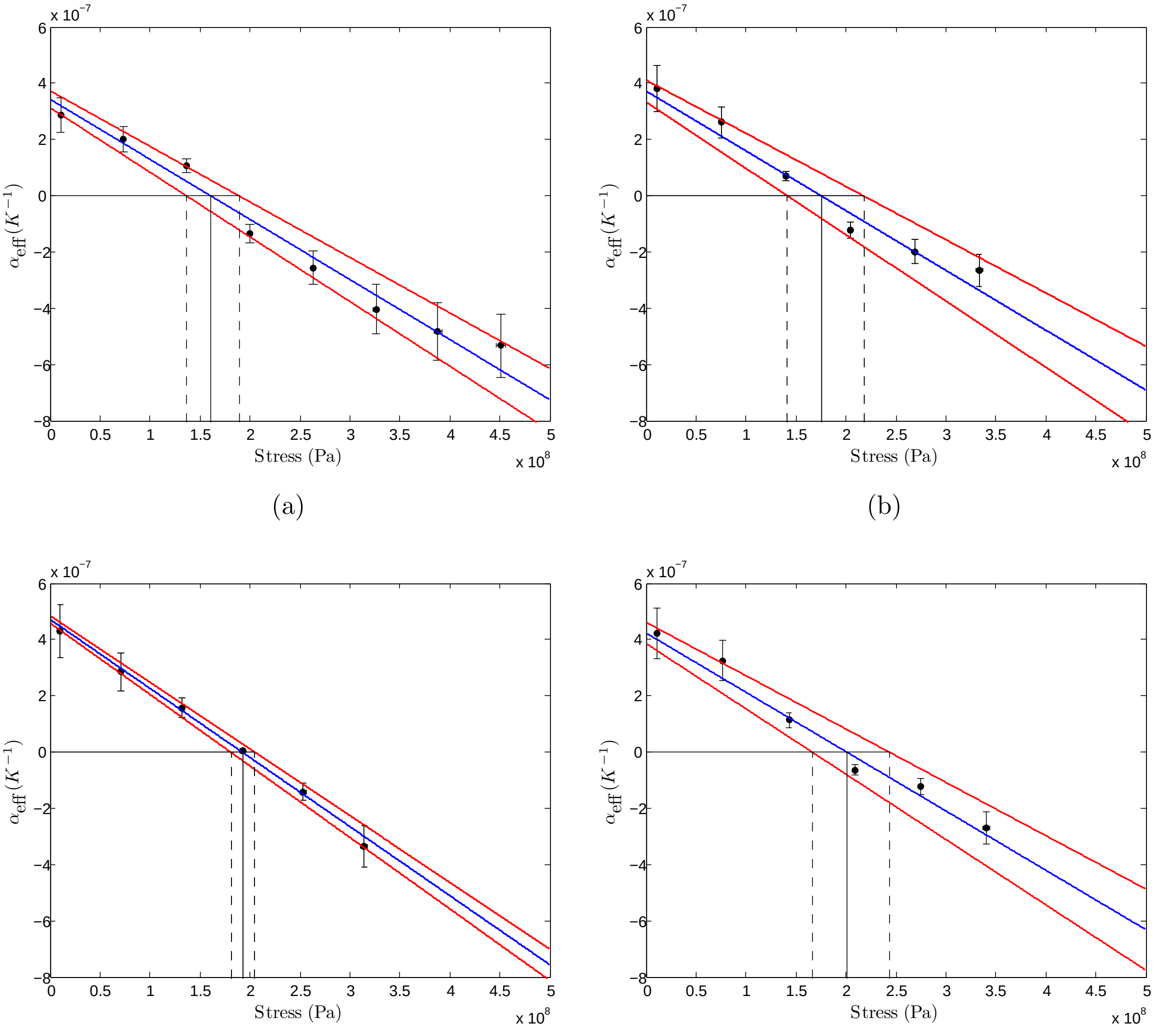

(a) (b) (c) (d)

Figure 3.18: *Plots showing how the effective thermal expansion coefficient varies with the static stress on four identical fibres. The plots show how the effective thermal expansion coefficient varies with the static stress for Fibre 1 (a), Fibre 2 (b), Fibre 3 (c) and Fibre 4 (d).*

Fibre	Fibre 1	Fibre 2	Fibre 3	Fibre 4
Value of α ($\times10^{-7}\mathrm{K}^{-1}$)	3.5 ± 0.3	3.7 ± 0.4	4.7 ± 0.1	4.3 ± 0.4
Value of β ($\times10^{-4}\mathrm{K}^{-1}$)	1.5 ± 0.1	1.5 ± 0.2	1.77 ± 0.06	1.5 ± 0.2
Nulling Stress (MPa)	163 ± 28	176 ± 43	192 ± 12	201 ± 41
Av. Room Temp (°C)	16.8 ± 0.5	21.6 ± 0.6	25.2 ± 0.8	18.6 ± 1.1
P-value to fit	0.20	0.22	0.99	0.13

Table 3.1: *Values determined for α, β, the stress at which thermoelastic loss will be nulled, the average room temperature which was recorded and the P-value of each line fit to the data from each of the fibres.*

From figure 3.18 and table 3.1 it is clear that there is a large amount of scatter in the data which was recorded this is shown more clearly in figure 3.19. The results were looked at to examine weather or not the scatter shown in figure 3.18 was correlated with room temperature. It was believed that if the room temperature fluctuated then this may affect the convection currents in the heating tube and hence the temperature change profile of the fibre between each successive run, but no correlation was found. This data is shown in figure 3.20.

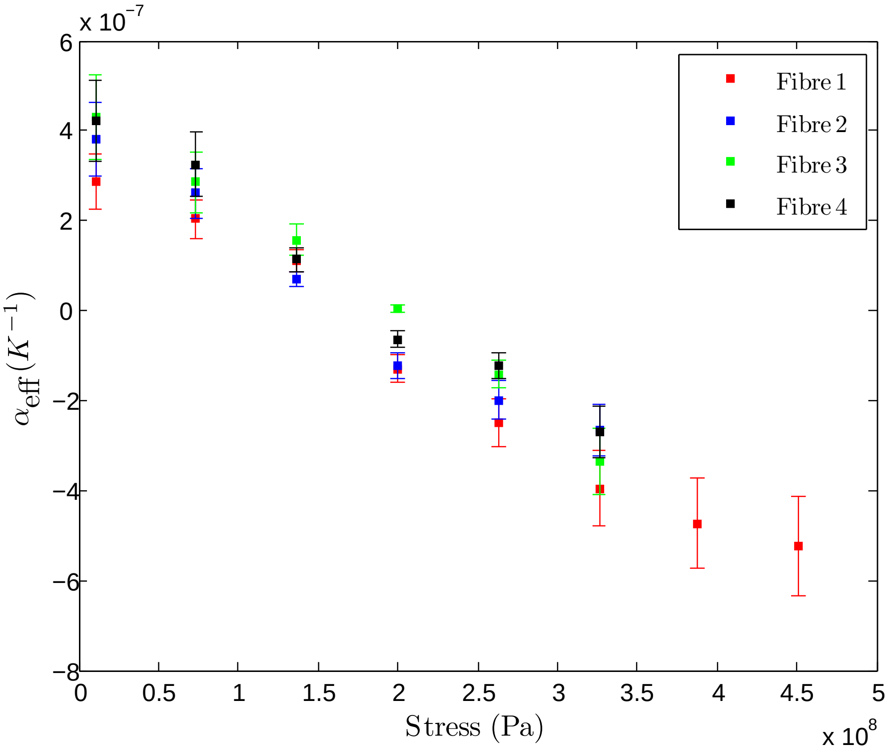

Figure 3.19: *Plot showing the data from all four fibre measurements in one plot.*

A plot of the average effective expansion coefficient from the experiment repeated four times (using identical fibres) against the average static stress in the 440 µm diameter section is shown in figure 3.21. Fibre 1 included data up to a maximum hung mass of 7.1 kg (450 MPa) while for Fibres 2, 3 and 4, the maximum mass on the fibre was only increased up to 5.2 kg (327 MPa). Thus the two data points shown by the triangle markers with the highest stress only

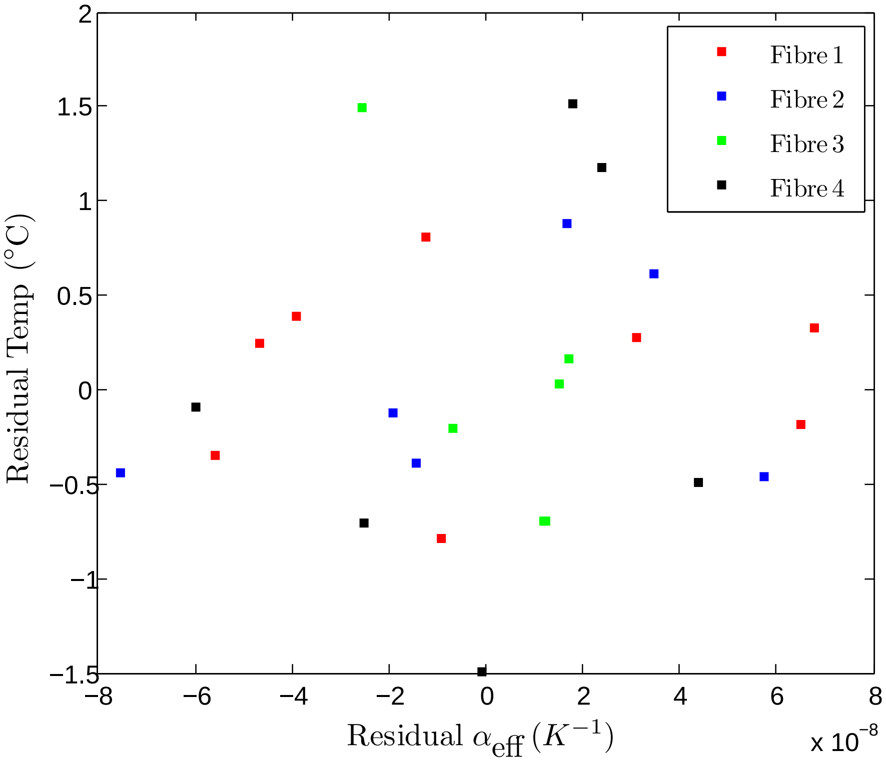

Figure 3.20: *Plot used to find correlations between the room temperature fluctuations from the average room temperature and the fluctuations in* α_{eff} *from the best line fits. No correlation could be determined.*

include measurements made on Fibre 1.

A linear best fit line to this data is shown by the blue line. This fit does not take into account the two highest stress values which were taken from Fibre 1 only, reflecting the same fitting process as used by Bell et al [145]. The gradient of this fit was used to calculate a value of β to be $(1.64\pm0.06)\times10^{-4}\,\mathrm{K}^{-1}$ which is higher than previous measured "bulk" and fibre values of silica [130–133, 146] where the elastic thermal coefficient was found to be $\sim 1.52\times10^{-4}\,\mathrm{K}^{-1}$. The y-axis intercept of the graph determines the value of α to be $(4.2\pm0.2)\times10^{-7}\,\mathrm{K}^{-1}$, where the error for these fitted values is shown by the red line in figure 3.21. The value of α determined here is lower than the "bulk" thermal expansion coefficient of $\sim 5.9\times10^{-7}\,\mathrm{K}^{-1}$ which has been directly measured [155, 156], although it does agree with samples of silica that have been aged at high

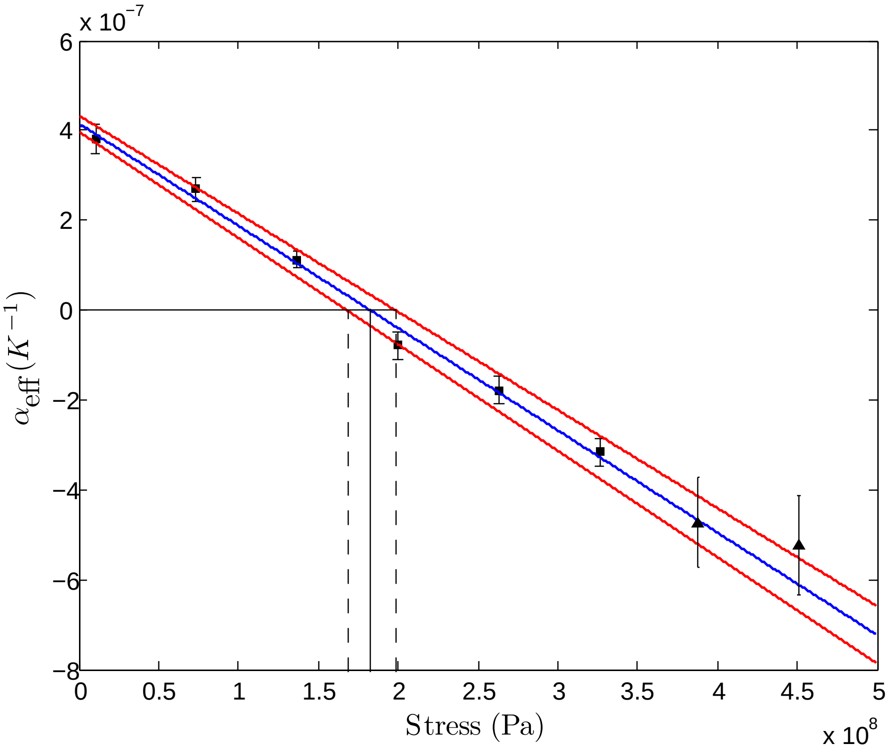

Figure 3.21: *Plot showing the average data from all four fibre measurements.*

temperatures of 1400°C [137]. For these, values of α as low as $3 \times 10^{-7}\text{K}^{-1}$ were found. It also confirms previously published indirectly measured values of α for heat treated silica fibres [132, 135]. The fused silica fibre measured in this chapter had undergone heat treatment during the manufacture process [129] and so it is expected to show a thermal expansion coefficient similar to samples aged or fabricated at higher temperatures.

The black line indicates the stress at which α_{eff} becomes zero, occurring at 182 ± 16 MPa where the error on this value is shown by the dashed black lines. The P-value statistic from the measured data and the theoretical straight line fit from figure 3.21 produced a value of 0.74 which is well above the 0.05 (95% confidence value) used to reject a null hypothesis [153]. It also shows that by taking the average of the results the scatter on the data has been reduced. Thus we are confident that the scatter in the data is consistent with a linear trend.

Other fitting techniques were also considered; firstly a fit was carried out where by all eight data points were fitted to, including the two highest stress values from Fibre 1. This did not affect the results greatly and returned an α value of $(4.1 \pm 0.2) \times 10^{-7}\,\mathrm{K}^{-1}$, a β value of $(1.60 \pm 0.06) \times 10^{-4}\,\mathrm{K}^{-1}$ and a nulling stress value of 184 ± 15MPa. The P-value returned from this method of fitting was 0.84. A final method of fitting which was tested involved taking the values of α_{eff} from figure 3.18 and calculating a weighted α_{eff} whereby the average values of the data points were weighted according to the individual errors on the mean. Again all eight data points were used in the best line fit and this produced an α value of $(4.0 \pm 0.1) \times 10^{-7}\,\mathrm{K}^{-1}$, a β value of $(1.55 \pm 0.04) \times 10^{-4}\,\mathrm{K}^{-1}$ and a nulling stress value of 186 ± 13MPa. The P-value returned from method of fitting was 0.99 suggesting that this fitting method is statistically better than the other methods used and this plot is shown in figure 3.22.

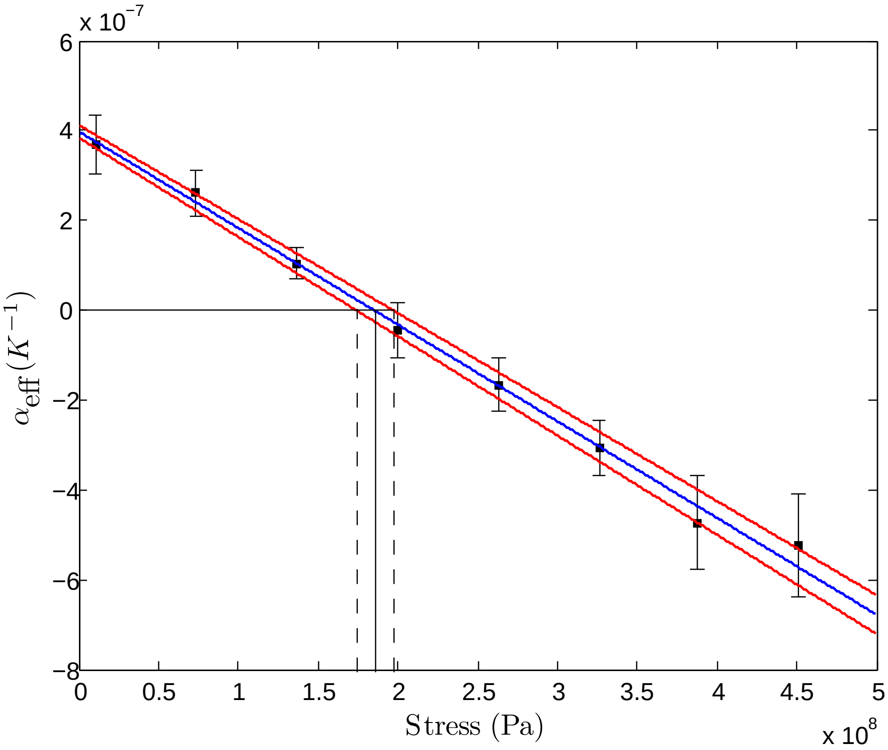

Figure 3.22: *Plot showing the weighted average data from all four fibre measurements.*

3.4 Effect of Heat Treatment on Silica

To understand how heat treatment affects the thermal expansion coefficient, the experiment was repeated with a uniform 2 mm silica stock hanging instead of a fibre. The expansion coefficient of the stock was measured, then the stock was polished with a hydrogen oxygen flame and the expansion coefficient of the stock was re-measured. The fibres are usually polished with a CO_2 laser before being pulled in order to reduce surface cracks on the silica fibre. During polishing the surface of the silica is heated so that it just flows and fills in surface cracks. The polishing process has been shown to increase the breaking strength of fibres [142, 143] and even decrease the surface loss mechanism of the silica [142]. In doing this test we found no change in the thermal expansion coefficient value due to polishing, was measured as $(4.4 \pm 0.3) \times 10^{-7}\,\mathrm{K}^{-1}$ when hanging a mass of 0.2 kg both before and after polishing. This data is shown in figure 3.23, suggesting that it is not the polishing of silica fibres that causes the range of thermal expansion values observed. Instead it is likely to come from the fabrication stage when the silica stock is heated using a CO_2 laser until it is molten and can be drawn into thin silica fibres.

3.5 Conclusions

We have measured for the first time the variation of the effective thermal expansion coefficient α_{eff} with stress in four identical silica fibres. These results provided a direct measurement of the thermal expansion coefficient and thermal elastic coefficients of a Suprasil 2A fused silica fibre. We determined the average value of α to be $(4.0 \pm 0.1) \times 10^{-7}\,\mathrm{K}^{-1}$ and β to be $(1.55 \pm 0.04) \times 10^{-4}\,\mathrm{K}^{-1}$. These values show that it is possible to null the effective thermal expansion of a fused silica fibre with a stress of $186 \pm 13\,\mathrm{MPa}$. In Advanced LIGO there are four fibres used to support the 40 kg silica test mass [14]. The majority of the bending energy contained in the fused silica suspensions is stored in

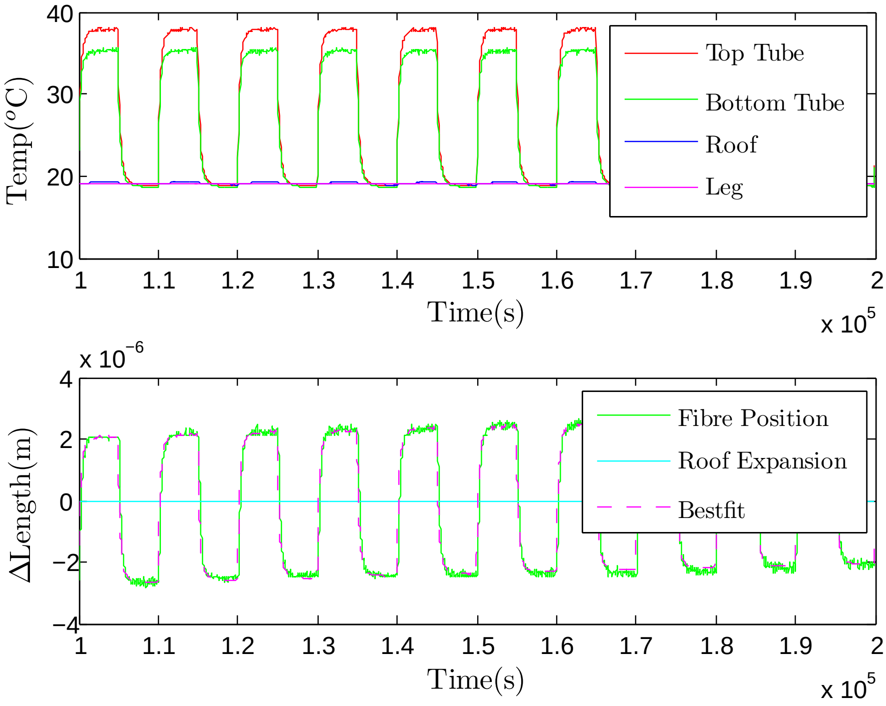

Figure 3.23: *Data taken when a mass of 0.2 kg was hanging from the polished stock.*

the 800 µm diameter region of the fibres. This corresponds to a stress in the 800 µm diameter region of 195 MPa. The stress value is just inside the one sigma error bars produced with this experiment for which thermoelastic loss can be nulled. For the values of α and β presented in this paper, we calculate that the total suspension thermal noise will be $\approx 9.7 \times 10^{-20}\,\mathrm{m}/\sqrt{\mathrm{Hz}}$, which is lower than the baseline sensitivity of $10^{-19}\,\mathrm{m}/\sqrt{\mathrm{Hz}}$ at 10 Hz. For comparison, if this cancellation effect did not happen and the α_{eff} was not nulled the total suspension thermal noise would be $\approx 1.8 \times 10^{-19}\,\mathrm{m}/\sqrt{\mathrm{Hz}}$. The data directly confirms that thermoelastic cancellation of the effective thermal expansions coefficient is essential to allow second generation gravitational wave detectors to reach their target sensitivity.

3.6 Future Work

The work presented in the chapter shows conclusively that the effective thermal expansion coefficient of a fused silica fibre can be nulled when the fibre is placed under the correct amount of static stress. The results also allow us to state that the total suspension sensitivity of aLIGO will not be limited by thermoelastic noise. The data shown here does, however, suffer from scatter which in turn has limited the accuracy and precision of the values provided in this chapter. We have accounted for this by taking an average of the four data sets recorded. The true cause of this scatter remains unknown and initial investigations in to the effects of room temperature variations did not uncover any correlation in the scatter.

One possible way to reduce this error would be to upgrade the aluminium roof which had the silica mass clamped to it, for a roof made out of invar. For this chapter we have accounted for a systematic error from the roof of 1.3×10^{-7}m/°C. Through the use of an invar roof this value could potentially be reduced by a factor of 10 leading to a more accurate result. The roof temperature only varied by <0.2°C and so this systematic effect does not explain such a large and varied scatter of $\pm 6 \times 10^{-8}\,\mathrm{K}^{-1}$. Even if no roof correction had been made it would only increase the effective alpha values by at most $2 \times 10^{-8}\,\mathrm{K}^{-1}$. It is instead more likely to be coming from longer term changes in the measurement environment. It is also interesting that each fibre appears to have a slightly different thermal expansion and thermal elastic coefficient (from table 3.1). We have also concluded that the variation in the thermal expansion coefficient does not come from the polishing process used for silica fibres and so this variation is more likely from the fibre fabrication or 'pulling' stage. This fluctuation in α and β may well just be a side effect of noisy data, nevertheless it would be interesting to study how the effect of laser power and the speed at which a fibre is fabricated varies the values of α and β. In chapter 5 we explore a new method for measuring α and β which is not subject to errors in convection currents and external material expansions.

Chapter 4

Measuring Weld Loss Using Cantilever Modes and Violin Modes

4.1 Introduction

When investigating ground based gravitational wave detectors, thermal noise from the silica fibres used to hang the test masses becomes extremely important in the detection bandwidth of 10 Hz to around a few hundred Hz. Losses that will lower the quality factor (Q value) of the material leading to increased thermal noise are bracketed into four main contributions. For silica suspensions they are the surface loss, weld loss, thermoelastic loss and bulk loss, as was discussed in chapter 2. In Advanced LIGO the contribution from surface loss and weld loss is about the same. Thermoelastic loss would be a dominant loss mechanism but its effects are minimised via the mechanism discussed in chapters 2, 3 and 5. Bulk loss is negligible in silica suspensions due to the high surface to volume ratio and the fact that bulk loss increases with frequency. So at frequencies below a few kHz bulk loss contributes only a small amount to the total mechanical loss. This chapter focusses on measuring the surface loss and weld loss for a monolithic silica suspension system. The results will allow a more robust estimate of the thermal noise performance in gravitational wave detectors to be made.

Weld loss was previously measured by Alastair Heptonstall [135]. In his paper, a thin section of 400 μm diameter silica fibre was welded with a CO_2 laser on to the side of a ground silica pin. The cantilever modes of the silica fibre were then excited and their decays, or ring downs were measured. Through the use of Finite Element Modeling (FEA) (as discussed in chapter 2) and regression fitting a value for the weld loss was determined. The welding that is done in the aLIGO [11–14] is different to the type of weld studied by Heptonstall; as it is the thick diameter 3 mm stock regions of the fibre which are CO_2 laser welded to a similar sized horn pin which stems from the bonded test mass 'ear'. The fibre is also welded end to end as shown in figure 4.1 and not as a side attachment. This 'ear' is hydroxy-catalysis bonded to the inner and end test mass mirrors [93] before the CO_2 laser weld is carried out. In this chapter we determine the weld loss that will be seen for a silica fibre when it is attached in this way (similar to aLIGO). This measure is important as the current weld loss values do not account for a weld which is created in this way and with aLIGO being limited in the strain sensitivity by weld loss we need an accurate weld loss measurement in order to make more robust thermal noise estimates as described in chapter 2.

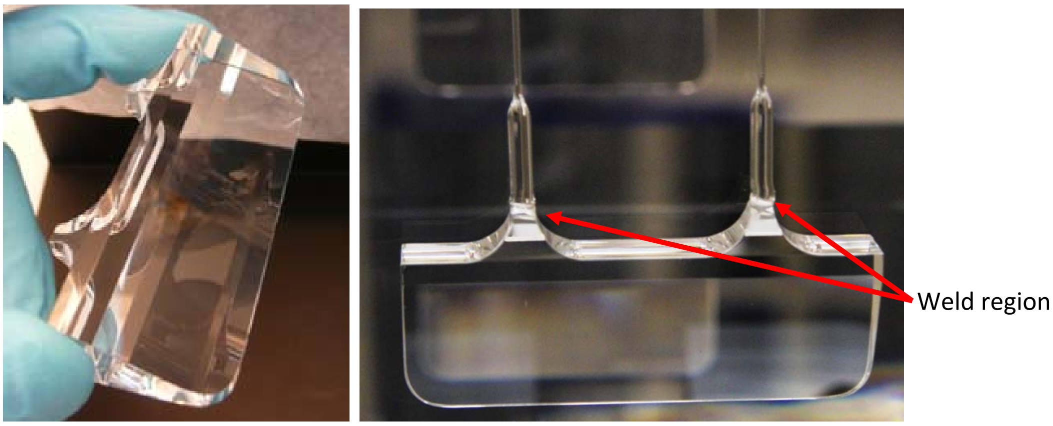

Figure 4.1: *A standard 'ear' where the flat face is hydroxy-catalysis bonded to the end mirror and the fibres are welded to the two horns.*

4.2 Experimental Considerations

In order to make sure our experiment was sensitive to weld loss, calculations were done using ANSYS to make sure that enough strain energy was concentrated into the weld region. If no energy is being transmitted into the weld region then the weld region will not contribute to the mechanical loss of the silica, meaning that we would not be sensitive to the mechanical dissipation of the weld region itself. Three different options were considered to check whether we would be sensitive to weld loss. The first idea was to weld a GEO fibre[1] straight on to an isolation mass pin and excite cantilever modes. However, for this case the silica neck region of the fibre stopped too much strain energy from reaching the weld region. For the second idea, a thin section of the fibre could be welded to the isolation mass pin similar to Heptonstall [135] except we would weld end to end rather than use the side technique of Heptonstall. This served as a good marker of the strain level needed in order to attain weld loss results. The third idea was to hang a mass from the fibre and monitor the violin mode ring downs. By exciting the violin modes of a fibre more bending strain energy would be pushed into the thicker stock and weld regions of the suspension, thus weld loss would become a more dominant loss mechanism. In contrast, cantilever modes, store the bending energy in the thinner less rigid parts of the suspension. Finite element models of all three cases were considered and a plot of the strain energy stored in the weld region for different modes are shown in figure 4.2. The results show that, both welding the thin section of the fibre to a thicker stock (Case 2) as was done by Heptonstall [135], and by hanging a mass from the fibre and monitoring the violin modes (Case 3), the weld loss is increased by around a factor of 100. In comparison to measuring cantilever modes of a standard GEO fibre (Case 1). This means the

---

[1] A GEO fibre is a silica fibre which is manufactured from 2mm diameter silica stock. The thin section of the fibre is 230µm in diameter and it is 25 cm long with ∼1.5 cm stocks at both ends.

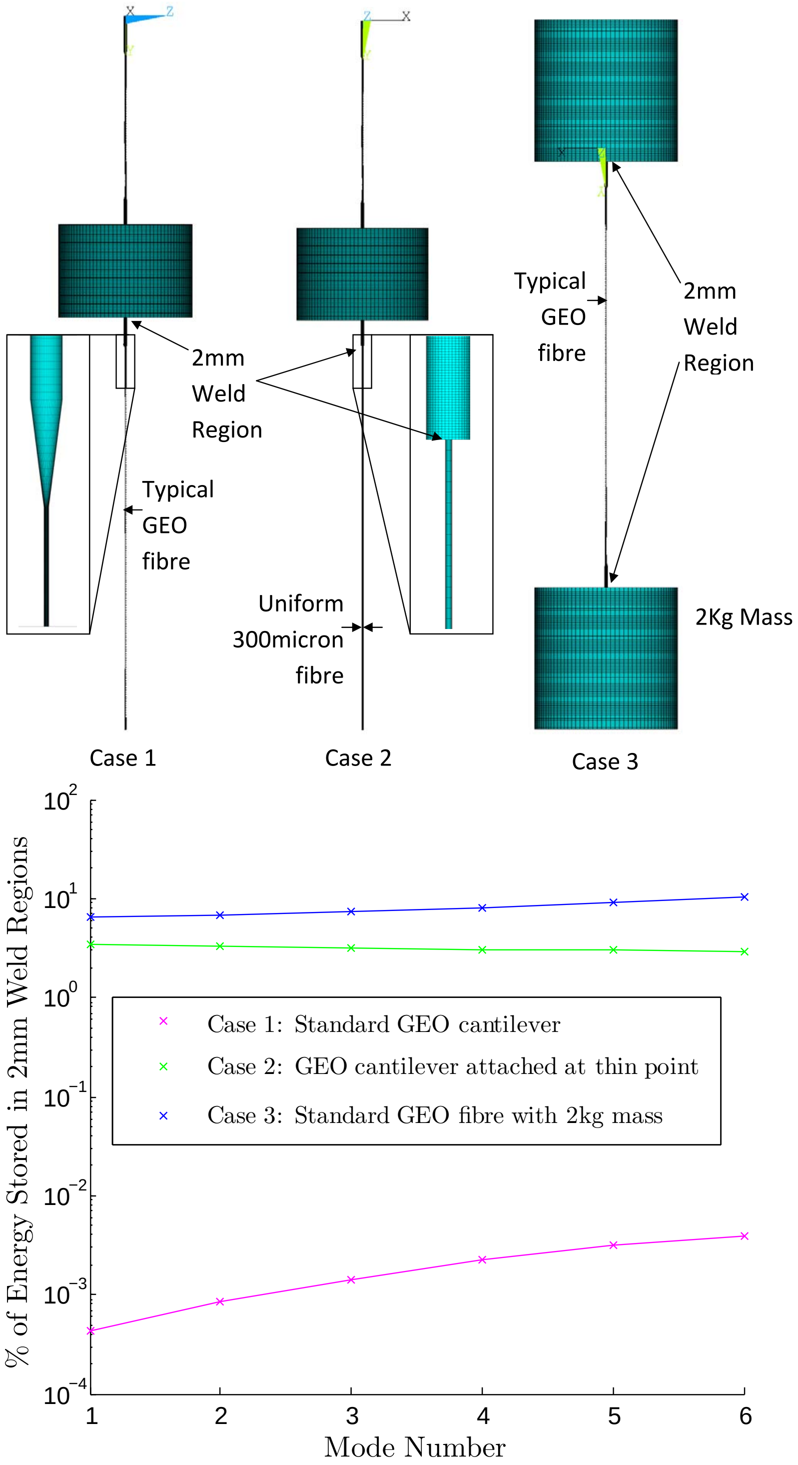

Figure 4.2: *3 ANSYS models to compare the percentage of strain contained in the weld region to that of the total strain energy in the system for each of the fibres resonant modes. Case 1 is a standard fibre with the 3mm stock welded to a 3mm ground pin. Case 2 has a 2mm stock welded to the thin part of a GEO fibre. Case 3 has both its 3mm stock welded to 3mm pins supporting a load of 2kg.*

loss in the weld region plays a more dominant role in the dissipation of energy with the contribution from weld loss to the total mechanical loss around the same as the surface loss, and above the thermoelastic loss contribution making it easier to measure directly.

It was decided to use a combination of violin modes and cantilever mode measurements to determine the weld loss. The idea was that the geometry shown in Case 3 would give information about the weld loss. Following this the fibre would then be cut to give a similar picture to Case 1, which would give us information about the surface loss, and thermoelastic loss terms, thus producing the most complete picture of loss in fused silica fibres.

4.3 Experimental Measurement of the Violin and Cantilever Mode Q Values

Care was taken to provide a set-up which minimised losses through effects such as mechanical recoil and gas damping [128]. The system used is shown in figure 4.3. The entire experiment was hung from a supporting frame which was created with the intention of limiting the recoil energy for a previous experiment [128]. A large mass value of 1.4 kg was chosen for the isolation mass in order to limit the energy transferred to the upper fibre. It was shown [128] that to limit the energy transferred into the upper stage of the pendulum, the isolation mass should be made as heavy as possible and that the energy stored in the upper stage decreases with increasing frequency when exciting modes in the lower fibre as shown by figure 4.4. This minimises strain energy from the excited fibre reaching the top clamping block and being dissipated by the metal tank which would then limit the Q value of the modes that could be measured. The isolation mass is hung from a silica fibre which was $\sim$400μm in diameter. This also reduces seismic noise from outside the vacuum system coupling in to the fibre movements being monitored as discussed in chapter 1.

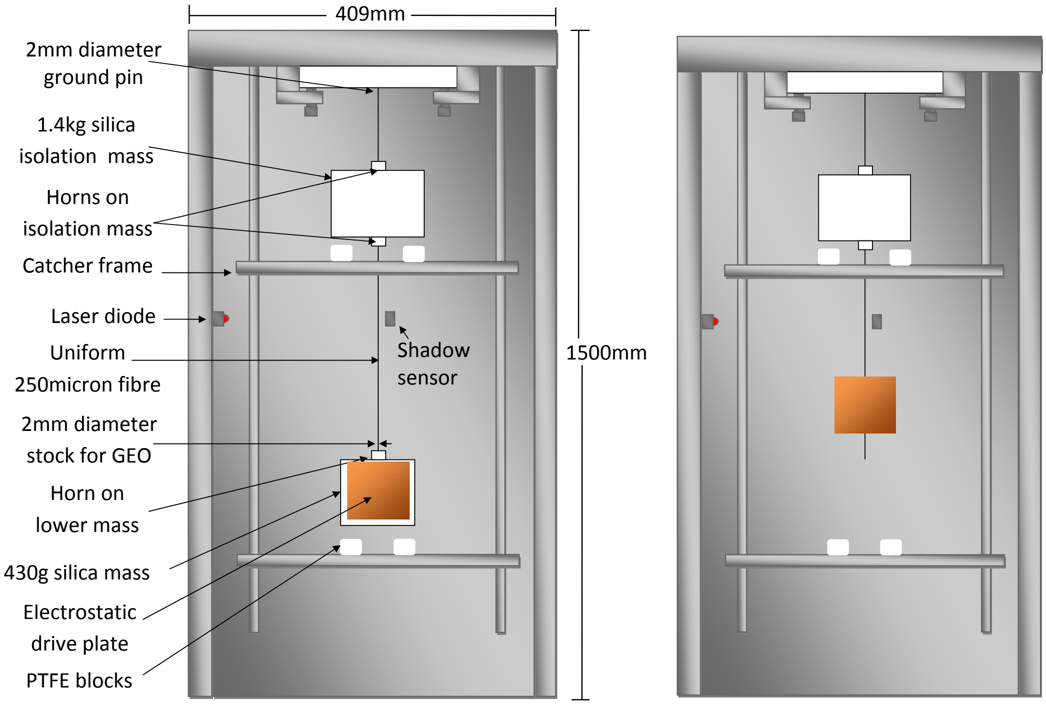

Figure 4.3: *Left: Set-up for measuring ring downs of violin modes. Right: Set-up for measuring ring downs of cantilever modes.*

Figure 4.5 shows that at the measurement frequency of ≥400 Hz the typical isolation of the system is $\geq 10^5$. Here we use the fact that the pendulum frequency of the upper stage is at 1.2 Hz. The top plate (shown in figure 4.6) and the masses are made from Heraeus High Optical Quality (HOQ) silica. The top plate is 50 mm thick and has a 2 mm diameter pin ground into it to which the top isolation fibre can be welded.

Both the isolation fibre and the fibre which had its modes excited and monitored were fabricated from Heraeus Suprasil 2A fused silica. The fibres were profiled as specified in [151], before being welded to the masses and transferred into the vacuum tank. The profile is shown in figure 4.7 and was suspended as described in section 4.4.

The modes were excited using the electrostatic drive plate which is connected to a high voltage amplifier and could provide an output of ±5 kV. This set-up was enclosed in a vacuum and was pumped with a turbomolecular pump

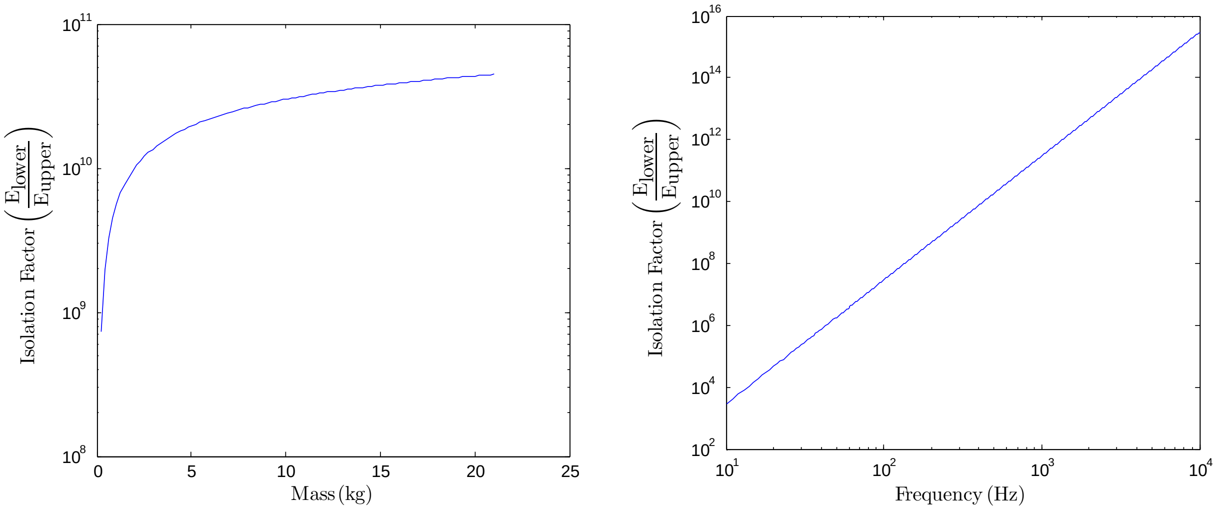

(a) (b)

Figure 4.4: *Plots showing how the modal energy is isolated from the metal tank with the use of an isolation mass and fibre. Plot (a) shows the isolation for a 400Hz violin mode as a function of isolation mass, and (b) shows the isolation for a* 1.4 *kg isolation mass as a function of violin mode frequency.*

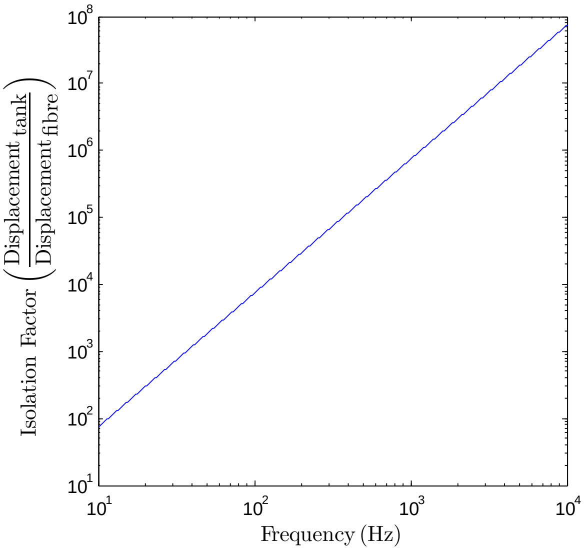

Figure 4.5: *Plot showing how the fibre being studied is isolated from the metal tank displacements.*

(BOC Edwards ACX250A) which achieved a base pressure of $\approx 2 \times 10^{-7}$ Torr. When performing these violin mode measurements it is important to consider

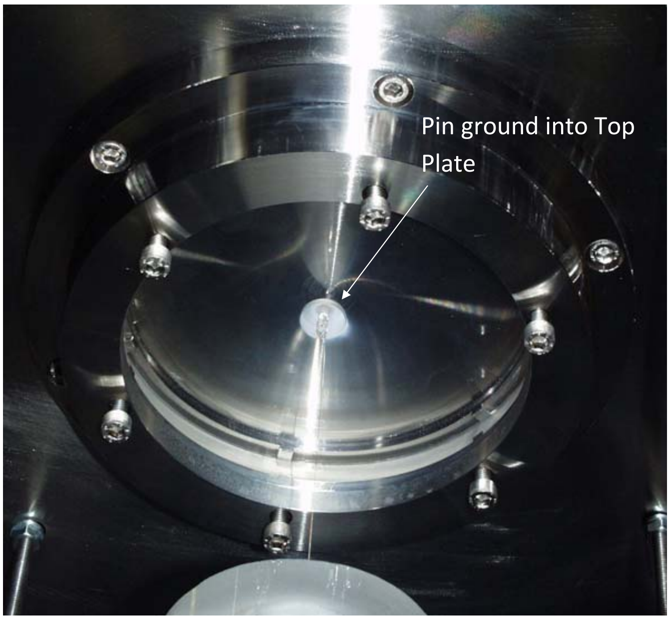

Figure 4.6: *Isolation mass, upper fibre and top clamp plate system.*

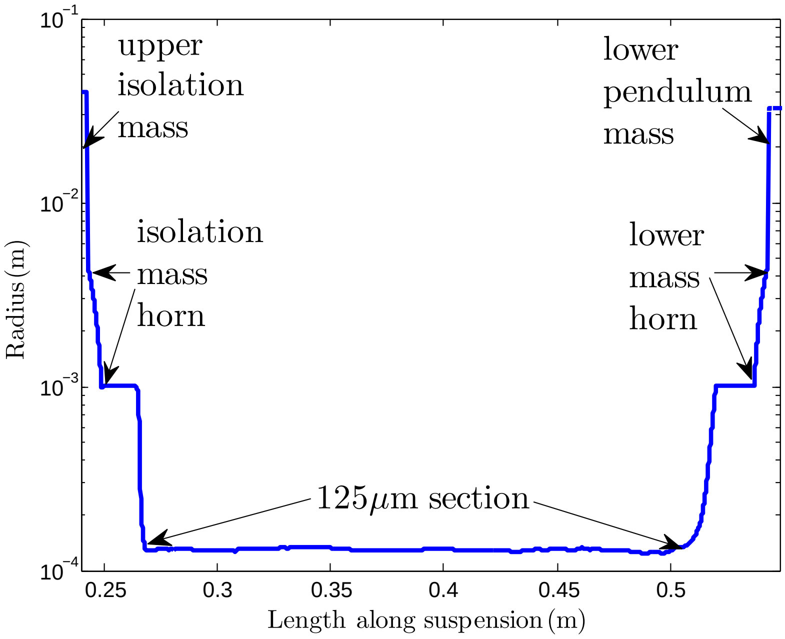

Figure 4.7: *Profile of fibre which has violin modes excited.*

how much energy will be dissipated from the system through collisions with residual gas molecules. This effect known as gas damping can be calculated by [128, 157, 158]

$$\mathrm{Q} = \left(\frac{\pi}{2}\right)^{\frac{3}{2}} \rho d f_0 \sqrt{\frac{RT}{M_m}} \frac{1}{P} \tag{4.1}$$

where ρ is the density of the silica fibre being oscillated, d is the diameter of the silica fibre, R is the gas constant, T is the temperature of the the residual gas, f_0 is the oscillating frequency of the silica fibre (in this case $> 400\,\mathrm{Hz}$), M_m is the molar weight of the residual gas and P is the gas pressure. The pressure is low enough to show that the Q expected from gas damping was $\approx 4 \times 10^{10}$ and as we were measuring Q's of the order 5×10^8 we were not limited by gas damping in this case.

4.4 CO_2 Laser Welding

As mentioned in section 4.1 the silica fibres used in Advanced LIGO are CO_2 laser welded to the corresponding attachment horns. In order to replicate these conditions the isolation mass and lower mass were manufactured with attachment horns. The horns for Advanced LIGO are square in shape, although a circular horn would be easier to work with as rotational alignment of the two masses would not be an issue. Horns also have the advantage that a CO_2 laser can be used to attach the fibre to the masses. Two separate horn designs were considered as shown in figure 4.8. ANSYS was used to study the energy distribution that will occur in the horns and fibres during a violin mode excitation. This analysis was done by building the fibre out of cylindrical beam elements and including a linear taper over a length of 1 cm where the fibre diameter increases to the stock profile. This was then meshed using a mesh density of 2 elements/mm, which previous convergence tests have shown to be more than sufficient [123, 128, 135, 159]. The graph in figure 4.8 shows that the strain energy stored in the horn region is only slightly increased for the circular horn which is easier and cheaper to manufacture.

Creating a monolithic suspension that could be CO_2 laser welded brought about additional challenges as the welding equipment is fixed in position and

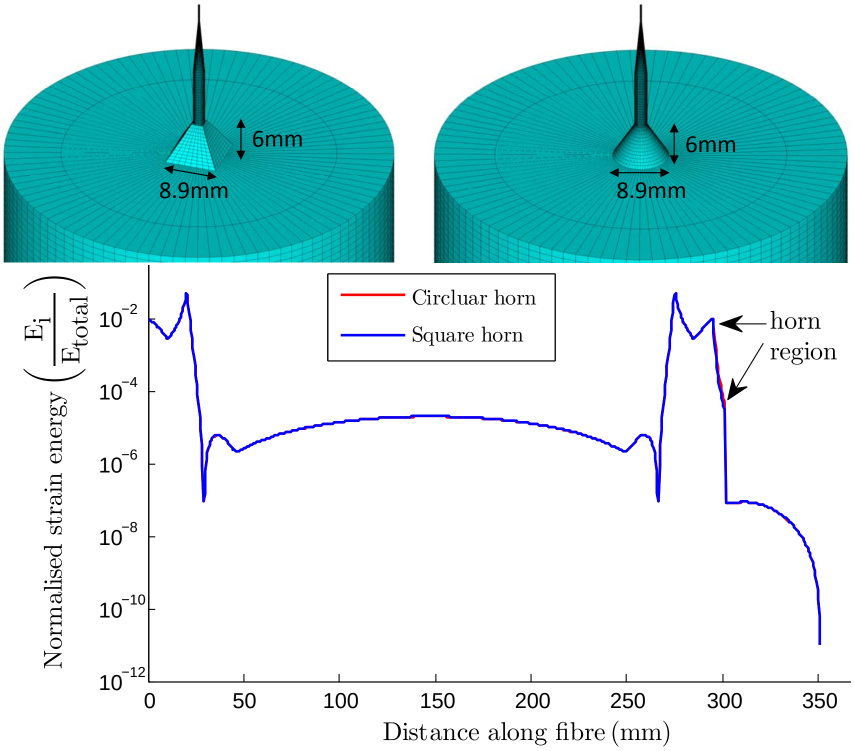

Figure 4.8: *An ANSYS model showing the two horn dimensions being considered. Top Left: GEO horn part replica, Top Right: A revised circular horn, Bottom: A plot showing how strain energy in the two horn designs varies for the first violin mode.*

can not be brought over to the vacuum tank. This meant that the entire monolithic suspension had to be welded outside of the vacuum system and then transported back to the tank to be installed. To do this a unit was designed to hold the top metal clamping ring, the isolation mass and the lower mass in place while the silica fibres are welded in position [13]. The mass holder unit and welding process is shown in figure 4.9. The process used gold plated mirrors to reflect the laser beam giving 360° access to the horn, while a vacuum extraction tube was used to absorb any silica vapour which was given off and could affect the losses measured [135]. Once the system was welded in place it could be transported back the vacuum system and have the top clamping ring bolted in place. The mass holder unit could then be removed leaving the silica suspension hanging freely. This process, whereby everything is welded and clamped externally before being moved into position and released, is very similar to the process used when welding and installing the QUAD suspension for aLIGO [160].

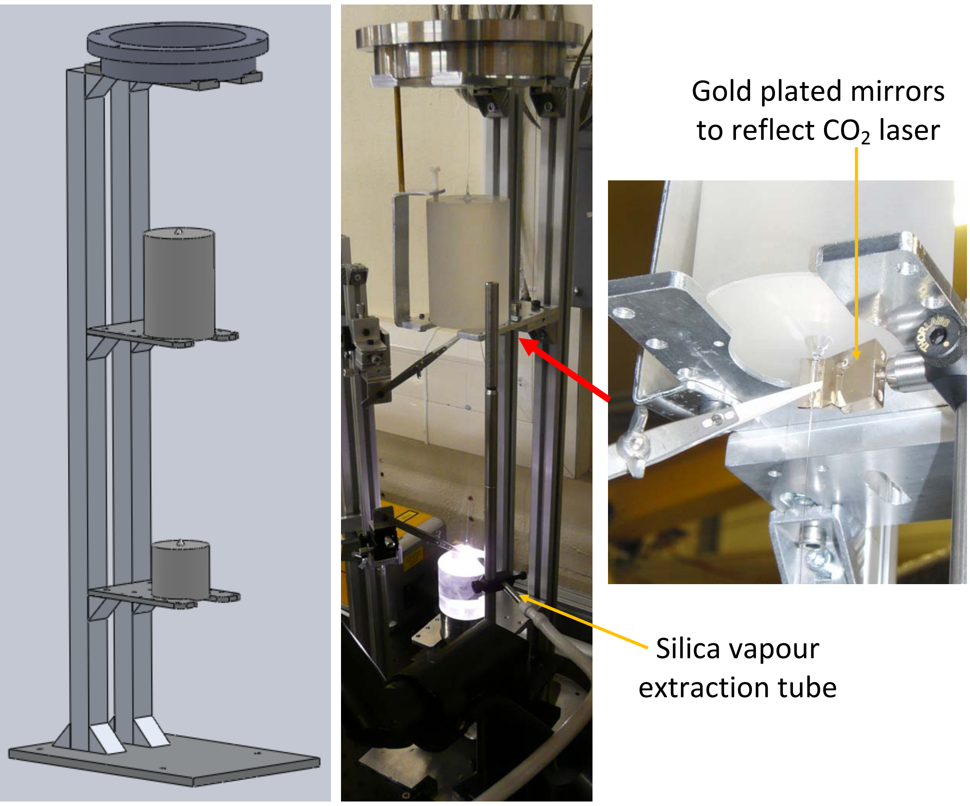

Figure 4.9: *Left: A Solidworks model of the apparatus used to support the isolation mass, lower mass and clamping ring so it can be transported and CO_2 laser welded. Right: A photo of the violin mode suspension system being CO_2 laser welded.*

4.5 2D Shadow Sensor

A shadow sensor was used to monitor the motion of the fibre. The sensor consists of a red light laser diode positioned to produce the fibres shadow across two photodiodes placed at 45 °, as shown in figure 4.10. Each diode measured 1 cm by 1 cm giving a linear readout region of around 0.7 cm. In order to make the diodes as sensitive as possible they were connected in parallel.

The cathode of one diode was connected to the anode of the other diode and vice versa. One of these connections was then grounded while the second connection provided the output as shown in figure 4.10. This allowed the output from each diode to be subtracted before being filtered by a Stanford Research amplifier (SR560) and amplified with a lock-in amplifier (SR830). By setting a reference frequency at 0.1 Hz from the mode frequency being studied a beat signal with a period of 10 seconds was produced. This 0.1 Hz signal was captured on the PC at a rate of 1 measurement per 100 ms which ensured no aliasing would occur. A schematic for this arrangement is shown in figure 4.11. If the fibre shadow was to stray outside of this linear region it would show up on the output signal as a harmonic and the ring down would not be an exponential decay.

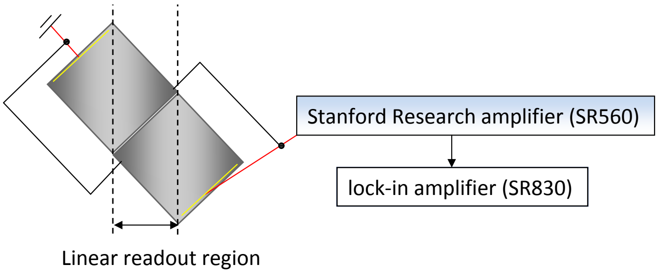

Figure 4.10: *Two photodiodes set at 45° with the linear detection region highlighted.*

To check the sensitivity of the shadow sensor, part of a fibre was placed on a translation stage. The fibre was then passed in front of the sensor in order to measure the minimum oscillation amplitude detectable. A plot of the voltage variation as the fibre is passed across the linear region of the readout system is shown in figure 4.12. A voltage to distance ratio of 4 V/mm was measured with a noise of 600 $\mu V/\sqrt{Hz}$ at 400 Hz as shown in figure 4.13. This results in a displacement sensitivity of $1.5 \times 10^{-7} m/\sqrt{Hz}$ at 400 Hz. It was a concern that when looking at a fibre using FEA it showed that two violin modes can occur at similar frequencies. Furthermore these modes of oscillation will be orthogonal to each other. One concern is that energy will couple into

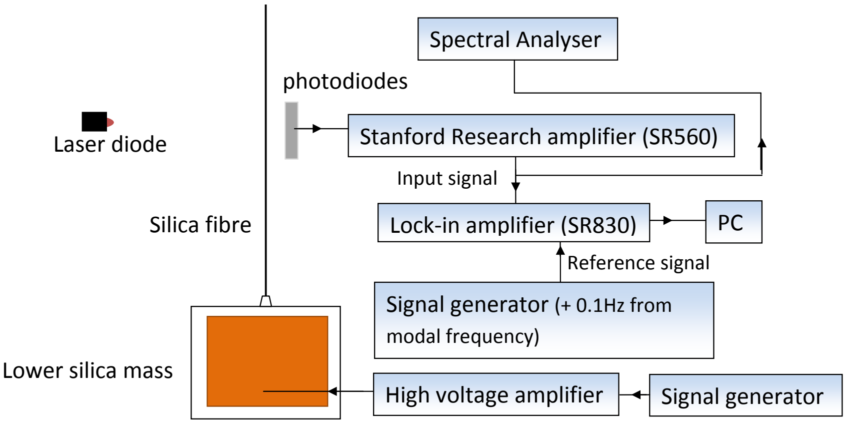

Figure 4.11: *Schematic set-up of circuitry attached to photodiodes used to measure violin mode ringdowns.*

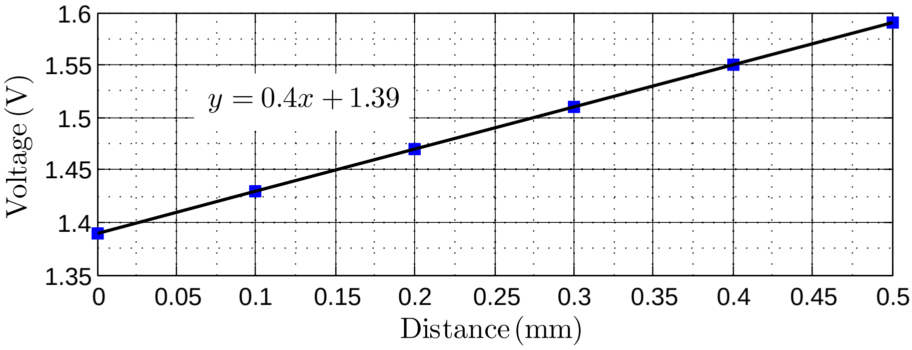

Figure 4.12: *Plot showing how the voltage from the photodiodes varies linearly as a 250µm diameter fibre is passed across the linear region of the photodiodes.*

the alternative mode and therefore produce an energy loss in two directions. The way around this is to have a sensor that can pick up motions in both dimensions and figure 4.14 shows the arrangement utilised. When the results were recorded it was later decided that this monitoring in two directions was not necessary as both orthogonal modes ring down at the same rate once an equilibrium is reached as mathematically described in equation 4.4. The 2D sensor also added extra complications when installing the fibre into the vacuum system and so for that reason we only monitored oscillations in the one direction, which was orthogonal to the electrostatic drive.

As expected, when the violin and cantilever modes were excited some of

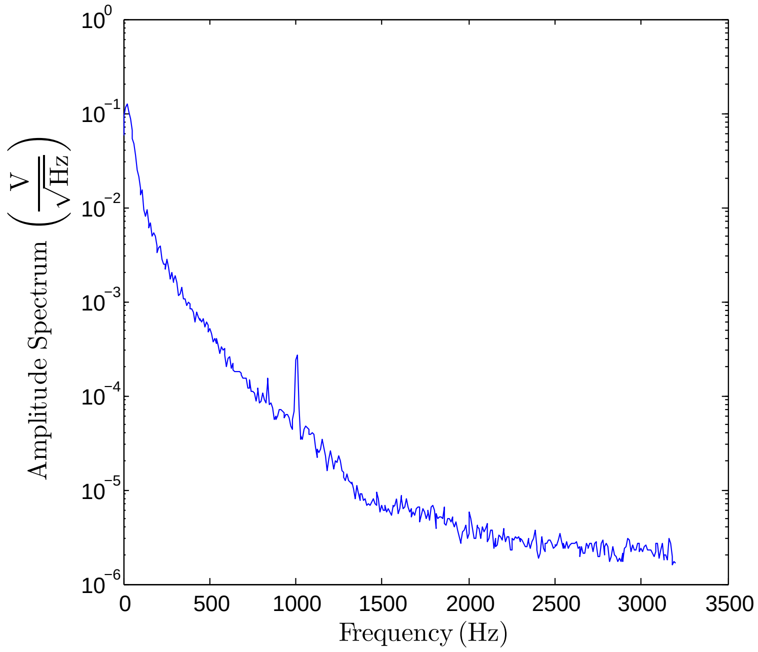

Figure 4.13: *Plot showing the read out noise from the photodiodes.*

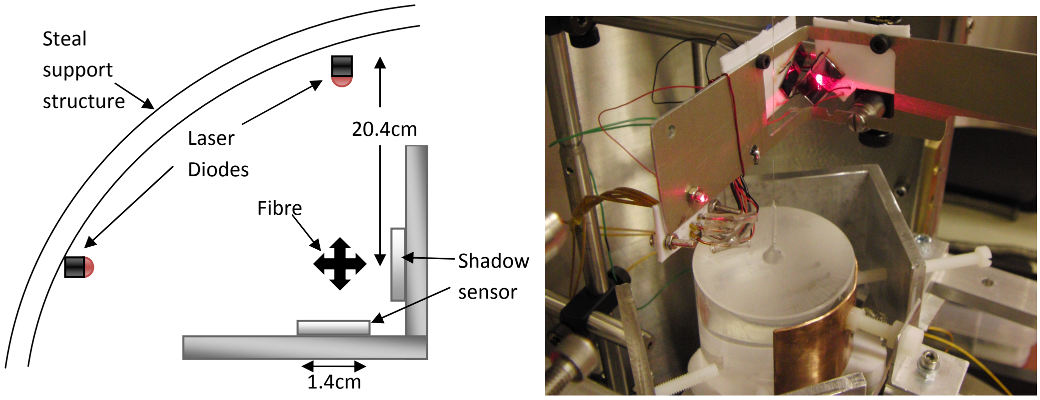

Figure 4.14: *Left: A plan view of the 2D shadow sensor. Right: A photo of the shadow sensor with one sensor working.*

the energy is coupled into the orthogonal mode. This happens because the orthogonal modes have closely spaced frequencies and thus a beat signal can be produced as energy gets transferred from oscillations in the X direction to oscillations in the Y direction. The energy is then redirected in the X direction and so on as shown in figure 4.15. Once the system has reached equilibrium point both the orthogonal modes ring down at the same rate. This energy transfer mechanism is discussed in [161]. It is the loss of these modes which

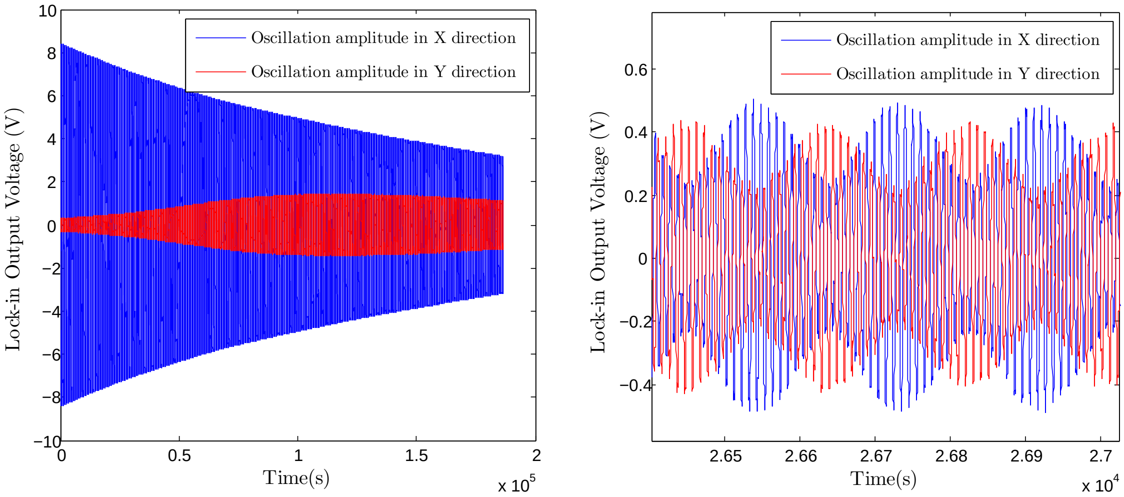

(a) (b)

Figure 4.15: *Plots showing energy being transferred to the orthogonal oscillation mode and back again: (a) shows the orthogonal oscillation mode being excited, and (b) is a zoomed in plot showing how the beat frequency is produced as the fibre oscillates in both the* X *and* Y *directions.*

we are interested in so in order to calculate the loss we monitor the decay envelope produced in figure 4.17. The lock-in amplifier gives two outputs; $x = r\cos\theta$ and $y = r\sin\theta$, when monitoring the ring down, where r represents the amplitude of the oscillating signal and θ is the phase difference between the reference signal and the signal being measured. This is useful as not only does it give information about the rms value of the input signal but it also gives information about the phase difference between the input signal and the reference signal. This allows the amplitude of the oscillations to be viewed, and it is this amplitude decay which will be fitted as shown in figures 4.16 and 4.17.

$$X = X_o e^{-\gamma t} cos \omega_o t \tag{4.2}$$

$$Y = Y_o e^{-\gamma t} cos(\omega_o + \Delta\omega)t \tag{4.3}$$

$$\text{Voltage Amplitude} = \sqrt{X^2 + Y^2} = A_o e^{-\gamma t} \tag{4.4}$$

where A_o is the time independent original amplitude of the oscillation and $\Delta\omega = 2\pi\Delta f_o$ where Δf_o is the difference in frequency between the orthogonal modes. When the natural log of this envelope is taken it forms a straight line.

$$Ln\,(\text{Voltage Amplitude}) = Ln\left(A_o e^{-\gamma t}\right) = -\gamma t + C \tag{4.5}$$

It is worth mentioning that the decay constant γ is the same for all cases whether monitoring amplitude decays in the X, Y or both directions as shown by figure 4.16. This is a unique property for the fibre modes studied here as they are homogenous and symmetric about the vertical axis. If the fibre was not symmetric or had for example one side more polished than the other then the system loss would decay very differently depending on the direction of oscillation in. The resonant frequency ω_o is known to be within better than 0.1 %. The frequency estimation is done by taking a fast Fourier transform (FFT) of the lock-in amplifier output as shown in figure 4.17. The FFT peak shows the difference between the lock-in-amplifier reference frequency and the fibre oscillation frequency. We can therefore determine the resonant frequency by subtracting this frequency away from our reference signal frequency. The reference signal on the lock-in amplifier was always set to be higher than the frequency being monitored. This was done by looking at the output signal from the photodiodes on a spectrum analyser and then tuning the reference signal for the lock-in amplifier to be 0.1 Hz away from the signal we wanted to measure.

$$\omega_o = 2\pi f_o = 2\pi\left(f_{\text{lock in amplifier reference signal}} - f_{\text{FFT peak}}\right) \tag{4.6}$$

The gradient of this line gives the value of γ from equation 4.5 which can be used to estimate the loss which was discussed in chapter 2 with equation 4.7.

$$\phi\left(\omega_o\right) = \frac{1}{Q\left(\omega_o\right)} = \frac{2\gamma}{\omega_o} = \frac{-2 \times \text{gradient of straight line}}{\omega_o} \tag{4.7}$$

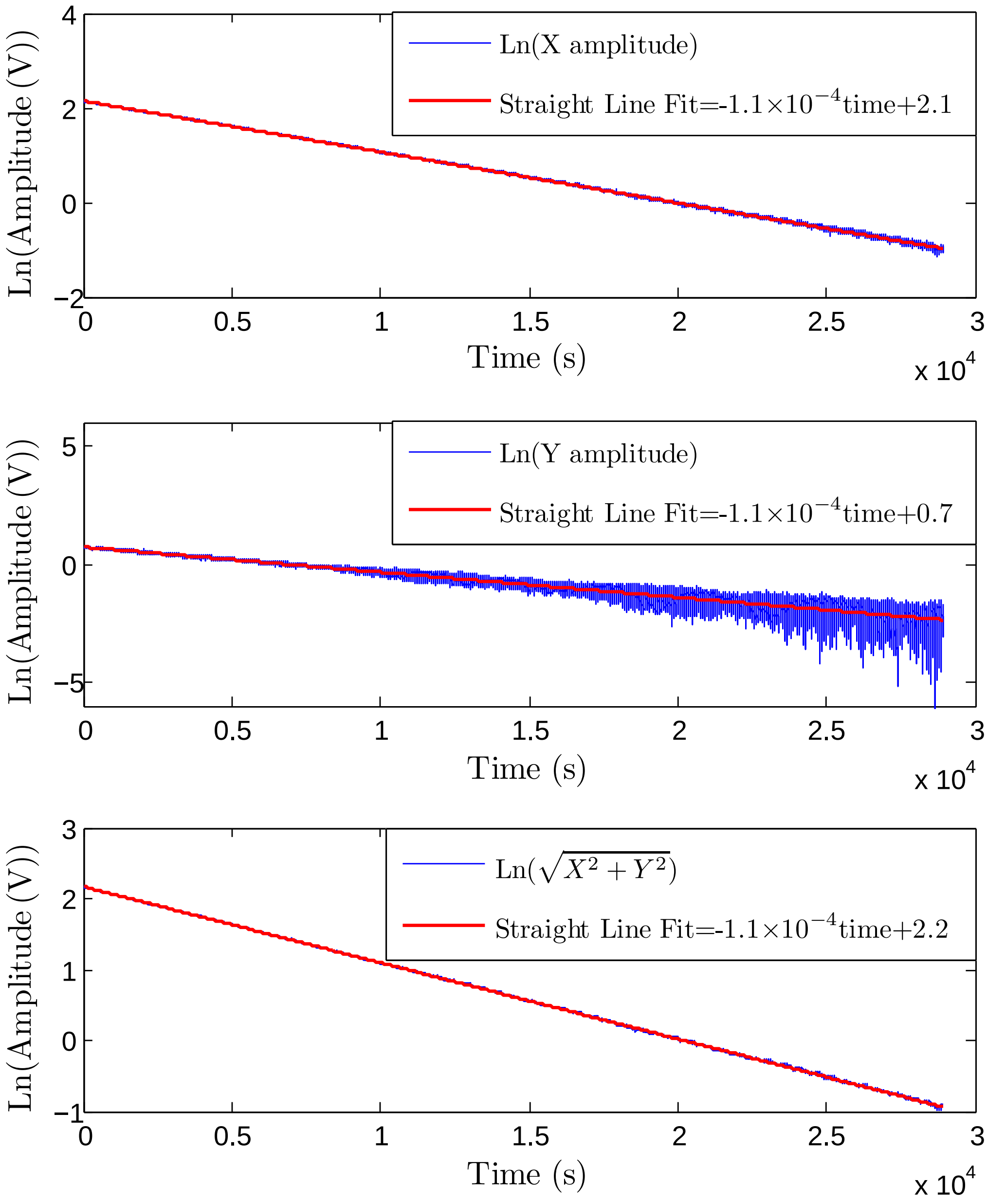

Figure 4.16: *Plots showing energy being lost from the two orthogonal modes combined is done so at the same rate as if only one of the orthogonal modes was being measured and so monitoring the oscillations in one direction does not affect the losses measured.*

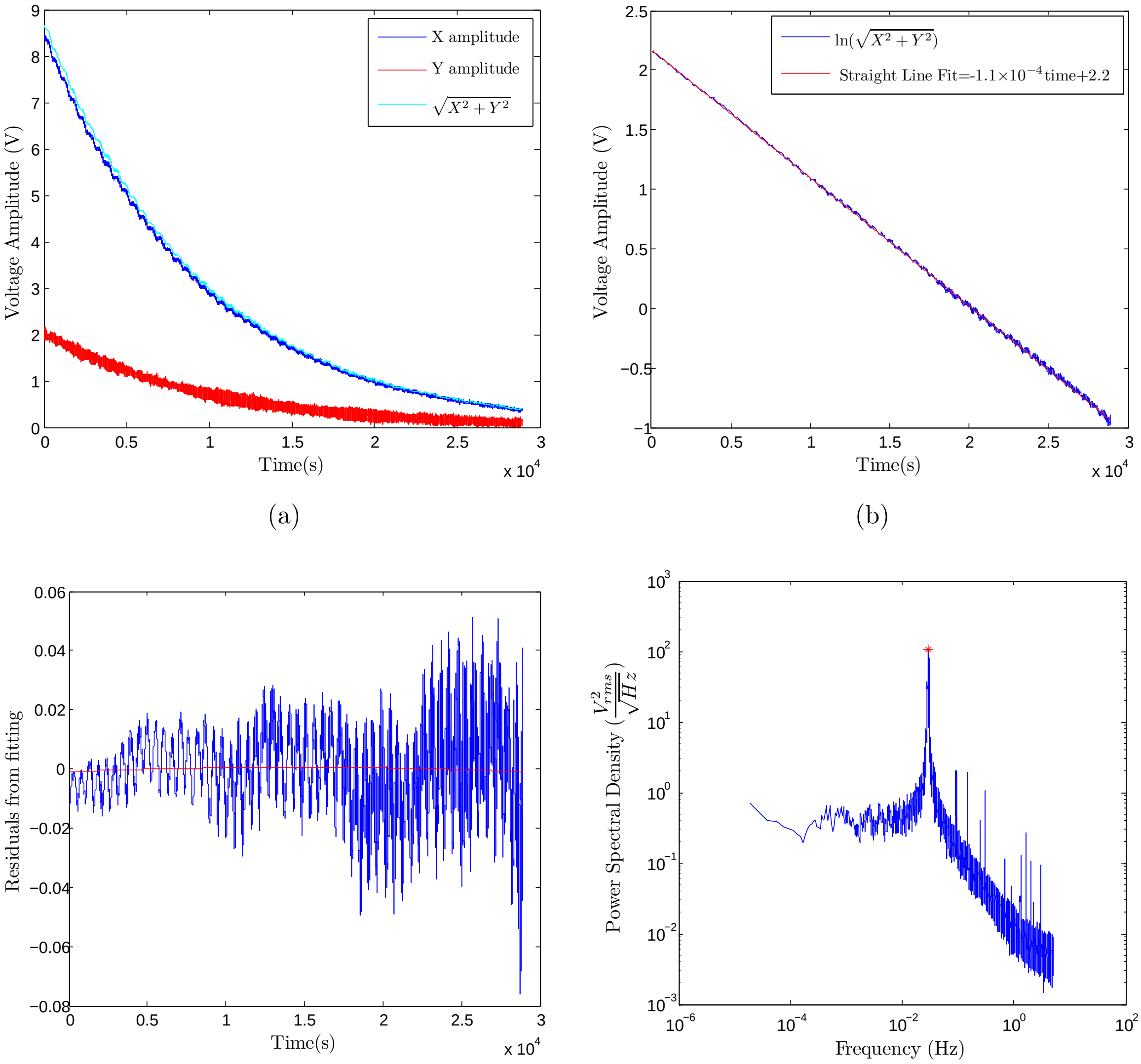

(a) (b)

(c) (d)

Figure 4.17: *Plots showing the different stages of analysis for monitoring the ring down of fibre modes: (a) the envelopes for the decays in the X and Y directions are recorded, (b) the natural log of the plots are taken and a straight line is fitted to the data, (c) the residuals from the straight line fitting are checked to ensure they look sensible, and (d) the FFT of the lock-in amplifiers output signal is checked to show the measured signal clearly.*

4.6 Results

Loss measurements were made of violin and cantilever modes and the fibre profiles were imported into ANSYS. A description of how fibre profiles are imported to ANSYS can be found in [159]. For this case we produced keypoints in ANSYS with a spacing interval of 0.1 mm (therefore 10 keypoints/mm). The corresponding circular dimension which were taken from the profiler data [151] were assigned and centered onto each of the associated keypoints. Lines were then formed between each of the adjacent keypoints. As we are dealing with fibres that have circular cross sections that vary with length, the cross section which is assigned to one keypoint will be different to that of the adjacent keypoints. A linear taper was therefore created between each of the adjacent cross sections. By choosing a suitable resolution of keypoints (more than 2 keypoints/mm), these linear tapers approximate to real curve profiles [159]. The profiles were compiled to produce the corresponding suspension models shown in figure 4.18. The loss of the system could then be modeled as discussed in chapter 2. Static analysis, where the top of the isolation fibre is clamped and gravity is applied to the system was carried out in ANSYS, to give information about the stress distribution of the fibre models. Following this a modal analysis extracted the strain energy distribution and the dilution values (section 2.4.3) of the systems when oscillating at the resonant frequencies. The frequencies and dilution values predicted by ANSYS are shown in table 4.1 alongside the actual measured frequencies of the system. The measured system frequencies were found to agree with the predicted ANSYS frequencies to better than 6%. This level of correlation is very good and shows that the real fibre suspension is being modeled accurately in ANSYS.

4.6.1 Markov Chain Monte Carlo

A regression fitting code was then used to determine values of $h\phi_{\mathrm{s}}$, ϕ_{weld} and α. In this case we chose a Markov Chain Monte Carlo (MCMC) regression fitting code [162] to extrapolate the loss term parameters (see chapter 2 for theory). The MCMC code was used over a nonlinear regression fit as it allowed the entire probability distribution of the prior space to be sampled. This

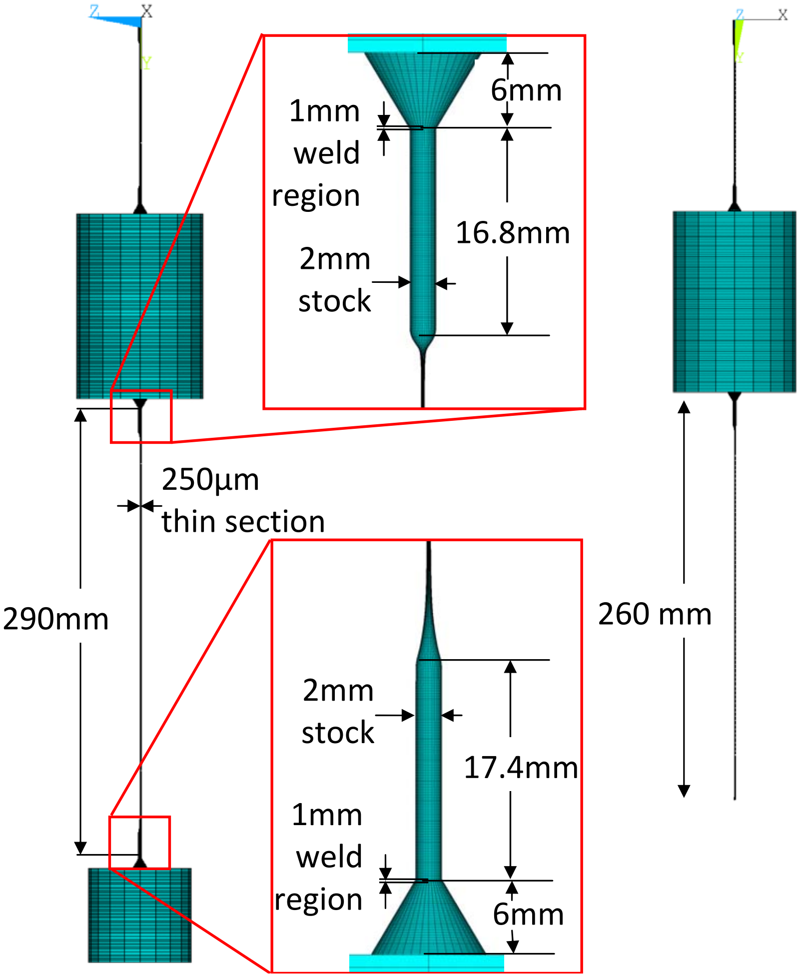

Figure 4.18: *Profiles of silica suspension compiled and imported to ANSYS in order to model the strain distribution along the fibre for both violin and cantilever modes.*

would prove useful as it allowed for non Gaussian peaks in probability to be observed if present. It also allowed the quadratic form of the nonlinear thermoelastic equation to be solved more easily. Solving to determine the bulk coefficient C_{bulk} value was not possible in this case as the resonant mode frequencies measured were too low for bulk loss to be a measurable loss term when compared with surface loss. Bulk loss contributes $< 20\%$ to ϕ_{total}, the total loss of the system. Solving for β the thermal elastic coefficient was also not possible as the violin mode frequencies were too far away from the Debye peak in the thermoelastic loss at $\sim$26 Hz. As a result thermoelastic

VIOLIN MODES			CANTILEVER MODES	
ANSYS (Hz)	Measured (Hz)	Dilution	ANSYS (Hz)	Measured (Hz)
391	411	36.69	3.69	3.79
781	822	34.38	22	22
1178	1238	31.14	62	61
1581	1659	26.94	121	115
1974	2074	22.31	199	189
2376	2496	18.73	297	282
2777	2923	15.36	415	394
3182	3348	12.23	553	523
			710	673
			888	841
			1086	1029

Table 4.1: *Comparison of ANSYS predicted resonant frequencies and the system frequencies that were measured. The dissipation dilution values are calculated from ANSYS as described in section 2.4.3 are also listed.*

loss contribution for the violin modes was low $< 30\%$ for the first two violin modes and $< 15\%$ of ϕ_{total} for modes of higher frequencies. The value of β was measured in chapter 3 and has also been studied in literature [130–133, 146] and so for this instance the value of β was fixed to be $1.55 \times 10^{-4}\,\text{K}^{-1}$ from chapter 3. Thermoelastic loss is the dominant loss mechanism for cantilever modes due to the modes being at low frequencies, but as there is no stress in the silica for these modes only α can be measured accurately. The MCMC code takes in all of the losses that were measured e.g. both violin and cantilever mode losses and did a global fit to the data.

The MCMC code used was originally written by Dr Matthew Pitkin and was edited by the author to be used for the task as described in this chapter. The MCMC regression [162] used the losses measured for violin and cantilever modes and compared them to the modeled suspension with loss given from the combination of ANSYS FEA and equation 2.43. The MCMC code works by defining the measured loss as being calculated from a combination of loss terms such as surface loss, weld loss and thermoelastic loss. Thus $y = F(\vec{\theta}|x_i)$ where y is the measured losses, $F(\vec{\theta}|x_i)$ is given by equation 2.43, x_i describes the known loss perimeters of the system such as fibre dimensions, frequencies and strain energies etc. $\vec{\theta}$ describes the unknown coefficients being fitted to the measured losses for this case $h\phi_s, \phi_{weld}$ and α were the unknown coefficients. A flow diagram illustrating the logic behind the iterative MCMC process is shown in figure 4.19 and is also described below.

1. Firstly a vector space Ψ is defined. In this case we know that the values to their order or magnitude $h\phi_s \sim 10^{-12}$m, $\phi_{weld} \sim 10^{-7}$ and $\alpha \sim 10^{-7}$K^{-1} and so we allow the MCMC code to search in a prior space from zero to a value one order of magnitude larger than what we are expecting so as not to bias the results. These three unknown variables make up $\vec{\theta}$ such that $\vec{\theta} = [h\phi_s, \phi_{weld}, \alpha]$. The variance σ_y^2 in the measured losses is also defined here. This can also be thought of as an error in $\vec{\theta}$ hence $\sigma_y^2 \rightarrow \sigma_{\vec{\theta}}^2$.

2. The misfit between the modeled loss and measured loss is calculated using the covariance matrix C, were C is the covariance matrix of the noise on the data.

3. A likelihood test is carried out to see if the values of $\vec{\theta}$ chosen are more or less probable than the initial or previous values chosen. If it is less probable, a test is done to see if it is still reasonably probable based on a random number. This allows the MCMC code to jump and sample a range of values across the prior space.

4. Depending on the outcome of step 3, if the values chosen were deemed likely then the values of $\vec{\theta}$ are recorded. Otherwise the values of $\vec{\theta}$ are thrown away and the previous values of $\vec{\theta}$ are reused.

5. New values of $\vec{\theta}$ are chosen for the next iteration and steps 2-5 are repeated for a number of cycles determined at the start by the user.

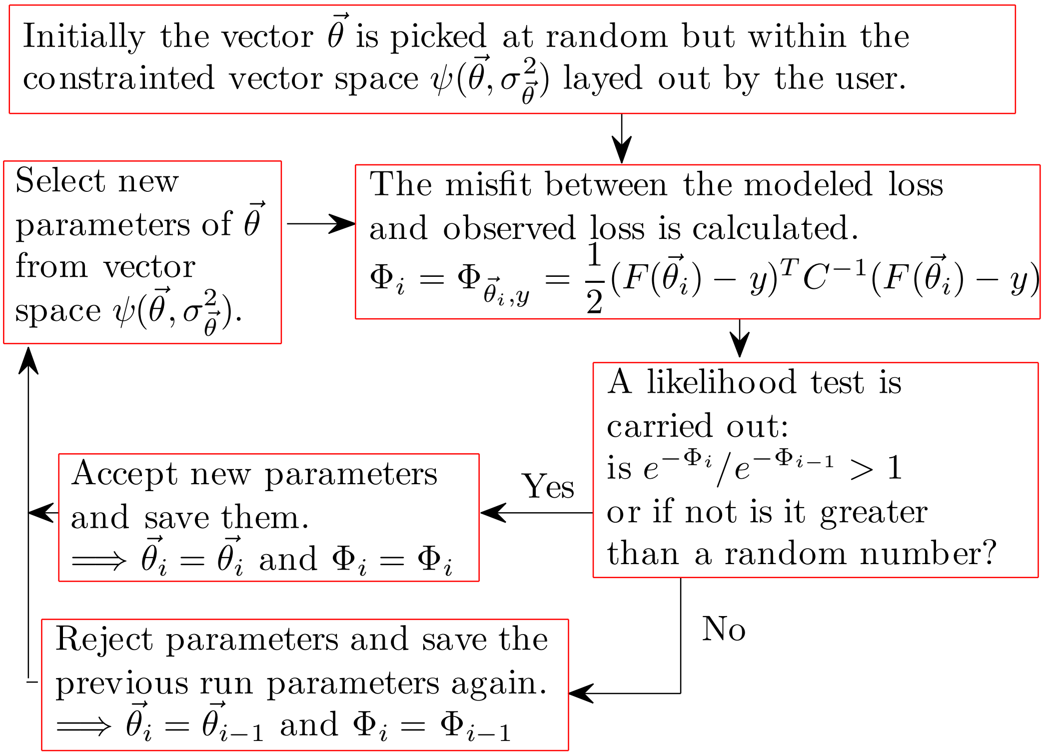

Figure 4.19: *Flow diagram showing how the iteration process of the MCMC regression code works.*

The MCMC code then places the component values of $\vec{\theta}$ that were recorded into discrete bins. The most probable bin is therefore the one that was recorded the most often. A histogram showing the recorded values of the MCMC run is plotted in figure 4.20. It is worth noting that for this example we used a burn-in of one million iterations and we used one million iterations to actually solve the problem and to provide convergence to the probability plots shown. During the burn-in process none of the data is saved and used in the results displayed. The burn-in stage allows the MCMC to converge towards the most likely values without skewing the result in bias of the initial random values of $\vec{\theta}$ that were selected. The MCMC regression was able to determine the three

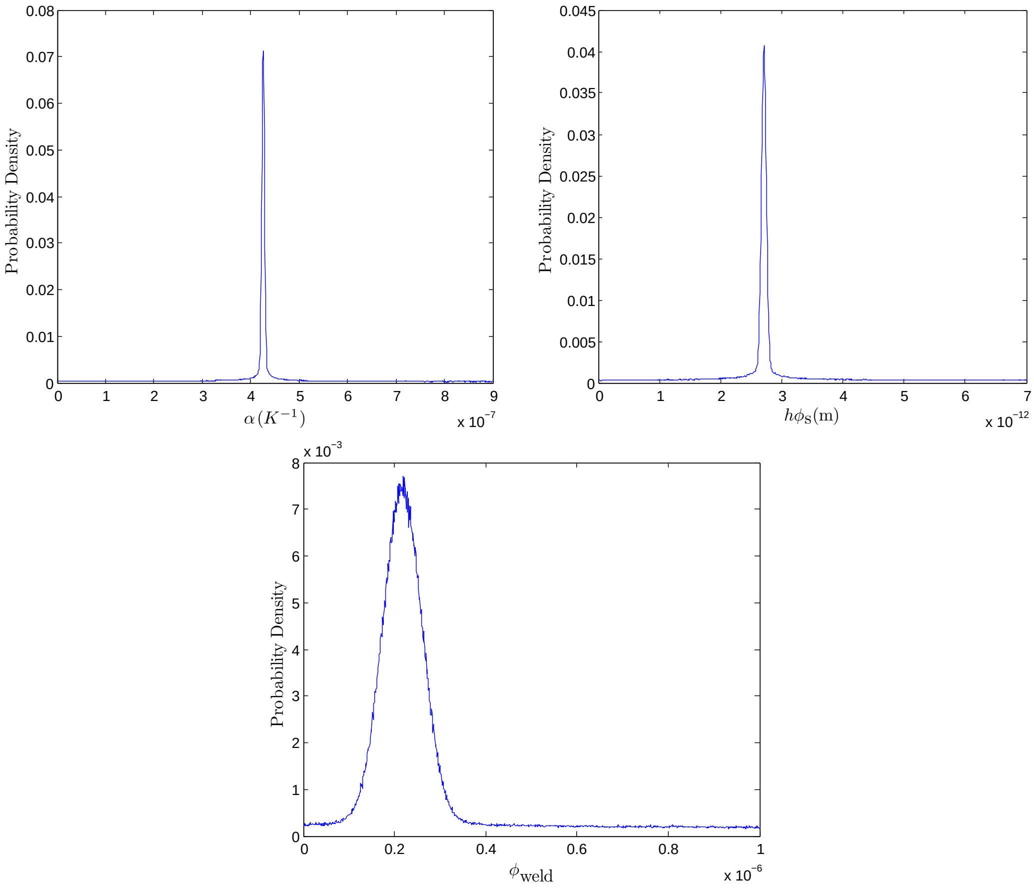

Figure 4.20: *Plots from the MCMC regression showing the probability of possible values for* α*,* $h\phi_s$ *and* ϕ_{weld}*.*

variables (α, $h\phi_{\rm s}$ and $\phi_{\rm weld}$) with relatively low uncertainty. This is because the thermoelastic and surface losses are both the dominant loss mechanisms for the cantilever modes. As is shown by figure 4.21a these two loss components vary depending on different parameters of the system. Thermoelastic loss has a distinctive frequency relation whilst surface loss depends on the suspension fibre geometry. It was this difference which allows the values of α and $h\phi_{\rm s}$ to be regressed from the cantilever mode data. As α and $h\phi_{\rm s}$ are well constrained this allowed the remaining "excess" loss being measured for the violin modes to be attributed to the weld loss $\phi_{\rm weld}$. The calculated values from the MCMC regression as shown in figure 4.20 were as follows: $\alpha = (4.3 \pm 0.2) \times 10^{-7}\,{\rm K}^{-1}$,

$h\phi_{\mathrm{s}} = (2.89 \pm 0.07) \times 10^{-12}\,\mathrm{m}$ and $\phi_{\mathrm{weld}} = (2.4 \pm 0.5) \times 10^{-7}$. Using these values and substituting them into the equations from section 2.4.5 we can see how well these values agree with our measured loss values (figure 4.21). The errors shown in figure 4.21 all come from the scatter between successive ring down measurements. This was by far the dominant error when compared to the room temperature variations of 2% and radius profile errors used to build the FEA model of $\pm 2 \times 10^{-6}$m. An adjusted R^2 and norm of residuals goodness of fit tests were used to see just how well the modeled loss and fitted values agreed with the measured data. The adjusted R^2 value is calculated from equation 4.8,

$$\text{adjusted } \mathrm{R}^2 = 1 - \frac{SS_{\mathrm{residuals}}/(n-K)}{SS_{\mathrm{total}}/(n-1)}, \tag{4.8}$$

where $SS_{\mathrm{residuals}}$ is the sum of the squares of the vertical distances of the points from the best-fit curve, SS_{total} is the sum of the squares of the vertical distances of the points from a horizontal line drawn at the mean loss value measured, n is the number of measured loss values used to fit the data and K is the number of parameters which have been fitted to the data which in this case was 3. For this test the adjusted R^2 value returns a number between 0 and 1. Higher values indicate that the model fits the data better so if the adjusted $\mathrm{R}^2 = 1$, all points lie exactly on the curve with no scatter. Likewise when the adjusted $\mathrm{R}^2 = 0$, the best-fit curve fits the data no better than a horizontal line going through the mean of all the measured loss values. The norm of residuals is calculated from equation 4.9

$$\text{Norm of Residuals} = \sqrt{SS_{\mathrm{residuals}}}, \tag{4.9}$$

The value returned from equation 4.9 gives a measure of how well the modeled values fit to the measured data and a number between 0 and infinity will be returned. The smaller the norm of residual value is the better a fit we have, with 0 being a perfect fit to the data. Even though a global fit was done to the data, due to figures 4.21a and 4.21b being on different orders of magnitude

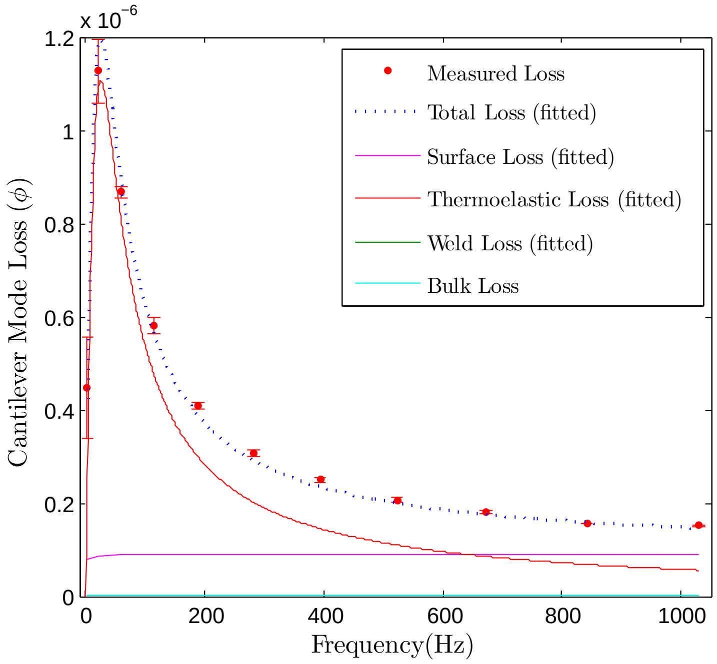

(a)

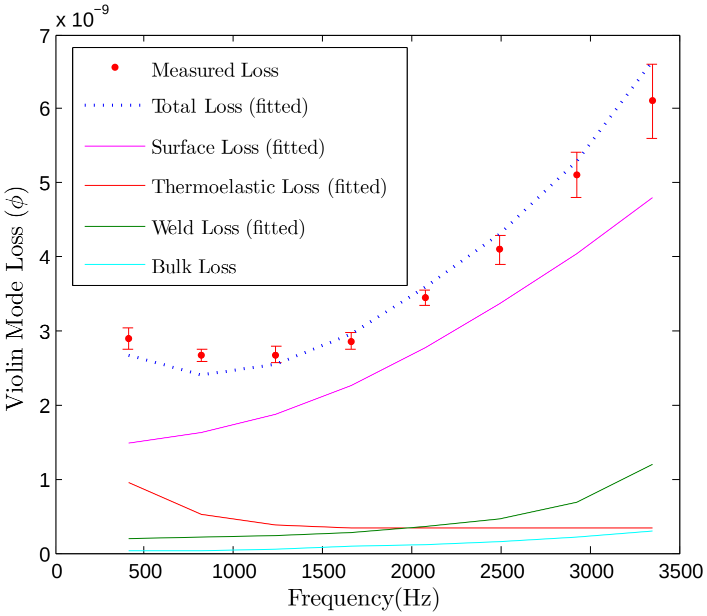

(b)

Figure 4.21: *Plots showing how the calculated MCMC results fit with the actual measured losses of cantilever modes (a) and violin modes (b).*

scales it is best to evaluate both data fits separately. By evaluating both fits separately the fitting tests are not bias or in favor of figure 4.21a. The adjusted R^2 and norm of residual values for figure 4.21a is 0.98 and 1.2×10^{-7}. For figure 4.21b the adjusted R^2 and norm of residual values are 0.99 and 7.4×10^{-10}. This gives us confidence that the model and values determined by the MCMC code are accurate.

The value of α determined here of $(4.3 \pm 0.2) \times 10^{-7}\,\mathrm{K}^{-1}$ is consistent with the values of α found in chapter 3 where this value was seen to vary between 3.5×10^{-7} and $4.7\times10^{-7}\mathrm{K}^{-1}$ it also agrees with values found in literature where α is seen to take on values between 3×10^{-7} and $5.9\times10^{-7}\mathrm{K}^{-1}$ [132, 135, 155, 156]. The values found in this chapter for $h\phi_{\mathrm{s}} = (2.89 \pm 0.07) \times 10^{-12}\,\mathrm{m}$ and $\phi_{\mathrm{weld}} = (2.4 \pm 0.5) \times 10^{-7}$ are lower than currently expected loss values seen in [135, 139, 141]. In these papers $h\phi_{\mathrm{s}}$ and ϕ_{weld} was determined to be $\sim 6.15 \times 10^{-12}\,\mathrm{m}$ and $\sim (5.7 \pm 2.5) \times 10^{-7}$ respectively. Values as high as 1.8×10^{-6} were also measured for the weld loss but this was attributed as coming from imperfections in the weld region shown in figure 4.23. The lower losses measured here are likely to be due to improved fibre manufacture techniques such as fibre polishing and CO_2 laser welding with a hoover to remove any silica deposition. $h\phi_{\mathrm{s}}$ actually agrees very well with more recent values being published for polished fused silica fibres where $h\phi_{\mathrm{s}}$ has been measured directly as being $3.4 \times 10^{-12}\,\mathrm{m}$ [142]. As the fibre studied here was polished before being pulled this is not surprising. The weld that was made here was very clean and showed no clear roughness or deformation between the stock of the fibre and the horn it was welded to as shown in figure 4.22. It is likely that the fact that there was no imperfections in the weld region has led to this lower weld loss being measured when compared to Heptonstall's welds [135] which are shown in figure 4.23 and displayed signs of imperfection.

Another interesting observation is that the first three violin mode losses measured at the lowest frequencies show a minimum turning point in the loss

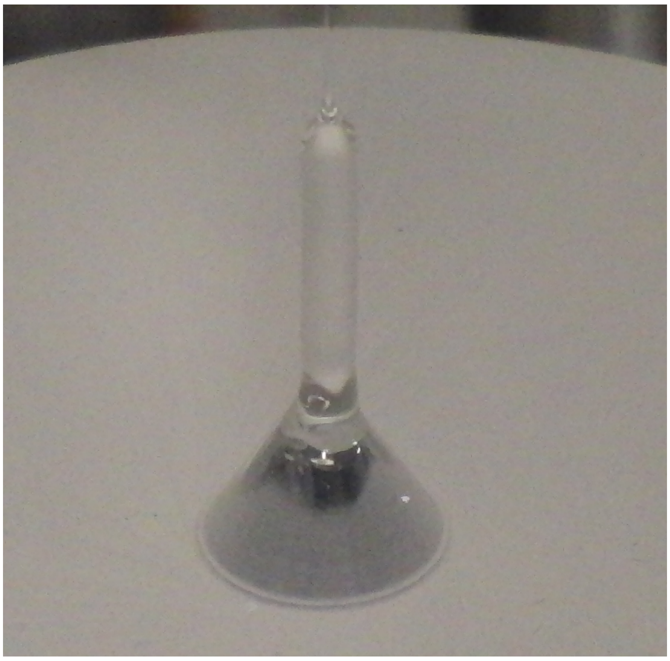

Figure 4.22: *Picture showing the low loss weld that was made between the silica horn and the stock of the fibre.*

which has never been measured before in violin modes. This comes from the thermoelastic loss term decreasing with increasing frequency and forming the left side of the minimum. On the right side of the minimum the loss is increasing this is because surface loss is now the dominant loss mechanism and the dilution value is decreasing as the violin mode number increases. The combination of these two effects alone is not enough to explain such a low violin mode thermoelastic loss term loss. This is the first evidence that in fact nonlinear thermoelastic loss [134] is at work in a silica suspension systems. Figure 4.24 shows the losses we would have measured if there was no reduction of thermoelastic loss through stress e.g. $\beta = 0$ and the α, $h\phi_{\mathrm{s}}$, ϕ_{weld} and C_{bulk} have kept the same values as above. The adjusted R^2 and norm of residual values to the fit shown in figure 4.24 are 0.61 and 1.8×10^{-9} and so when compared with the fit from figure 4.21b this is a poorer fit, and it suggests that the thermoelastic loss does indeed behave in a nonlinear way as described

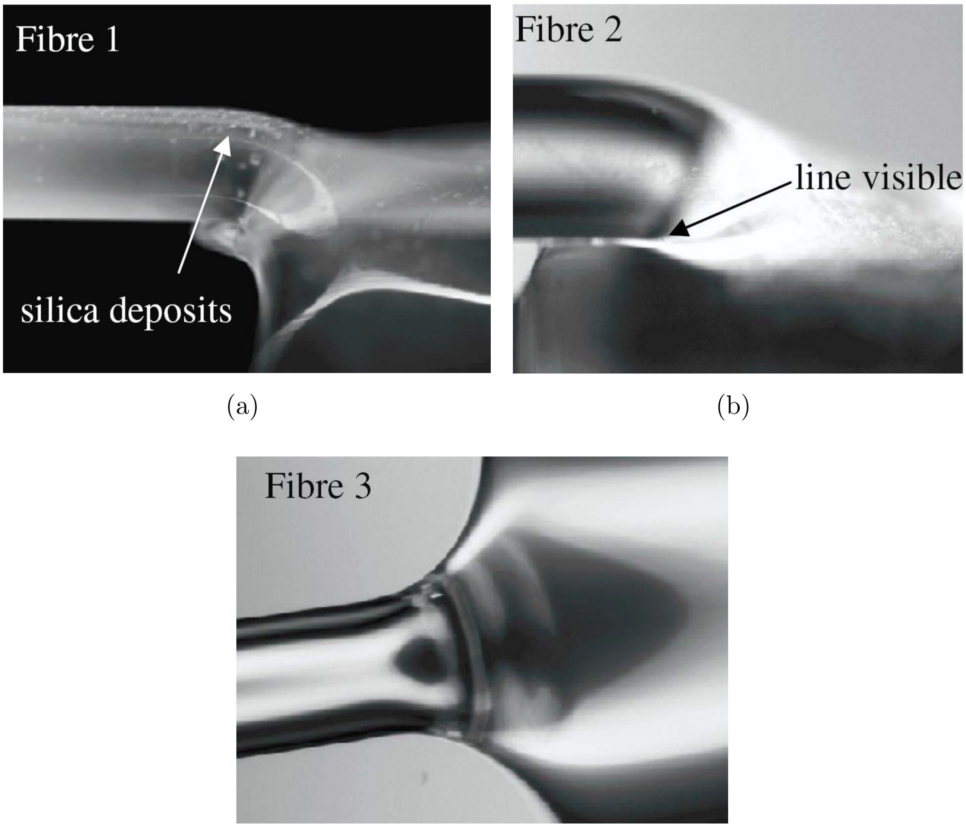

(a) (b)

(c)

Figure 4.23: *Microscope images of three different fibre* CO_2 *laser welds studied by A. Heptonstall et al [135]. Fibre 1 (a) shows traces of silica vapour deposits on surface, fibre 2 (b) shows a line along welded interface, and fibre 3 (c) shows no obvious weld defects.*

by equation 2.34 [134].

4.7 Conclusions

The results from this chapter display great promise for the suspension sensitivity of aLIGO. It has been shown conclusively that the suspension loss values of $h\phi_{\mathrm{s}}$ and ϕ_{weld} can be made lower than the previously measured values [135, 139, 141]. In taking the values measured in this chapter and plotting the suspension sensitivity for aLIGO we can see that the total suspension

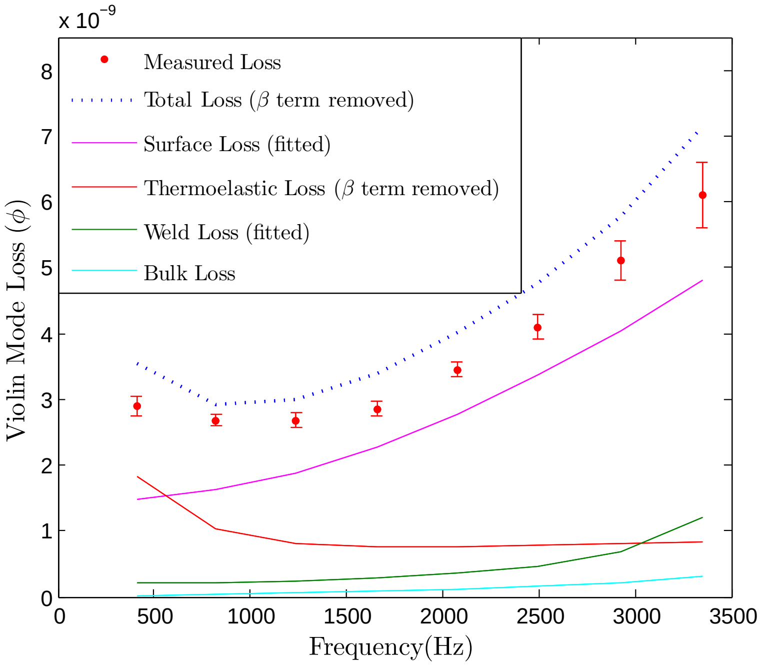

Figure 4.24: *Plot showing the measured losses and the violin mode losses we would see if there was no nonlinear thermoelastic loss cancellation.*

thermal noise of aLIGO has decreased from $\approx 9.7 \times 10^{-20}\,\mathrm{m}/\sqrt{\mathrm{Hz}}$ to as low as $\approx 7.1 \times 10^{-20}\,\mathrm{m}/\sqrt{\mathrm{Hz}}$ at 10 Hz. The improvement is shown in figure 4.25 Even more encouraging is the fact that the welding and fibre manufacturing procedure used here does not deviate from that already planned for use in aLIGO meaning that no change is needed to to the current installation procedures [11–14] in order to attain this low thermal noise and hence increased sensitivity curve.

4.8 Future Work

The measurements made in this chapter show that potentially the thermal noise of the aLIGO suspension system can easily beat the target design sensitivity noise level of $1 \times 10^{-19}\,\mathrm{m}/\sqrt{\mathrm{Hz}}$ at 10 Hz. In chapter 3 it was shown that the thermoelastic loss can also potentially be suppressed if the correct amount of stress is applied to the fused silica suspension fibres. As 10 Hz is a low fre-

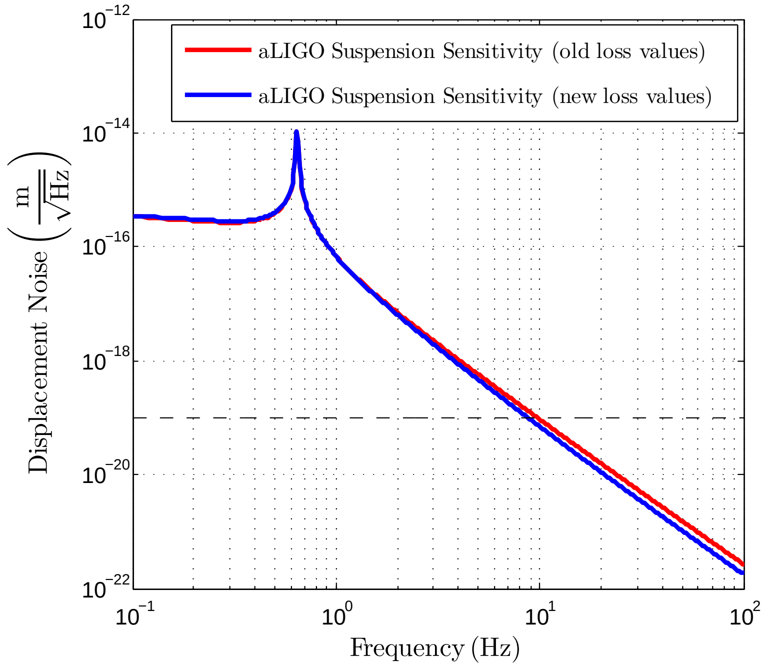

Figure 4.25: *Plot showing the how the results from this chapter can increase the suspension sensitivity of aLIGO.*

quency it is very close to the Debye peak of the thermoelastic loss. This means that we cannot simply rely on the loss values determined in this chapter if we are to make an accurate and robust estimates of the total suspension thermal noise. For that reason chapter 5 focusses on showing that the nonlinear thermoelastic loss does indeed occur in loaded fused silica suspensions. We do this by measuring the cancellation of thermoelastic loss directly via the mechanical loss as opposed to measuring the effective thermal expansion coefficient which was done in chapter 3.

Chapter 5

Measuring Thermoelastic Cancellation in Violin Modes

5.1 Introduction

In chapter 3 it was proven experimentally for the first time that the effective thermal expansion coefficient for a fused silica fibre can be nulled when the correct amount of static stress is applied to the fibre. Chapter 4 provided the first evidence of this nulling being visible through direct measurement of the mechanical loss. This chapter looks at the mechanical loss of fused silica and aims to measure the thermoelastic cancellation directly. This will be done by monitoring the changes in mechanical loss when a fused silica fibre has its resonant fundamental violin mode excited and is placed under varying amounts of static stress.

5.2 Experimental Set-up

To study the thermoelastic loss in more detail it was decided to create a system that would allow us to vary the stress on a silica fibre so as to see the thermoelastic loss being nulled for the correct amount of stress. This is very challenging however, as when a thin 250μm diameter silica fibre like the one used in chapter 4 is placed under tension from a 400 g mass (just 80 MPa of stress) the resonant violin modes resonate at frequencies $\geq$400 Hz. As a result the thermoelastic loss contribution of the mechanical loss falls off rapidly with increasing frequency, as demonstrated in figures 2.6 and 4.21. A second problem is that the thermoelastic loss cancellation is expected to occur at a stress of around 195 MPa, as discussed in chapter 3. So in order for the thermoelastic loss to be the most dominant loss contribution, and hence to allow us to be sensitive to the effects of stress variation, the resonant fundamental violin mode of the system must be reduced. We must be as close to the Debye peak frequency of thermoelastic loss as possible, which for a 250μm diameter silica fibre is at $\sim$22 Hz. In order to achieve the low frequency resonant violin mode required, a silica fibre was fabricated which had a thick 3 mm diameter section in the middle of two 250 μm diameter sections. This fibre was fabricated with a CO_2 laser based pulling machine [129] using the following method. Firstly, 3 mm stock was used and a 15 cm length of this stock was polished [142, 143]. The laser was then positioned 3 cm lower than the top of the polished section and a uniform 250μm section of fibre was 'pulled' to be roughly 9 cm long. The laser was then repositioned 9 cm lower so as to leave a 9 cm long 3 mm diameter polished stock region. From this position an identical 'pulling' procedure was used to give a uniform 250μm section the same length as before. A profile of the fibre which was used, and its connection to the isolation mass and lower silica mass from chapter 4 is shown in figure 5.1.

One of the challenges faced is how to increase the stress on the silica without external loss mechanisms affecting the results. It was decided that the best way to increase the stress was to hang steel masses from a fused silica fibre which was flame welded to a ground pin on the lower silica mass. The first metal mass had a silica horn super glued on to the top of it and the stress was varied by bolting on additional masses. The set-up used for the experiment is shown in figure 5.2 and the construction of the metal masses are shown in figure 5.3. After the violin modes were taken the silica fibre was cut and cantilever modes

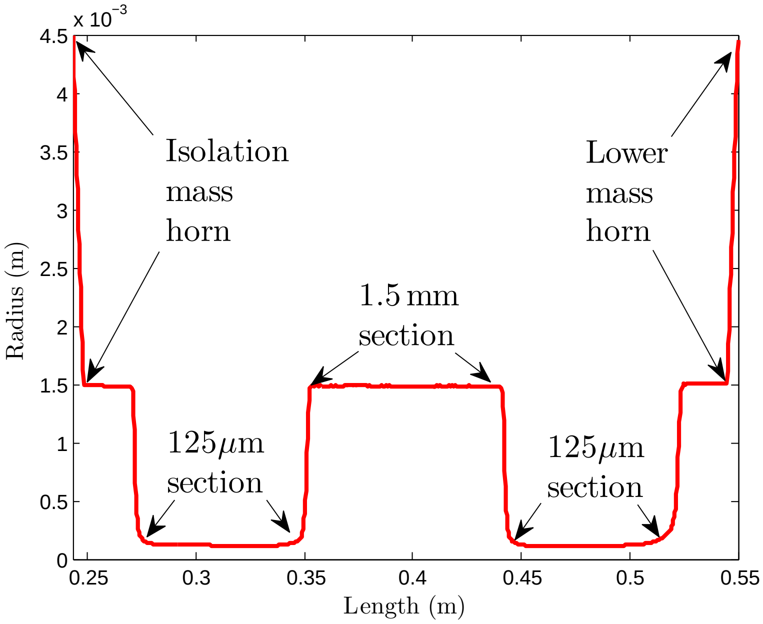

Figure 5.1: *Profile of specially created thick middle fibre which produces a lower frequency fundamental violin modes.*

were measured as was done in chapter 4. Due to the thick middle section of the fibre two sets of cantilever modes were measured with the two different cantilever mode arrangements shown in figure 5.4.

The system was constructed and welded as described in section 4.4 using a CO_2 laser. However, the lower steel masses were flame welded onto the lowest stage isolation fibre. To vary the stress on the suspension steel masses could be added or removed from the lowest stage isolation fibre. Adding or removing these masses was very awkward to do inside the vacuum system, and for this reason the lower stage masses were cut free and re-welded on to the system after each mass was added or removed. This reduced the risk of breaking the ground silica pin or worse, damaging the silica fibre on which modes are being excited.

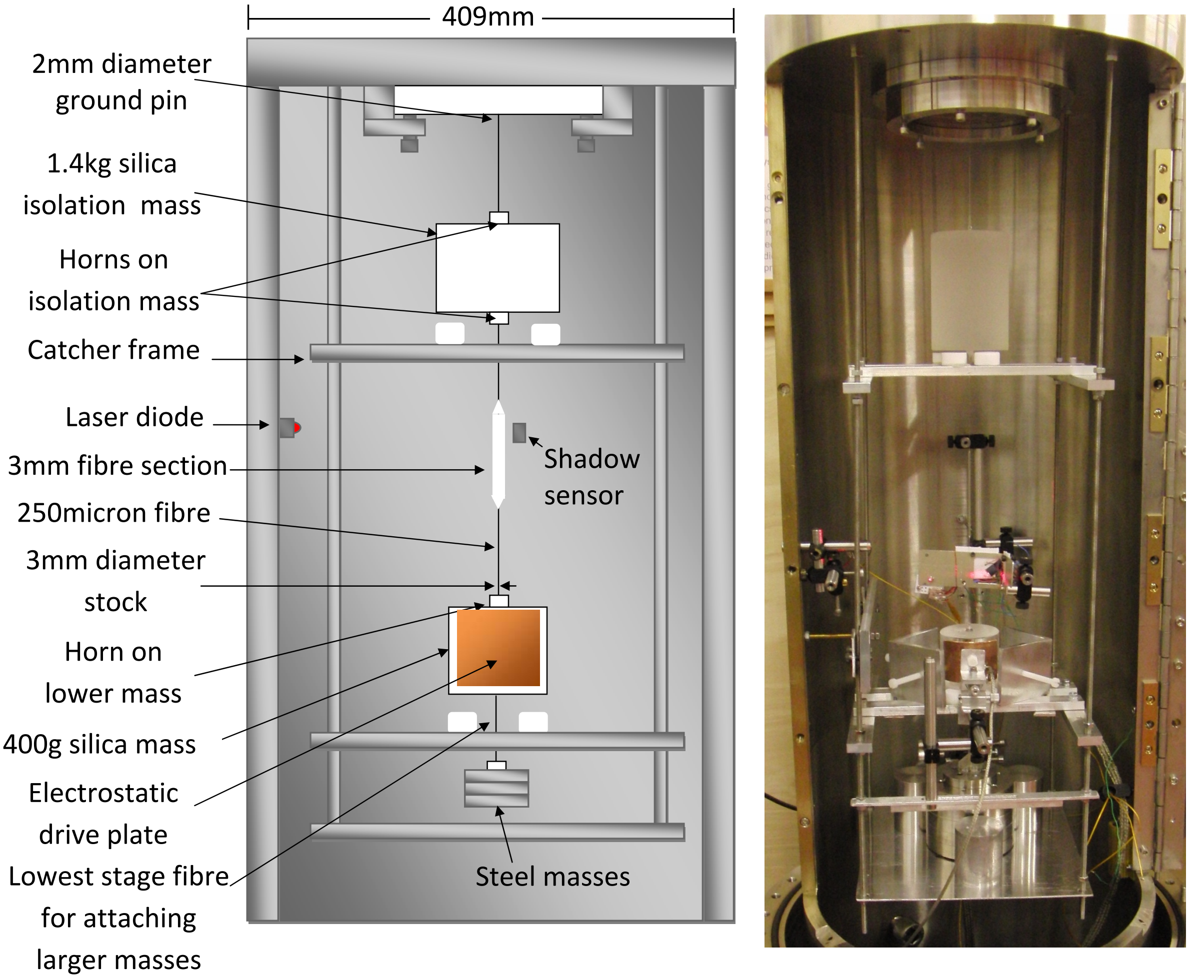

(a) (b)

Figure 5.2: *A schematic drawing (a) and picture (b) of the set-up used for measuring low frequency violin modes.*

5.3 Measurements of the Low Frequency Violin Mode Q Values

Figure 5.5 shows the profiled suspension model which was compiled and imported into ANSYS. It can be seen from figure 5.5 that for the fundamental violin mode of this fibre geometry, it is the thick 3 mm section which is displaced the most and so it was decided later that in order to measure these modes effectively the laser and sensing diodes should be positioned so as to

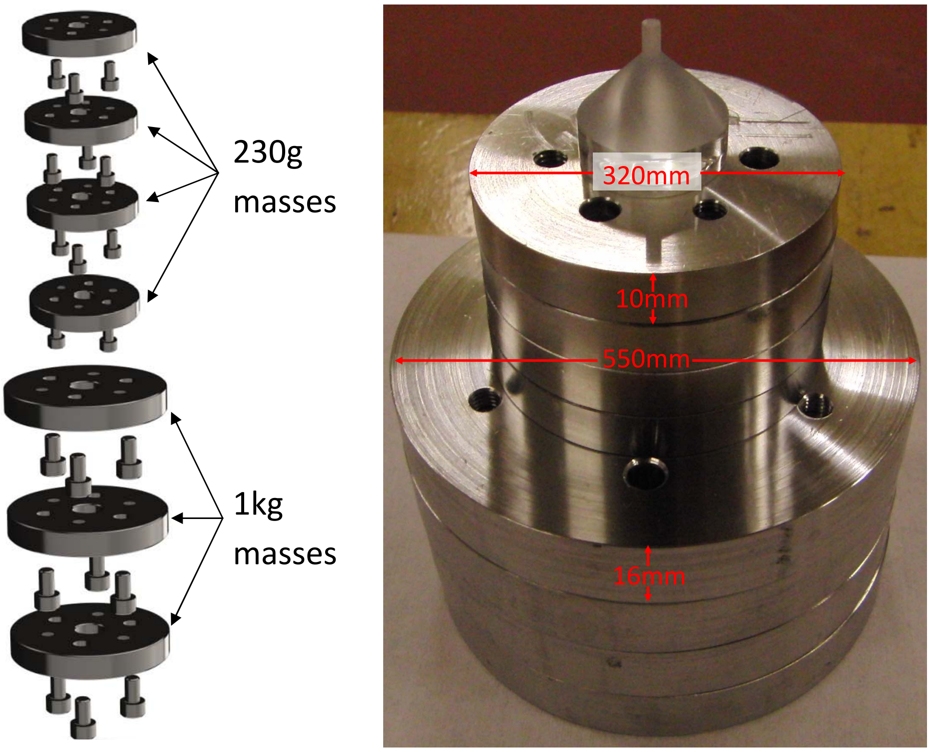

Figure 5.3: *Left: Schematic of the steel masses used to increase the stress on the silica fibre. Right: Picture of the steel masses used to increase the stress on the silica fibre with a silica horn glued on top.*

monitor the displacement of the thick middle section. Initial measurements were carried out trying to monitor the movements of the thin section, however this data was very noisy and it was very difficult to determine the level of loss. The reason for this excess and varying noise coming from the photodiode sensor was not clear but a test was carried out to determine if the noise was caused by the fibre or if the laser/sensing diodes were at fault. We concluded that the excess noise was related to the fibre as, when the laser was not directed at the fibre, the dc noise level from the diodes remained constant. It is possible that this noise arises from a combination of light scattering as illustrated by figure 5.6 and mode coupling of the fibre as discussed later in section 5.5.1. The method used here to observing ring downs is the same as the method used in chapter 4 which did not display the same noise problems. This suggests

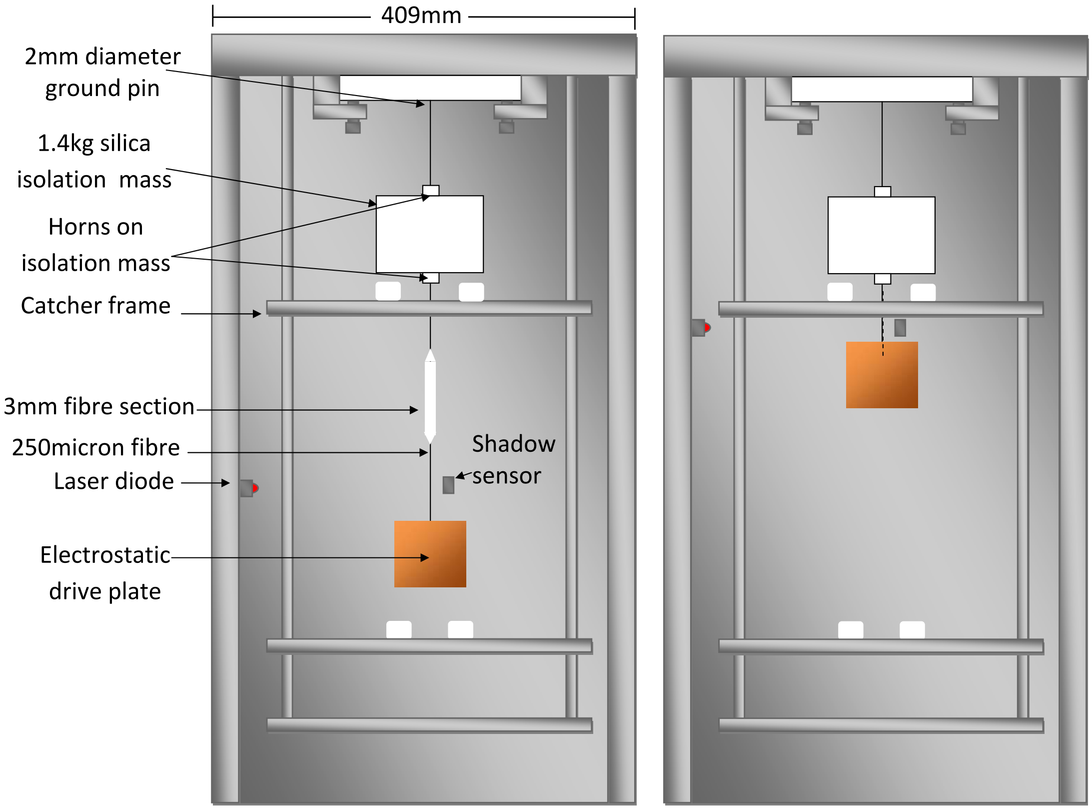

(a) (b)

Figure 5.4: *Set-ups for measuring ring downs of the first (a) and second (b) set of cantilever modes.*

that this excess noise must be related in some way to the thick middle section or to the lower stage metal masses being used.

When the shadow sensor and laser were repositioned to look at the middle thick section of the fibre excess noise was reduced and a correlation could be seen between the ring down of the violin modes and the DC noise level from the diode sensor as shown in figure 5.7. To remove the noise from the ring down measurement the mean value of the dc noise was subtracted from the measured noise to give a 'noise amplitude'. This amplitude was then correlated with the fluctuations in the ring down and subtracted to give the clean ring down measurement as shown in figure 5.7.

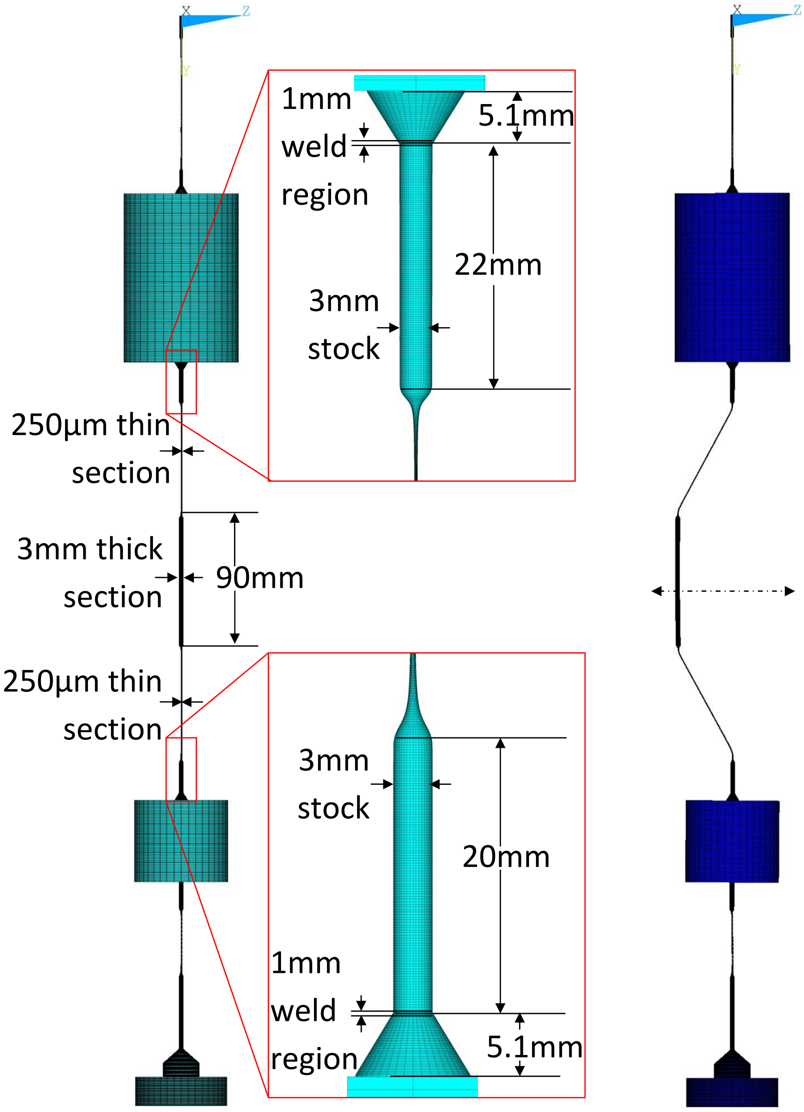

Figure 5.5: *Left: Profiles of silica suspension compiled and imported to ANSYS. Right: A picture of the fundamental violin mode shape produced in ANSYS.*

5.4 Dilution of Thick Middle Fibres

As the thick middle fibre shown in figures 5.1 and 5.5 has a unique shape and mode profile, more work on dilution was carried out to ensure that the system was being modeled correctly. Dilution was discussed earlier in section 2.4.3. In that section it was shown that the dilution can be calculated from ANSYS using a ratio of the kinetic energy to that of the strain energy of the system as

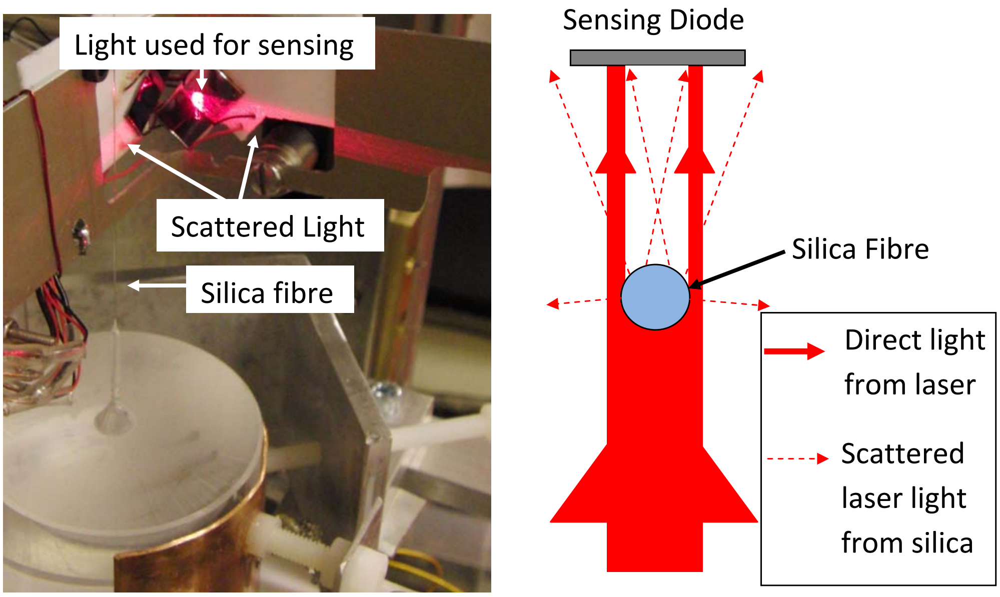

Figure 5.6: *Left: Photo of the laser light being scattered off the silica fibre. Right: A schematic of how the light is being scattered via reflection and refraction.*

described by equation 2.29. It was not immediately obvious that this equation would still hold when considering the new fibre geometry. To test that the equation was still valid for a thick middle fibre oscillation a thick middle fibre model was built in ANSYS supporting a 400g mass. The value of dilution calculated from equation 2.29 was compared to equation 5.1 derived by Barton [120] where the dilution is calculated directly from the ratio of longitudinal energy to that of the bending energy stored in the fibre. This can be simplified to the following expression

$$\mathrm{D} = \frac{\text{Longitudinal Energy}}{\text{Bending Energy}} = \frac{4\sum_{i=1}^{n}(dy/dx)^2dx}{\pi\sum_{i=1}^{n}r^4(d^2y/dx^2)^2dx}. \tag{5.1}$$

In this equation y is the displacement of each element $1...n$ of the fibre, x is the length of each element in the fibre and r is the radius of the fibre section being studied. A plot of the fibre profile used for this test, as well as the displacement, the strain energy and the kinetic energy distributions predicted by ANSYS are shown in figure 5.8. Both equation 2.29 and 5.1 predicted a

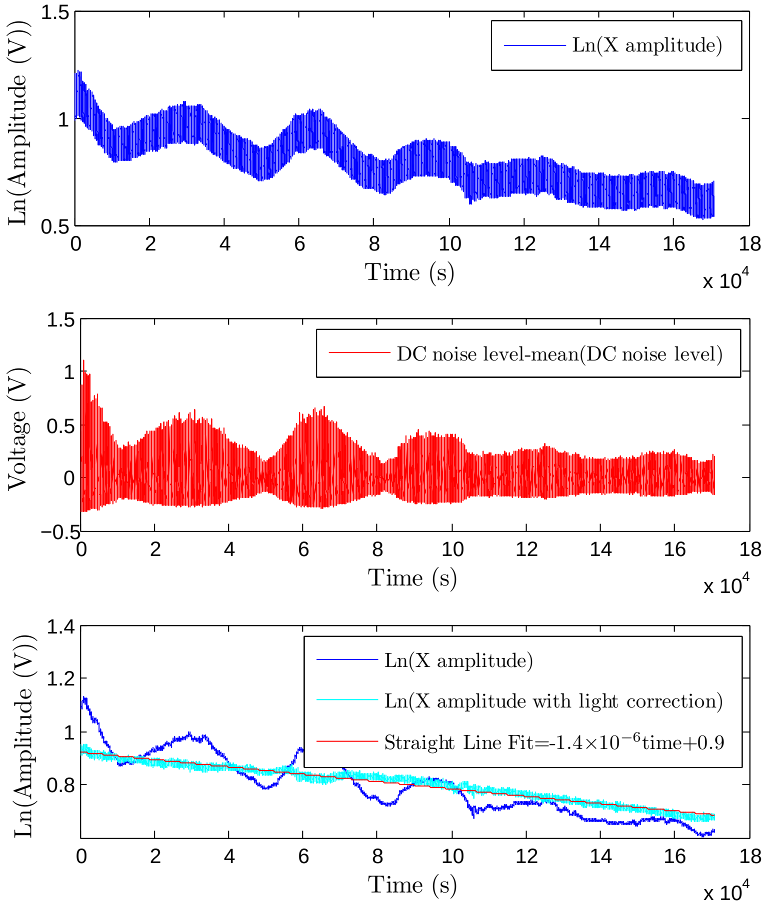

Figure 5.7: *Top: Plot showing the noisy ring down measurement made. Middle: Plot showing that the noise from the sensor was correlated with the ring down noise. Bottom: Plot showing how the correlated noise from the diode could be filtered away from the ring down measurement.*

dilution value of ∼20 showing that taking the ratio of strain and potential energies is an acceptable way to calculate dilution for this shape of fibre mode.

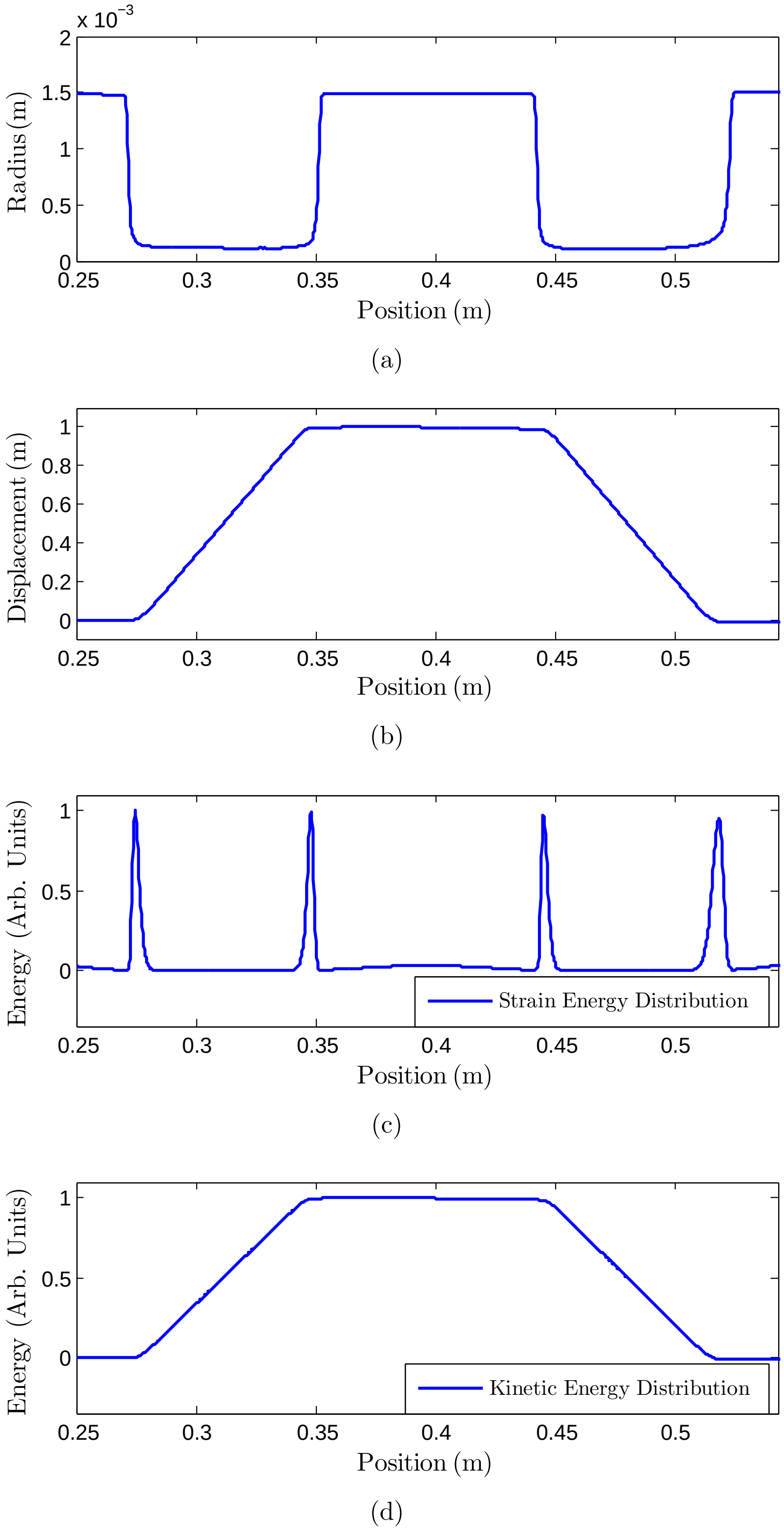

(a)

(b)

(c)

(d)

Figure 5.8: *Plots showing how the fibre displacements and energy ratios were compared to ensure dilution from ANSYS was being calculated correctly for a thick middle fibre. Plot (a) shows the fibre profile used to test the dilution calculations, (b) shows the displacement of elements in ANSYS, and (c,d) show the strain energy and kinetic energy distribution respectively calculated from ANSYS.*

The measured values of the fundamental violin mode frequencies along with the predicted frequencies and dilution values returned from ANSYS are listed in table 5.1. From table 5.1 we can see that as more mass is added to the system the dilution values for the violin modes only increase very slightly and for the highest mass case, the dilution actually decreases. This is because more of the strain energy is being driven into the thicker 3 mm stock regions of the fibre which has a larger second area moment and so this begins to decrease the dilution values as described by equation 2.27. Naively it might have been expected that the dilution factor would increase proportionally as the square root of the tension on the fibre as described by equation 2.27. A plot showing how the strain distribution in the fibre varies with the stress on the fibre is shown in figure 5.9. In itself, this is an interesting result as future upgrades being considered for aLIGO involve using larger test masses to effectively increase the dilution value and make the detectors more sensitive. As an interesting comparison the same fibre was modeled in ANSYS but the

FUNDAMENTAL VIOLIN MODE				
Mass supported (g)	Measured (Hz)	ANSYS (Hz)	Dilution	Measured Loss
400	44.6	46	20.9	2.24×10^{-8}
630*	56.3	58	21.9	1.00×10^{-6}
730*	60.8	62.5	22.3	7.78×10^{-8}
860	65.5	67	22.5	1.09×10^{-8}
1090	73.3	74	22.7	1.07×10^{-8}
1320	80.3	82	22.6	7.27×10^{-9}
1630	88.0	89	22.9	3.19×10^{-9}
1860	93.8	95	21.9	4.04×10^{-9}

* Results with abnormally high loss values thought to be dissipating energy through a resonant structural mode.

Table 5.1: *Comparison of ANSYS predicted resonant frequencies and the system frequencies that were measured. The dissipation dilution values are calculated from ANSYS as described in section 2.4.3 are also listed.*

thick middle section was replaced to make the fibre have a uniform cross section along its length. The fundamental violin modes were then modeled for the uniform fibre supporting a 400g and then a 1860g mass. The dilution values returned from these fibre models were 32 and 39 respectively. This is very important as it shows that if we increase the tension on the silica fibres by a factor of 4 we do not simply double the dilution, instead care must be taken to analyse the strain distribution for each mass case. This will be very important when considering future upgrades to suspension systems for gravitational wave detectors. The measured values of the cantilever mode frequencies along with the predicted frequencies from ANSYS are listed in tables 5.2 and 5.3.

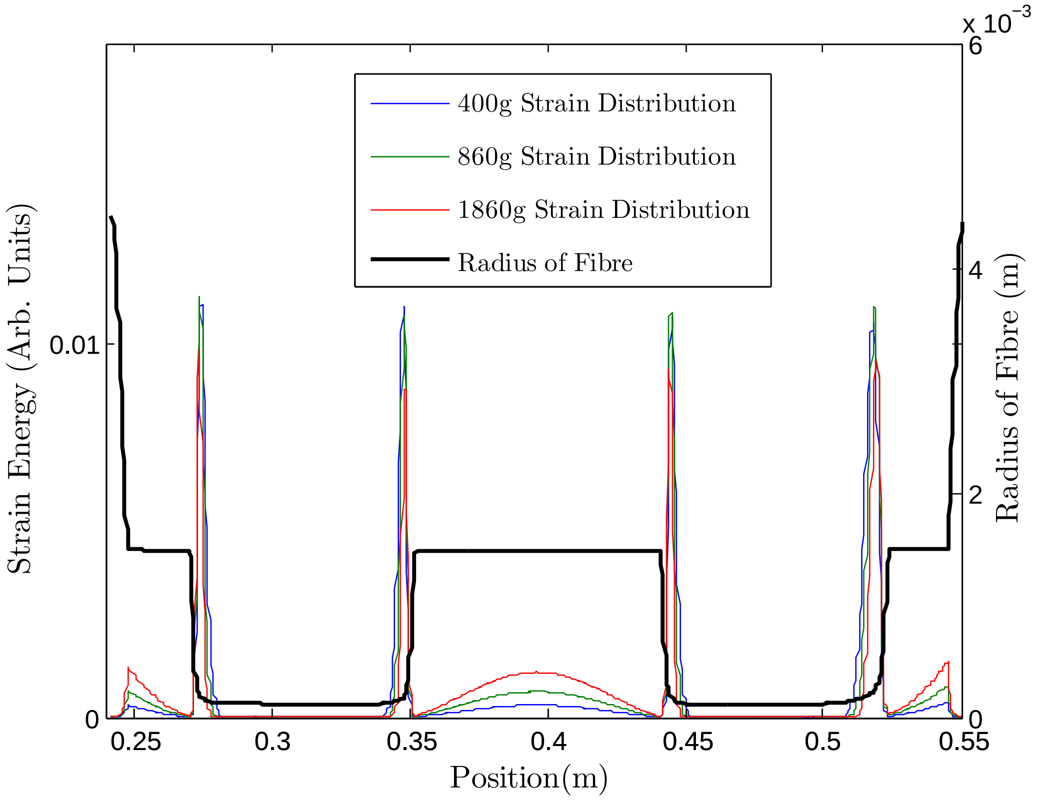

Figure 5.9: *A plot showing how the strain distribution of the fundamental violin mode varies as the fibre is made to support different amounts of mass. The plot shows that for larger masses less energy is stored in the thin region of the fibre and more is placed in the 3 mm diameter sections.*

CANTILEVER MODES	
Measured (Hz)	ANSYS (Hz)
1.59	1.60
11.6	11.4
26.3	25.5
207	200
623	600
1254	1204
2088	2008
3121	3001

Table 5.2: *Comparison of ANSYS predicted resonant frequencies and the system frequencies that were measured for the cantilever modes studied using the set-up shown in figure 5.4a.*

CANTILEVER MODES	
Measured (Hz)	ANSYS (Hz)
34.3*	37.4
211	218
605	614
1195	1206
1992	1999
2996	2995

* Results with abnormally high loss values thought to be dissipating energy through a resonant structural mode.

Table 5.3: *Comparison of ANSYS predicted resonant frequencies and the system frequencies that were measured for the cantilever modes studied using the set-up shown in figure 5.4b.*

5.5 Results

The data was gathered from all of the resonant modes and analysed using the MCMC regression fitting code as detailed in section 4.6.1. In this chapter the main loss terms which are important and dominate the losses measured are thermoelastic loss and surface loss. All of the other terms such as weld and bulk loss are negligible and contribute <3% to the total losses measured, for this reason these loss contributions were assigned the same values as those determined in chapter 4.

A global fit to all of the data (violin modes and cantilever modes combined) did not return a well accepted result as the α and $h\phi_s$ agreed well with the results in chapter 4 but a negative β value was returned which conflicts with the results seen in chapter 3. To find out why this negative β value was being returned the data had to be analysed in parts. Firstly only the data from the modes measured using the set-up shown in figure 5.4a was analysed. The regression fit to this data determined the value of α to be $(3.5\pm0.3)\times10^{-7}\,\mathrm{K}^{-1}$ and the value of $h\phi_\mathrm{s}$ to be $(4.7\pm0.4)\times10^{-12}\,\mathrm{m}$. The second step involved analysing just the data gathered from the set-up shown in figure 5.4b. It was decided to exclude the data which had abnormally high losses marked in table 5.1 and 5.3, as it would require fitted loss parameters which are outside realistic boundaries. It was deduced that, due to the high loss modes having a sharp increase in loss constrained to a specific frequency bandwidth, that it was an effect of strain energy being transferred to a resonant structural mode, this is discussed later in section 5.5.1. The value of α was found to be $(3.7\pm0.2)\times10^{-7}\,\mathrm{K}^{-1}$ and the value of $h\phi_\mathrm{s}$ to be $(3.0\pm0.2)\times10^{-12}\,\mathrm{m}$. All of these values are within expected limits [132, 135, 139, 141, 142, 155, 156] and agree with values determined in chapters 3 and 4. They also provide a good fit to the data gathered as shown in figure 5.10a where the norm of residuals value is 6×10^{-8} and the adjusted R^2 value is 0.99. Figure 5.10b also shows a good fit to the data where the norm of residuals value is 6×10^{-8} and the adjusted R^2 value is 0.92.

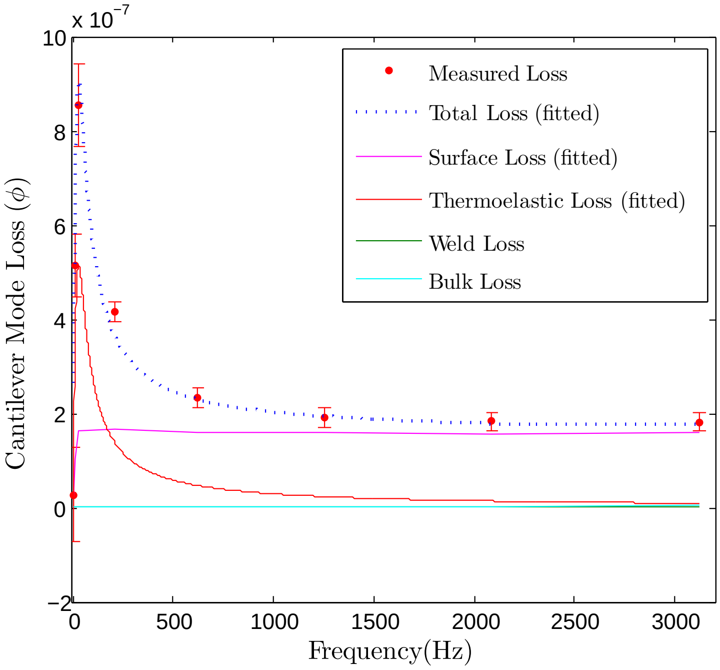

(a) *Measurements from the set-up shown in figure 5.4a and modes listed in table 5.2 with the loss contributions from the MCMC regression also plotted.*

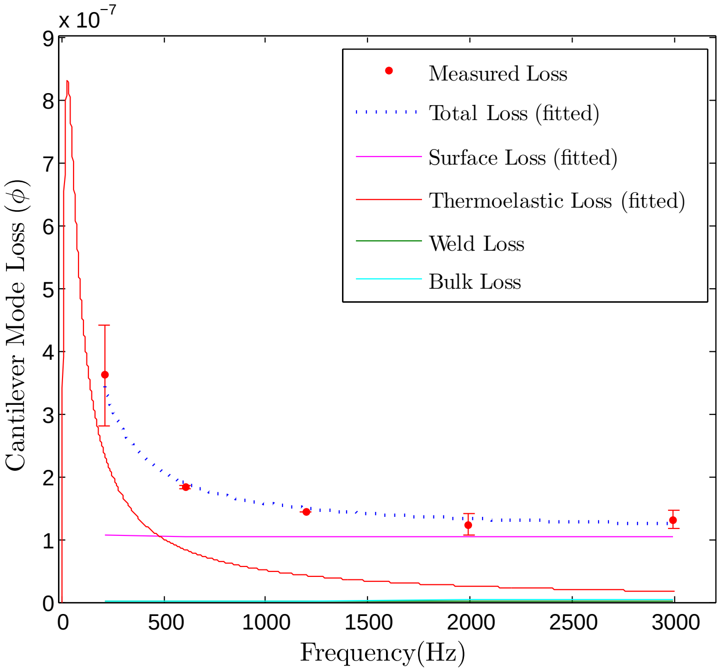

(b) *Measurements from the set-up shown in figure 5.4b and modes listed in table 5.3 with the loss contributions from the MCMC regression also plotted.*

Figure 5.10: *Plots showing how the calculated MCMC results fit with the actual measured cantilever mode losses. (a) Details measurements from the set-up shown in figure 5.4a and modes listed in table 5.2 with the loss contributions from the MCMC regression also plotted. (b) Shows measurements from the set-up shown in figure 5.4b and modes listed in table 5.3 with the loss contributions from the MCMC regression also plotted.*

From the data shown in figure 5.10 the average values of α and $h\phi_{\mathrm{s}}$ for the fibre can be fixed as $(3.6\pm0.3)\times10^{-7}\,\mathrm{K}^{-1}$ and $(3.9\pm0.9)\times10^{-12}\,\mathrm{m}$. The values were then substituted into the MCMC code loss calculation and used to model the losses measured for the fundamental violin modes from the set-up shown in figure 5.2 and listed in table 5.1. As these violin modes are excited and decay under varying levels of stress the MCMC code was used to determine the thermoelastic loss contribution for each of the violin modes and hence obtain the value of β which is discussed in section 2.4.4. The value of β which was returned from the MCMC fit to the data in figure 5.11a was given as $(-1.6\pm1.4)\times10^{-5}\,\mathrm{K}^{-1}$. This fit returned a norm of residuals value of 1.2×10^{-8} and an adjusted R^2 value of 0.64.

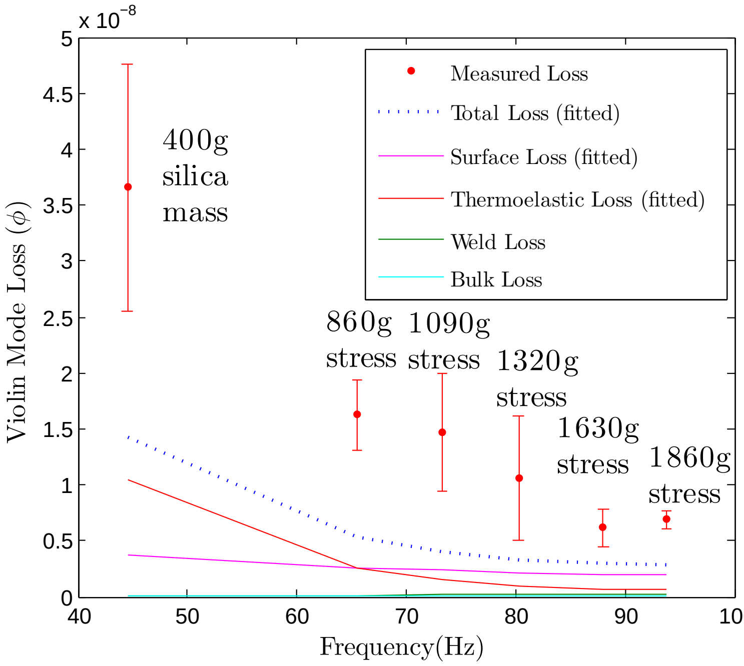

(a)

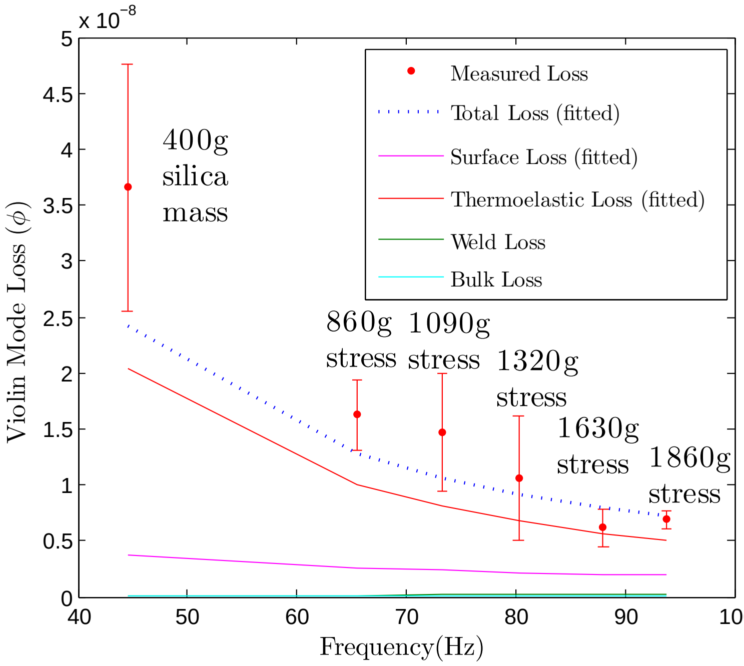

(b)

Figure 5.11: *Plots showing how the violin mode losses measured correlate with both the MCMC regression fitted losses (a) and the expected losses that were anticipated (b). (a) Details measurements from the set-up shown in figure 5.2 and modes listed in table 5.1 with the loss contributions determined from the MCMC regression also plotted. (b) Shows the losses that were expected assuming* $\beta \approx (1.58 \pm 0.09) \times 10^{-4} K^{-1}$ *plotted instead of the fitted* β *value.*

While the fit shown in figure 5.11a is reasonably good, the value of β for a fused silica fibre was proven in chapter 3 and 4 to be a positive value $\approx (1.58 \pm 0.09) \times 10^{-4}\mathrm{K}^{-1}$ which makes the negative β value measured surprising. For comparison figure 5.11b shows the results which were expected if β had the same value as measured in chapter 3 of $\sim (1.58 \pm 0.09) \times 10^{-4}\mathrm{K}^{-1}$. This fit returned a norm of residuals value of 2.8×10^{-8} and an adjusted R^2 value of -0.80. The data then does not agree with a modeled loss when the value of β is assumed to be $(1.58 \pm 0.09) \times 10^{-4}\mathrm{K}^{-1}$. From figure 5.11b it can be clearly seen that the most likely reason for this poor fit is that the violin mode losses measured are too large to be attributed to purely the fundamental violin mode of fused silica. It is possible that these high losses are due to excess damping from some kind of mechanism that has not been accounted for, this could also explain why the violin modes as shown in figure 5.11 had such a large error in determining their loss values.

The losses being measured for the violin modes should be around the order of 10^{-9} and so even a small amount of excess loss is enough to drastically effect the violin mode Q value. Gas damping was ruled out as a possible loss mechanism as it would only limit the measured loss by $\sim 2.5 \times 10^{-10}$ as calculated by equation 4.1. Gas damping is also discussed later in section 6.4.2.

5.5.1 Mode Coupling Loss

Mode coupling was considered in section 4.5 where it was demonstrated that when a violin mode or cantilever mode decayed it was capable of coupling energy into an orthogonal modes of a similar frequency. The energy coupling between orthogonal modes did not effect the losses measured mainly because the loss of the orthogonal mode loss matched that of the originally excited mode. Thus the energy was just transferred back and forth between the modes [161] decaying at a constant rate as illustrated by figures 4.15b and 4.16. It is possible that if energy is being coupled to another mode with a higher loss this could explain the losses measured in this experiment. The resonant modes of the vacuum tank were predicted using FEA to see if there were any modes present that energy could couple into. This analysis was carried out previously by A. Heptonstall [128], where it was shown that the lowest resonant mode of the vacuum tank was 126 Hz which is well separated from the system frequencies which are being measured in this case. Thus the coupling of violin modes with resonant tank modes is unlikely to be the reason for the high losses observed.

What is interesting is that when measuring the decay of the violin modes for the modes at 56.3 and 60.8 Hz exceptionally high losses were measured. The mode at 56.3 Hz had a loss two orders of magnitude higher than was expected if all of the energy had been dissipated by the fundamental violin mode. Further analysis with FEA in ANSYS showed that a vertical bounce mode of the suspension resided at ∼54 Hz. One explanation for the high losses measured is that energy from the low loss violin mode was coupling in to the higher loss bounce mode and dissipating energy at a higher rate. The vertical bounce mode loss, $\phi_{\text{bounce loss}}$, is made up from a contribution of surface loss, $\phi_{\text{surface bounce}}$, and bulk loss, $\phi_{\text{bulk}}(\omega)$. The surface loss contributes a factor of 2 more for bounce modes than it does for the bending modes [163]. This is because it is now the entire circumference of the fibre which is contributing to the loss of a bounce mode as oppose to the bending modes when there is only contributions from the inside and outside surface of the bending region. Therefore the surface loss of a bounce mode can be written as:

$$\phi_{\text{surface bounce}} = 2 \times \phi_{\text{surface bending}}. \tag{5.2}$$

As the fibre does not bend during a vertical mode oscillation there are no thermal gradients set-up which would have contributed to thermoelastic loss [128, 163] and hence we can neglect thermoelastic loss for bounce modes. It is possible that even more energy is being dissipated through clamping loss[2], ϕ_{clamp}, where the top silica plate is connected to the metal structure or at the connection between each of the metal masses of such that

$$\begin{aligned}\phi_{\text{bounce loss}} &= \phi_{\text{surface bounce}} + \phi_{\text{bulk}}(\omega) + \phi_{\text{clamp}} \\ &\approx 1.17 \times 10^{-7} \qquad \text{for } \phi_{\text{clamp}} \to 0.\end{aligned} \tag{5.3}$$

It is clear from the results shown in figure 5.10 that as the violin mode frequencies being studied diverge from the vertical bounce mode frequency the loss measured decreases and converges towards the values that were expected to be measured. The loss through frequency dependant mode couplings for high mechanical Q systems can be described by equation 5.4

$$\phi_{\text{bounce-coupling}} = C_c(f)\phi_{\text{bounce loss}}. \tag{5.4}$$

In this equation $C_c(\omega)$ is a Lorentzian function which describes how much energy is transferred from the violin mode to the bounce mode such that

$$\phi_{\text{bounce-coupling}} = \frac{C_1\phi_{\text{bounce loss}}}{(f_{\text{b}} - f)^2 + C_2}, \tag{5.5}$$

where C_1 and C_2 are constant values, f_{b} is the frequency of the resonant bounce mode and f is the violin mode frequency from which energy is being extracted. Figure 5.12 shows how the residuals between the losses measured and the expected losses vary as a function of frequency. The blue line shows an attempted fit to this data using equation 5.5. This fit is not accurate due to the small amount of data but it illustrates how coupling energy into the vertical bounce mode has potentially limited our ability to observe the thermoelastic loss cancellation directly. The inferred loss mechanism is puzzling as it appears to show a linear dissipation relation to the violin mode frequency. The reason that this is odd is because for one violin mode oscillation at 54 Hz

---

[2] As the clamping loss is not quantified it stops any correlations with silica loss and advanced LIGO mode coupling to be made.

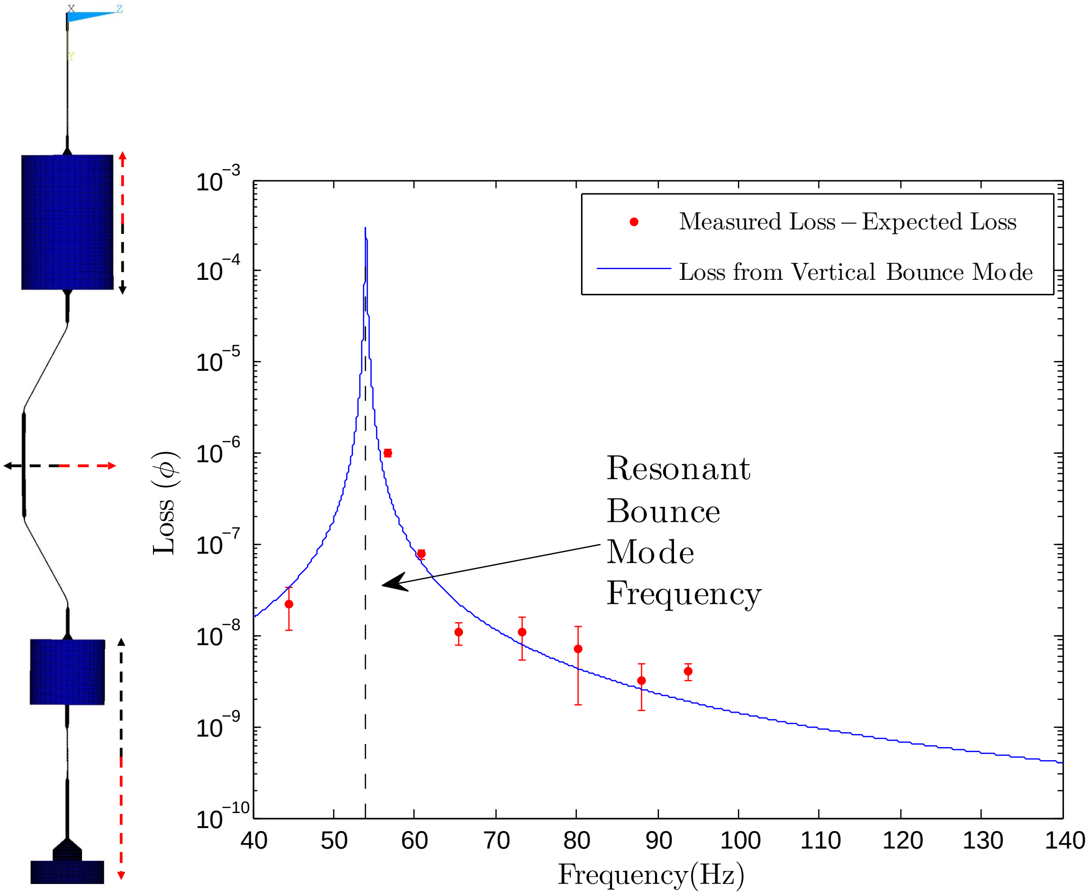

Figure 5.12: *Left: Image illustrating how violin mode energy could couple into vertical bounce. Right: Plot showing how the excess losses measured can be attributed to coupling with a vertical bounce mode as described by equation 5.5. Here* $\phi_{bounce\ loss} \sim 1.17 \times 10^{-7}$, $C_1 = 25.6$ *and* $C_2 = 1 \times 10^{-2}$.

the bounce mode being induced on the masses should be at twice the violin mode frequency, hence at 108 Hz well away from the loss peak which is observed in figure 5.12b. One explanation is that the bounce modes; while being driven at twice the frequency of natural resonance perhaps this is enough to excite bounce modes when the oscillations are in phase.

5.6 Conclusions

In this chapter we have built on the lessons learnt in chapter 4 and attempted to study low frequency violin modes. These modes maximised the thermoelastic loss contributions from fused silica fibres under varying degrees of stress in order to observe thermoelastic loss cancellation directly. The thick middle fibre pulled from 3 mm stock placed the majority of the strain energy in the thin section of the fibre whilst bringing the frequency of these modes closer to the thermoelastic loss Debye peak. It also minimised the loss contributions from the weld region and the steel masses used to vary the stress. From the data gathered in this chapter we have not been able to measure thermoelastic cancellation directly. We can however infer that energy has been dissipated via mode energy coupling with the vertical bounce mode which is something that has never been studied in great detail or considered before and was unexpected. If the thermoelastic loss cancellation is to be measured using violin modes the contribution from this vertical mode must be reduced. From figure 5.12 we can estimate that to bring the bounce mode loss coupling to an acceptable level of $\sim 1 \times 10^{-10}$ the violin modes being measured must be at least 100 Hz away from the bounce mode frequency. It shows that the thick middle section of these fibres has unfortunately helped to drive more energy into the bounce mode. It is possible that for a thinner fibre with less violin mode inertia this coupling would be reduced as no limiting effects were measured in the set-up used for chapter 4.

There are at least two bounce mode frequencies for a double pendulum system which will be of concern for future experiments of this type. The first is a bounce mode of the lower stage mass and the resonant frequency of this mode can be described by

$$f_{\mathrm{b}} \approx \frac{1}{2\pi}\sqrt{\frac{YA}{LM_{\mathrm{lower}}}} \tag{5.6}$$

where Y is the Young's modulus of the suspension fibre, A is the fibres cross sectional area, L is the length of the silica fibre and M_{lower} is the mass of the lower silica stage. It can be calculated that for a lower silica mass stage of 400g the bounce mode frequency is ~31 Hz. The second bounce mode is at a higher frequency and describes the isolation mass and lower stage silica mass moving in anti-phase with each other while the center of mass position between them remains constant. The bounce mode frequency can be described by

$$f_{\text{b}} \approx \frac{1}{2\pi}\sqrt{\frac{YA}{LM}} \tag{5.7}$$

where $M = \frac{M_{\text{upper}}+M_{\text{lower}}}{M_{\text{upper}}M_{\text{lower}}}$ with M_{upper} being the mass of the upper isolation stage. It is this frequency which has been attributed to the high losses measured at around 54 Hz. It is apparent from equations 5.6 and 5.7 that by using the thick middle fibre geometry tested in this chapter it will not be possible to lower the bounce mode loss contribution enough using larger masses without breaking the fibre. Even if a larger mass was used the tension on the fibre would be increased and the violin mode frequency would also increase further from the thermoelastic loss Debye peak making it difficult to study the nonlinear thermoelastic loss cancellation in the same way, especially when mode coupling would also be contributing to the losses.

5.7 Future Work

Making a direct measurement of the nonlinear thermoelastic loss cancellation is a very challenging measurement. It is made all the more difficult by the thermoelastic loss contribution falling off rapidly with frequency as the measurement frequency diverges from the Debye peak as described in equation 2.34.

As this experiment did not yield the required results a new experimental set-up must be designed. From the work presented in this chapter we observe that using a thick middle fibre to lower the resonant violin mode frequencies couples far too much energy into the vertical bounce mode to make the effects of thermoelastic loss observable. For this reason we must reconsider using a normal fibre violin mode similar to the one used in chapter 4. The most simple and effective solution that would give the required results would be to increase the length of the silica fibre shown in figure 4.7 by a factor of 2. This will reduce the violin mode resonant frequencies by a factor of 2. The stocks of the fibre which connect to the silica masses should be kept 3 mm in diameter to minimise the weld loss contribution. The geometry of this proposed re-design is shown in figure 5.13. It is possible that by varying the stress on the fibre

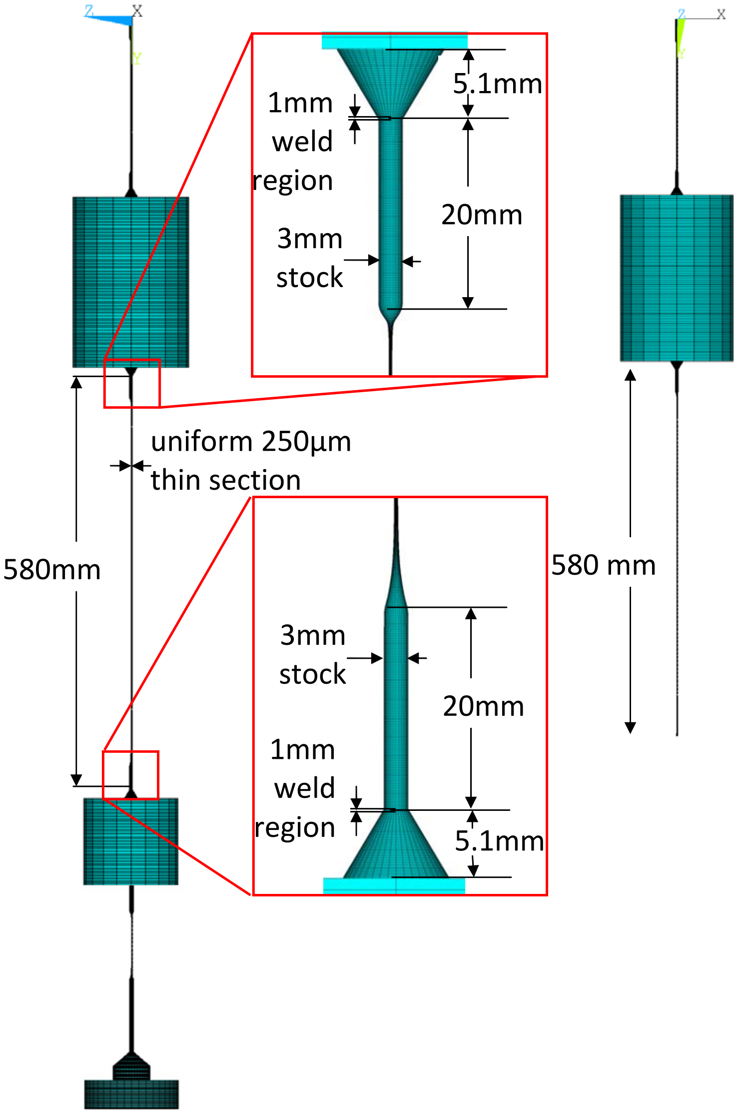

Figure 5.13: *Image showing the geometry of a fibre for the proposed experiment which may show nonlinear thermoelastic loss cancellation.*

and by measuring multiple violin modes with this newly proposed re-design we may be able to see the effects of nonlinear thermoelastic loss when compared to that of the thermoelastic loss with no dependance of Young's modulus varying with temperature.

The plots in figure 5.14 show how the losses from this redesigned experiment will vary depending on whether or not the thermoelastic loss behaves linearly or nonlinearly. Figure 5.14 shows the losses that will be seen when the stress of the silica is varied.

It is hoped that by taking measurements as was carried out previously in chapter 4 it will be possible to determine how the thermoelastic loss of fused silica behaves under stress. We hope to confirm that the thermoelastic loss does indeed follow the nonlinear trend which is essential for allowing second generation gravitational wave detectors to reach their target sensitivity.

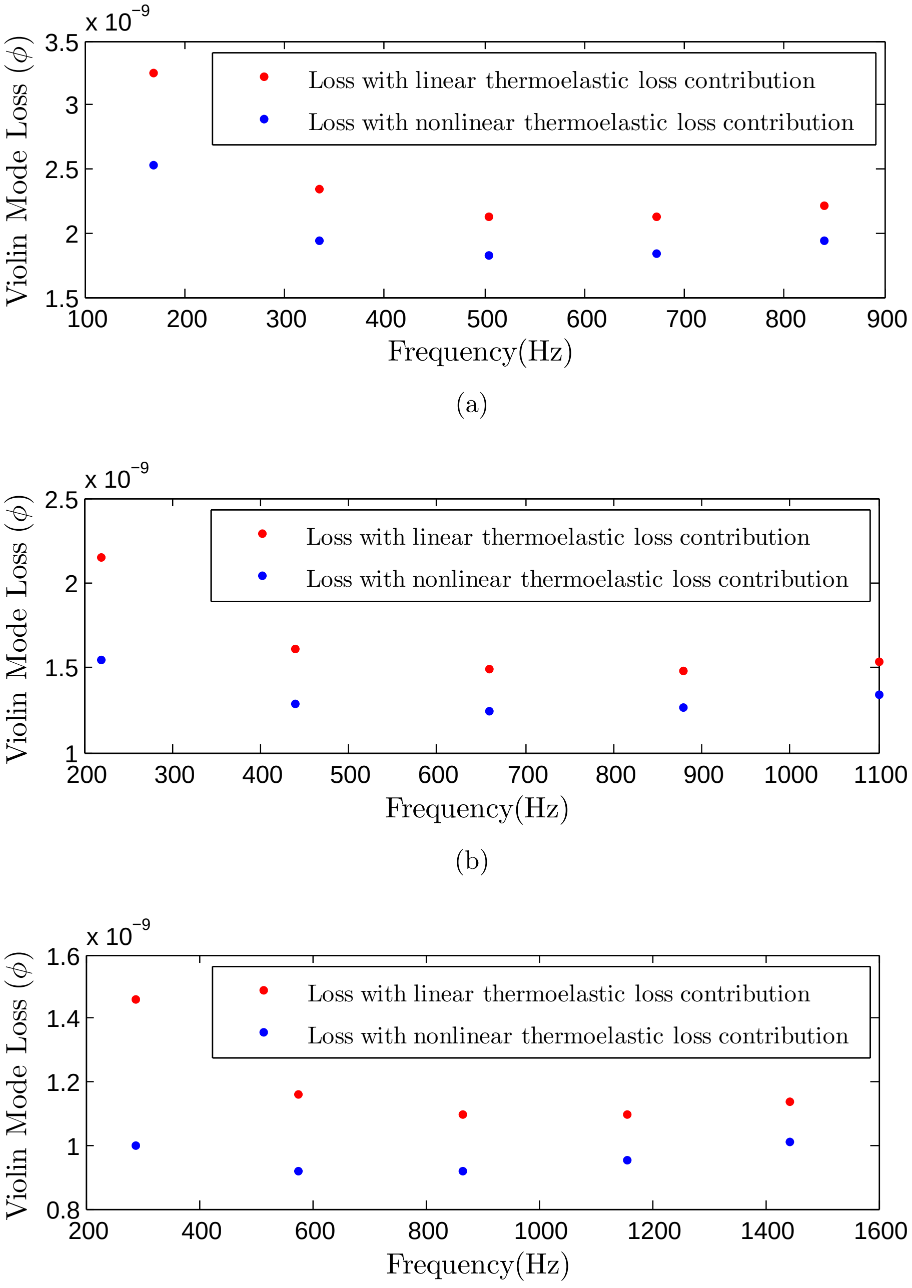

(a)

(b)

(c)

Figure 5.14: *Plot showing the loss comparison for three separate stress cases. Plots show the loss comparison for a 400 g (a), 800 g (b), and (c) a 1.2 kg stress case.*

Chapter 6

Mechanical Loss in 20-30μm Diameter Silica Fibres

6.1 Introduction

To improve the sensitivity of future gravitational wave detectors the effects from quantum noise must be reduced. At high frequencies the noise source in gravitational wave interferometers is due to the statistical counting of photons, called shot noise as described in section 1.5. In order to reduce shot noise the laser power can be increased. However, in doing so, radiation pressure noise increases at lower frequencies due to incident photons hitting the end mirrors and transferring momentum to the mirrors. There exists a laser power at which these two noise sources are optimised. At that power the detector will be running at what is known as the Standard Quantum Limit (SQL). It is however possible to 'beat' the SQL at a non-optimum laser power through the use of non-classical light or by using a technique called quantum non-demolition (QND) squeezed light [164] or "squeezing" [42, 76, 77].

To test and verify this technique quantum noise limited interferometers, such as the current km scale detectors, could be used. This would be impractical however because the detectors will be part of the international network and taking data. Therefore, a number of research groups around the world have proposed prototype experiments where lower levels of laser power can be used by scaling down the mass of the suspended mirrors. In this case the entire suspension system including the silica fibres used to hang the mirrors are also scaled down. In this chapter an experiment is described which is designed to measure the mechanical loss of thin silica fibres being developed to suspend the 100 g mirrors in the Hannover AEI 10 m prototype [18, 19] as shown in figure 6.1. As described in chapter 2 the sensitivity of these experiments will be related to the mechanical loss of the suspension systems through the fluctuation-dissipation theorem. Thin fibres have a large surface to volume ratio and so any loss measured will be dominated by the surface. In this chapter the loss of several AEI suspension fibres with a diameter of 20-30 μm

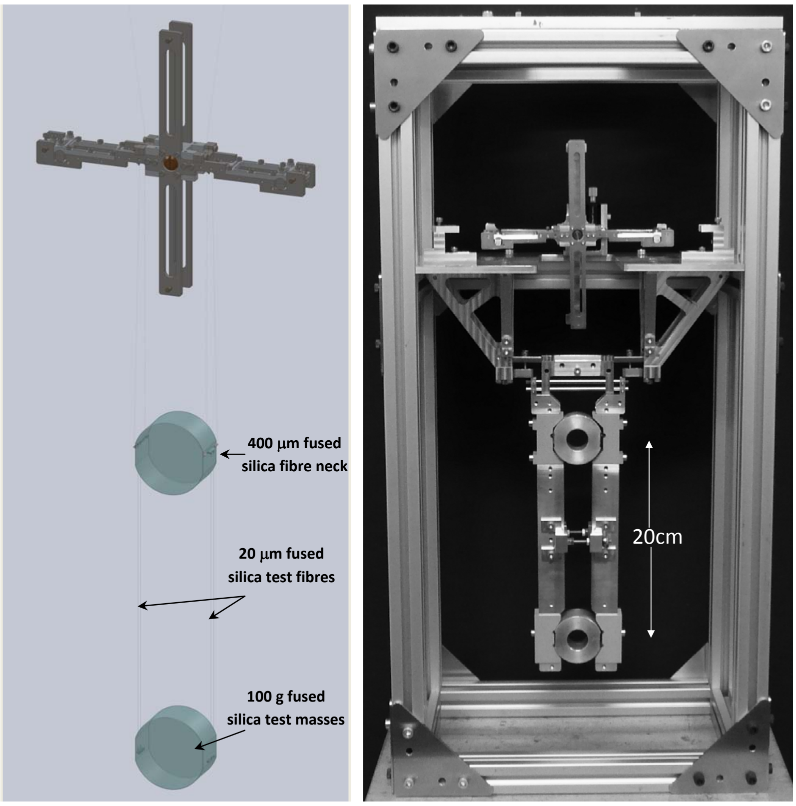

Figure 6.1: *Left: Solidworks model of AEI triple cascade suspension with an all silica last stage. Right: Full metal suspension prototype designed and built at Glasgow University.*

are measured and from these results the thermoelastic loss and surface loss of thin silica fibres is determined. The weld loss is also determined but this refers to a section that is 440 μm in diameter (above the fibre neck region) which is similar to the final AEI suspension design which will be used. This is essential for providing robust thermal noise estimates for the AEI suspensions. It is also important to make the loss of AEI suspensions as low as possible in order to be sensitive and able to measure the SQL at around the 100 Hz frequency bandwidth. The target thermal noise for the silica suspension to be used in the AEI prototype is $10^{-20}\mathrm{m}/\sqrt{\mathrm{Hz}}$ at 100 Hz [18, 19].

6.2 Experimental Set-up for Measuring Thin Fibres

Figure 6.2 shows the reflection monitor used to study the motion of fibres. Here a laser beam is reflected off the surface of the thin fibres and monitored using a split photodiode. This setup is possible due to the thin geometry of the fibres and the fact that they can be observed through a vacuum view port. The neck of the fibres is hydrogen flame welded onto a machined silica post bonded onto a silica cylinder of ≈0.5 kg. The fibres themselves have a

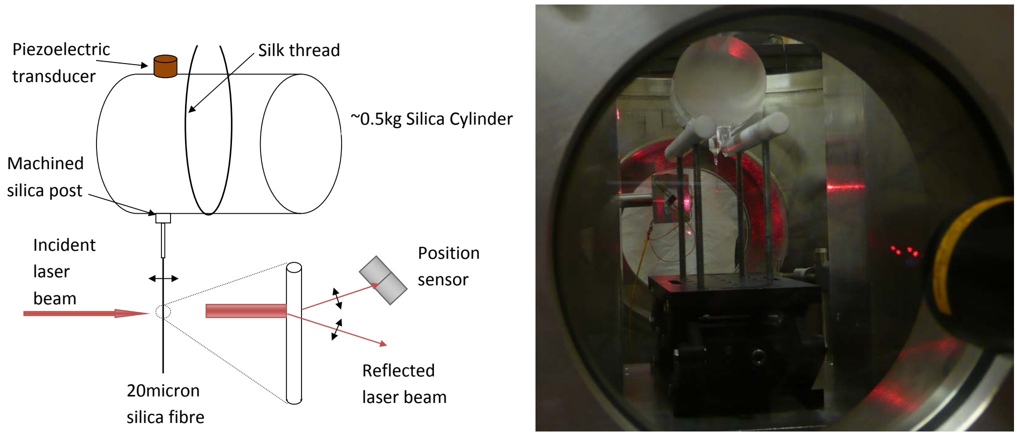

Figure 6.2: *Reflection set-up for thin fibre monitoring*

neck that is 440 µm in diameter before tapering to 20-30 µm. The fibres were fabricated in a unique way using the CO_2 laser based pulling machine [129]. Firstly a uniform 440 µm fibre was created from a 3 mm diameter section of fused silica stock. The CO_2 laser was then reset to focus on the centre of this 440 µm section from which the motors of the pulling machine were used again to create a 20-30 µm fused silica fibre with 440 µm diameter ends. A profile showing one of the six fibres which were studied is plotted in figure 6.3. The error on this diameter measurement is ±3 µm. The fibres were then cut in half so as the cantilever modes of the fibres could be studied. These modes were excited using a piezoelectric transducer attached on top of the cylindrical mass to which the fibres were welded (see figure 6.2). A piezoelectric transducer was used for thin fibre measurements over a electrostatic drive plate, as the fibres used were very thin allowing them to be displaced easily. It was a concern that an electrostatic drive would touch or surface charges would attract the fibre as it drifted around in air currents a thereby damaging the fibre surface.

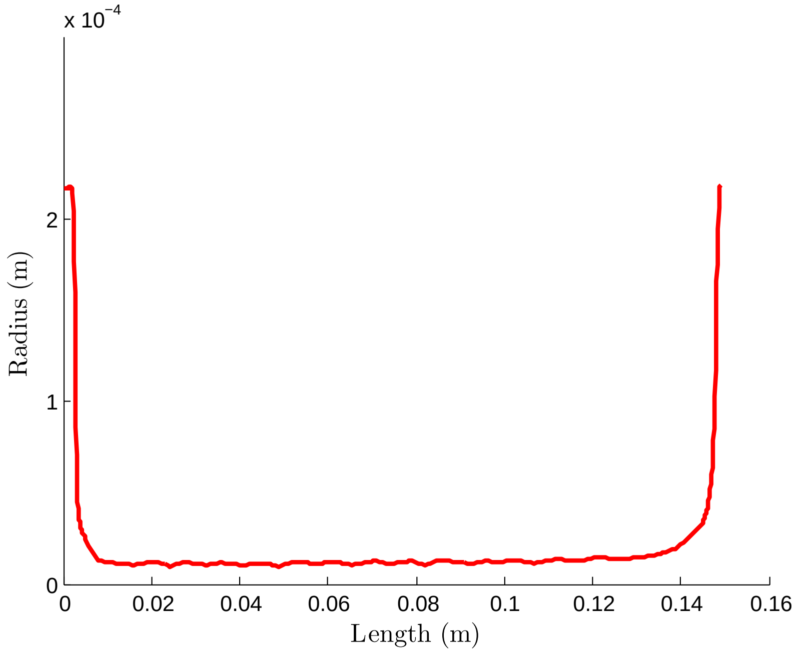

Figure 6.3: *Profile of an AEI fibre used.*

During the initial measurement run two separate cut fibres were studied and had their ring downs measured. After having the ring downs of the cut fibres measured one of the fibres was cut again making it shorter. Following this the new fibre modes were excited and the ring downs were re measured to check that the losses did not vary as a function of length and to give an error in the loss values measured. This cutting of the fibre was not continued as it was clear that larger errors came from the regression fitting process rather than the repeated loss measurements of the fibres. The fibres were so thin that observing them with the naked eye was difficult. In cutting the fibres there was also a risk of damaging the surface of the silica by accidentally touching the fibre as it floated around, easily perturbed by air currents outside of a vacuum. Static charges from gloves also made cutting the fibre difficult and so it was decided not to cut the fibre after measuring the first set of cantilever modes.

6.3 Preliminary Results

Figure 6.4 shows the profile of the first two fibres used for the initial measurements on which cantilever modes were excited. The ring downs of cantilever modes between the frequency range of 100 Hz to 15000 Hz were recorded and the losses were calculated as described in section 4.5 from equation 6.1.

$$\phi\left(\omega_o\right) = \frac{1}{Q\left(\omega_o\right)} = \frac{2\gamma}{\omega_o}, \tag{6.1}$$

where γ is the amplitude decay constant and ω_o is the resonant frequency of the mode being studied.

A sample of the initial results obtained is shown in figure 6.5. In this case the fibre was initially cut to have a thin section 5.5 cm long and the losses of the fibre modes measured. The fibre was then cut again making the thin section 3 cm long and the new modes measured. Notice that there are two points in figure 6.5 circled. These modes had abnormally low losses. This is

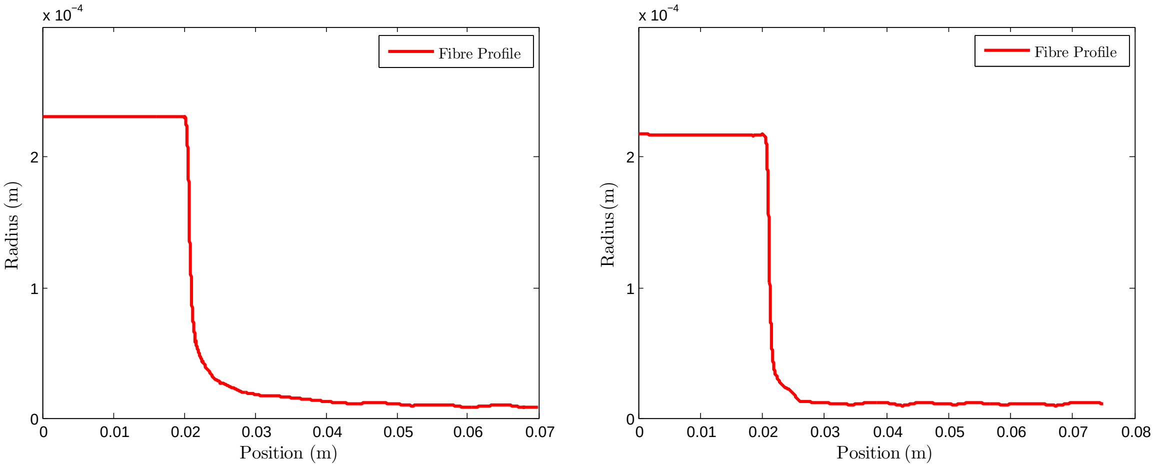

(a) (b)

Figure 6.4: *Plots showing the profiles of two AEI fibres that have been cut and used for cantilever loss measurements. (a) Shows the profile of Fibre 1 where the fibre has been cut to be 5 cm long in the thin section. (b) Shows the profile of Fibre 2 where the fibre has been cut to be 5.5 cm long in the thin section, this fibre was later cut to be 3 cm long.*

because the mode being excited is not a cantilever mode of the thin section but rather a mode of the thicker 440 μm stock. This means that most of the strain energy is being stored in the thicker section of the fibre as shown in figures 6.6 and 6.7.

Thus from equation 2.41 the surface loss contribution is now reduced as there is a smaller surface to volume ratio for modes of the thicker part of the system. In order to determine the surface loss for a thin AEI fibre the loss measurements had the thermoelastic [125] and bulk loss [141] terms as described by equation 2.34 and 2.42 removed as these contributed less than $< 20\%$ and $< 2\%$ to the total loss, respectively. In removing both loss contributions the remaining surface loss contribution still had to be accounted for, therefore a least squares fit was used to calculate the value of $h\phi_s$. The weld loss value was also not fitted as it contributed less than 2% of the total loss to the majority of the ring downs measured. Any attempt to regression fit the values of α

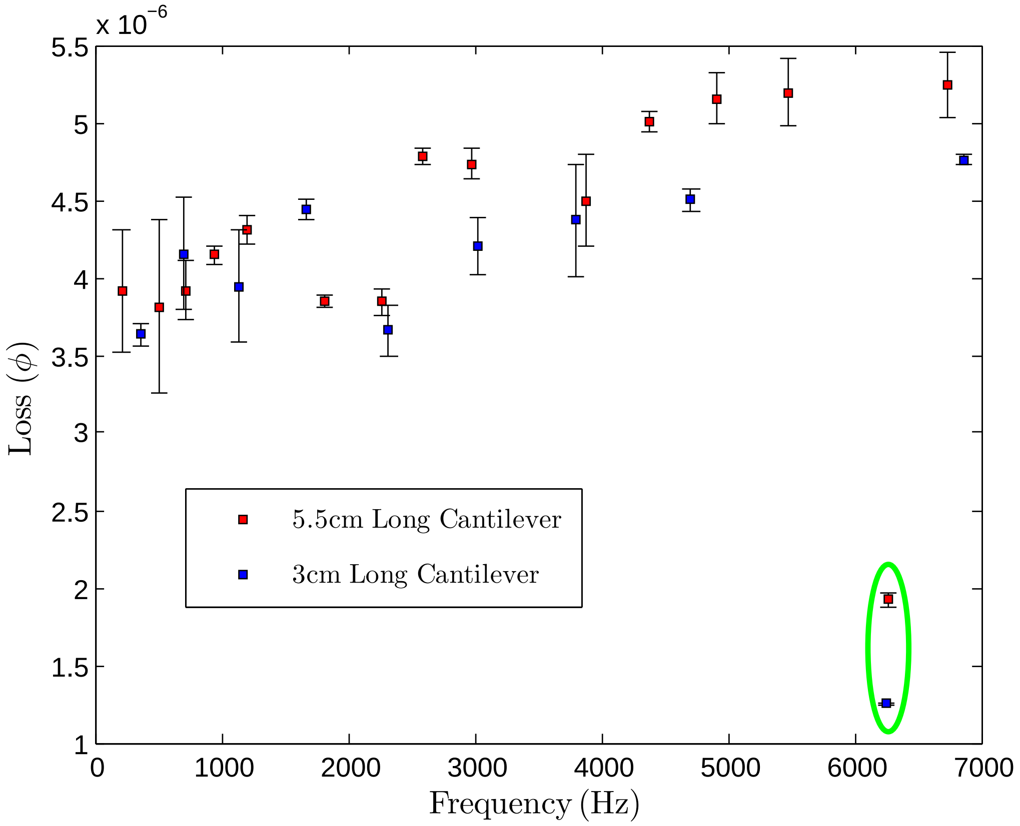

Figure 6.5: *Plot showing how the cantilever modes of the AEI fibre vary with frequency.*

from thermoelastic loss and ϕ_{weld} from weld loss resulted in negative loss values being determined which is unrealistic. For that reason α was assumed to be $3.7 \times 10^{-7}\mathrm{K}^{-1}$ and the weld region was treated as a surface. The regression calculated values of $h\phi_\mathrm{s}$ are shown in table 6.1.

	Length of thin section (cm)	$h\phi_\mathrm{s}$ (m)
Fibre 1	5	$(1.53 \pm 0.22) \times 10^{-11}$
Fibre 2	5.5	$(1.20 \pm 0.18) \times 10^{-11}$
	3	$(1.16 \pm 0.17) \times 10^{-11}$

Table 6.1: *Calculated $h\phi_s$ values for each of the fibres studied.*

As the AEI fibres are short and so thin they have significant tapering between the 440 µm section and the 20-30 µm region. This is a concern when

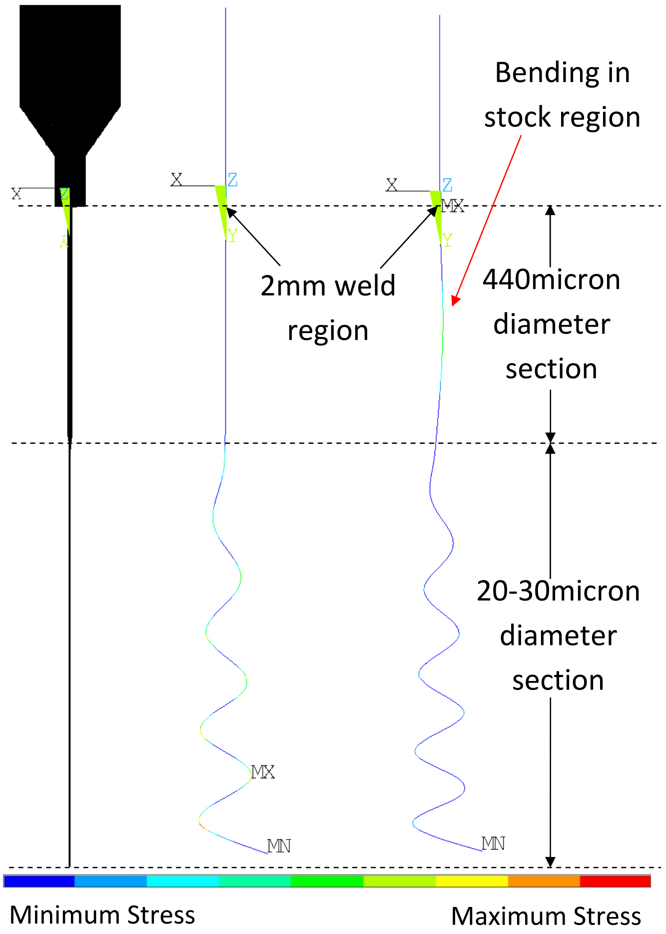

Figure 6.6: *Left: ANSYS mode shape for an AEI fibre mode with normal loss. Right: ANSYS mode shape for an AEI fibre mode corresponding to the lower losses see in figure 6.5.*

modeling the fibres in ANSYS as this scale of fibre had not been modeled before. To ensure that the tapering of the fibres was being modeled accurately a keypoint density of 10 keypoints/mm was chosen; this is five times the density used for aLIGO suspensions and ensures that the correct dimensions of the fibre are being modeled. To ensure that strain energy of the fibres' was also being correctly modeled a convergence check was carried out similar to ones used for aLIGO fibres [123, 128, 135, 159]. The convergence check of dilution is shown in figure 6.8 for a 20-30 µm section mode at 10,000 Hz. From section 2.4.3 the dilution of a vertically hanging silica fibre with no mass sus-

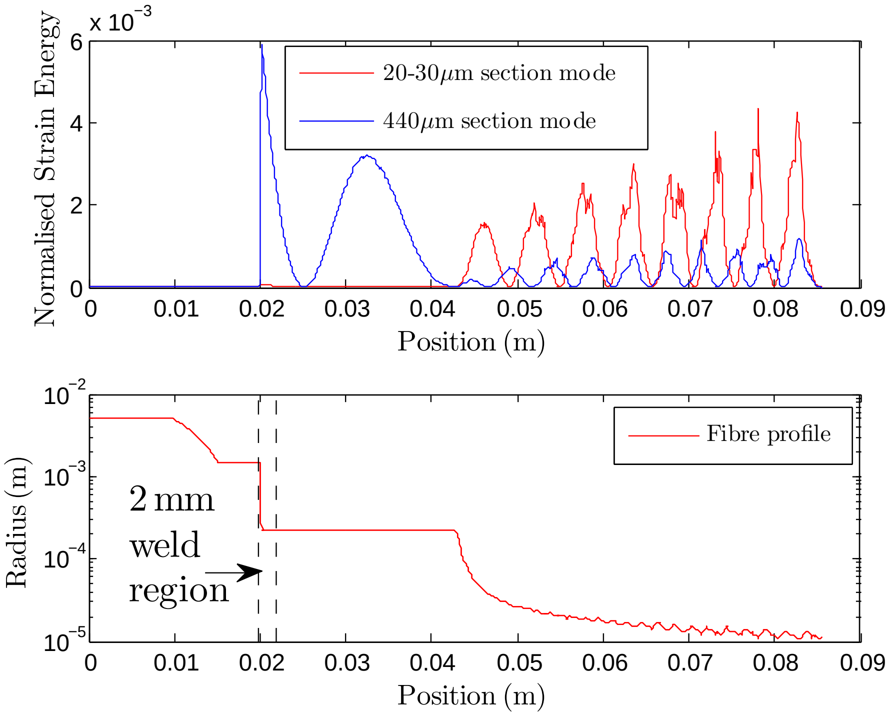

Figure 6.7: *Top: Strain distribution comparison from ANSYS of modes from the 440*µ*m section and the 20-30*µ*m section. Bottom: Profile of fibre modeled.*

pended from it is ≈ 1 and so if a dilution value of ~ 1 is predicted by ANSYS then we can say that the ANSYS solution has converged. This then allows us to use the strain energy distribution given by ANSYS and assume that it is modeling the strain distribution of the system correctly.

6.4 Excess Losses and Gas Damping

The surface losses in section 6.3 did not correspond with previously seen surface loss values measured in chapter 4 and 5 and also in literature [139, 141, 142] where a value of the order $\sim 10^{-12}$m was measured. One possibility considered as a cause for this high loss was energy being transferred to the upper 0.5 kg silica mass through mode coupling. Figure 6.9 shows an ANSYS model where the 0.5 kg fused silica mass was modeled as a solid. The first two modes of this mass were calculated from FEA to be at 27 kHz and 32 kHz, well above and

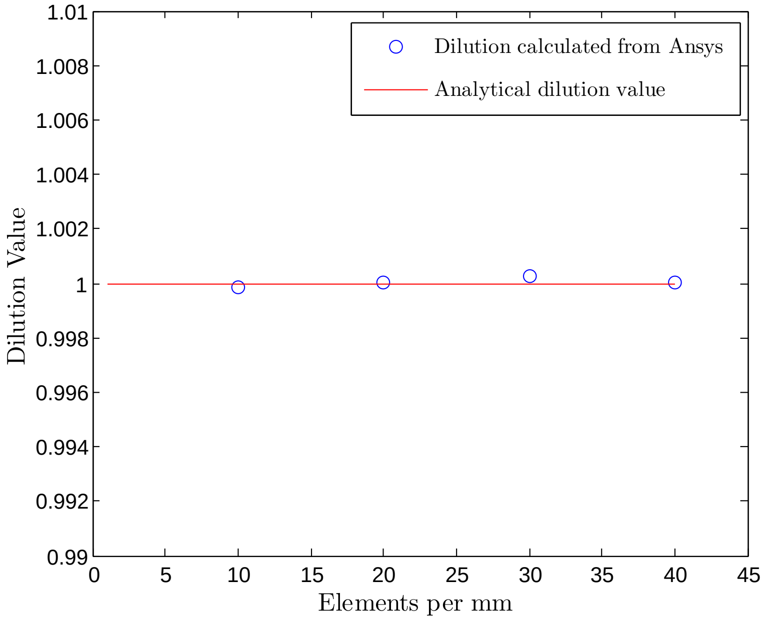

Figure 6.8: *Plot showing that with a mesh density 10 elements/mm the Finite Element model has reached a converged value.*

away from the resonant modes of the cantilever being measured. This finding suggested that this is not the way in which excess energy is being dissipated.

6.4.1 Recoil Losses

An experimental check was also carried out to make sure that no excess loss arose from the upper 0.5 kg silica mass vibrating and dissipating energy. For this test the modes of the silica fibre were excited and while these modes were decaying the piezo output (from the piezo initially used to excite the cantilever modes) was monitored. If energy was being dissipated in the upper mass then the piezo would be shaken and an output signal at the same frequency to the fibre modes would be detected on a spectral analyser. The results of this test are shown in figure 6.10. The results show clearly that there is no vibrational energy from the cantilever modes being dissipated in the piezo at a level which is observable above the piezo noise level. There are however peaks in the piezo output spectrum but these do not correspond with any of the cantilever mode

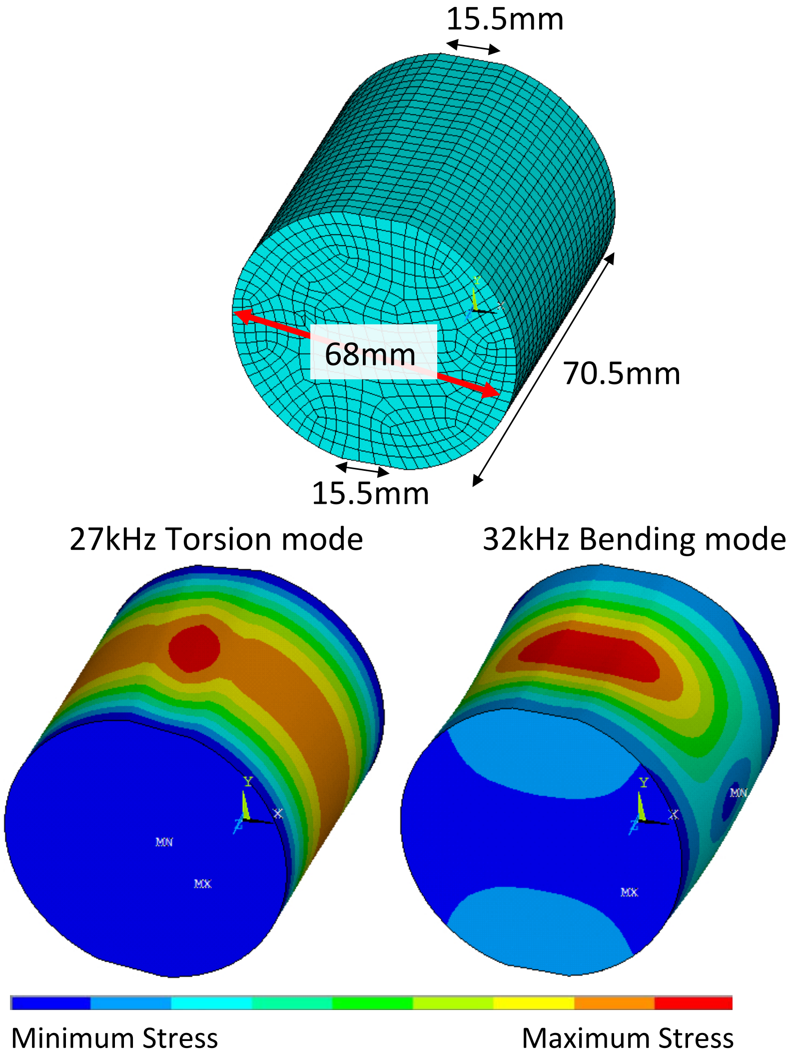

Figure 6.9: *ANSYS models of the 0.5 kg mass where the first two modes are at 27 kHz and 32 kHz.*

frequencies and are likely to arise from electrical noise in the turbo pumps, vacuum gauges and other electrical equipment. A further check with ANSYS showed that less than $10^{-7}\%$ of the strain energy from the fibre modes was reaching the low loss silica mass.

6.4.2 Gas Damping

Another experimental check was carried out to make sure that the high losses observed in table 6.1 were not being caused by excess gas damping. All mea-

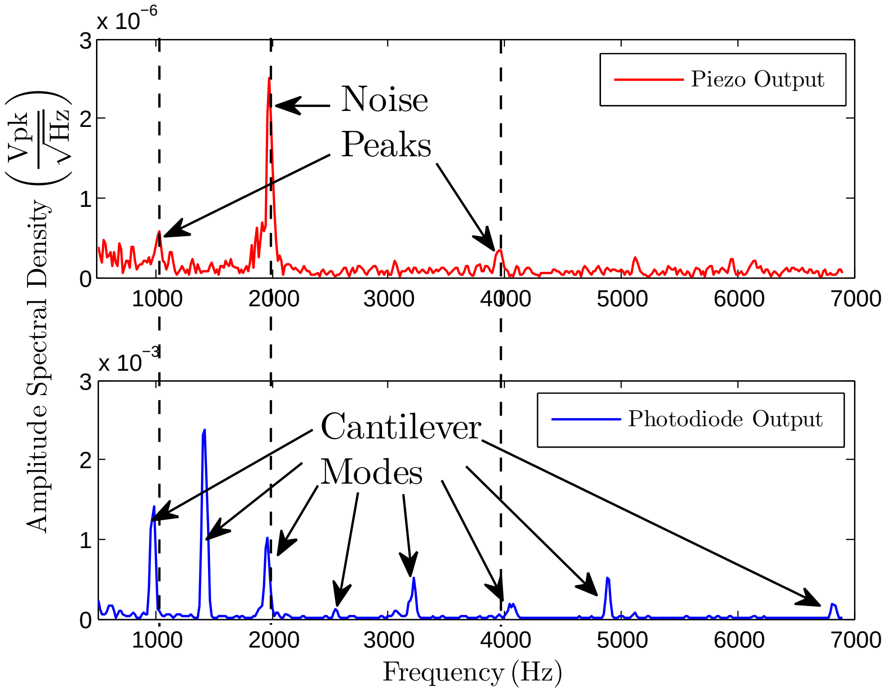

Figure 6.10: *Plots showing an amplitude spectral density from the piezo and photodiodes when cantilever modes are oscillating on the fused silica AEI fibre. No modes at 27 kHz or 32 kHz were observed.*

surements were made at a gas pressure of $\sim 9 \times 10^{-7}$ Torr in a vacuum tank. Equation 4.1 indicates that gas damping was an unlikely source of this excess loss. The loss calculated from gas damping on a fibre of 20µm at 1000 Hz is predicted to be $\sim 1 \times 10^{-9}$ well below the value of 4×10^{-6} measured in figure 6.5. To ensure that thin fibres are not more sensitive to gas damping effects, the loss of a mode at 5810 Hz was observed over a range of gas pressures from 9×10^{-7} Torr to 2×10^{-3} Torr. This gas pressure range was created by pumping the vacuum tank down to a base pressure of $\sim 9 \times 10^{-7}$ Torr. The vacuum was then baked for three days before leaking nitrogen gas into the vacuum tank through a needle value to increase the gas pressure. The plot shown in figure 6.11 shows that the effects of gas damping, as predicted by equation 4.1, agree well with what was observed experimentally and shows that at low pressures of $< 1 \times 10^{-4}$ Torr the measurements are not limited by gas damping.

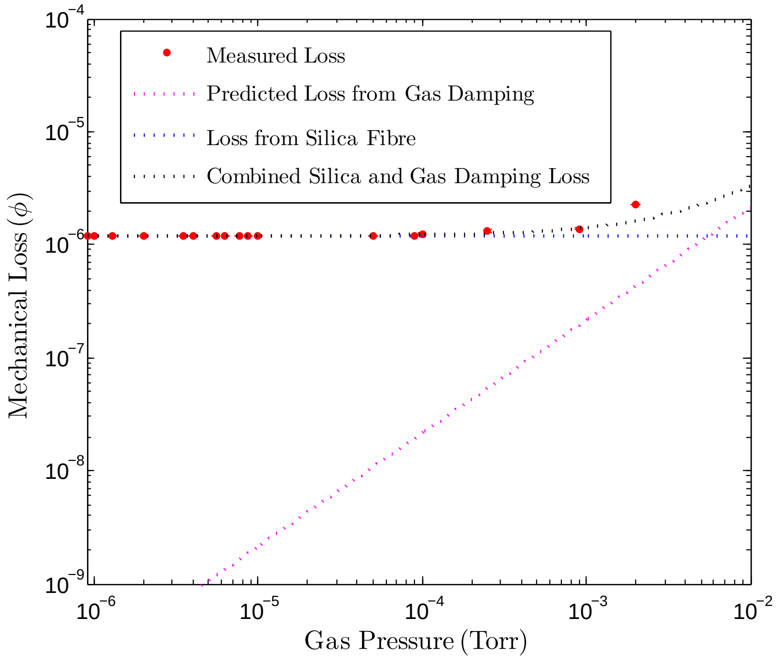

Figure 6.11: *Plot showing the mechanical loss varying as the gas pressure of the vacuum tank is increased.*

6.4.3 Water Vapour

The measured high loss must instead be attributed to a layer of water being held on the surface of the fibre even after being placed in a vacuum for weeks at a time. The experiment from section 6.3 was repeated but the vacuum was baked at 80°C for three days before loss measurements were taken. This was found to decrease dramatically the fibre loss value, as shown in figure 6.12.

When losses were measured after having fitted the vacuum bake, we were able to measure much lower surface losses. It was also interesting to note that for modes corresponding to oscillations of the thick 440 µm section the loss was higher than the nominal level, suggesting that for the 440 µm section modes we were now sensitive to weld loss.

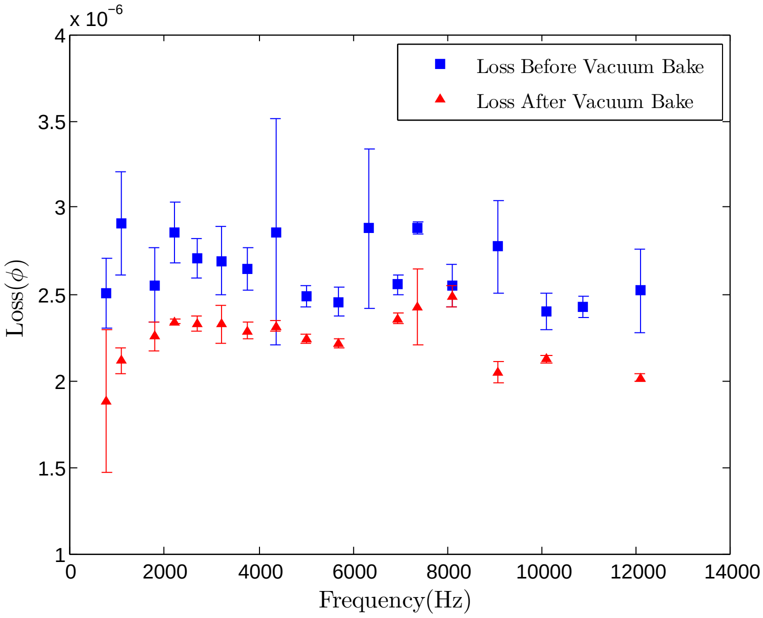

Figure 6.12: *Plot showing how the measured loss of an AEI fibre decreases as water is evaporated from the surface of the silica.*

6.5 Results

Figure 6.13 shows the profiles of four identically fabricated fibres that were studied after the vacuum had been pumped to a pressure of $\sim 9 \times 10^{-7}$ Torr and baked for three days at a temperature of 80°C. Figure 6.14 shows the losses measured and the corresponding weighted least squares fits for α, $h\phi_{\mathrm{s}}$ and ϕ_{weld} terms. The results shown in table 6.2 provide fits which explain the measured

	$h\phi_{\mathrm{s}}$ (m)	$\alpha\,(\mathrm{K}^{-1})$	ϕ_{weld}	Norm of Residuals
Fibre 1	$(6.3 \pm 0.6) \times 10^{-12}$	$(4.9 \pm 2.6) \times 10^{-7}$	$(6.2 \pm 1.1) \times 10^{-6}$	1.5×10^{-6}
Fibre 2	$(1.9 \pm 0.4) \times 10^{-11}$	$(2.7 \pm 2.7) \times 10^{-7}$	$(2.8 \pm 1.2) \times 10^{-5}$	4.6×10^{-6}
Fibre 3	$(3.6 \pm 0.1) \times 10^{-12}$	$(3.3 \pm 1.2) \times 10^{-7}$	$(9.1 \pm 0.5) \times 10^{-6}$	7.8×10^{-7}
Fibre 4	$(2.9 \pm 0.2) \times 10^{-12}$	$(3.7 \pm 1.6) \times 10^{-7}$	$(1.1 \pm 0.1) \times 10^{-5}$	1.1×10^{-6}

Table 6.2: *Calculated α, $h\phi_s$ and ϕ_{weld} values for each of the fibres studied after baking. The norm of residuals value is also listed to show how well the data matched the fit.*

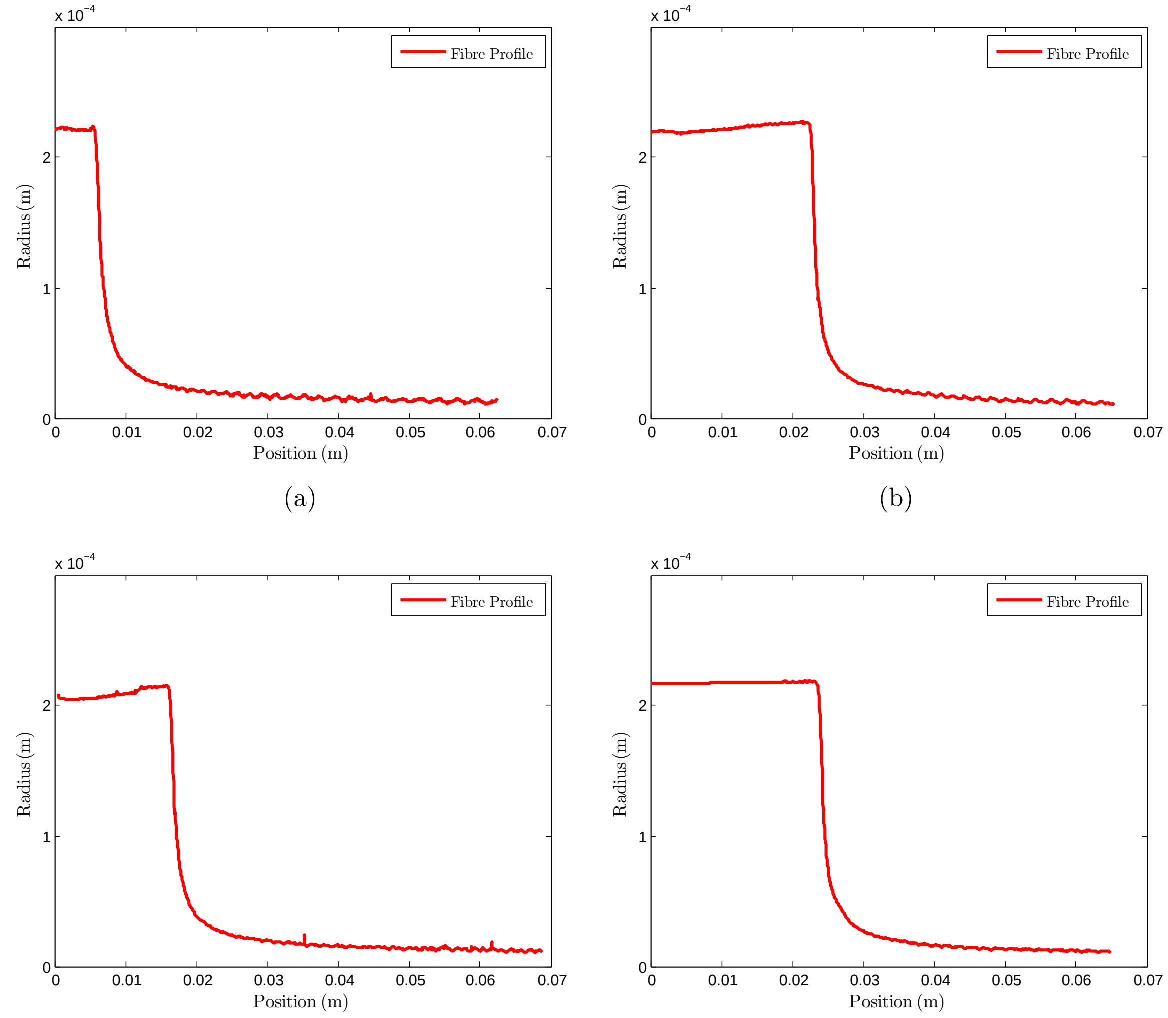

(a) (b) (c) (d)

Figure 6.13: *Plots showing the profiles of four AEI fibres that have been cut and used for loss measurements. The plots show the profiles for Fibre 1 (a), Fibre 2 (b), Fibre 3 (c) and Fibre 4 (d).*

losses to a high accuracy as shown by the norm of residuals value calculated by equation 4.9. The values of α determined here for each of the fibres is within acceptable limits, where a value of between $3 \times 10^{-7}\mathrm{K}^{-1}$ and $5.9 \times 10^{-7}\mathrm{K}^{-1}$ has been measured previously for heat treated silica [132, 135, 137, 155, 156]. These results also agree with measurements of α made in chapters 3, 4 and 5. The surface losses measured for fibres 1 and 2 suggest a higher surface loss

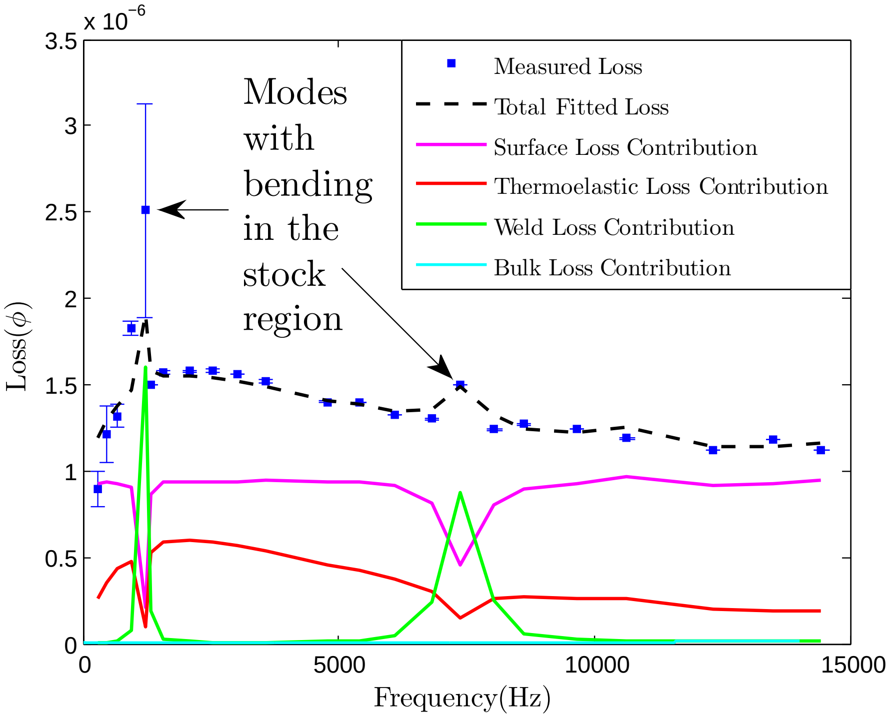

Figure 6.14: *Plot showing how the calculated thermoelastic, surface and weld loss contributions fits the measured losses for Fibre 3.*

than normal. This is probably due to the fibre being touched or damaged during the installation stages. The surface of thin fibres provides the dominant loss mechanism due to the increased surface to volume ratio. As we have seen from the results in section 6.3 even a thin layer of surface moisture is enough to increase the loss of these thin fibres by an order of magnitude. It is plausible that dust particles or scratches on the surface from mishandling of the fibre brought about the higher losses seen for fibres 1 and 2 even though the procedure for installing the fibres remained unchanged. Alternatively the system may not have been baked for long enough under low pressure. The values calculated for $h\phi_{\mathrm{s}}$ with the exception on fibres 1 and 2 match with surface loss values found in chapter 4 and 5. They are also consistent with recent published results [142], where the value of $h\phi_{\mathrm{s}}$ was measured as being $\sim 3 \times 10^{-12}$m. While the surface loss measured for fibre 1 is higher than expected it actually agrees well with previous values of surface losses measured for fused silica where $h\phi_s$ was found to be $\sim 6.15 \times 10^{-12}$m [135, 139, 141].

The value of ϕ_{weld} found in this chapter is over one order of magnitude higher than that observed in both chapter 4 and by Heptonstall et al [135]. There are a number of reasons as to why this might be the case. Firstly, the thin fibres were flame welded using a hydrogen oxygen flame which gives off water vapor as a byproduct of burning. If this vapor became trapped in the weld region it may explain the higher loss angle compared to CO_2 laser welds. Weld loss is also thought to come from thermal stresses developing in the silica as it is melted and cooled, leaving behind a residual stress in the material. Thinner fibres were used than previously studied in chapter 4 and [135]. For thinner fibres there is a much higher surface to volume ratio, dramatically increasing the rate at which heat is transferred into and away from the material. This in turn would have left behind a much larger residual stress. The other factor which may have led to more residual stress in the material was that these fibres were welded by hand and no machinery or tooling was used to hold the fibres [165] in a steady position. Small bends in the weld, as shown by figure 6.15, and may then explain the higher excess weld losses seen in the weld region for fibres 2, 3 and 4.

6.5.1 Cross Polariser Stress Imaging

To try and map in order to understand the residual stresses which could have been left over from the weld process, resulting in the high weld losses measured in table 6.2, a cross polariser polariscope set-up was utilised [136]. The technique is based on the property of birefringence. When an optically transparent non-crystalline photoelastic material such as silica is placed under stress the material exhibits birefringence in the stressed region. The effect is known as artificial birefringence and was first observed by Brewster in 1815 [166–168]. In 1853, Maxwell related the birefringence of a photoelastic material to its stress

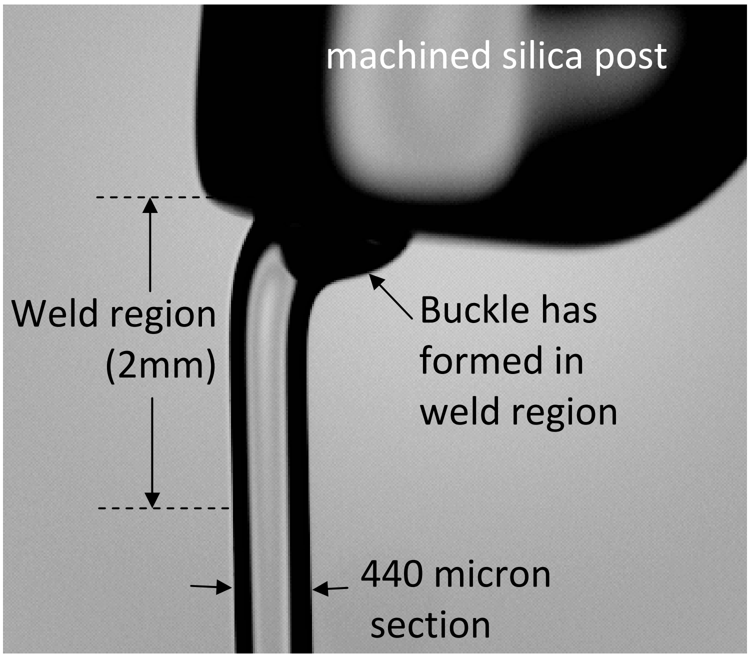

Figure 6.15: *Picture showing a bad weld which has had a small shear stress applied during the welding procedure.*

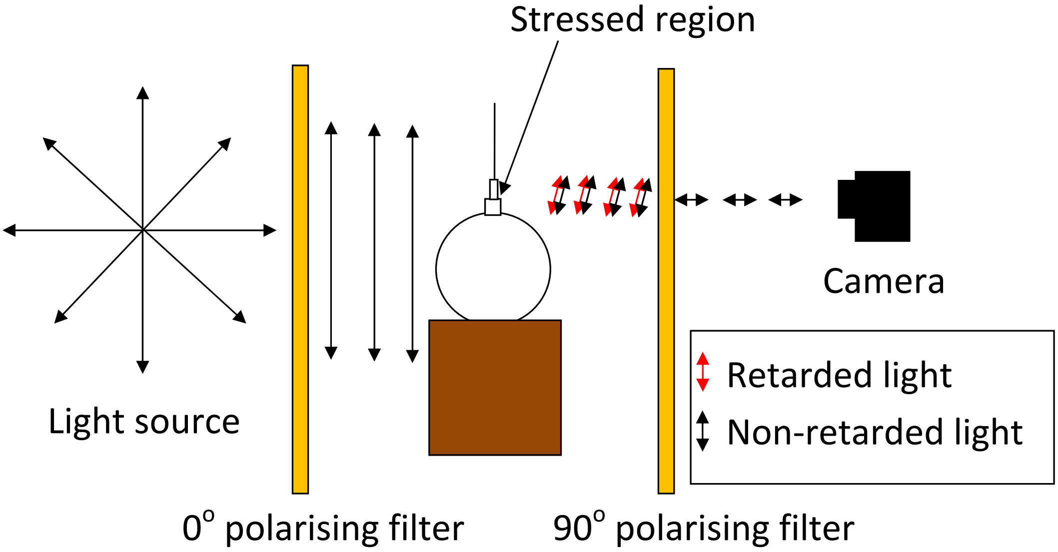

Figure 6.16: *Schematic showing how the cross polariser polariscope set-up was utilised.*

and developed the stress optic law [169, 170]. A schematic of the set-up used to study the artificial birefringence of fused silica is shown in figure 6.16. In figure 6.16 the initial light source is emitting light with multiple polarisations. This light is passed through a 0^o polariser and so all the light being transmitted to the sample (in this case the weld region of the silica) is linearly polarised at zero degrees. When this light reaches the stressed silica, the electromagnetic wave components are transmitted along the two principle stress directions of the silica. Each light component experiences a different amount of refraction dependent on the birefringent properties of the material. The two light components transmit through the silica sample but are now out of phase due to the different refractive indexes experienced by the light components. When the two light components recombine they form a state of light with a new degree of polarisation. This new polarisation angle is related again to the amount of retardation experienced between the two components. The magnitude of the relative retardation is given by the stress-optic law [169, 170],

$$\Delta = \frac{2\pi t}{\lambda} C(\sigma_1 - \sigma_2), \tag{6.2}$$

where Δ is the induced retardation measured in Brewsters (1 Brewster= $10^{-12}\mathrm{m}^2/\mathrm{N}$), λ is the wavelength of the light being transmitted, C is the stress-optic coefficient which for fused silica is $3.55 \times 10^{-12}\mathrm{m}^2/\mathrm{N}$ [171], t is the thickness of the sample and σ_1 and σ_2 are the two principle stresses. As there are now two light waves, the two waves interact to produce a fringe pattern. This fringe pattern can be described by $N = \Delta/2\pi$ where N is the fringe number being looked at. The second polariser at 90^o is used to remove the original unperturbed light which passed through the 0^o filter. Figure 6.17 shows what is seen when thermally stressed plastic is placed in the cross polariser. When the AEI fibre weld region was observed in the cross polariser set-up (as shown in figure 6.18) no clear birefringent image of the weld stresses could be seen. It is perhaps not surprising that the stresses from the polariser set-up could not be clearly seen. The small and circular geometry of the fibre made resolving the stress images very difficult. The stress-optic law (equation 6.2) is known to work well

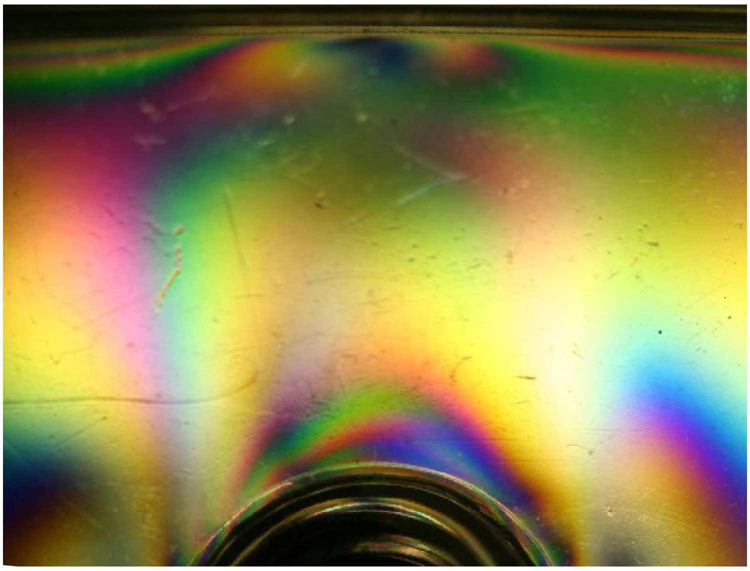

Figure 6.17: *Photo of protective goggles which have been thermally stress and put in the cross polariser set-up. The stress birefringence can be clearly seen as multiple colour fringes.*

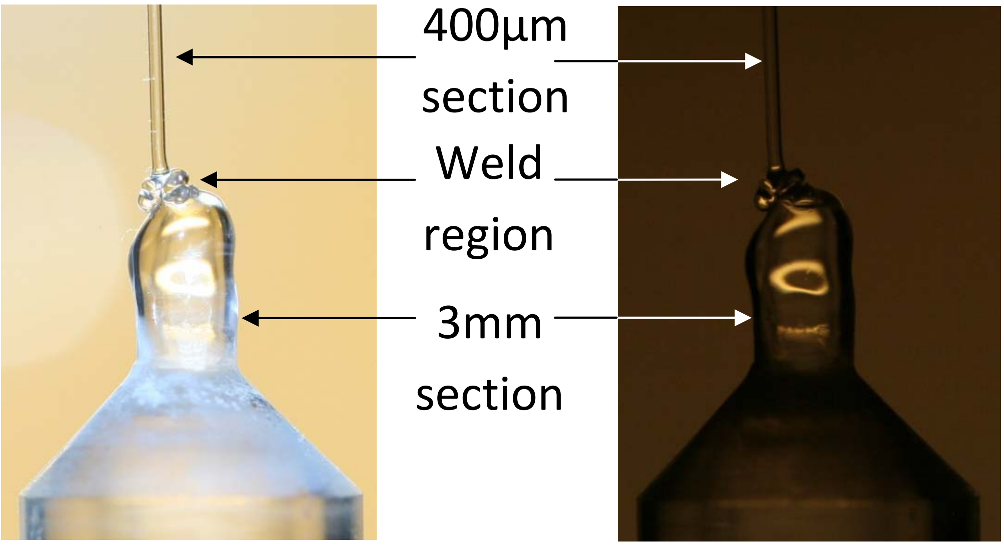

Figure 6.18: *Photo of an AEI fibre weld region before and after it was placed in the cross polariser set-up. No obvious birefringence can be seen.*

on uniform thickness silica samples [136] but studying circular geometries is a challenge for the future. The non-uniform thicknesses of the samples combined with effects from the focussing and scattering of light will make this study very complicated and difficult.

6.6 Conclusion

This chapter clearly demonstrated that the surface loss of thin 20-30 μm silica fibres can match that of thicker fibres studied in chapter 4. This is encouraging as it will allow the AEI suspension system to reach the target sensitivity of $10^{-20}\mathrm{m}/\sqrt{\mathrm{Hz}}$ at 100 Hz [18, 19]. The weld losses measured in this chapter are large. However this experiment was initially designed to measure the surface and thermoelastic loss of thin silica fibres. The weld loss is only measurable as a side effect of modes in the upper stock region being excited, a finding not initially expected. As weld loss was not expected to contribute to the loss proper precautions were not made when creating the weld regions studied. This is possibly why such large loss values have been measured. For the final AEI silica suspension much more care will be taken to create the weld region; with a weld region being created using a set-up similar to that used for aLIGO [165]. In the final AEI suspension, welding will be performed with a CO_2 laser beam focussed down to a spot size of ~ 0.5mm. This size of laser beam will create a much smaller weld region than the 2 mm studied in this chapter. During the welding process the fibre will also be held securely with tweezers and gold plated mirrors are used to provide heat to the fibre from all angles creating a more uniform weld. Moreover, an extraction pipe will be used to remove excess silica vapour which may form on the fibre as discussed in section 4.4. A picture of the final welding procedure to be used for these fused silica suspensions is shown in figure 6.19. In doing this the weld region will show no imperfections (silica vapour, lines or bulges) unlike those studied in this chapter. The lack of imperfection will reduce loss from the weld region considerably [135].

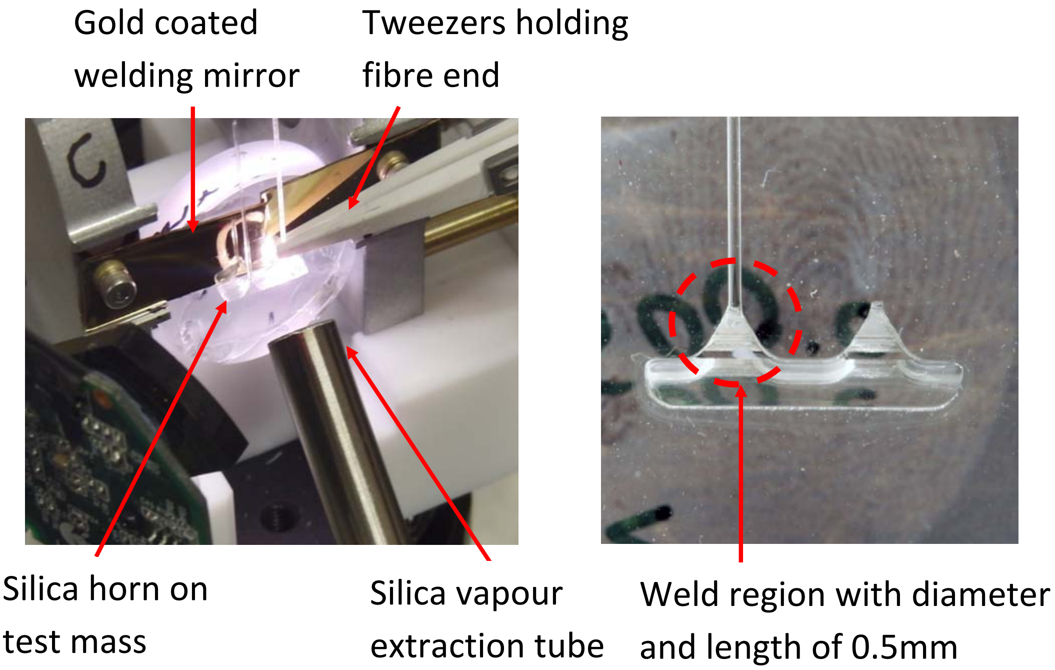

Figure 6.19: *Picture showing the weld procedure developed at the University of Glasgow which will be used for the final AEI suspension system [165].*

Chapter 7

Conclusions

The direct detection of gravitational waves is one of the most awaited tests of General Relativity, with long base line interferometry being the most promising method for their detection. The data which was gathered from the network of first generation gravitational wave detectors placed new constraints on a variety of astrophysical sources after reaching their design sensitivity. The first generation detector network is currently off-line except for GEO-HF which remains in "astrowatch" while the rest of the network is upgraded to form the second generation of detectors e.g. Advanced LIGO and Advanced VIRGO. It is predicted that when this second generation of detectors go online in 2015-16, they will make the first direct detection of gravitational waves along with placing better constraints on currently unknown astrophysical parameters.

In order to make the first direct detection of gravitational waves the strain sensitivity of Advanced LIGO will be increased by a factor of 10, allowing the volume of the universe that can be searched to be increased by a factor of 1000 [10, 12, 14]. Thermal noise of the mirror coatings and suspensions used to hang the test masses are the fundamental noise sources which will limit the sensitivity of advanced LIGO. Suspension thermal noise results from the random vibrations of atoms in the test mass mirrors and suspension fibres affecting the sensitivity of the detector at frequencies of $<$100 Hz.

The thermal noise levels in the gravitational wave detector suspension system can be predicted using the fluctuation dissipation theorem. The theorem shows that thermal noise is dependent upon the quality factor (Q, inverse of the mechanical loss) of the suspension design. The mirrors used in the detectors are hung from quadruple pendulums [11, 13] providing low frequency seismic noise isolation. The quadruple pendulums also store energy in the conservative gravitational field which is important as it allows the suspension thermal noise to be reduced via dissipation dilution [120]. The thermal noise is further reduced via the use of ultra low loss monolithic fused silica suspensions in the final stages of the pendulum. The mechanical loss of this silica material is made up of various terms including thermoelastic loss, surface loss, weld loss and bulk loss. This thesis has presented a complete study of these loss mechanisms which will limit the suspension sensitivity of gravitational wave detectors. This has allowed us accurately to predict the suspension thermal noise of aLIGO and to ensure that aLIGO will be capable of reaching its target design sensitivity of $10^{-19}\,\mathrm{m}/\sqrt{\mathrm{Hz}}$ at $10\,\mathrm{Hz}$.

It has been experimentally demonstrated in this thesis that the effective thermal expansion coefficient of a fused silica fibre can be nulled by placing the fibre under a particular level of stress of around 186 ± 13MPa. During the study we were also able to measure directly that the thermal expansion coefficient α, of a fused silica fibre fabricated using a CO_2 laser is in the region between $(4.2 \pm 0.5) \times 10^{-7}\mathrm{K}^{-1}$ while the coefficient of thermal elasticity β, was also measured to be $(1.58 \pm 0.09) \times 10^{-4}\mathrm{K}^{-1}$. This is an important result as it demonstrated for the first time that β for a fused silica fibre fabricated in this way is indeed positive [145] which allows for nonlinear thermoelastic cancellation [134]. Nulling of the effective thermal expansion coefficient should lower the thermoelastic noise contribution in silica suspensions and is essential for allowing second generation gravitational wave detectors to reach their target thermal noise sensitivity. Evidence for this nonlinear thermoelastic loss cancellation contributing to the mechanical loss of fused silica suspensions was provided in chapter 4. Further research to make a direct measurement of the nonlinear thermoelastic loss cancellation is still an anticipated result. This measurement was attempted in chapter 5 by using a thick middle fibre geometry and exciting fundamental violin modes under varying degrees of stress. However, due to the challenges faced with making these measurements the desired result was not achieved due to what appears to be bounce mode coupling loss. A new experimental design has been suggested in this thesis, the results of which could provide an interesting insight into how the thermoelastic loss contributes directly to the thermal noise of a detector.

The Q values of a monolithic fused silica suspension were measured to study the remaining dominant loss terms that limit the thermal noise sensitivity of silica suspensions. From this study it was determined that the surface loss term, $h\phi_{\mathrm{s}} = (2.89 \pm 0.07) \times 10^{-12}\mathrm{m}$ and the weld loss term, $\phi_{\mathrm{weld}} = (2.4 \pm 0.5) \times 10^{-7}$. Both of these values are lower than previous measurements made for fused silica [135, 139, 141]. It is believed that this improvement in the surface loss compared to other measurements (by a factor of 2) comes from the fused silica stock being polished with a CO_2 laser before the fibre was fabricated [142]. It was also shown that this surface loss value is consistent with smaller diameter fused silica fibres for applications in other kinds of interferometers. The low surface loss in thinner fibres was found to vary with the amount of water vapour being held on the surface of the silica which can dramatically increase the surface losses observed. For this reason thinner fibres must be baked under vacuum to evaporate water from the surface if they are to achieve a low thermal noise.

The improvement in the weld loss that was observed is believed to be a result of welds being created that showed no imperfections such as buckling, voids, inclusions or silica vapour deposits on the surface which previous studies have shown to increase the weld loss contribution [135]. The welding set-up used for this study is similar to that used for creating the aLIGO welds where a CO_2 laser is used to melt the silica stock and attach it to the ‘ear’, while a suction pipe is used to remove any silica vapour given off during heating. During this process special tooling was used to hold the horn and stock steady during the welding process in order to achieve an accurate, reproducible and uniform weld region [13]. Lack of tooling and care in creating welds likely to be the cause of the higher weld losses values which have been observed for thinner fibres in chapter 6 and also in previous literature [135]. Thus further research is needed to see if the weld loss observed for thinner fibres can be reduced by constructing homogenous welds in a more reproducible way. All of these loss values and measurements presented in this thesis will allow for more robust thermal noise predictions of the suspension thermal noise to be made in aLIGO.

Bibliography

[1] A. Einstein. Die Grundlage der allgemeinen Relativitatstheorie. *Annalen der Physik*, 49:769, 1916.

[2] R.A. Hulse and J.H. Taylor. Discovery of a pulsar in a binary system. *The Astrophysical Journal*, 195:51–53, 1975.

[3] P.A.R. Ade, R.W. Aitken, D. Barkat, S.J. Benton, C.A. Bischoff, J.J. Bock, et al. BICEP2 I: Detcection of b-mode polarization at degree angular scales. *arXiv:1403.3985v2*, 18th Mar 2014.

[4] A.G. Polnarev. Polarization and anisotropy induced in the microwave background by cosmological gravitational waves. *Soviet Astronomy*, 29(62):607–613, 1985.

[5] B. Schutz. Determining the Hubble constant from gravitaitonal wave observations. *Nature*, 323:310–311, 1986.

[6] M. Pitkin, S. Reid, S. Rowan, and J. Hough. Gravitational wave detection by interferometry (ground and space). *Living Review Relativity*, 14, 11th July 2011.

[7] H Lück, M Hewitson, P Ajith, B Allen, P Aufmuth, C Aulbert, et al. Status of the GEO600 detector. *Classical and Quantum Gravity*, 23(8), 2006.

[8] C. Bradaschia, R. Del Fabbro, A. Di Virgilio, A. Giazotto, H. Kautzky, V. Montelatici, D. Passuello, et al. The VIRGO project: A wide band antenna for gravitational wave detection. *Nuclear Instruments and Methods in Physics Research Section A: Accelerators, Spectrometers, Detectors and Associated Equipment*, 283, 1990.

[9] J.R. Smith. The path to the enhanced and Advanced LIGO gravitational-wave detectors. *LIGO Scientific Community*, 19th May 2009.

[10] P. Fritschel. Second generation instruments for the Laser Interferometer Gravitational wave Observatory (LIGO). *Proceedings of SPIE Gravitational Wave Detection*, 4856:282, 2003.

[11] N.A. Robertson, G. Cagnoli, D.R.M. Crooks, E.Elliffe, J.E. Faller, P. Fritschel, S. Gossler, A. Grant, A. Heptonstall, J. Hough, H. Luck, R. Mittleman, M. Perreur-Lloyd, M.V. Plissi, S. Rowan, D.H. Shoemaker, P.H. Sneddon, K.A. Strain, C.I. Torrie, H. Ward, and P. Willems. Quadruple suspension design for Advanced LIGO. *Classical and Quantum Gravity*, 22nd Oct.

[12] G.M. Harry (for the LIGO Scientific Collaboration). Advanced LIGO: the next generation of gravitational wave detectors. *Classical and Quantum Gravity*, 27(8), 6th Apr 2010.

[13] A.V. Cumming, A.S. Bell, L. Barsotti, M.A. Barton, G.Cagnoli, D.Cook, et al. Design and development of the Advanced LIGO monolithic fused silica suspension. *Classical and Quantum Gravity*, 29(3), 12th Jan 2012.

[14] S.M. Aston, M.A. Barton, A.S. Bell, N. Beveridge, B. Bland, A.J. Brummitt, et al. Update on quadruple suspension design for Advanced LIGO. *Classical and Quantum Gravity*, 29(23), 22nd Oct 2012.

[15] F. Acernese, P. Amico, M. Alshourbagy, F. Antonucci, et al. The Virgo 3km interferometer for gravitational wave detection. *Journal Of Optics A: Pure and Applied Optics*, 2008.

[16] S.E. Whitcomb. Ground-based gravitational-wave detection: now and future. *Classical and Quantum Gravity*, 25(11), 15th May 2008.

[17] T. Accadia, F. Acernese, M. Alshourbagy, P. Amico, F. Antonucci, et al. Virgo: A laser interferometer to detect gravitational waves. *Published by IOP publishing for Sissa Medialab*, May 2012.

[18] S. Gossler et al. The AEI 10 m prototype interferometer. *Classical and Quantum Gravity*, 27(8), 6th Apr 2010.

[19] F. Kawazoe, G. Bergmann, A. Bertolini, M. Born, Y. Chen, and A.V. Cummning. The AEI 10m prototype interferometer frequency control using the reference cavity and it's angular control. *Journal of Physics: Conference Series*, 363, 2012.

[20] Sir I. Newton. Philosophiae naturalis principia mathematica. *Londini, jussi Societatus Regiae ac typis Josephi Streater; prostat apud plures bibliopolas*, 1687.

[21] J.C. Maxwell. A dynamical theory of the electromagnetic field. *Philosophical Transactions*, 1864.

[22] A. Einstein. On the electrodynamics of moving bodies. *Annalen der Physik*, 17:891, 1905.

[23] A.A. Michelson and E.H. Morley. *American Journal of Science*, 34, 1887.

[24] A.S. Eddington. The total eclipse of 1919 May 29 and the influence of gravitation on light. *The Observatory*, 42:119–122, Mar 1919.

[25] J.H. Taylor, R.A. Hulse, L.A. Fowler, G.E. Gullahron, and J.M. Rankin. Further observations of the binary pulsar PSR B1913+16. *The Astrophysical Journal*, 206:L53–L58, 1976.

[26] J.H. Taylor and J.M. Weisberg. A new test of general relativity - gravitational radiation and the binary pulsar PSR B1913+16. *The Astrophysical Journal*, 253:908–920, 1982.

[27] J.M. Weisberg, D.J. Nice, and J.H. Taylor. Timing meassurements of the relativistic binary pulsar PSR B1913+16. *The Astrophysical Journal*, 722, 2010.

[28] B.S. Sathyaprakash and B.F. Schutz. Physics, astrophysics and cosmology with gravitational waves. *Living Reviews, Relativity*, 12(2), 4th Mar 2009.

[29] P.R. Saulson. *Fundamentals of Interferometric Gravitational Wave Detectors.* World Scientific Publishing Co., 1994.

[30] J. Aasi, J. Abadie, B. P. Abbott, R. Abbott, T. D. Abbott, M. Abernathy, et al. Prospects for localization of gravitational wave transients by the advanced ligo and advanced virgo observatories. *arXiv:1304.0670v1*, 2013.

[31] J. Abadie et al. Predictions for the rates of compact binary coalescences observable by ground-based gravitational-wave detectors. *Classical and Quantum Gravity*, 27(17), 16th July 2010.

[32] B.F. Schutz. Gravitational wave sources. *Classical and Quantum Gravity*, 13(11A):A219–A238, 1996.

[33] J. Logue, C.D. Otto, I.S. Heng, P. Kalmus, and J. Scargill. Inferring core-collapse supernova physics with gravitational waves. *arXiv:1202.3256[gr-qc]*, 2012.

[34] C.D. Otto. The gravitational-wave signature of core-collapse supernovae. *Classical and Quantum Gravity*, 26(6), 2009.

[35] E. Naker. Short-hard gamma-ray bursts. *Physics Reports*, 442:166–236, 25th Jan 2007.

[36] B. Abbott, R. Abbott, R. Adhikari, J. Agresti, P. Ajith, et al. Implications for origin of GRB070201 from LIGO observations. *The Astrophysical Journal*, 681:1419–1430, 10th July 2008.

[37] K. Thorne. Gravitational waves. *World Scientific, Singapore*, 1995.

[38] B. Abbott, R. Abbott, R. Adhikari, P. Ajith, B. Allen, G. Allen, R. Amin, S. B. Anderson, et al. Beating the spin-down limit on gravitational wave emission from the crab pulsar. *The Astrophysical Journal*, 683:45–49, 2008.

[39] S. Chandrasekhar. Solutions of two problems in the theory of graviational radiation. *Physics Review Letters*, 24:611–615, 30th Jan 1970.

[40] B. Zink, O. Korobkin, E. Schnetter, and N. Stergioulas. Frqequency band of the f-mode Chandrasekhar-Friedman-Schutz instability. *Physics Review D*, 81:371–388, 4th Mar 2010.

[41] R.V. Wagoner. Gravitational radiation from accreting neutron stars. *The Astrophysical Journal*, 278:345–348, 1984.

[42] J. Hough, H. Walther, B.F. Schutz, J. Ehlers, H. Welling, I.F. Corbett, and V. Kose. Proposal for a joint german-british interferometric gravitational wave detector. *Max-Planck-Institut fur Quantenoptik Report*, 147, 1989.

[43] The LIGO Scientific Collaboration and The Virgo Collaboration. An

upper limit on the stochastic gravitational-wave background of cosmological origin. *Nature Letters*, 460, 20th Aug 2009.

[44] S. Detweiler. Pulsar timing measurements and the search for gravitational waves. *The Astrophysical Journal*, 234:1100–1104, 15th Dec 1979.

[45] G.H. Janseen, B.W. Stappers, M. Kramer, et al. European Pulsar Timing Array: In 40 years of pulasrs: Millisecond pulsars, magntars and more. *American Institute of Physics Conference Series*, 983:633–635, 2008.

[46] R.N. Manchester. The Parkes Pulsar Timing Array project. In 40 years of pulsars: Millisecond pulsars, magnetars and more. *American Institute of Physics Conference Series*, 983:584–592, 2008.

[47] F. Jenet, L.S. Finn, J. Lazio, et al. The North American Nanohertz Observatory for Gravitational Waves. *arXiv:0909.1058v1*, 2009.

[48] G. Hobbs, A. Archibald, Z. Arzoumanian, et al. The International Pulsar Timing Array project: Using pulsars as a gravitational wave detector. *Classical and Quantum Gravity*, 27(8), 2010.

[49] J.H. Taylor and J.M. Weisberg. Further experimental tests of relativistic gravity using the binary pulsar PSR B1913+16. *The Astrophysical Journal*, 345:434–450, Oct 1989.

[50] A.de Waard, M.Bassan, Y. Benzaim, et al. Preparing for science run 1 of MiniGRAIL. *Classical and Quantum Gravity*, 23(8):79+, 24th Mar 2006.

[51] S.R. Furtado, O.D. Aguira, and D.S. Almeida. Progress report on the detection of very high sensitivity parametric transducer for the Mario Schenberg gravitational wave detector. 32, 2006.

[52] C. Frajuca. Resonant transducers for spherical gravitational wave detectors. *Brazilian Journal of Physics*, 35, Dec 2005.

[53] M. Bonaldi, C.M. Cerdonio, L. Conti, M. Pnard, G.A. Prodi, and J.P. Zendri. A broad band detector of gravitational waves: The dual torus. 4th Feb 2003.

[54] J. Weber. Gravitational-wave-detector events. *Physical Review Letters*, 20:1307–1308, June 1968.

[55] P. Astone, D. Babusci, M. Bassan, P. Bonifazi, P. Carelli, G. Cavallari, et al. Study of the coincidences between the gravitational wave detectors EXPLORER and NAUTILUS in 2001. *Classical and Quantum Gravity*, 19(21):5449–5463, 16th Oct 2002.

[56] L.S. Finn. No statistical excess in EXPLORER/NAUTILUS observations in the year 2001. *Classical and Quantum Gravity*, 20(4):L37–L44, 29th Jan 2003.

[57] M.E. Gertsenshtein and V.I. Pustovoit. On the detection of low frequency gravitational waves. *JETP*, 41:605–607, Aug 1962.

[58] M. Ando and the TAMA Collaboration. Current status of the TAMA300 gravitational-wave detector. *Classical and Quantum Gravity*, 22(18), 2005.

[59] Nation States. Mechanical properties of fused silica: Poisson ratio for fused quartz. `www.forum.nationstates.net`.

[60] R. Weiss. Electronically coupled broadband gravitational antenna. *Research Laboratory of Electronics (MIT)*, (105):54, 1972.

[61] J. Hough, S. Rowan, and B.S. Sathyaprakash. The search for gravitational waves. *Journal of Physics B: Atomic, Molecular and Optical Physics*, 38(105):S497–S519, 24th Apr 2005.

[62] D. Shoemaker, R. Schilling, L. Schnupp, W. Winkler, K. Maischberg, and A. Rudiger. Noise behaviour of the garchin 30-meter prototype gravitational-wave detector. *Physical Review D: Particles and Fields*, 38(2), 23rd Apr 1988.

[63] H. Grote, K. Danzmann, K.L.Doolet, R. Schnabel, J. Slutsky, and H. Vahlbrunch. First long-term application of squeezed states of light in a gravitational-wave observatory. *arXiv:1302.2188v3*, page 2, 23rd Apr 2013.

[64] K.D. Skeldon, K.A. Strain, A.I. Grant, and J. Hough. Test of an 18m long suspended modecleaner cavity. *Review of Scientific Instruments*, 1996.

[65] J. Hough. The search for gravitational waves. *Particles, Strings and Cosmology, 13th International Symposium*, 2008.

[66] R.W.P. Drever. A gravity-wave detector using optical cavity sensing. *Proceedings of the 9th International Conference on General Relativity and Gravitation, Cambridge University Press*, page 265, 1983.

[67] R.W.P. Drever, J. Hough, A.J. Munley, S.A. Lee, R. Spero, S.E. Whitcomb, et al. Optical cavity interferometers for gravitational wave detection. *Laser Spectroscopy V*, pages 33–40, 1981.

[68] A. Abramovici, W.E. Althouse, R.W.P. Drever, et al. LIGO-The Laser Intereferometer Gravitational-Wave Observatory. *Science*, 256:325–333, 1992.

[69] P.A. Seoane, S. Aoudia, G. Auger, S. Babak, E. Barausse, M. Bassan, V. Beckmann, and P. Binétruy. The gravitational universe: A science theme addressed by the eLISA mission observing the entire universe. 2013.

[70] G. Racca and the Review board. L1 mission reformulation, NGO - New Gravitational wave Observer, technical and programmatic review report. 2013.

[71] K. Danzmann and the LISA study team. LISA: Laser Interferometer Space Antenna for gravitational wave measurements. *Classical and Quantum Gravity*, 13(11A):A247–A250, 1996.

[72] K. Kuroda. Status of the LISA project. Nov 2010. ET meeting.

[73] European Space Agency. Esa's new mission to study the invisable universe. `http://www.esa.int/Our_Activities/Space_Science/ESA_s_new_vision_to_study_the_invisible_Universe`.

[74] J. Hough and S. Rowan. Laser interferometry for the detection of gravitational waves. *Journal of Optics A: Pure and Applied Optics*, 7:S257–S264, 9th May 2005.

[75] W.A. Edelstein, J. Hough, J.R. Pugh, and W. Martin. Limits to the measurement of displacement in an interferometric gravitational radiation detector. *Journal of Physics E: Scientific Instruments*, 11, 1978.

[76] R.E. Slusher, L.W. Hollberg, B. Yurke, J.C. Mertz, and J.F. Valley. Observation of squeezed states generated by four-wave mixing in an optical cavity. *Physical Review Letters*, 55, 1985.

[77] H. Vahlbruch, M. Mehmet, N. Lastzka, B. Hage, S. Chelkowski, A. Franzen, S. Gossler, K. Danzmann, and R. Schnabel. Observation

of squeezed light with 10db quantum noise reduction. *arXiv: 0706.1431*, 2007.

[78] A.H. Safavi, S. Goblacher, J.T. Hill, J. Chan, M. Aspelmeyer, and O. Painter. Squeezed light from a silicon micromechanical resonator. *Nature*, 500:185–189, 7th Aug 2013.

[79] The LIGO Scientific Collaboration. Enhancing the sensitivity of the ligo gravitational wave detector by using squeezed states of light. *Nature Photon*, 7:613–619, 1st Oct 2013.

[80] B.J. Meers. Recycling in laser-interferometric gravitational-wave detectors. *Physical Review D*, 38:2317–2326, Oct 1988.

[81] D. Schinier, J. Mizuno, G. Heinzel, H. Luck, A. Rudiger, R. Schilling, M. Schremple, W. Winkler, and K. Danzmann. Power recycling in the garching 30m prototype interefrometer for gravitational-wave detection. *Physics Letters A*, 225:210–216, 3rd Feb 1997.

[82] R. Adhikari. *Sensitivity and Noise Analysis of 4km Laser Interefrometric Gravitational Wave Antennae.* PhD thesis, Massachusetts Institute of Technology, 2004.

[83] R.W.P. Drever. Gravitational radiation. *North Holland Publishing Company*, 1983.

[84] L. Cunningham, M. Barton, G.D. Hammond, N. Robertson, K. Strain, and C. Torrie. Estimate of thermal and seismic noise from aLIGO quad suspension blade springs. *LIGO DCC*, LIGO-T1300595-v1, 28th June 2013.

[85] D. Shoemaker. `http://www.ligo.caltech.edu`.

[86] S. Hughes and K.Thorne. Seismic gravity-gradient noise in interferometric gravitational-wave detectors. *Physical Review D*, 58:122002, 1998.

[87] J. Harms, R. DeSalvo, S. Dorsher, and V. Mandic. Gravity-gradient subtraction in 3rd generation underground gravitational wave detectors in homogeneous media. *arXiv:0910.2774*, 2009.

[88] V.B. Braginsky, M.L. Gorodetsky, and S.P. Vyatchanin. Thermo-refractive noise in gravitational wave antennae.

[89] M. Evans, S. Ballmer, M. Fejer, G. Harry P. Fritschel, and G. Ogin. Thermo-optic noise in coated mirrors for high-precision optical measurements. *Physical Review D*, 78:102003–1–102003–10, 2008.

[90] A. Rudiger, R. Schilling, L. Schnupp, W. Winker, H. Billing, and K. Maischberger. A mode selector to suppress fluctuations in laser geometery. *Optica Acta*, 28(5):641–658, 1981.

[91] P. Campsie, G.D. Hammond, J. Hough, and S. Rowan. Development of a torsion balance for measuring charging noise. *Journal of Physics: Conference Series*, 363, 2012.

[92] D.H. Gwo. Ultra precision and reliable bonding method. 2001.

[93] P.H. Sneddon, S. Bull, G. Cagnoli, D.R.M. Crooks, E.J. Elliffe, J.E. Faller, M.M. Fejer, J. Hough, and S. Rowan. The intrinsic mechanical loss factor of hydroxy-catalysis bonds for use in the mirror suspensions of gravitational wave detectors. *Classical and Quantum Gravity*, 20(23):5025–5037, 17th Oct 2003.

[94] E. Gustafson. LSC white paper on detector research and developement. 1999.

[95] S. Kawamura. Status and plans for future generations of ground-based interferometric gravitational wave antennas. *Classical and Quantum Gravity*, 20(10), 2003.

[96] G.M. Harry (for the LIGO Scientific Collaboration). Advanced LIGO: the next generation of gravitational wave detectors. *Classical and Quantum Gravity*, 27, 2010.

[97] R. Powell. `http://www.atlasoftheuniverse.com`.

[98] C. Cutler and K.S. Throne. An overview of gravitational-wave sources. *arXiv:gr-qc/0204090*, 2002.

[99] J. Hough, K.A. Strain, S. Rowan, H. Ward, G. Woan, and G. Cagnoli. Investigations in gravitational waves: Glasgow university rolling grant proposal 2004-2009. *Institute for Gravitational Research: Glasgow*, 2009.

[100] H. Luck, C. Akeldt, J. Degallaix, A. Freise, H. Grote, M. Hewitson, S. Hild, J. Leong, M. Prijatelj, K.A. Strain, B. Willke, H. Wittel, and K. Danzmann. The upgrade of GEO600. *Journal of Physics: Conference Series 228 012012*, 2010.

[101] B. Willke, P. Ajith, B. Allen, P. Aufmuth, C. Aulbert, S. Babak, R. Balasubramanian, B.W. Barr, S. Berukoff, A. Bunkowski, et al. The GEO-HF project. *Classical and Quantum Gravity*, 23(8), 2006.

[102] T. Uchiyama, K. Kuroda, M. Ohashi, S. Miyoki, et al. Present status of large-scale cryogenic gravitational wave telescope. *Classical and Quantum Gravity*, 21(5):S1161, 13th Feb 2004.

[103] The ET Science Team. Einstein gravitational wave telescope conceptual design study. 2011.

[104] GWIC Roadmap Committee. The gravitational waves international committee roadmap:the future of gravitational wave astronomy. Technical report, Department of Physics and Astronomy, Kelvin Building, University of Glasgow, G12 8QQ, June 2010.

[105] S. Fairhurst. Improved source localization with LIGO India. *arXiv:1205.6611v2*, 2012.

[106] S. Kawamura et al. The Japanese space gravitational wave atenna-DECIGO. *Classical and Quantum Gravity*, 23(9):s125–s131, 2006.

[107] M. Ando et al. DECIGO and DECIGO pathfinder. *Classical and Quantum Gravity*, 27(8):10, 6th Apr 2010.

[108] S. Kawamura, M. Ando, N. Seto, S. Sato, T. Nakamura, K. Tsubono, et al. The Japanese space gravitational wave atenna: DECIGO. *Classical and Quantum Gravity*, 28, 18th Apr 2011.

[109] W.M. Folkner and D.J. Seidel. Gravitational wave missions from LISA to Big Bang Observer. *American Institute of Aeronautics and Astronautics*, 2005.

[110] D. Abbott, B.R. Davis, N.J. Phillis, and K. Eshraghian. Simple derivation of the thermal noise formula using window-limited fourier transforms and other conundrums. *IEEE Transactions on education*, 39(1), Feb 1996.

[111] R. Brown. A brief account of microscopical observations made on the particles contained in the pollen of plants. *London and Edinburgh philosophical magazine and journal of science*, 4:161–173, 1828.

[112] A. Einstein. Investigations on the theory of brownian movement. *New York Press*, 1956.

[113] H.B. Callen and T.A. Welton. Ireversibility and generalised noise. *Physical Review*, 83:34, 1951.

[114] H.B. Callen and R.F. Greene. On a theorem of irreversible thermodynamics. *Physical Review*, 86:702, 1952.

[115] H. Nyquist. Thermal agitation of electric charge in conductors. *Physical Review*, 32:110–113, 1928.

[116] P.R. Saulson. Thermal noise in mechanical experiments. *Physical Review D; Particles and Fields*, 42(8), Oct 1990.

[117] J.V. Fitzgerald. Anelasticity of glass. *Journal of the American Ceramic Society*, 34(10), 1951.

[118] C.C. Speake, T.J. Quinn, R.S. Davis, and S.J. Richman. Experiment and theory in anelasticity. *IOP Publishing Ltd*, 1999.

[119] A.S. Norwick and B.S. Berry. Anelastic relaxation in crystalline solids. *Academic Press, Mew Rork and London*, 1972.

[120] M. Barton. Dissipation dilution. *LIGO DCC*, LIGO-T070101-00, 2008.

[121] G. Cagnoli, J. Hough, D. DeBra, M.M. Fejer, E. Gustafson, S. Rowan, and V. Mitrofanov. Damping dilution factor for a pendulum in an interferometric gravitational wave detector. *Physics Letter A*, 272:39–42, 17th July 2000.

[122] G.I. Gonzalez and P.R. Saulson. Brownian motion of a mass suspended by an anelastic wire. *Journal of the accoustical society of America*, 96(207), 1994.

[123] R. Kumar. *Finite element analysis of suspension elements for gravitational wave detectors.* Masters thesis, School of Physics and Astronomy,

University of Glasgow, University of Glasgow, University Avenue, Glasgow, G12 8QQ, Aug 2008.

[124] G. Harry, A. Heptonstall, M. Evans, and N. Robertson. Q's of LASTI violin modes. *LIGO DCC*, LIGO-T1000468-v2, 2010.

[125] A.V. Cumming, A. Heptonstall, R. Kumar, W. Cunningham, C. Torrie, M. Barton, K.A. Strain, J. Hough, and S. Rowan. Finite element modelling of the mechanical loss of silica suspension fibres for advanced gravitational wave detectors. *Classical and Quantum Gravity*, 26, 2009.

[126] C. Zener. Internal friction in solids. *Physical Review*, 52:230–235, 1937.

[127] V.B. Bransky, M.L. Gorodetsky, and S.P. Vyatchanin. Thermodynamical fluctuations and photo-thermal shot noise in gravitational wave antennae. *Physics Letters A*, 1999.

[128] A.W. Heptonstall. *Characterisation of Mechanical Loss in Fused Silica Ribbons for use in Gravitational Wave Detector Suspensions.* PhD thesis, Department of Physics and Astronomy, University of Glasgow, 2004.

[129] A. Heptonstall, M.A. Barton, A. Bell, G. Cagnoli, C.A. Cantley, D.R.M. Crooks, A. Cumming, A. Grant, G.D. Hammond, G.M. Harry, J. Hough, R. Jones, D. Kelley, R. Kumar, I.W. Martin, N.A. Robertson, S. Rowan, K.A. Strain, K. Tokmakov, and M.V. Veggel. Invited article: CO_2 laser production of fused silica fibers for use in interferometric gravitational wave detector mirror suspensions. *Review of Scientific Instruments*, 82:011301, 2011.

[130] S. Spinner. Elastic moduli of glasses at elevated temperatures by a dynamic method. *Journal of the American Ceramic Society*, 39:113–118, 1956.

[131] S. Spinner and G.W. Cleek. Temperature dependence of young's modulus of vitreous germania and silica. *Journal of Applied Physics*, 38, 1960.

[132] P. Willems, V. Sannibale, J. Weel, and V. Mitrofanov. Investigations of the dynamics and mechanical dissipation of a fused silica suspension. *Physics Letters A*, 297:37–48, 2002.

[133] J.W. Marx and J.M. Sivertsen. Temperature dependence of elastic moduli and internal friction of silica and glass. *Journal of Applied Physics*, 24:81–87, 1953.

[134] G. Cagnoli and P.A. Willems. Effects of nonlinear thermoelastic damping in highly stressed fibres. *Physical Review B*, 65(174111):1–20, 24th Apr 2002.

[135] A.W. Heptonstall, M. Barton, C. Cantley, A. Cumming, G. Cagnoli, J. Hough, R. Jones, R. Kumar, I. Martin, S. Rowan, C. Torrie, and S. Zech. Investigation of mechanical dissipation in CO_2 laser-drawn fused silica fibres and welds. *Classical and Quantum Gravity*, 27(3), 2010.

[136] R. Kumar. *Aspects of suspension design for the development of advanced gravitational wave detectors.* Phd thesis, School of Physics and Astronomy, University of Glasgow, University of Glasgow, University Avenue, Glasgow, G12 8QQ, June 2013.

[137] G.K. White. Thermal expansion of reference materials: copper, silica and silicon. *Journal Physics D: Applied Physics*, 6:2070–2078, 1973.

[138] Heraeus Quartz Tech. Suprasil grade 2A datasheet, quartz glass for optics and data properties. `www.heraeus-quarzglas.com/media/webmedia_local/downloads/broschren_mo/dataandproperties_optics_fusedsilica.pdf`.

[139] A. Gretarsson, G.M. Harry, S.D. Penn, W.J. Startin, S. Rowan, G. Cagnoli, and J. Hough. Pendulum mode noise in advanced interferometers: a comparison of fused silica fibres and ribbons in the presence of surface loss. *Physics Letters A*, 2000.

[140] A.M. Gretarsson and G.M. Harry. Dissipation of mechanical energy in fused silica fibers. *Review of Scientific Instruments*, 70(10):4081–4087, Oct 1999.

[141] S.D. Penn, A. Ageev, D. Busby, G.M. Harry, A.M. Gretarsson, K. Numata, and P. Willems. Frequency and surface dependence of the mechanical loss in fused silica. *Physics Letters A*, 352:3–6, 2006.

[142] A. Heptonstall, M. Barton, A. Bell, A. Cumming, A. Grant, E. Gustafson, G. Hammond, J. Hough, R. Jones, R. Kumar, I. Martin, N. Robertson, S. Rowan, K. Strain, and K. Tokmakov. Enhanced characteristics of fused silica fibers using laser polishing. 2013. `http://dcc.ligo.org/P1200114`.

[143] K.V. Tokmakov, A.Cumming, J. Hough, R. Jones, R. Kumar, S. Reid, S. Rowan, N.A. Lockerbie, A. Warnner, and G. Hammond. A study of the fracture mechanisms in pristine silica fibres utilising high speed imaging techniques. *Journal of Non-Crytalline Solids*, 358:1699–1709, 2012.

[144] B.A. Proctor, I. Whitney, and J.W. Johnson. The strength of fused silica. *Proceedings of Royal Society London A*, 297:534–557, 1967.

[145] C.J. Bell, S. Reid, J. Faller, G.D. Hammond, J. Hough, I.W. Martin, S. Rowan, and K.V. Tokmakov. Experimental results for nulling the effective thermal expansion coefficient of fused silica fibres under a static stress. *Classical and Quantum Gravity*, 31(065010), 14th Feb 2014.

[146] V.P. Mitrofanov and K.V. Tokmakov. Effect of heating on dissipation of mechanical energy in fused silica fibers. *Physics Letters A*, 308:212–218, 2003.

[147] C. Bell, S. Reid, G.D. Hammond, J. Hough, I.W. Martin, and S.Rowan. Measuring the effective thermal expansion coefficient of fused silica. *LIGO DCC*, LIGO-T0900416-v2, 2012.

[148] F.C. Nix and D. MacNair. The thermal expansion coefficient of pure meatals: Copper, gold, aluminium, nickel, and iron. *Physical Review*, 60:597–605, 15th Oct 1941.

[149] M. Matsui and S. Chikazumi. Analysis of anomalous thermal expansion coefficient of Fe-Ni invar alloys. *Journal of the physical society of Japan*, 45(2):458–465, Aug 1978.

[150] Momentive. Mechanical properties of fused silica: Poisson ratio for fused quartz. `www.momentive.com/WorkArea/DownloadAsset.aspx?id=24696`.

[151] A. Cumming, R. Jones, M. Barton, G. Cagnoli, C.A. Cantley, D.R.M. Crooks, G. D. Hammond, A. Heptonstall, J. Hough, S. Rowan, and K.A. Strain. Apparatus for dimensional characterization of fused silica fibers for the suspensions of advanced gravitational wave detectors. *Review of Scientific Instruments*, 82, 2011.

[152] J.A. Beattie, B.E. Blaidell, J. Kaye, H.T. Gerry, and C.A. Johnston. *Proceedings of the American Academy of Arts and Science*, 17:371–388, 1941.

[153] M. Abramowitz and I.A. Stegan. Handbook of mathematical functions. *New York, NY: Dover*, 1965.

[154] H. Montulsky and A. Christopolus. *Fitting models to biological data using linear and non linear regression: A practical guide to curve fitting.* Oxford University Press, 2004.

[155] B. Kuhn and R. Schadrack. Thermal expansion of synthetic fused silica as a function of OH content and fictive temperature. *Journal of Non-Crystalline Solids*, 355:323–326, 2009.

[156] M.N. Darrouj and R.G. Faulkner. Apparatus for the absolute measurement of the linear thermal expansion coefficient of solids over a wide temperature range. *Journal Physics E: Scientific Instruments*, 22:2070–2078, 1989.

[157] R.G. Christian. The theory of oscillaing-vane vacuum gauges. *Vacuum*, 16:175–178, 1966.

[158] N.A. Roberst and J. Hough. Gas damping in Advanced LIGO suspensions. *LIGO DCC*, LIGO-T0900416-v2, 2009.

[159] A.V. Cumming. *Aspects of mirrors and suspensions for advanced gravitational wave detectors.* PhD thesis, University of Glasgow, 2008.

[160] S. Barnum, H. Radkin, K. Mason, and R. Mittleman. All BSC, Install complete cartridge into chamber procedure, aLIGO. *LIGO DCC*, LIGO-E1200344-v4, 11th Feb 2014.

[161] S. Reid. *Studies Of Materials For Future Ground-Based and Space Based Interferometric Gravitational Wave Detectors.* PhD thesis, Department of Physics and Astronomy, University of Glasgow, 2006.

[162] P.C. Gregory. Bayesian logical data analysis for the physical sciences: A comparative approach with mathematica support. *Cambridge: Cambridge University Press*, 2005.

[163] P. Willems, C. Lamb, A.W.Heptonstall, and J. Hough. Search for stress dependance in the internal friction of fused silica. *Physics Letters A*, 319:8–12, 29th Sept 2003.

[164] C.M. Caves. Quantum-mechanical noise in an interferometer. *Physical Review D*, 23(8), 1981.

[165] A. Cumming. Suspension systems for the AEI 10m prototype. *LIGO DCC*, LIGO-G100344-v3, 20th Sept 2012.

[166] D. Brewster. Experiments on the depolarization of light as exhibited by various mineral, animal and vegetable bodies with a reference of the phenomena to the general principle of polarization. *Philosophical Transactions, Royal Society of London*, pages 29–53, 1815.

[167] D. Brewster. On the communication of the structure of doubly refracting crystals to glass, muriate of soda, flour spar and other substances by mechanical compression and dilatation. *Philosophical Transactions, Royal Society of London*, 105:60–64, 1815.

[168] D. Brewster. On the effects of simple pressure in producing that species of crytallization which forms two oppositely polarised images and exhibits the complementary colours of polarised light. *Philosophical Transactions, Royal Society of London*, 105(60), 1815.

[169] E.G. Coker and L.N.G. Filon. A treatise on photoelasticity. *Cambridge University Press*, 1931.

[170] A. Kuske and G. Robertson. Photoelastic stress analysis. *London: John Wiley and Sons*, 1974.

[171] N.K. Sinha. Normalised dispersion of birefringence of quartz and stress optical coefficient of fused silica and plate glass. *Physics and Chemistry of Glasses*, 19(4):69–77, 1978.